

# Plasma–material interactions in current tokamaks and their implications for next step fusion reactors

G. Federici<sup>a</sup>

ITER Garching Joint Work Site,  
Garching, Germany

C.H. Skinner<sup>b</sup>

Princeton Plasma Physics Laboratory,  
Princeton University, Princeton,  
New Jersey, USA

J.N. Brooks<sup>c</sup>

Argonne National Laboratory, Argonne,  
Illinois, USA

J.P. Coad

JET Joint Undertaking, Abingdon,  
United Kingdom

C. Grisolia

Tore Supra, CEA Cadarache,  
St.-Paul-lez-Durance,  
France

A.A. Haasz<sup>d</sup>

University of Toronto, Institute for Aerospace Studies, Toronto,  
Ontario, Canada

A. Hassanein<sup>e</sup>

Argonne National Laboratory, Argonne,  
Illinois, USA

V. Philipps

Institut für Plasmaphysik, Forschungszentrum Jülich,  
Jülich, Germany

C.S. Pitcher<sup>f</sup>

MIT Plasma Science and Fusion Center, Cambridge,  
Massachusetts, USA

J. Roth

Max-Planck-Institut für Plasmaphysik,  
Garching, Germany

W.R. Wampler<sup>g</sup>

Sandia National Laboratories, Albuquerque,  
New Mexico, USA

D.G. Whyte<sup>h</sup>

University of California, San Diego, La Jolla,  
California, USA

# Contents

<b>1. Introduction/background</b>	1968
1.1. Introduction	1968
1.2. Plasma edge parameters and plasma–material interactions	1969
1.3. History of plasma facing materials	1973
<b>2. Plasma edge and plasma–material interaction issues in next step tokamaks</b>	1977
2.1. Introduction	1977
2.2. Progress towards a next step fusion device	1977
2.3. Most prominent plasma–material interaction issues for a next step fusion device	1980
2.4. Selection criteria for plasma facing materials	1995
2.5. Overview of design features of plasma facing components for next step tokamaks	1998
<b>3. Review of physical processes and underlying theory</b>	2002
3.1. Introduction	2002
3.2. Sputtering erosion/redeposition processes	2002
3.3. Erosion by arcing	2012
3.4. Erosion during off-normal plasma events	2014
3.5. Hydrogen recycling and retention in plasma facing materials	2016
<b>4. Existing experimental database on plasma–material interactions in tokamaks</b>	2029
4.1. Introduction	2029
4.2. Measurements of plasma–material interactions	2029
4.3. Review of tokamak erosion/redeposition experience	2033
4.4. Experimental evidence for arcing in tokamaks	2043
4.5. Disruption erosion in simulation devices and tokamaks	2044
4.6. Control of plasma–material interactions	2051
4.7. Database on H isotope retention and removal	2056
4.8. Dust and flake experience	2076
<b>5. Application of models and predictions for next step tokamaks</b>	2082
5.1. Introduction	2082
5.2. Plasma edge modelling	2084
5.3. Sputtering erosion and co-deposition modelling	2088
5.4. Modelling of erosion during ELMs and off-normal events	2094
5.5. Modelling of particle–wall recycling	2097
5.6. Modelling of long term implanted tritium inventory/permeation	2102
<b>6. Conclusion and future R&amp;D priorities</b>	2104
6.1. Erosion and co-deposition effects	2105
6.2. Tritium retention and control of the in-vessel tritium inventory	2107
6.3. Requirements for modelling and interpretation of tokamak data	2108
6.4. Need for improved wall diagnostics	2109
6.5. Dust effects	2109
6.6. A next step fusion reactor without carbon plasma facing components	2109
6.7. Concluding remarks	2110
<b>7. Glossary of terms and acronyms</b>	2110

**Abstract.** The major increase in discharge duration and plasma energy in a next step DT fusion reactor will give rise to important plasma–material effects that will critically influence its operation, safety and performance. Erosion will increase to a scale of several centimetres from being barely measurable at a micron scale in today’s tokamaks. Tritium co-deposited with carbon will strongly affect the operation of machines with carbon plasma facing components. Controlling plasma–wall interactions is critical to achieving high performance in present day tokamaks, and this is likely to continue to be the case in the approach to practical fusion reactors. Recognition of the important consequences of these phenomena stimulated an internationally co-ordinated effort in the field of plasma–surface interactions supporting the Engineering Design Activities of the International Thermonuclear Experimental Reactor project (ITER), and significant progress has been made in better understanding these issues. The paper reviews the underlying physical processes and the existing experimental database of plasma–material interactions both in tokamaks and laboratory simulation facilities for conditions of direct relevance to next step fusion reactors. Two main topical groups of interaction are considered: (i) erosion/redeposition from plasma sputtering and disruptions, including dust and flake generation and (ii) tritium retention and removal. The use of modelling tools to interpret the experimental results and make projections for conditions expected in future devices is explained. Outstanding technical issues and specific recommendations on potential R&D avenues for their resolution are presented.

<sup>a</sup> Corresponding author: e-mail: federig@ipp.mpg.de, tel. +49-89-32994228; fax. +49-89-32994110.

<sup>b</sup> Supported by the United States Department of Energy under Contract DE-AC02-76CH03073.

<sup>c</sup> Supported by the United States Department of Energy under Contract W-31-109-Eng-38.

<sup>d</sup> Supported by the Natural Sciences and Engineering Research Council of Canada and ITER Canada.

<sup>e</sup> Supported by the United States Department of Energy under Contract W-31-109-Eng-38.

<sup>f</sup> Supported by the United States Department of Energy under Contract DE-FC02-99ER54512.

<sup>g</sup> Supported by the United States Department of Energy under Contract DE-AC04-94AL85000.

<sup>h</sup> Supported by the United States Department of Energy under Grant No. DE-FG03-95ER54301.

## 1. Introduction/background

### 1.1. Introduction

Fusion power is a promising long term candidate to supply the energy needs of humanity [1]. Substantial fusion power has been produced in two large magnetic confinement devices: TFTR (10.7 MW) and JET (16 MW). An International Thermonuclear Experimental Reactor (ITER) to generate 1500 MW has been successfully designed, but the high cost of construction has led to work on a reduced scale option (see glossary). In magnetic confinement devices the edge plasma (see glossary) and surrounding material surfaces provide a buffer zone between the ‘astrophysical’, high temperature conditions in the plasma core and the normal ‘terrestrial’ environment. The interaction between the edge plasma and the surrounding surfaces profoundly influences the conditions in the core plasma (see glossary) and is a key engineering issue. Robust solutions to issues

of plasma–material interactions (PMIs) are required to realize a commercially attractive fusion reactor. The edge plasma needs to provide good thermal insulation and prevent impurity influx from poisoning the burning core plasma (see glossary). The wall has to withstand the intense heat load and particle flux from the core plasma, over months or years of operation, with little or no maintenance. The wall surface plays an important role in the recycling of hydrogen isotopes, and in plasma fuelling. The approach to practical fusion reactors inevitably leads to an increase in plasma energy content, pulse duration and cumulative run time. Plasma physics effects and PMIs that are only partially observed or accessible in present day experiments will become important. Higher heat loads, more intense transient heating events (i.e. edge localized modes (ELMs) and disruptions (see glossary)), and the predicted magnitude of plasma facing component (PFC) damage by melting and evaporation are critical issues [2] (Section 2.3.2). The orders of magnitude increase of the

duty cycle (see glossary) in a next step device will lead to centimetre scale erosion of PFCs. This represents a three to four orders of magnitude increase from present tokamaks, a change that is much larger than the change in any of the core physics parameters needed for ignition (see glossary). Erosion of carbon in deuterium–tritium fuelled tokamaks will lead to co-deposition with tritium, and tritium retention will constrain operations [3, 4] (Section 2.3.3). Dust generated by erosion must be controlled (Section 2.3.4).

Our knowledge of PMI processes has greatly expanded during the past two decades. Significant advances have been made in uncovering the physical principles that govern the behaviour of plasma facing materials (Section 3). The release of wall material into the plasma is now better understood. Advances in wall conditioning techniques have led to impressive gains in performance in many tokamaks (Sections 1.3 and 4.6). Probes installed in large tokamaks specifically for materials studies have provided time resolved erosion measurements to benchmark models (Section 4.2). The low sputtering yield (see glossary) of tungsten and molybdenum PFCs has been exploited to produce clean core plasmas (Section 4.3). These and other advances have greatly improved the knowledge base of PMI in next step machines (Section 5).

The present review surveys PMIs in magnetic fusion devices, in particular, the tokamak, since this is the most common approach and the most advanced candidate for a reactor. We critically discuss the implications of PMIs in contemporary facilities for the design, and the selection of materials for the first wall and divertor chamber components in a next step long pulse device. Often, the design features and parameters of ITER are used in this paper to exemplify issues that are generic to a reactor scale next step experimental facility. Extensive cross-referencing among related topics is incorporated to facilitate finding particular topics in the review. A glossary of acronyms and technical terms is provided at the end of this review in order to make the material more easily accessible to those new to this field.

Detailed information on PMIs is reported in a biannual conference series [5] and in specialized journal issues [6]. Early work is surveyed in Refs [7, 8]. The physics of divertors in tokamaks has also been reviewed [9], and a book on the plasma boundary of magnetic fusion devices has recently been published [10]. A separate review is planned that will concentrate on tritium retention in plasma facing materials [11]. Novel high power density wall concepts includ-

ing liquid walls are presented in Ref. [12]; these may offer the potential for attractive fusion energy systems if a number of challenging engineering science issues can be solved. A comprehensive review of the technical basis for the design of ITER is available; it focuses on the plasma physics database provided by the present generation of tokamaks and on the methodologies used to predict ITER performance [13].

## 1.2. Plasma edge parameters and plasma–material interactions

The edge plasma and the wall are a strongly coupled system whose interactions range over an extraordinary width of scale, from eV scale atomic interactions to hundred megajoule disruptions. This 27 order of magnitude range in energy rivals the ratio between the size of a grain of dust and the  $3 \times 10^{21}$  m scale of the known universe! Not surprisingly, the subject spans several technical disciplines (materials physics, chemistry, atomic and molecular physics and plasma physics, from cold, mostly neutral plasmas, to multi-keV temperature plasmas). This section introduces the configuration of the PFCs of modern tokamaks and their interaction with the plasma.

PMIs critically affect tokamak operation in many ways. Erosion by the plasma determines the lifetime of PFCs and creates a source of impurities (see glossary), which cool and dilute the plasma. Deposition of material onto PFCs alters their surface composition and can lead to long term accumulation of large in-vessel tritium inventories. Retention and recycling of hydrogen from PFCs affect fuelling efficiency, plasma density control and the density of neutral hydrogen in the plasma boundary, which impacts particle and energy transport.

The primary driver for the interactions between core plasma, edge plasma and wall is the power deposited or generated in the plasma core. The fraction of this power which is not radiated from the plasma core as bremsstrahlung (see glossary) or line radiation is transported across field lines to the edge plasma. The edge plasma has a strong influence on the core plasma transport processes and thereby on the energy confinement time (see glossary) [8] and plays an essential role in the transition from the low (L) to the enhanced (H) plasma confinement regime [14]. A schematic representation of the regions of the plasma and the boundary walls in a divertor tokamak is shown in Fig. 1.

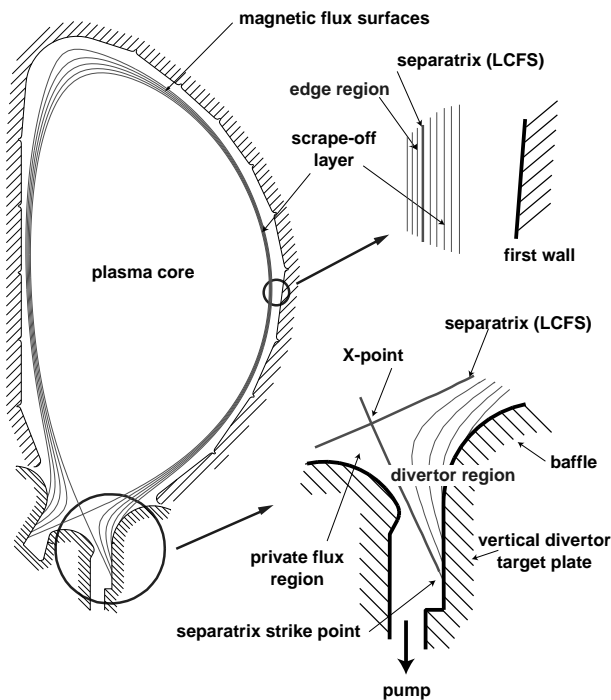


**Figure 1.** Poloidal cross-section of a tokamak plasma (with a single magnetic null divertor configuration), illustrating the regions of the plasma and the boundary walls where important PMIs and atomic physics processes take place. The characteristic regions are: (i) the plasma core, (ii) the edge region just inside the separatrix, (iii) the scrape-off-layer (SOL) plasma outside the separatrix, and (iv) the divertor plasma region, which is an extension of the SOL plasma along field lines into the divertor chamber. The baffle structure is designed to prevent neutrals from leaving the divertor. In the private flux region below the X point, the magnetic field surfaces are isolated from the rest of the plasma.

The outermost closed magnetic field surface is characterized by a zero in the poloidal magnetic field within the vessel known as an ‘X point’. This boundary is called the last closed flux surface (LCFS) or separatrix (see glossary). Magnetic field surfaces inside the LCFS are closed, confining the plasma ions. The edge region, just inside the LCFS, contains significant levels of not fully ionized impurities, and perhaps also neutral particles. Impurity line radiation and neutral particles transport some power from here to the wall. The remaining power,  $P_{SOL}$ , enters the region outside the LCFS either by conduction or by convection. This region is known as the scrape-off layer or ‘SOL’ (see glossary) as here the power is rapidly ‘scraped off’ by electron heat conduction along open field lines, which are diverted to intersect

with material targets, in what is known as a ‘divertor’ (see glossary); see inset in Fig. 1.

Cross-field transport of power continues in the SOL, either through conduction and/or convection, and the relative rates of the cross-field versus parallel transport along magnetic field lines determine the power width of the SOL,  $\lambda_p$ . Since parallel transport is very rapid compared to cross-field transport rates, the SOL is very thin in the radial direction. The power e-folding width  $\lambda_p$  (the distance required to decrease by a factor  $1/e$ ) typically ranges between 3 and 10 mm at the outside midplane in present devices and is expected to be 5 to 30 mm wide in a device such as ITER [13]. Typically, density and temperature SOL e-folding widths are factors of two to five larger than power widths [9].

The interaction of the edge plasma with the PFCs is determined by plasma density, temperature, flows, power fluxes and neutral fluxes, and is most intense in the vicinity of the ‘strike point’, where the separatrix intersects the divertor target plate (see inset in Fig. 1). The plasma density and temperature determine the flux density and energy of plasma ions striking plasma wetted surfaces. These, in turn, determine the rate of physical sputtering, chemical sputtering, ion implantation and impurity generation (Section 1.2.4). In addition, the plasma conditions determine where eroded material is redeposited, and to what degree co-deposition of tritium occurs (Sections 4.3, 4.7 and 5.3). The power flow determines the level of active structural cooling required. Neutral fluxes also cause erosion and co-deposition, even on areas that are not in direct contact with the plasma.

### 1.2.1. Plasma interaction with the divertor

We define the divertor to be the volume below the X point, which also usually means below the divertor baffle structure (see glossary), see Fig. 1. We assume that plasma ions strike the divertor plate, are recycled back into the plasma either as atoms or molecules and are ionized/dissociated primarily in the divertor, i.e. not directly penetrating the confined plasma or the SOL outside the divertor. Neutrals are prevented from leaving the divertor either by the opacity of the divertor plasma itself (through ionization) or are simply blocked by the mechanical baffle structure. Such a divertor condition we call an ‘opaque divertor’ [9]. In the ‘detached regime’ (see glossary), the plasma temperature (density) in the divertor is significantly lower (higher) than in the SOL outside of the divertor, for example, at

the outside midplane. Plasma detached regimes are present at moderate or high levels of collisionality in the SOL, i.e. sufficiently high that parallel field temperature gradients can be sustained between the main SOL, where power enters by cross-field transport from the confined plasma, and the sink of power, in or near the divertor. Detached conditions are usually found at moderate to high levels of the ratio of plasma density/input power in present machines [9]; see Sections 5.2.1. With typical plasma temperatures of  $\approx 100$  eV at the midplane and of  $\approx 3$  eV in a detached divertor, the corresponding ion energies will be about 500 and 15 eV, respectively. The difference in erosion rate between these two energies can be enormous since 15 eV is below the physical sputtering threshold for most materials (Section 3.2.1).

We see from Fig. 1 that the SOL width varies around the poloidal circumference, being smallest at the outside midplane and expanding near the divertor, particularly near the X point. Typical expansion factors are  $\approx 4$  between the divertor plate and the midplane, reflecting the decrease in the poloidal field in the divertor compared with the midplane location. This expansion has a very beneficial effect in that it effectively reduces the power flux on the divertor plates, while increasing the plasma volume available for volumetric loss mechanisms such as impurity/hydrogenic radiation and volume recombination [9, 15]. Radiative processes (e.g. due to intrinsic or intentionally added impurities in the divertor region) can produce further reduction in power flux. Most present divertor machines have reduced the power flowing to the divertor plate by factors of  $>5$ , using radiative processes [9] (Section 2.3.1). Thus, through flux expansion and radiative processes, the divertor can deliver a factor  $>20$  reduction in incident power density over what would be experienced by a (hypothetical) toroidal belt limiter normal to the SOL in the main chamber [16].

The PFC materials are optimized for the plasma conditions in the specific regions. For example, near the baffle region of the divertor (Fig. 1) there lies the interface between the hot SOL plasma outside the divertor ( $>100$  eV) and the high neutral density in the divertor. This region is expected to generate significant fluxes of energetic charge exchange atoms (see glossary), which bombard the neighbouring structures. These particles have energies  $>100$  eV, and up to perhaps several keV, and cause physical sputtering of PFCs in the baffle region. For this reason, the present ITER design calls for a high  $Z$  material, tungsten, in this region, which has a low

yield for physical sputtering [17]. The selection of plasma facing materials is further discussed in Section 2.4 and Refs [17–19].

### 1.2.2. Additional divertor functions

In addition, the divertor must simultaneously perform two other essential functions — helium exhaust and impurity control. High neutral pressures and high pumping speeds at the entrance of the pump duct are necessary to remove helium ash and maintain high fusion reactivity in the core plasma [20–22]. In addition, strong pumping of hydrogen isotopes aids in plasma density control and possibly in impurity compression (see below).

Second, despite the low plasma temperatures in the divertor, impurities are inevitably present, either through chemical sputtering (in the case of graphite), from C and O impurity surface contaminants, or from impurity gases, which have been intentionally added to the discharge to increase radiative cooling [23–25]. The divertor must ensure that these impurities are not transported into the plasma core. Both the flow of recycling fuel ions to the plate and the net flow in the SOL in cases where very strong divertor pumping is present (with main chamber puffing [23]), tend to compress/sweep impurities into the divertor. In fact, recent results in several divertor tokamaks have shown that the concentration of impurities in the divertor gas can be enhanced by factors of  $>3$  over that present in the core plasma [23, 25, 26]. Such a situation is very encouraging, suggesting that relatively pure core plasmas can be obtained, while maintaining a relatively impure and highly radiating divertor. Some considerations on impurity production and plasma contamination for a next step reactor are included in Section 2.3.1. The database for impurity production via erosion in tokamaks is reviewed in Section 4.3.

### 1.2.3. Plasma interaction with the main chamber wall

The wall is a major source of neutral atoms and molecules, and hence of plasma ions. Outside the divertor, in the region between the SOL plasma and the vessel wall, the density of neutrals is relatively low, typically a factor of 30–300 smaller than in the divertor. However, when spatially integrated over the large chamber wall, the total flux (in particles per second) can be quite significant, in absolute number comparable to the number of recycling ions at the divertor plates. Energetic hydrogen from the plasma

can be retained in the wall or return as neutrals to the plasma edge. Since the quantity of hydrogen in the wall is typically much greater than the quantity in a plasma, small relative changes in recycling of hydrogen from the wall strongly affects fuelling of individual discharges. Neutral particles coming from the wall readily cross magnetic field lines, increasing in energy as they repeatedly charge exchange into the boundary plasma until they are ionized. They then diffuse back out across field lines as ions carrying plasma power through convection. Since the divertor is likely to be opaque to recycling neutrals, this main chamber recycling goes on independently from the divertor [9, 27]. In addition to this cross-field flow, there may be additional parallel and poloidal flows in the SOL in the main chamber induced by a variety of forces; observations in JET [28, 29] and JT-60U [30] imply strong drift around the SOL from the outer to the inner divertor, for a  $\mathbf{B} \times \nabla B$  direction which is downwards in the vessel (Section 5.3.1).

The average ion leaves and re-enters the plasma many times over the course of a discharge — this process is called recycling, and average recycling times are in the range of 1 to 10 ms. Typically, the flux of hydrogen isotopes from the wall is a larger global particle source into the plasma than external fuelling by gas puffing [31], pellet injection (see glossary) [32] or neutral beam injection [33]. Wall released hydrogen (H, D or T) can lead to an uncontrolled density rise, and high plasma performance in present machines is often only possible when the influx of hydrogenic ions and impurities from the wall is controlled by wall conditioning (Section 4.6). Hydrogen (protium) influx is undesirable as it dilutes the reactivity of a deuterium–tritium plasma.

Wall conditioning has been used since the early phases of fusion research to provide the necessary conditions for plasma production and high plasma performance (Section 1.3) [34–42]. High temperature bake and specialized discharges are used to deplete hydrogen trapped in the wall and to either volatilize and pump out contaminants from the wall, or to bind them chemically to the wall by gettering (Section 4.6). Extrapolation of currently used tokamak wall and surface conditioning methods to long pulse reactor tokamaks is not straightforward and is briefly discussed in Section 2.3.1.4.

Many advances in plasma performance in the last decade have been achieved through improved wall conditioning, for example: boronization in Alcator C-Mod [43, 44] and DIII-D [45, 46], JT-60U [47], TEXTOR [48], START [49], and, most recently, the

best performance has occurred on MAST [50] and NSTX [51]. Lithium conditioning in TFTR [52–54] produced a dramatic 64 times increase in the fusion triple product ( $n_e \tau_E T_i$ ) (see Fig. 2 and Section 4.6 for a more detailed discussion). Liquid lithium is being explored as a potential plasma facing material in fusion reactors [55], and its use may open very attractive, stable, high beta ‘zero recycling’ regimes [56]. Even when the plasma confinement does not improve, the use of wall conditioning permits density and recycling control, greatly widening the operational space in JET [57], ASDEX-Upgrade [58], and during long duration ( $>1$  min) plasma discharges on Tore Supra [59]. Although a predictive theory of the relation between wall composition and plasma performance is lacking, some correlations of ‘cause’ and ‘effect’ are emerging. TFTR L mode energy confinement was found to be correlated to the same parameters as are important for TFTR supershots [60] (see glossary). In both regimes the plasma transport coefficients increased with increased edge deuterium influx, suggesting a physical connection between energy confinement and hydrogen influx from the wall. A candidate for such a connection is shear stabilization of ion toroidal gradient modes [61], which has reproduced the sensitive dependence of TFTR confinement on edge recycling.

#### 1.2.4. Physical and chemical sputtering and its consequences

Plasma ions approaching the material surfaces are accelerated by the sheath potential to an energy of  $E_0 \approx 2T + 3ZT$ , where  $T$  is the plasma temperature adjacent to the material and  $Z$  is the ion charge.

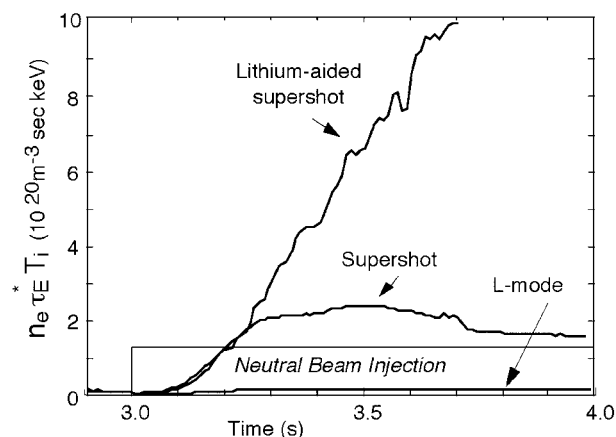


**Figure 2.** Showing the dramatic  $64 \times$  increase in the fusion triple product  $n_e \tau_E T_i$  in TFTR with wall conditioning.

Above a certain threshold, the exchange of kinetic energy between the impacting ions and the atoms in the top monolayers of the material can knock surface atoms out into the plasma in a process termed physical sputtering. A fairly complete theory of physical sputtering now exists (Section 3.2). The predicted sputtering yields, as well as the expected trends with species properties (e.g. atomic mass, surface binding energy), have been experimentally verified in both tokamaks and laboratory devices. Incoming ions can also react chemically with surface atoms releasing atoms and molecules into the plasma. This chemical erosion process depends on molecular potentials and is significantly more complex than physical sputtering.

While physical sputtering is greatly reduced in a low temperature detached divertor plasma (Section 1.2.1), chemical erosion has a weak energy threshold and can cause significant erosion of carbon. This reduces the lifetime of divertor components (Section 5.3) and creates the opportunity for the redeposition of released carbon with tritium, giving rise to operational and safety concerns (Sections 2.3.3, 4.7 and 5.3). The importance of these consequences has stimulated vigorous recent investigations of the dependence of chemical erosion on a wide variety of plasma and surface parameters such as surface temperature, incident species and energy, and incident flux. The complex role of molecular neutral and radical states and their transport/interactions with the plasma is posing a substantial challenge to PMI modelling. The flux dependence is a key parameter of interest for next step devices (Section 5.3). Material mixing (e.g. metals sputtered from the first wall depositing on a carbon divertor plate) can further complicate these already complex PMI phenomena.

The use of partially detached plasmas (see glossary) in current tokamaks has been found to change the carbon divertor erosion rate, dramatically, for example, eliminating net carbon erosion due to physical sputtering in the DIII-D outer divertor and leading to net deposition in both legs of the ASDEX-Upgrade LYRA divertor (Sections 4.3.4 and 4.7.1.3). In particular, there are high levels of hydrocarbon molecules in the divertor plasma, which are dissociated by the plasma, resulting in high flux densities of carbon atoms and carbon bearing molecules. The most dramatic result of this was the surprisingly large amount of deposition and associated tritium retention in the inner divertor louvres in JET (see Ref. [62] and Section 4.7.1.2).

Sputtered wall material represents a source of impurities for the plasma. It has been shown from modelling that impurities entering the plasma in the main chamber are more efficient in contaminating the core than impurities entering at the divertor plate [9, 63]. Contamination of the core plasma with impurities from the wall dilutes the hydrogenic fuel (for a fixed plasma density) and causes energy to be lost by radiation. High Z elements such as tungsten are very efficient radiators and concentrations much above  $10^{-5}$  impurity ions per hydrogen ion are intolerable. Low Z impurities, on the other hand, are stripped of their electrons and do not radiate appreciably in the high temperature plasma core; thus, graphite and beryllium (the latter was especially used in the past, in JET) cover large portions of the plasma facing first wall area in most of today's tokamaks, although the dilution problem remains (Section 1.3). A recent comparison of three tokamaks with carbon PFCs has indeed shown very similar erosion/redeposition and hydrogenic retention patterns [64] (see also Section 4.3), with a marked asymmetry between the inner and outer divertor legs that remains largely unexplained (see Section 5.3).

### 1.3. History of plasma facing materials

Plasma–material interactions have been recognized as a key issue in the realization of practical fusion power since the beginning of magnetic fusion research. As early as 1951, Spitzer [65] recognized the threat to plasma purity by impurities arising from PMIs and proposed a divertor to help alleviate the problem. In the following early years of research in the 1950s on stellarators and pinches [66–69], relatively primitive vacuum techniques were employed, resulting in severely contaminated plasmas (primarily carbon and oxygen desorbed from the wall). These discharges had such poor confinement and low plasma temperatures that even these low Z impurities were not fully stripped in the plasma core, resulting in large central radiation losses.

By the time of the first tokamaks in the 1960s in the USSR and subsequently elsewhere, means of reducing the level of carbon and oxygen were being employed [70, 71]. These included the use of stainless steel vacuum vessels and all metal seals, vessel baking and discharge cleaning. Ultimately, these improvements, along with improved plasma confinement, led to the first production of relatively hot and dense plasmas in the T-3 tokamak ( $\approx 1$  keV and  $\approx 3 \times 10^{19} \text{ m}^{-3}$ ) [72, 73]. These plasmas were cleaner



and with low  $Z$  elements fully stripped in the core but still had unacceptable levels of carbon, oxygen and metallic impurities. The metallic contamination inevitably consisted of wall and limiter materials. At one point it was thought that metallic impurity production was related to unipolar arcs (see glossary) [71], whose tracks could be visually observed on wall structures. It was later concluded that impurity production by arcs in stable, well behaved discharges was relatively minor [74] (see also Sections 2.3 and 4.4). Early work in this field has been reviewed by Behrisch [70] and McCracken and Stott [71].

### 1.3.1. Limiter and divertor tokamaks

Early in magnetic fusion research it was recognized that localizing intense PMIs at some type of ‘sacrificial’ structure was desirable if only to ensure that the vacuum walls were not penetrated. Hence, the birth of the ‘limiter’, usually made very robust, from refractory material and positioned to ensure a gap of at least several centimetres between the plasma edge and more delicate structures such as bellows, electrical breaks, vacuum walls, etc. Even with these precautions, vacuum wall penetration by trapped electrons has been reported [75]. Typical materials used for limiters (see glossary) in these early days included stainless steel in ATC [76] and ISX-A [77] and many others, molybdenum in Alcator A [78], TFR [79], tungsten in ST [80] and PLT [81] and titanium in PDX [82]. A number of novel experiments have also been carried out with gold in DIVA [83], aluminium in ST [84], alumina in PETULA [85] and boron carbide in TFR [79]. A list of major toroidal plasma devices, past and present, is shown in Table 1, giving their location, years of operation, limiter/divertor/wall materials and getter (see also glossary).

By the mid-1970s, the divertor concept, originally developed for the C-stellarator at Princeton [86, 87], was being tried on a number of tokamaks, starting with DIVA in Japan [88], T-12 in the USSR [89] and DITE in the UK [90]. The original divertor concept intended to remove the source of first plasma contact to some remote location away from the thermonuclear plasma where impurities generated by the wall contact could be retained [65]. In addition, it was hoped that wall produced impurities would be swept by the SOL into the divertor and be retained there. By the early 1980s [91–94], it was also recognized that, in addition to these functions, the divertor should make it easier to reduce the plasma tem-

perature immediately adjacent to the ‘limiting’ surface, thus reducing the energies of incident ions and, thus, the physical sputtering rate. Complementary to this, high divertor plasma and neutral densities were found. The high plasma density has several beneficial effects in dispersing the incident power [9], while the high neutral density makes for efficient pumping. Pumping helps with plasma density control, divertor retention of impurities and, ultimately, is necessary for helium exhaust in a reactor.

A number of tokamaks continue to explore concepts other than the standard axisymmetric divertor, in particular, TEXTOR [95] and Tore Supra [96]. TEXTOR is devoted to PMI issues, and a large area carbon pump limiter has been used to handle both power and helium exhaust. Near steady state operation has been achieved in Tore Supra in limiter discharges, demonstrating active heat removal by PFCs. In addition, Tore Supra has investigated the performance of an ergodic divertor [97] (see glossary). This concept uses internal coils to ergodize (see glossary) the plasma boundary, creating conditions in some ways similar to that present in the SOL of conventional divertor tokamaks, i.e. reduced plasma temperature adjacent to surfaces and better impurity screening (see glossary).

### 1.3.2. Plasma facing materials

By the late 1970s, various tokamaks were starting to employ auxiliary heating systems, primarily neutral beam injection (NBI). Experiments with NBI on PLT resulted in the achievement of the first thermonuclear class temperatures [81, 98, 99]. PLT at the time used tungsten limiters, and, at high NBI powers and relatively low plasma densities, very high edge plasma temperatures and power fluxes were generated, resulting in tungsten sputtering and high core radiation from partially stripped tungsten impurity ions. For this reason, PLT switched limiter material to nuclear grade graphite. Graphite has the advantage that eroded carbon atoms are fully stripped in the plasma core, thus reducing core radiation. In addition, the surface does not melt if overheated — it simply undergoes sublimation. This move to carbon by PLT turned out to be very successful, alleviating the central radiation problem. For these reasons, carbon has tended to be the favoured limiter/divertor material in magnetic fusion research ever since.

By the mid-1980s, many tokamaks were operating with graphite limiters and/or divertor plates. In addition, extensive laboratory tests/simulations

**Table 1.** Major toroidal confinement devices. Location, approximate years of operation, limiter material, divertor plate material (if applicable), plasma facing wall material and gettering technique are given

Name	Location	Operation	Limiter	Divertor	Wall	Getter
TOKAMAKS						
Alcator A	MIT, USA	1972–1979	Mo, C	N/A	StSt	Ti
Alcator C	MIT, USA	1978–1983	Mo, C	N/A	StSt	
Alcator C-Mod	MIT, USA	1993–	Mo	Mo	StSt	B
ASDEX	Garching, Germany	1980–1990	StSt, C, Cu	Ti, Cu	StSt	C, B, Ti
ASDEX-Upgrade	Garching, Germany	1991–	C	C, W	StSt	B
ATC	Princeton, USA	1972–1978	StSt	N/A	StSt	Ti
Compass	Culham, UK	1990–	C	C	StSt	
DITE	Culham, UK	1976–1992	Mo, Ti, C	C, Mo	StSt	Ti, Cr
DIVA	Naka, Japan	1974–1979	Au	Ti	Au	Ti, C
Doublet II	GA, USA	1969–1973	W, SiC	N/A	StSt	Ti
Doublet III	GA, USA	1978–1984	StSt, W, C	StSt, C	StSt	
DIII-D	GA, USA	1986–	C	C	StSt, C	C, B
ISX-A	Oak Ridge, USA	1977–1979	StSt, C	N/A		
ISX-B	Oak Ridge, USA	1980–1987	StSt, Be, TiB <sub>2</sub> , TiC, B, C	N/A	StSt	Cr
JET	Euratom/Culham, UK	1983–	Inconel, C, Be	C, Be	Inconel	C, Be
JFT	JAERI, Japan	1972–	Mo, C, SiC, TiC, TiN	N/A		Ti
JT-60	JAERI, Japan	1985–1991	TiC, C,	TiC, C,	Inconel	—
JT-60U	JAERI, Japan	1991–	C	C	Inconel	B
FT	Frascati, Italy	1978–1989	StSt	N/A	StSt	—
FTU	Frascati, Italy	1990–	StSt, Inconel, Mo, W	N/A	StSt	Si
NSTX	Princeton, USA	1999–	C	C	StSt	B
ORMAK	Oak Ridge, USA	1973–1977	W	N/A	Au, StSt	
PBX	Princeton, USA	1984–1998	C	C	StSt	B
PDX	Princeton, USA	1978–1983	Ti	Ti		Ti
PLT	Princeton, USA	1976–1985	W, StSt, C	N/A		Ti
ST	Princeton, USA	1971–1976	Al, Mo	N/A		Al
START	Culham, UK	1990–1998	C	C		B, Ti
TCV	Lausanne, Switzerland	1993–	C	C	C	B
TdeV	Montreal, Canada	1987–1998	C	C	StSt	B, Li
TEXT	Austin, USA	1980–1992	StSt	N/A	StSt	
TEXTOR	Jülich, Germany	1980–	StSt, C	N/A	IN	C, B, Si
TFR	Fontenay-aux-Roses, France	1973–1986	C, W, Mo, BC	N/A	StSt	
TFTR	Princeton, USA	1982–1997	TiC, C	N/A	StSt	Cr, Li
Tore Supra	Cadarache, France	1988–	C and CFC	Ergodic divertor	StSt	B
T-10	Kurchatov, Russian Federation	1976–	C, StSt	N/A		B
STELLARATORS AND HELICAL DEVICES						
ATF	Oak Ridge, USA	1988–1992	StSt, C	N/A	StSt	Cr, Ti
LHD	NIFS, Japan	1998–	StSt, C	StSt, C	StSt	Ti
W7AS	Garching, Germany	1988–	TiC, B/C	TiC, B/C	StSt	B

on graphite had begun, primarily aimed at understanding the chemical reactions between graphite and hydrogenic plasmas, i.e. chemical erosion (Sections 1.2.4 and 3.2). Early laboratory results suggested that carbon would be eroded by hydrogenic ions with a chemical erosion yield of  $\approx 0.1 \text{ C/D}^+$ , a yield several times higher than the maximum physical sputtering yield. Another process, radiation enhanced sublimation (RES), was discovered at elevated temperatures, which further suggested high erosion rates for carbon (Section 3.2.5). The ability of carbon to trap hydrogenic species in co-deposited layers became recognized (Section 3.5). These problems, along with (anticipated) poor mechanical properties of graphite in a neutron environment (which had previously been known for many years from fission research [100]), led to the consideration of beryllium as a plasma facing material, primarily promoted at JET [101]. Beryllium has the advantage of being a low Z material, non-reactive with hydrogenic isotopes and a good thermal conductor. However, beryllium has several negative features, including a low melting temperature (1560 K), potential toxicity in manufacturing and relatively high physical sputtering rates. Nevertheless, two small tokamaks successfully tested beryllium (ISX-B [102], UNITOR [103]), and this led to extensive JET operation with beryllium limiters, divertor plates and evaporative gettering [101]. In fact, melting and evaporation of the beryllium limiters was extensive in all three tokamak experiments cited [101–103]. One immediate and clearly beneficial effect of beryllium operation was the observation of strong oxygen gettering by the evaporated beryllium.

At present, carbon is the dominant material in the major tokamaks worldwide, with the exception of Alcator C-Mod at MIT, USA [104], which uses molybdenum, and FT-U at Frascati, Italy [105], which has used a variety of moderate to high Z materials. Many machines have expanded graphite coverage to include virtually all of the vacuum vessel wall, in addition to the limiter/divertor plates (e.g. DIII-D [106]). In some cases, the inner wall is used as a large area limiter, and such structures, if carefully constructed, are able to handle enormous power loads, greatly exceeding the power limits of divertor plates (e.g. TFTR [107–109]).

Over the years, a variety of divertor plate materials have been used (see Table 1). In general, the success with carbon in limiter machines led to the use of carbon for divertor plates, although there are a number of cases where metals have been used. The

argument for carbon in the case of divertor plates is not as strong as in the case of limiter machines. Carbon or other low Z materials are most suited to high edge plasma temperatures, typically at low plasma density, as one finds at the edge of a high powered limiter device. Again, this is related to the fact that carbon is fully stripped in the core of tokamak discharges and thus does not cool by line radiation. On the other hand, when the plasma temperature adjacent to material surfaces is low as in most divertor plasmas, the incident particle energies can very often be below the physical sputtering threshold of higher Z materials. In contrast, carbon has a low energy threshold for chemical erosion (Section 3.2). This, along with the fact that ion fluxes are very high in the divertor (high plasma density), means that relatively high erosion rates are expected and found for carbon divertor plates [110–112] (Sections 3.2 and 5.3). As a consequence, large hydrogenic retention has been found in films forming primarily on cold surfaces (see Section 4.7). The last decade of divertor research has seen a return of interest in metals which had been largely put aside in favour of carbon. Sputtered high Z metal atoms, such as tungsten, have a lower ionization potential and lower velocity than sputtered carbon and are quickly ionized close to the surface and are promptly redeposited onto the target near their point of origin. Divertor machines that have tried high Z metal divertor plates in the low temperature/high-recycling mode (e.g. molybdenum in Alcator C-Mod [113, 114] and tungsten in ASDEX-Upgrade [115]) have indeed found very low levels of net erosion at the divertor plate. The installation of tungsten tiles on the inner wall of ASDEX-Upgrade has also yielded very encouraging results [116, 117]. No influence is observed on plasma discharges, and central radiation, intrinsic impurities, confinement H mode (see glossary) threshold, density and beta limits (see glossary) are unchanged. High heat flux components clad by tungsten that meet the severe normal operation thermal load requirements of the divertor have also been developed and successfully tested, although the response to off-normal events, such as disruptions, remains a concern (Sections 2.4 and 2.5).

A key decision for a next step device is the choice of plasma facing materials. Historically, carbon has been favoured as a plasma facing material as it has excellent thermal properties and carbon impurities in the plasma lead to only small increases in radiated power. Carbon is currently chosen to clad the ITER divertor target, near the strike points, because

of its greater resilience to excessive heat loads during ELMs and plasma disruptions (see glossary and Sections 2.4 and 2.5). However, the operation of a next step device with carbon PFCs will be severely affected by the divertor erosion and tritium retention through co-deposition of T with C. For the latter, efficient in situ methods of mitigation and retrieval are required in order to avoid frequent interruptions imposed by precautionary operating limits set by safety considerations or necessitated by fuel economy (Section 2.3.3). These issues become even more challenging in the design of a commercially attractive fusion reactor.

## 2. Plasma edge and plasma–material interaction issues in next step tokamaks

### 2.1. Introduction

In this section, we discuss several important aspects of the PMIs that are expected to show up in a next step fusion facility. We point out significant differences from present experiments that open new design, operation and safety issues. The physical processes and the underlying theory that support the understanding of these areas will be reviewed in Section 3, and the present experimental database and modelling of effects expected in a next step reactor presented in Sections 4 and 5, respectively.

Very often the design features and parameters of the 1998 ITER design [119], or of the most recent reduced size and reduced cost option originally called the ITER-FEAT [119], are presented and used in the context of this article to exemplify issues that are generic to any reactor scale next step tokamak facility.

### 2.2. Progress towards a next step fusion device

#### 2.2.1. Advances in today's fusion devices and prospects

Much of the significant progress in magnetic fusion science has centred around the tokamak concept, which has represented the main approach to magnetic confinement fusion since its inception almost 50 years ago [120]. This concept also offers great promise of future performance enhancement. Reference [13] summarizes the qualitative and quantitative aspects of the most recent advances in toka-

mak physics and provides recommended extrapolation methodologies, together with uncertainty estimates and physics design specifications for use by the designers of the ITER facility.

In current tokamaks, with discharge durations of a few seconds, heat transport within the plasma has been reduced by suppressing turbulence, plasma pressure limits have been increased, the potential for steady state operation by bootstrap (see glossary) and external non-inductive currents has been demonstrated, and concerns about handling exhaust heat and helium ash have been allayed. Progress in the development of regimes of operation, which have both good confinement and magnetohydrodynamic stability has enabled the production of significant bursts of fusion power from deuterium–tritium plasmas in TFTR ( $\approx 11$  MW) [121] and JET ( $\approx 16$  MW) [122–124] and, more importantly, opened up the study of the physics of burning magnetically confined plasmas. Improvements of plasma performance and control have occurred owing to remarkable advance in various areas of physics and engineering. As an example, magnetic coil systems and their associated feedback control systems have been developed for stable confinement of the plasma; they produce many variations of plasma shape in order to optimize plasma performance. Superconducting coils (see glossary) have been used in magnetic confinement systems; as a result, very long discharges have been produced in the superconducting tokamaks Tore Supra [125] and TRIAM-1M. The latter device holds the world record in pulse duration (2 h) using non-inductive current drive (see glossary) by lower hybrid waves, albeit in low density, low power discharges [126]. This clearly shows the potential for steady state operation. Plasma heating technologies have been developed and deployed at the tens of megawatt level. Non-inductive methods of driving the plasma current in low to moderate density plasmas have been employed successfully. The theoretically predicted self-driven or bootstrap current has been confirmed and has significantly enhanced prospects of steady state operation. Plasma diagnostic techniques have improved with higher temporal resolution and more extensive spatial coverage. New techniques to measure the plasma current profile and rotation have enabled deeper insight into plasma transport [127–130]. Tritium fuelling systems have been implemented and safely operated. Integrating and extending these advances towards long pulses or steady state burning plasmas is now the focus of international tokamak research, which aims

at proceeding to the construction of a physics and technology integration step [19, 131].

Such a device will encompass two parallel objectives, the creation and study of burning plasmas and the development and demonstration of the fusion technology required to make fusion a practical source of energy. The physics goals include: (i) exploration of the physics of burning plasmas in a plasma of sufficient duration so that all plasma physics processes and plasma-wall interactions will have reached steady state; (ii) sustaining plasma purity sufficient to maintain fusion gain; (iii) exploration of the physics of a radiative divertor designed to handle high power flows at a reactor relevant scale; and (iv) development of robust techniques to mitigate and avoid disruptions at energies not accessible in present machines. The technology goals encompass: (i) demonstration of key first generation technologies needed to engineer future magnetic fusion reactor systems such as superconducting magnets, divertor systems to exhaust the power and particles from the plasma, remote handling systems for the remote installation and repair of device components and subcomponents; (ii) providing a test bed for plasma facing materials exposed to long duration power and particle fluxes; (iii) demonstration of an efficient tritium fuel cycle, including rapid removal of co-deposited tritium; and (iv) testing tritium breeding blanket concepts. While some aspects of the relevant individual physics phenomena could be studied separately on somewhat smaller existing or new devices, the integration of long pulse reactor scale burning plasmas, together with the relevant enabling technologies, is the key mission of a next step device.

Several issues such as plasma control, the handling of large plasma power and particle fluxes, and the associated intense PMIs go beyond a specific device configuration and are generic to all approaches to magnetic fusion reactors. Much of what will be learned from a next step experimental tokamak facility such as ITER will be directly applicable to any 'alternate' magnetic confinement concept, especially those utilizing a toroidal configuration.

For the past decade, it has been internationally accepted that burning plasma physics is the next frontier of fusion plasma physics. The importance of moving to reactor scale devices motivated the Governments of the European Union, Japan, the Russian Federation (the former USSR) and the United States to initiate, in 1987, the ITER Conceptual Design Activities (ITER/CDA). The promise of the ITER/CDA design, which was completed in 1990

[132], in 1992 led to the ITER Engineering Design Activities (ITER/EDA) agreement [133], aimed at developing a detailed engineering design for a reactor scale tokamak facility that would achieve controlled ignition and extended burn. As envisioned by the ITER agreement, the ITER device would be the central element of an international 'one-step-to-a-reactor' strategy. The resulting overall design concept and the designs for the various systems and subsystem have been documented in the 1998 ITER design report [119]. Despite the achievement of the ITER/EDA objectives, concerns over the cost of the programme, and the advances in physics and technology made during the ITER/EDA period, have increased the motivation and potential rewards for seeking a lower cost design by modifying the technical objectives. Currently under consideration is a fusion device, ITER-FEAT, with a reduced physics and testing mission (e.g. an energy amplification factor (see glossary) of  $Q \approx 10$ , a moderate pulse length of about 400 s up to steady state, a minimum fusion power of  $\approx 400$  MW and neutron wall loadings (see glossary) of  $\approx 0.5 \text{ MW} \cdot \text{m}^{-2}$ ) [19, 119, 134, 135]. In an enhanced physics performance mode, such a device has the potential to demonstrate ignition. In addition, strong emphasis is placed on the goal of achieving steady state operation (i.e. non-inductive operation with  $Q = 5$  and with a pulse length of the order of 3000 s).

To overcome some of the remaining uncertainties, the next step fusion device must be designed with sufficient flexibility to operate under a variety of experimental scenarios and to allow modifications during operation that would take advantage of results from earlier phases. It is expected that, after construction, an experimental fusion reactor would operate for about 20 years as an experimental facility. The early phase of the experimental programme would emphasize physics explorations. The intermediate phase would concentrate on the achievement of reliable quasi steady state operation with moderate neutron flux. Later phases would focus on the accumulation of neutron fluence and operating time for fusion nuclear and materials science studies and for integrated component testing. Making design choices that are consistent with nuclear technology and remote maintenance requirements is imperative.

A major objective of the next step device is to provide a test facility for the development of nuclear component technology. The superconducting magnet, heating, fuelling, tritium handling, and most other systems will be based on technology that can

**Table 2.** Distinctive features of a next step device and related PMI issues.

- 
- |  |   |
|--|---|
| <p>(1) <b>High energy content</b> (<i>several hundreds MJ versus few MJ in current devices</i>) <b>and power flow</b> (<i>several hundred MW in the SOL versus few MW in current devices</i>):</p> <ul style="list-style-type: none"> <li>• more intense disruptions and disruption related damage effects (e.g. material ablation and melting), resulting in local damage and in a substantial influx of impurities into the plasma;</li> <li>• plasma power densities in the divertor will be higher than in present day experiments and require an effective, reliable way to disperse the power on the divertor surfaces.</li> </ul> <p>(2) <b>Long pulse duration</b> (<i>few hundred s versus few s in current devices</i>):</p> <ul style="list-style-type: none"> <li>• requires active cooling of PFCs and vessel structures and techniques to pump helium ash during each pulse;</li> <li>• requires effective control of plasma purity and PMIs to achieve high plasma performance.</li> </ul> <p>(3) <b>High duty factor</b> (<i>3%–10%</i>) <b>or pulse repetition rate</b>:</p> <ul style="list-style-type: none"> <li>• high performance plasma operation with limited shutdown times for wall conditioning and tritium recovery from co-deposited films;</li> <li>• remote maintenance with acceptable shutdown times.</li> </ul> <p>(4) <b>Long cumulative run time</b> (<i>several thousands of hours of operation over several calendar years</i>):</p> <ul style="list-style-type: none"> <li>• the erosion lifetime of PFCs may be sufficiently short that several replacements will be required during the lifetime of the device;</li> <li>• large scale erosion also raises tritium retention and dust (safety) issues that may determine feasibility of reactor design;</li> <li>• neutron damage effects in the bulk of surrounding materials and structures (e.g. loss of thermal conductivity of carbon based materials, swelling, embrittlement, etc.);</li> <li>• plasma facing surfaces will be modified in situ by the plasma, which will mix the plasma facing materials. The composition, physical structure and properties of deposited materials will be different to manufactured materials.</li> </ul> <p>(5) <b>Routine operation with large amount of tritium</b> (<i>10–100 g/pulse versus fractions of g in current devices</i>):</p> <ul style="list-style-type: none"> <li>• this requires a closed fuel cycle with efficient reprocessing of the exhaust stream (e.g. limited but successful operation experience of TFTR and JET);</li> <li>• requires adequate tritium supply, minimization of the inventory of tritium retained on in-vessel components and efficient methods of recovery;</li> <li>• address safety concerns of any vulnerable tritium inventory.</li> </ul> <p>(6) <b>Superconducting magnet technology</b> (<i>if adopted</i>):</p> <ul style="list-style-type: none"> <li>• a thick neutron shield is required to protect the toroidal and poloidal coils, thereby increasing the major radius and the overall size of the device; neutron and gamma irradiations destroy organic insulators and superconductors, and also increase the resistivity of the stabilizing Cu (typical limit is <math>&lt;10^9</math> rad);</li> <li>• since the superconducting magnets will remain energized during the interval between pulses, certain techniques used in tokamaks for between-pulse wall preparation/conditioning will not be feasible;</li> <li>• long pulse devices have to be ‘self-conditioned’ during normal operation because of plasma/wall equilibration and wall saturation on a time scale of 100–1000 s.</li> </ul> <p>(7) <b>Fast remote maintenance for repair/refurbishment of the in-vessel and some of the ex-vessel components</b>:</p> <ul style="list-style-type: none"> <li>• viability of remote methods of maintenance, repair and upgrading of fusion devices, is a key technology for development of fusion reactors (e.g. limited but very successful experience at JET);</li> <li>• requires a specific system, component and subcomponent design philosophy to minimize shutdown times (fast remote maintenance and repair) and to meet stringent constraints imposed by a radioactive environment.</li> </ul> <p>(8) <b>Safety</b>:</p> <ul style="list-style-type: none"> <li>• Requires stringent and detailed safety assessments and safety related procedures and controls;</li> <li>• Stringent worker and public radiation protection measures;</li> <li>• Public education to establish safety and risk in context.</li> </ul> | <p>be extrapolated to a prototypical fusion reactor. Future fusion reactors must be capable of replenishing the tritium fuel they consume and provide</p> |
|--|---|
- 

a startup tritium inventory for subsequent reactors. However, it is expected that this technology will not be sufficiently developed to be incorporated into a

next step machine at the outset. The nuclear testing role of a facility such as ITER is fulfilled mainly through the installation of tritium breeding blanket test modules (see glossary), introduced through ports specifically designed for this purpose. The tests foreseen on modules include the demonstration of a breeding capability that would lead to tritium self-sufficiency in a reactor, the extraction of high grade heat, and electricity generation. It is anticipated that, in parallel with this activity, advanced structural materials, capable of handling higher heat fluxes, higher neutron fluences, and with better waste disposal qualities, would be developed for use in future devices. Such materials are not yet ready for use as the main structures of a next step tokamak. After the next step device, a fusion demonstration reactor (DEMO) is envisaged to establish the technological reliability and economic feasibility of fusion power generation.

### 2.2.2. Distinctive features of a next step tokamak

There are some essential differences between today's tokamak research facilities and viable design options for a next step device. They are summarized in Table 2, together with the related primary issues. The increase in pulse duration and cumulative run time, together with the increase in plasma energy content, will represent the largest changes in operation conditions in future fusion devices such as ITER. These will have by far the greatest consequences, giving rise to important PMIs, which are only partially observed and accessible in present day experiments, and will open new design, operation and safety issues. Table 3 compares some of the characteristic design and operation parameters of today's divertor tokamaks and ITER. For the latter, parameters of the ITER-FEAT [119, 134, 135] and 1998 ITER designs [119] are included for comparison.

Present day machines operate in short pulse mode, with plasmas maintained for periods of the order of seconds, between which pause times of 5–30 minutes are typical. The power and particle loads are small enough to be handled by making the PFCs, e.g. limiter modules or divertor plates (Fig. 1), of materials such as graphite, and by cooling between discharges. In present day tokamak devices, erosion of the main chamber wall and divertor strike plates acts as a source of impurities in the discharge, but does not affect the component lifetime, mainly because of the very low duty cycle ( $\approx 10^{-4}$ ). Erosion effects are on the scale of microns for a typical run cam-

paign ( $\approx 1000$ – $5000$  s/operation year) [64]. Similarly, fuel economy has never been an issue in deuterium fuelled experiments, and only recently have the limitations associated with the use of tritium, and its incomplete recovery in recent experiments in TFTR [121] and JET [124], brought the issue of fuel retention under closer scrutiny.

In contrast, long plasma duration and high duty cycle operation in a next step device such as ITER will lead to a magnitude of erosion/redeposition and tritium co-deposition that will affect operational availability, owing to the necessity of tritium removal and/or divertor plate replacement. Also, divertor heat loading caused by disruptions and Type-I ELMs (see glossary) [136] would imply melting/ablation for any material in the divertor wetted by the plasma (Section 5.4).

### 2.3. Most prominent plasma-material interaction issues for a next step fusion device

The most serious PMIs in a next step device are anticipated to occur in the divertor. This is primarily due to the concentration of power and particles onto relatively small areas of the divertor structure (Section 1.2). The most serious issues include power and particle control, response to off-normal events, tritium inventory and dust control [137]. These issues will be discussed in the following sections.

#### 2.3.1. Power dispersal and density control

##### 2.3.1.1. *Power dispersal and removal*

The thermal power, consisting of fusion alpha particle heating power (20% of the total fusion power for a DT reacting plasma), auxiliary heating power, ohmic heating power (see glossary), and the helium ash, must be exhausted from a thermonuclear plasma. This strongly influences several aspects of reactor design (impurity control, material selection, safety, etc.), and has an impact on reactor engineering.

As noted in Section 1.2.1, the peak power load on the divertor plates, in the absence of divertor radiation, is determined by the competition between parallel and perpendicular transport in the SOL, resulting in very small radial decay lengths, of the order of a few centimetres. Typical values of the parallel power density flowing in the SOL of a device such as ITER and today's tokamaks are shown in Table 3. For ITER, the typical peak heat flux on the  $\approx 10$  m<sup>2</sup>

**Table 3.** Comparison of characteristic parameters\* of contemporary divertor tokamak research facilities and ITER.

Parameters	Moderate-size tokamaks <sup>a</sup>	Large-size tokamaks <sup>b</sup>	ITER-FEAT <sup>c</sup> (1998) ITER design <sup>d</sup>
Major/minor radius (m)	1.65/0.5 (AUG)	3.25/1 (JT-60U)	6.2/2 {8.14/2.80}
Aspect ratio ( $A = R/a$ )	3.3 (AUG)	3.2 (JT-60U)	3.1 {2.9}
Vertical elongation ( $k = b/a$ )	1.9 (DIII-D)	1.8 (JET)	1.7 {1.6}
Triangularity (at 95% poloidal flux)	0.3 (AUG)	0.1–0.4 (JET)	0.35 {0.24}
Plasma volume/area (m <sup>3</sup> /m <sup>2</sup> )	14/44 (AUG)	82/150 (JET)	840/680 {2000/1200}
Wall/divertor plate areas (m <sup>2</sup> )	30/7–9 (AUG)	200/30 (JET)	680/80 {1200/200}
Plasma current (MA)	2–3 (DIII-D)	6 (JET)	15 {21}
Toroidal field on axis/at the coil (T)	8.0/17.3 (C-Mod)	3.8/6 (JET)	5.3/10 {5.68/12.5}
Material of toroidal field coils	Cu	Cu	Nb <sub>3</sub> Sn and NbTi
$Q = P_{fus}/P_{heating}$	0	0.2:5s, 0.62 <sup>e</sup> (JET)	10 {∞}
Type I ELM energy range (MJ)	0.02–0.04 (DIII-D)	0.1–0.6 (JET)	8–20 {25–80}
ELM deposition time (ms)	1 (DIII-D)	0.1 (JET)	~0.1–1
Plasma thermal energy (MJ)	1.2 (AUG)	15 (JET)	350 {>1000}
Disruption thermal quench time (ms)	0.1–1 (C-Mod)	1–10 (JET)	1–10
Disruption surface energy density (MJ · m <sup>−2</sup> )	0.03 (AUG)	0.1 (JET)	10–100
Disruption magnetic energy (MJ)	~1 (AUG)	10–15 (JET)	310 {~1100}
Disruption current quench time (ms)	10 (AUG)	~10 (JET)	25 {50}
Maximum halo current in VDEs (MA)	0.4 (C-Mod/AUG)	0.8 (JET)	6 {10}
Potential for runaway avalanche	No	No	Yes
$Z_{eff}$	1.3–3 (AUG)	1–3 (JET)	1.65 {<1.9}
Available volt-seconds (V · s)	10 (AUG)	15 (JET)	≤50 {≤80}
Energy confinement time (s) ELMy H mode	≥0.2 (AUG)	0.1–1 (JET)	3.7 {6}
Fusion power, $P_{DT}$ (MW)	—	16.1 (JET) <sup>f</sup>	>400 {1500}
Maximum auxiliary heating power (MW)	20 (AUG)	<32 (JET)	80 {100}
Maximum radiation from plasma core (MW)	8 (AUG)	5–10 (JET)	≤30 {~120}
Power entering the SOL (MW)	15 (AUG)	10–15 (JET)	120 {400}
Parallel power flux in the SOL (MW · m <sup>−2</sup> )	>150 (AUG)	100–200 (JET)	~400 {~2000}
Radial power $e$ -folding distance (m)	(3–5) × 10 <sup>−3</sup> (AUG)	(1–1.2) × 10 <sup>−2</sup>	~9 × 10 <sup>−3</sup>
Upstream plasma density (m <sup>−3</sup> )	(0.5–1.5) × 10 <sup>20</sup> (AUG)	~0.9 × 10 <sup>20</sup> (JET)	~3.5 × 10 <sup>19</sup> {1 × 10 <sup>20</sup> }
Peak div. power loads w. and w/o rad. (MW · m <sup>−2</sup> )	≥1–2 (5–10)	≥1–2 (5–10)	10–20/(5–20)
Baking temperature (K)	420 (AUG)	>570JET/JT-60U	510
Divertor pumping speed (m <sup>3</sup> × s <sup>−1</sup> )	~80 (AUG)	130 (JET)	<75 {200}
Pulse duration (inductive) (s)	<10	<25 (10div) JET	400 {≥1000}
Typical number of pulses per day	20 (AUG)	20–30 (JET)	≥10
Cumulative run time (s/operation year)	~7000 (AUG)	~20000–30000(JET)	>1 × 10 <sup>6</sup>
Duty cycle	≤10 <sup>−3</sup>	≤3 × 10 <sup>−3</sup>	~10%
Peak (net) divertor erosion rate (nm/s)	3–10 (DIII-D)	1–10	~7 {~16}
D (T) quantity introduced per pulse (g)	0.03 (AUG)	~0.2 (JET)	120 {300}
D/T wall retention (% fuelling rate)	10–40 (AUG)	10–40 (JET)	2–5 g/pulse {2–20}
Tritium removal from co-deposited films	not required	required	required
Authorized on-site tritium inventory (g)	—	5 (TFTR) – 90 (JET)	≥4000
Authorized in-vessel tritium inventory (g)	—	2 (TFTR) – 20 (JET)	~350 {~1000}
Peak DT (14 MeV) neutron rate (n/s)	—	1.2 × 10 <sup>17</sup> (JET)	5.3 × 10 <sup>20</sup>
Peak 14 MeV neutron flux (neutrons · m <sup>−2</sup> · s <sup>−1</sup> )	—	~6 × 10 <sup>14</sup> (JET)	~2 × 10 <sup>17</sup> {~4.4 × 10 <sup>17</sup> }
Lifetime neutron fluence (MW · a · m <sup>−2</sup> )	—	~0.001 (JET)	~0.3 {~1}
Remote handling maintenance	no	Yes	Yes

\* Denotes maximum values;

<sup>a</sup> Examples: Alcator C-Mod, DIII-D, ASDEX-Upgrade (AUG), etc.;<sup>b</sup> Examples: JET, TFTR, JT-60U;<sup>c</sup> Refers to the ITER-FEAT design;<sup>d</sup> Refers to the 1998 ITER design;<sup>e</sup>  $Q$  of 0.62 was achieved transiently;<sup>f</sup> >10 MW for 0.7 s; >4 MW for 3.5 s.



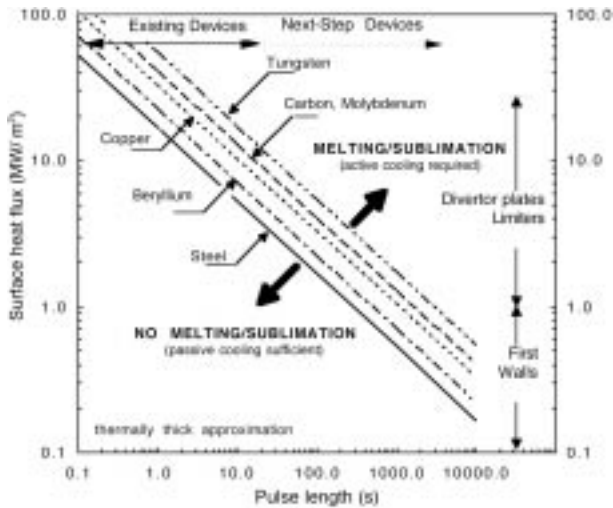


**Figure 3.** Combination of surface heat flux and pulse length required to vaporize the surface of an uncooled 'thermally thick' material.

SOL intercepted divertor area could be as high as  $20\text{--}30\text{ MW}\cdot\text{m}^{-2}$ , without radiative cooling, and these values are near or beyond the limit that can be handled by conventional materials and cooling technologies.

The combination of surface heat flux and pulse length required to vaporize the surface of an uncooled 'thermally thick' material is shown in Fig. 3. It can be seen that for heat fluxes in the range of  $0.1\text{--}1\text{ MW}\cdot\text{m}^{-2}$  (expected, for example, on the tokamak first wall), passive cooling is sufficient for existing devices, but not for next step devices with pulse lengths exceeding 100 s. For heat fluxes in the range of 1 to  $10\text{ MW}\cdot\text{m}^{-2}$  (i.e. on the limiters, divertor collector plates), passive cooling becomes marginal even in existing machines, and active cooling is required for any device with pulse length greater than a few seconds. A typical compromise for present devices involves the use of a robust refractory material such as graphite, coupled to cooling only between discharges (although some have demonstrated full active cooling, e.g. Tore Supra [138]). Figure 4 shows the dependence of the surface heat flux that produces melting of beryllium and tungsten and sublimation of carbon on the pulse length, for cases with passive and active cooling. Finally, under heat fluxes experienced during Type I ELMs (e.g. up to  $1\text{ GW}\cdot\text{m}^{-2}$ , lasting for up to about 1 ms) and plasma disruptions (e.g. up to several  $\text{GW}\cdot\text{m}^{-2}$ , lasting for about 1–10 ms), active cooling will not be able to prevent surface ablation or melting since the ther-

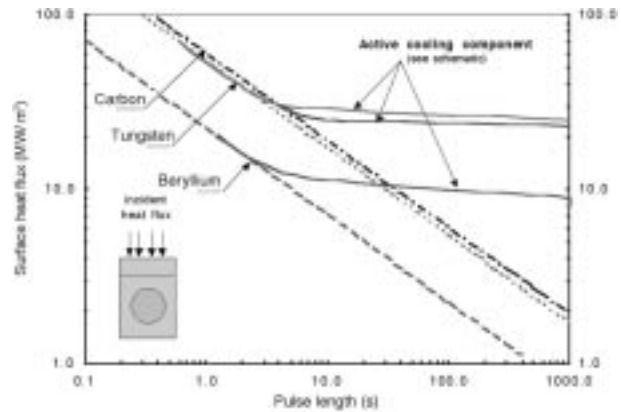


**Figure 4.** Dependence of the surface heat flux that produces melting of Be, and W and sublimation of C, on the pulse length, for case (a) with dashed lines of an uncooled 'thermally thick' material, and (b) with continuous lines of a typical actively cooled divertor component.

mal diffusion time (i.e. the time for heat transfer through the materials of the PFCs) is much longer (i.e. typically, seconds) than the duration of the event [139].

The high power density expected to be flowing in the SOL of a next step device calls for means of dispersing this power in order to reduce it to acceptable levels for steady state heat removal, i.e. about  $5\text{--}10\text{ MW}\cdot\text{m}^{-2}$ . The current strategy is to convert most of the flowing heat flux to impurity radiation in the outer periphery of the core plasma (Fig. 1), as well as from the SOL and divertor plasmas, and redistributing that heat flux over the very large side wall area of the divertor region in ITER [140–143]. Such a scenario can lead to the 'detached divertor' state [9]. This could be achieved, for example, by introducing noble gas ions, such as neon, argon or krypton (via controlled feedback loops for either pellet injection into the core plasma or gas puff into the SOL). However, the amount of radiation is constrained by the requirement to maintain the power flow through the separatrix above the H mode threshold (see Chapter 4 of Ref. [13]). Power dispersal by impurity radiation has been successfully implemented in today's tokamak experiments, and present machines have produced discharges where essentially 100% of the power is radiated in the main chamber boundary and divertor [13]. More recently, experimental and computational work has examined the radiation from carbon impurities intrinsic to all tokamaks [144]. Carbon is known to radiate effectively at low temperatures in the divertor plasma and is the dominant radiation

source in the many detached plasma experiments that have used only deuterium puffing.

Two dimensional plasma fluid and neutral transport codes, such as those discussed in Section 5.2, have been successfully applied to the study of SOL and divertor plasma experiments; in many cases, they are reasonably successful in describing the observed phenomena. The results are in satisfactory agreement with observations of divertor detachment [145]. In these models, it is seen that carbon impurities, sputtered physically and chemically from the graphite divertor strike plates, radiate as part of an uncontrolled but self-regulating loop. To date, these codes are important design tools for divertor layouts and/or for assessing the divertor performance of a given design under different operating conditions.

### 2.3.1.2. *Density control and helium exhaust*

Density control and helium exhaust are also aspects of tokamak operation that are important for any fusion reactor. Fusion power production depends sensitively on the core deuterium and tritium densities, which are controlled via a combination of pumping and fuelling. Fuelling in the main chamber (and, possibly, in the divertor) is required to establish an initial plasma, to replenish the DT consumed during burn and to replenish the DT pumped out with the helium. External pumping is required to remove the helium ash and to provide density control. The two primary methods of fuelling the core plasma in existing tokamaks are injection of fuel gas at the vessel wall (at the edge of the plasma) and injection of frozen D<sub>2</sub> pellets at high velocities directly into the core [146]. For reactor-like conditions (large plasmas and high plasma pressures) the pellet cannot penetrate very far, and fuel deposited near the edge can be quickly lost because of edge instabilities such as ELMs [147]. Recently, ASDEX-Upgrade [148] and DIII-D [149] have shown that pellet launch from the high field side of the plasma allows deeper pellet penetration and greater fuelling efficiency. This is the fuelling scenario favoured for a device such as ITER.

Maintaining the He ash concentration below  $\approx 5\text{--}10\%$  is required in a burning plasma to avoid excessive fuel dilution. Helium must be able to diffuse out of the core, and, once out of the core, must be efficiently pumped away to prevent its return [13, 150]. A pumpout time for He,  $\tau_{He}$ , that is less than ten times the energy confinement time,  $\tau_E$ , is sufficient for a reactor [120]. Studies in current

tokamaks [13, 151, 152], and code predictions for next step conditions [153], have confirmed that for ELMy H mode plasmas the thermal power and the He ash can be exhausted at the rates required for ITER. At the same time, good quality confinement and sufficiently high density and plasma beta (see glossary) can be maintained to produce the required fusion power. A disadvantage of operation in ELMy H mode is the relatively large (pulsed) ELM thermal energy loading on the divertor that represents a critical design challenge (Section 2.3.2).

### 2.3.1.3. *Erosion lifetime*

Erosion/redeposition in next step devices will affect operational availability because of the necessity of divertor plate replacement, and remote handling procedures to accomplish this are incorporated in the present design. High energy density disruptions ( $10\text{--}100\text{ MJ}\cdot\text{m}^{-2}$  in  $1\text{--}10\text{ ms}$ ) and Type I ELMs ( $\leq 1\text{ MJ}\cdot\text{m}^{-2}$  in  $0.1\text{--}1\text{ ms}$ ) (Section 2.3.2) will cause melting/ablation for *any* material in the divertor. While details of the damage caused by such disruptions are somewhat uncertain, calculations also show severe heating of nearby divertor components not directly wetted by the plasma (Section 5.4).

The general trends for the erosion lifetime of the ITER-FEAT, near the strike points, are illustrated in Fig. 5, for typical partially detached plasma operation (see glossary). A similar analysis was also carried out for fully detached plasma conditions [155]. The erosion lifetime is dependent on the maximum allowable thickness for the armour material and the erosion rate (material loss rate) due to sputtering, disruption and ELM vaporization and melting. The maximum thickness of the divertor tiles near the strike points is determined by imposing a maximum surface temperature under nominal ‘partially detached’ operation ( $\approx 10\text{ MW}\cdot\text{m}^{-2}$ ). For example, about 1770 K are reached for 20 mm CFC tiles (including degradation of the thermal conductivity resulting from neutron effects) and about 1570 K for 10 mm W tiles. The minimum thickness is taken to be  $\approx 2\text{ mm}$  or more (assuming that adequate cooling can be provided since otherwise a large fraction of the potential lifetime would be unused). The remaining thickness as a function of the number of shots is shown in Fig. 5 and includes the effects of physical sputtering and chemical erosion (only for carbon), erosion during ELMs, disruptions and slow transients (e.g. due to loss of control of detachment

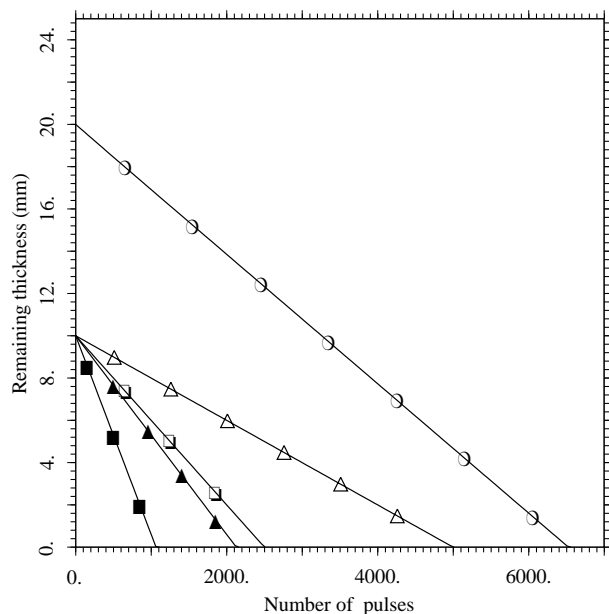


**Figure 5.** Remaining thickness versus number of pulses for initially 20 mm thick CFC and 10 mm thick W targets. The energy deposited during ELMs is assumed to be  $0.4 \text{ MJ} \cdot \text{m}^{-2}$  with a duration of  $\approx 200 \mu\text{s}$ , which is presently assumed as the reference value based on experimental evidence from various machines, frequency 1 Hz. The assumed frequency of disruptions and of slow transients is 10%. Peak net chemical erosion rate for CFC is assumed  $\approx 6 \text{ nm/s}$  (Section 5.3). Vaporized thickness during disruptions is assumed to be  $5 \mu\text{m}$  per event for CFC and W. In addition, for W, a melt layer of  $180 \mu\text{m}$  is assumed to be formed, part of which could be lost (e.g. 20% or 50%). For the assumed initial thicknesses of the target, vaporization and melting (the latter only for the case of W) during slow transients are negligible. Due to melting during ELMs, and depending on the heat flux in between ELMs, a 15 mm W target (not shown in the figure) will be eroded in less than one hundred pulses down to 12 mm for an assumed ELM energy density of  $E = 0.4 \text{ MJ} \cdot \text{m}^{-2}$  (7 mm for  $0.5 \text{ MJ} \cdot \text{m}^{-2}$ ). Symbols are: open circles refer to CFC; open squares refer to W with 20% melt loss during disruptions and ELMs; closed squares refer to W with 50% melt loss; open triangles refer to a case where the disruption frequency has been halved to 5% and with 20% melt loss, closed triangles refer to the same reduced disruption frequency with a 50% melt loss.

when the full power of the SOL strikes the target for several seconds, and the heat flux reaches  $20 \text{ MW} \cdot \text{m}^{-2}$ ).

The erosion lifetime of 20 mm carbon-fibre-composite (CFC) target, for ‘tolerable’ Type I ELMs

(i.e.  $\leq 0.4 \text{ MJ} \cdot \text{m}^{-2}$ ), is estimated at  $>5000$  shots and is determined by chemical erosion. Under similar conditions, the erosion lifetime of an initially 10 mm thick W is determined by disruptions, depends on the loss of melt layer, and is of the order of 800–2000 pulses. However, for W concerns remain on whether generation of surface irregularities might form hot spots in normal steady heat flux operation. For larger ELMs (i.e.  $> 0.6 \text{ MJ} \cdot \text{m}^{-2}$  with a duration of  $\approx 200 \mu\text{s}$ , a 10 mm W or a 20 mm CFC target can typically survive only a few pulses (10–100), e.g. up to a  $10^4$ – $10^5$  ELMs with a frequency of a few Hz. Thus, it is clear that operation which results in Type I and/or giant ELMs must be avoided. The effects of ELMs are further discussed in Section 5.4.3. Also, there are major incentives to avoid the occurrence of disruptions whenever possible and to reduce or mitigate the direct or consequential effects. For example, a factor 2 reduction in the assumed disruption frequency (from 10% to 5%) would yield a much higher erosion lifetime for a tungsten armour (i.e. 1700–4000 shots for an initially 10 mm thick W target, depending on the melt layer loss). In spite of the significant incentives, disruption mitigation avoidance in tokamaks in general, and in ITER in particular, remains as a goal to be achieved, particularly in operational regimes close to known operation limits — density, beta, and marginal radiation energy balance.

#### 2.3.1.4. Plasma contamination and wall conditioning

Impurity production (i.e. erosion) is not the only factor in plasma contamination. Equally important is the efficiency of impurity transport into the core plasma, and this depends critically on location (limiter versus divertor), plasma edge parameters, and wall surface material. Local divertor impurity sources strongly affect the radiation in the divertor. However, impurities produced in the main chamber are more efficient in contaminating the core plasma [9], especially those from first wall surfaces that are physically closest to the core (e.g. protection limiters, antennas and other protruding parts) and that receive considerable ion fluxes [156]. In ITER, modelling shows that the core plasma conditions are highly sensitive to neutral influx, and therefore, the divertor is designed in such a way that maximum isolation is achieved between the highly radiating divertor with its high neutral density and the main plasma chamber. In contrast to the divertor, erosion rates at the wall are predicted to be low enough that the tiles

do not need replacement [157, 158], but because of the large wall area, the total amount of eroded material is significant. This material will most likely end up in the divertor, probably contributing to tritium co-deposition, affecting the composition of materials surfaces and, consequently, changing the divertor performance. Also, there is some concern about the effects resulting from the impact of energetic particles (charge exchange neutrals and ions) on the first wall surfaces such as mechanical degradation of materials and production of dust. However, for metals such as beryllium and possibly tungsten, such microdamage was found to have a favourable effect as it reduces the implanted tritium inventory (Sections 3.5 and 5.6).

The first wall in several divertor tokamaks is an area that experiences net erosion, while the inner divertor is a region of net redeposition and the outer strike point undergoes net erosion. The mechanisms for the redistribution of carbon from areas of erosion to areas of redeposition are not all clear, and there is no satisfactory explanation for the extent to which interactions at the divertor and main chamber contribute to the observed redeposition (Sections 4.3 and 5.3). The observations of erosion/redeposition asymmetries on inner and outer targets are a function of the  $B \times \nabla B$  drift direction. This is one of the important influences controlling the parameters in the divertor, which themselves determine the degree of erosion/redeposition (in addition to surface temperatures, etc.).

It is, in general, difficult to compare the impurity control capabilities of different tokamaks. The  $Z_{eff}$  (see glossary) of the core plasma is certainly a measure of the core cleanliness; however, the primary deficiency in this benchmark is that it does not tell us the shielding capability of a given operational scenario and how it varies with the  $Z$  of the impurity. Even so, there have been several comparisons of different operational scenarios in a single tokamak. For example, in ASDEX it was found that the core  $Z_{eff}$  was 2–3 for limiter operation, and 1–2 for divertor operation [13]. Similar comparisons have been made in C-Mod with a smaller variation but similar trends [13]. In general, the  $Z_{eff}$  in diverted tokamaks tends to be lower than in limiter tokamaks.

Carbon and tungsten are the present candidates for use in the ITER divertor (Section 2.4). The plasma compatibility of carbon and tungsten impurities in a burning plasma experiment has to be assessed from two different points of view. The tolerable amount of carbon (concentration  $<1.5\%$ ) in the

plasma is limited by the dilution of the fuel (dilution limited) while that for tungsten (concentration  $<2 \times 10^{-5}$ ) is limited by radiation losses in the plasma core. Carbon has a relatively high chemical sputtering yield (1 to 2%) at hydrogen (H, D, T) fluxes lower than  $10^{22} \text{ m}^{-2} \cdot \text{s}^{-1}$  (Section 3.2). This large source term of carbon could pollute the plasma beyond the above mentioned limit even when considering the relatively good impurity retention in a divertor. This implies that designs of next step tokamaks should minimize surfaces clad by carbon. Owing to the low concentration limit for tungsten, a large source would be intolerable. Experience in modern divertor tokamaks [115, 117] indicates that for plasma edge conditions similar to those anticipated in a next step tokamak, most of the sputtered tungsten would be locally redeposited within one gyroradius. In addition, because of the high sputtering threshold, W is predominantly sputtered by impurity ions, and thus the total sputtered flux is relatively low. This combination of a low source term and high impurity retention in the divertor makes W a candidate plasma facing material in the divertor of a next step tokamak. However, melt layer issues remain. There is a need to gain more operational experience with tungsten in present day tokamaks, and experiments are ongoing in ASDEX-Upgrade [117] to determine its suitability in areas of the main chamber.

A wide variety of wall conditioning techniques have been developed and applied in tokamaks (Section 4.6.2) over the past two decades, and wall conditioning in a next step device is projected to also involve a variety of different methods [13]. However, extrapolation of wall and surface conditioning methods to a device such as ITER, and to reactor tokamaks in general, is not straightforward. Specific design related features, e.g. superconducting magnets, combined use of different wall materials and operational limitations, will preclude or limit the utilization of some of the most extensively used current surface conditioning techniques. The increased duty factor (see glossary) will result in a substantially different wall conditioning situation than in present tokamaks. The permanent presence of the toroidal field will preclude glow discharge cleaning (GDC); see glossary. Applicability of standard pulse or Taylor discharge cleaning methods [159] is likely to be very limited. Therefore, electron cyclotron resonance (ECR) and/or ion cyclotron resonance (ICR) conditioning (see glossary) are envisioned for between-pulse cleaning. The feasibility of these methods for conditioning in present tokamaks is under

investigation, and promising results have been already obtained [40, 41, 160, 161].

The uses of other wall conditioning techniques are more speculative. Diborane ‘flushing’ [162, 163], i.e. chemical ‘passivation’ of oxygen by the injection of  $B_2D_6$  gas, is not affected by magnetic fields and may be a useful technique between pulses. The effect of periodic thin film deposition such as boron will be, at most, transient. Such transient deposition could be important for discharge initiation or real time erosion control. However, a new technique for lithium wall coating by a laser generated aerosol [164] operates during the discharge and has the potential to sustain a Li coating in long pulse machines. The use of beryllium as first wall material in ITER should provide oxygen control since some of this wall material will be sputtered and redeposited elsewhere in the machine where it could act as a natural getter.

Finally, appropriately modified wall conditioning techniques (e.g. He/O discharges or baking in an oxygen atmosphere) are also being studied as a means of removing the co-deposited tritium inventory in ITER (Sections 2.3.3 and 4.7.2). The detailed operational requirements for baking the PFCs in ITER will be determined both by the basic plasma operation requirements, and by the PFC materials and the conditions under which they are used. In this respect, mixed material effects resulting from the use of different armour materials in different regions of the machine (Section 2.4) add significant uncertainties. However, it is quite clear that the introduction of oxygen for the removal of tritium will compromise the surface conditions needed for plasma operation.

### 2.3.2. Effects of disruptions and other plasma disturbances

#### 2.3.2.1. General remarks

All existing tokamaks are subject to occasional rapid plasma termination events, called ‘disruptions’. In the early years, disruptions were mainly regarded as a nuisance, and the limited time and spatial resolution of the diagnostics prevented much progress in their understanding [165]. In present day large size machines, such as JET, TFTR and JT-60U, disruptions have already caused significant machine damage, e.g. melting or erosion of PFCs, short circuits in external supplies and deformation of in-vessel structures [13]. The situation is predicted to be more severe in future fusion devices, such as ITER, where heat loads and forces will be up to two orders of mag-

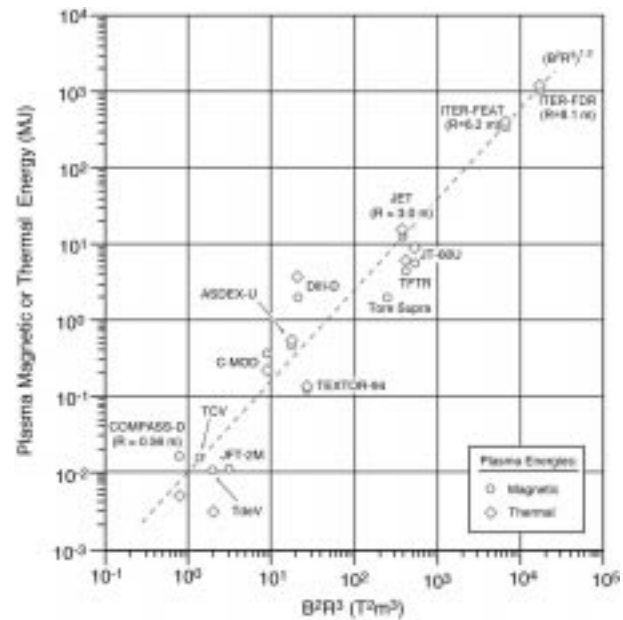


**Figure 6.** Plasma magnetic and thermal energies in tokamaks. Magnetic and thermal data are not necessarily simultaneous. Magnetic energies are estimated from major radius,  $R$ , minor radius,  $a$ , plasma elongation,  $k$  (see glossary), and toroidal field,  $B_T$ , and assume a safety factor,  $q_{95} \approx 3$ . Energy shown is only internal plasma energy: magnetic energy outside the plasma is not included. Thermal energies are derived from Refs [166, 168]. Relative auxiliary heating, and hence plasma energy capabilities, vary among experiments. The  $(B^2 R^3)^{1.2}$  ‘scaling’ fit is empirical and has been drawn by eye. Data are for the 1998 ITER design (labelled as ITER-FDR) and the most recent ITER-FEAT design parameters. The increase in  $W_{mag}/R^2$  and  $W_{th}/R^2$  from COMPASS-D to the 1998 ITER design is about 70. This applies for the scaling of radiation of thermal energy to the first wall. For divertor thermal energy deposition, if one assumes a fixed SOL width, then the increase in energy loading per unit area from JT-60U and JET to the 1998 ITER design scales as  $W_{th}/R$  and increases by about 40. (Figure provided by J. Wesley of General Atomics).

nitude larger (Table 3). The underlying disruption erosion mechanisms are described in Section 3.4. The experimental database, mainly from disruption simulation facilities, is presented in Section 4.5, whereas the erosion effects projected in a next step device are discussed in Section 5.4.

Disruptions can generally be divided into two basic categories: major disruptions and vertical displacement events (VDEs) (see glossary) leading to a disruption. These differ in the sequence of events.

In a major disruption, the plasma first becomes unstable as a result of reaching an operational limit, in density or beta, which leads to the growth of a large magnetohydrodynamic (MHD) mode (see glossary). In present devices, this is sometimes initiated by a small piece of material falling into the plasma. The resulting rapid cooling of the plasma periphery can result in an unstable plasma. The large MHD activity causes a loss of nested confinement (magnetic field) surfaces. The thermal energy is rapidly lost (thermal quench), and the current profile flattens, causing a drop in the plasma inductance (see glossary) and a corresponding upward spike in the current. Finally, the high resistivity of the cold plasma results in a rapid decay of the plasma current (current quench). The plasma radial and vertical positions are frequently lost after the thermal quench as a consequence of the change in the current profile. In a VDE, the results are similar but the sequence is different. The first event is a loss of the vertical position, and the plasma moves vertically with the cross-section and the edge safety factor,  $q$  (see glossary), decreasing as the plasma scrapes off against the first wall. The plasma then disrupts: thermal quench occurs (typically, there is no current spike), followed by a current quench.

#### 2.3.2.2. *Effects of disruptions and design considerations*

Extensive progress has been made in understanding and quantifying the impact of disruptions on an ITER scale device [13]. Disruptions will have the same underlying causes as those in present day tokamaks; their consequences will, however, be much severer [166]. First, the plasma thermal energy in ITER will be 10–100 times larger than in JET and up to a 1000 times higher than in Alcator C-Mod [167]; see Fig. 6 [166, 168]. More importantly, the ‘specific energy’ during the thermal quench of an ITER disruption (i.e. the plasma thermal energy divided by the surface area of the PFCs wetted by the plasma), which provides a measure of the severity of the PMI in disruptions, will be about 10–100 MJ·m<sup>−2</sup> in a time of the order of 1–10 ms. Thus, the specific energy in ITER will be 10 times larger than in JET and JT-60U and about 40 times larger than in Alcator C-Mod.

Although the time scale for energy deposition in the rapid ‘thermal quench’ phase of a disruption will be somewhat longer in ITER than in present day tokamaks, it will still be insufficient for heat trans-

fer through the material of PFCs. Thus, disruptions in ITER will cause ablation and melting of surface material of the divertor target area, and possibly a good fraction of the divertor walls [169, 863]. Calculations and experiments show that a vapour shield should form in front of the divertor targets, dispersing the majority of the incident energy flux to the divertor chamber walls via radiation. This, in turn, could cause thin melt and vaporization layers to form over nearby components (Sections 3.4 and 5.4). This wall ablation, which is expected to dominate the PMIs during disruptions in ITER, is energetically impossible in present day tokamaks.

Second, VDEs will produce much larger forces on vessel components in ITER than in present day tokamaks. As the plasma column moves during a VDE, a substantial fraction of the plasma current is transferred to a ‘halo’ region around the main plasma. Since the halo intersects the vessel wall, the return path for this ‘halo current’ (see glossary) passes through conducting components of the vessel structures. The flow of this return current will be perpendicular to the main magnetic field, thus exerting a large mechanical force on these structures. The ITER design allows for halo currents that are approximately the same fraction of the total plasma current as is observed in present day experiments [13]. In addition, plasmas with strongly shaped cross-sections, such as in ITER, are also subject to a particular kind of disruption, in which the entire plasma column moves vertically (e.g. owing to a fault in the vertical position feedback control system) without a disruption thermal quench. The main difference between this type of event and a thermal quench initiated ‘vertical disruption’ is that in the latter the thermal energy loss has essentially been completed before appreciable vertical motion develops. The VDE will lead to intense PMIs such as impurity release and wall melting and vaporization. Because of the longer duration, deleterious effects may result at the armour/heat sink interface in the regions of the first wall where the plasma intersects the PFC wall surfaces. These effects are not present or appreciable in present experiments, whereas in ITER they are expected to deposit several tens of MJ·m<sup>−2</sup> over times of the order of a fraction of a second (Section 5.4).

Third, the high electric fields produced by disruptions can also give rise to production of runaway electrons (see glossary) with multi-MeV energy (Section 4.5.2.3). Although, in recent years, significant progress has been made in characterizing the

**Table 4.** Type, range of parameters and major consequences of plasma transient events in the ITER design. The numbers refer to the ITER-FEAT and (in parenthesis) to the 1998 ITER design.

Event	Key Characteristics	Major Consequence(s) and/or comments(s)
Disruptions	frequency: $\sim 10\%$ ; thermal energy $\approx 0.35$ GJ $\{\approx 1$ GJ}; thermal quench time: 1–10 ms; magnetic energy $\approx 0.31$ GJ $\{\approx 1$ GJ}; current quench time: 50–1000 ms; max. current decay rate: 500 MA/s.	– vaporization (and also melting for metals) of divertor targets, and nearby surfaces; – during the thermal quench, 80–100% of the thermal energy ( $W_{th}$ ) is transported by conduction to divertor; $\leq 30\%$ by radiation to first wall or baffle; – during the ensuing current quench phase, 80–100% of the energy is transferred to the first wall by radiation, with a poloidal peaking factor of $\sim 2$ ; $\leq 20\%$ by conduction and localized radiation during VDEs; – initiates VDE and runaway conversion.
VDEs	duration $\approx$ plasma quench; direction = up or down (depending on changes of plasma current and inductance); halo current $\leq 40\%$ .	– follows each disruption; – slow current quench $\rightarrow$ worst VDE; – part of the magnetic energy ( $W_{mag}$ ) is lost to the first wall; – produces in-vessel halo currents and forces on in-vessel components.
Loss-of-equilibrium-control VDE	frequency: 1% of pulses drift $\approx 1$ –5 s to wall contact onset; first wall contact initiates H mode loss, $W_{th}$ loss, melting, rapid current quench or disruption	– initiated by poloidal field control failure; – electromagnetic effects (halo current/vertical force); – major thermal effects on first wall; – affected first wall region: upper/inside or divertor entrance baffles.
Runaway current conversion	knock-on avalanche, $E \approx 10$ –15 MeV, $W_{th} \approx 60$ MJ $\{\approx 500$ MJ}	– many uncertainties (see text); – toroidal localization depends on first wall alignment; – shutdown species will influence runaway electrons current.
Fast shutdown (active control)	$\tau_{th}, \tau_{mag} \leq 1$ s; by impurity or H/D injection.	– fast plasma power and current shutdown means for thermal protection of the first wall and divertor targets; – by impurity or D injection; D favoured to minimize runaway conversion.
ELMs Type I or Giant ELMs	frequency: 2–0.5 Hz, $\Delta W_{th}/W_{th} \sim 2$ –6% deposition time: 0.1–1 ms;	– Type I and Type III ELMs are frequently observed; – $\sim 50$ –80% of the energy lost from the core plasma is observed to strike the divertor target (e.g. in DIII-D, ASDEX-Upgrade); – JET, DIII-D, ASDEX-Upgrade reported inboard energies, 2–4 times that on outer divertor (see text for further details).
ELMs Type II	frequency: high; amplitude: small	– associated with high triangularity plasma configurations; – database for Type II ELMs is too small for use in ITER design.
ELMs Type III	$\Delta W_{th}/W_{th}$ is a factor 5–10 less than for Type I ELMs.	– Type III are fairly universally observed; – prevalent in regimes associated with detached divertor operation and at heating power near the H mode threshold power, both of which are relevant to ITER operation; – have a small amplitude and should not be a concern for erosion.

major elements involved in runaway generation (see, e.g. Ref. [13]), there are still substantial uncertainties related to the quantification of material damage

effects and the database from tokamaks is somewhat limited in this respect. Table 4 summarizes the main types of transient plasma event expected in a device

such as ITER, as well as their characteristics and major consequences.

The thermal quench duration is estimated to be 1–10 ms; this range reflects uncertainty in extrapolation of data to ITER size and plasma temperature, and also the observation that thermal quenches are sometimes single step and sometimes multistep. The location of the thermal quench deposition is expected to be within the divertor. Since a SOL widening of up to ten times is sometimes seen in present experiments, part of the SOL and, therefore, of the energy may be deposited on the wall region near the divertor entrance and/or the first wall. Partitioning of the energy between the inner and outer divertor is relatively uncertain; however, data typically show more energy to the inside divertor. Dissipation (80–100%) of the magnetic energy in the current quench phase will be primarily by radiation to the first wall, with a poloidal peaking factor of  $\leq 2$ .

VDEs and runaway electron events during the current quench phase will result in more localized energy deposition on the first wall. For further details, see Refs [13, 170, 171]. Any misalignment of the first wall tiles will increase local heat deposition.

#### 2.3.2.3. *Other plasma disturbances, e.g. ELMs*

Other plasma disturbances such as sawteeth (see glossary), ELMs and other recurring bursts of MHD activity are routine aspects of normal plasma operation and will continue during the entire pulse. The main characteristics and the resulting consequences of these events are summarized in Table 4. A detailed discussion of these processes is beyond the scope of this review, and the interested reader is referred to Refs [2, 13, 172]. ELMs [136] produce a periodic very rapid expulsion of thermal energy and particles from the edge region into the SOL and, finally, to the surfaces of the divertor and/or first wall, which must be designed to withstand these types of events. ELMs transiently reduce the temperature and density at the top of the H mode transport barrier and thereby affect core confinement. In addition, they lead to increased transient peak heat loads on and increased erosion of the divertor plates [173]. Although ELMs are instabilities localized to the periphery of the core plasma, scaling studies from current tokamaks indicate that 3–10% of the thermal energy of the core plasma can be quickly ( $\approx 0.1$ –1 ms) lost to the divertor [172]. This represents energy densities that surpass the severest disruptions in current tokamaks, and ELMs occur every second or so! The predicted

material damage, by evaporation and melting, represents critical design issues for a next step tokamak device [2] (Sections 2.3.1.3 and 5.4.3).

#### 2.3.2.4. *Disruption and ELM mitigation*

Disruption avoidance would conserve the operational lifetime of in-vessel components and avoid loss of operational time for wall reconditioning. However, despite these significant incentives, disruption avoidance remains a goal to be achieved, particularly in regimes close to known operation limits. Therefore, when designing PFCs, it is important to distinguish between events that will be handled by avoidance from events that must be included in the design. At present, the ITER divertor is being designed to accommodate disruptions for lengthy operating periods before replacement will be required. For this reason carbon has been selected near the strike points to withstand the power loads of disruptions without melting. As an alternative, during the early phase of ITER, special limiters could be used to handle VDEs, runaway electrons, etc. Such limiters, however, may not be suitable during the later phase of ITER, where long lifetime, tritium inventory, etc. become important issues.

There has been some experience with disruption mitigation in existing tokamaks using large gas puffs or pellet injection of noble gases (He, Ne, Ar), which tend to dissipate the stored kinetic energy through impurity line radiation. These techniques reduce power loading on the divertor plate by a factor of two to three, as well as vessel forces due to poloidal halo currents (e.g. see Ref. [174]). The injection of a solid impurity pellet (commonly termed a killer pellet) into a tokamak plasma is capable of effecting a rapid non-disruptive shutdown of plasma energy and current. These pellets are typically composed of moderate or high Z materials, and the pellet size and velocity are chosen such that the pellet can penetrate deeply into the plasma core. Impurity pellet shutdown experiments demonstrating non-disruptive dissipation of the plasma thermal and/or magnetic energies have been performed in JT-60U [175–177], ASDEX-Upgrade [178, 179], DIII-D [174, 180, 181], Alcator C-Mod [182], JET [183] and TFTR [184, 185]. The efficacy of killer pellet shutdown clearly depends on having sufficient penetration of the pellet into the plasma such that the resulting impurities are deposited more or less uniformly all over the plasma cross-section. Rapid anomalous inward transport of the injected radiat-



ing impurities has been observed [186]. This tends to cause effective radiation cooling over the entire plasma radius, with 90–100% of the stored kinetic and magnetic energy being radiated.

Effective shutdown also depends on selecting an impurity that radiates strongly at the moderate plasma temperatures (typically, a few hundred eV) that arise following the initial adiabatic cooling produced by the pellet. In present experiments, these features are obtained by tailoring the pellet species and mass (see, e.g. [178]) and, to a more limited extent, the injection velocity to provide strong radiative cooling. However, injection of high Z impurities leads to the generation of potentially damaging large runaway currents [174, 187]. In DIII-D [174], signatures from runaway electrons have been observed on all argon pellet discharges and on many neon pellet discharges. Deuterium injection avoids, in principle, this problem but the amount of injected material required is very large. Recently, massive bursts of helium gas have been used to mitigate the deleterious effect of VDEs and density limit disruptions in the DIII-D tokamak [174, 188]. Because of the high plasma densities achieved, no runaway electron production was expected and none was observed. Most of the energy flowing towards the divertor is seen to be dissipated as radiation in the main chamber. The simplicity and expected reliability of this technique makes it a strong candidate for disruption mitigation in large scale devices. Injection of hydrogen or helium liquid jets has also been proposed as a new concept for disruption mitigation and fast shutdown in tokamaks [189]. Liquid jets can rapidly cool the plasma to reduce divertor heat loads and large halo current forces, while simultaneously raising the density sufficiently to prevent runaway electron generation [190]. Another novel method for fast shutdown of a large, ignited tokamak consists of the injection of 30–45 (6 mm) deuterium pellets doped with a small (0.0005%) concentration of krypton, and the simultaneous rampdown of the plasma current and shaping fields over a period of several seconds using the poloidal field system [191].

Unlike disruptions, which must be practically eliminated in a working reactor, ELMs will continue to be present in order to provide particle and impurity control. Transient peak loads during ELMs in future devices are relatively uncertain, owing to the uncertainty on the thermal energy loss from the core plasma during an ELM, the fraction of energy deposited on the target plates, the deposition profile on the divertor target and the duration of ELM

energy deposition. However, it is quite clear that Type I and giant ELMs pose a significant problem on ITER [2]. Encouragingly, high confinement modes with small ELM amplitudes (often classified as Type II ELMs, although it has not been verified whether all these modes correspond to the same phenomenon) have been observed in several devices, e.g. grassy ELMs in DIII-D [13], ‘minute’ ELMs in JT-60U [13], and the enhanced  $D_\alpha$  (EDA) mode in Alcator C-MOD [192]. Recent experience at JET has shown that discharges with radiofrequency (RF) heating only had low amplitude ELMs, and that it may be possible to use shallow pellets to trigger ELMs, thereby lowering their amplitudes. Measurements from ASDEX-Upgrade [193], as well as new experiments with gentle gas puffing in DIII-D [194], show a much lower normalized ELM energy loss (typically, a factor of four) than the results in [172], with only modest degradation of confinement. Near the H mode threshold, Type III ELMs (whose amplitude is much smaller than that of Type I ELMs) have been observed [136].

### 2.3.3. Control of the in-vessel tritium inventory

#### 2.3.3.1. *In-vessel tritium inventory in plasma facing components*

Safe management and accounting of tritium will be crucial for the acceptance of fusion as an environmentally benign power source. Tritium retention in plasma facing materials has emerged as a primary concern for next step fusion devices fuelled with mixtures of D and T, with strong implications for in-vessel component design, material selection, operational schedule and safety. Special controls imposed on the handling of tritium [195–197] require that the quantity of tritium retained in the torus be accounted for and the inventory limited [198, 199] in order to permit continued operation within the licensed site inventory limit. An excessive tritium inventory in the torus would present a safety hazard in the form of a potential tritium release to the atmosphere in case of a loss-of-vacuum accident. For example, in TFTR, the quantity of tritium permitted in the vessel was restricted to <2 g to limit release to the environment in the event of a major vacuum leak and simultaneous failure of tritium containment systems. Besides tritium inventory control, tritium removal from the wall is required to control plasma fuelling by tritium implanted in the wall and to reduce the tritium outgassing and thus to mini-

**Table 5.** Tritium in current facilities and future devices

Parameters	TFTR			JET		Next Step <sup>a</sup>
Year	1993–95	1996	1997	1991	1997	
Peak fusion power (MW)	10.7	8.5	7.8	1.8	~16	500–1500
Total discharge duration (s)	8	4.2	6.5	10–30	20–30	300–1000
Total number of discharges	14 724	5324	3619	2	~593	>10 <sup>4</sup>
Discharges with NBI	6134	2167	1609	2	>50%	—
Discharges with tritium NBI	500	124	107	2	~134	—
Typical number of tritium pulses per day	0–5	0–5	0–5	—	10	10–20
<i>T</i> processed by facility (g)	73	17	15	0.1	100	—
<i>T</i> introduced in the torus and NBIs (g)	3.3	0.84	1.1	0.005	35 <sup>b</sup>	—
<i>T</i> introduced per pulse (g/pulse)	<0.048	<0.01	<0.014	—	<0.25	50–200
<i>T</i> inventory in the torus and NBIs (g)	1.7	1.6	1.8	0.004	11.5 <sup>c</sup>	—
Average retention (excluding cleanup)	51% <sup>d</sup>	51% <sup>d</sup>	51% <sup>d</sup>	—	40%	<10%
Increment of tritium inventory (g)	1.7	0.81	0.76	0.004	11.5 <sup>e</sup>	<20 g/pulse
<i>T</i> removed during cleanup period (g)	0.96	0.49	0.98	0.0045	5.5 <sup>e</sup>	~99% <sup>f</sup>
<i>T</i> remaining at end of cleanup period (g)	0.74	1.06	0.85	—	~6 <sup>e</sup>	—
<i>T</i> permitted in the vessel (g)		2		20 (first wall)		<1000 <sup>g</sup>
				11 (cryopumps)		
<i>T</i> permitted on site (g)		5		90		~4000 <sup>g</sup>
Fuel cycle	open	open	closed	closed		closed
Exhaust processing		batch		batch		semicontinuous
Breeding blanket		—		—		Test modules <sup>h</sup>

<sup>a</sup> Estimated values.<sup>b</sup> 0.6 g by NBI and the rest by gas puffing.<sup>c</sup> This was the tritium inventory in all systems outside the active gas handling system (AGHS) (i.e. NBIs, torus), but individual analysis of batches of gas from the different subsystems indicate that the torus contributes >90% of the inventory (see Section 4.7).<sup>d</sup> This is an average value over the period 93–97, excluding dedicated tritium removal campaigns.<sup>e</sup> Some cleanup was also done in the middle of DTE1, in order to repair a small water leak in the fast shutter of the neutral beam. At that time 11.4 g of *T*<sub>2</sub> had been introduced into the torus and about 4.6 g of tritium was retained on the walls. The wall load was reduced to 2.3 g in a four day period with ~120 pulses.<sup>f</sup> Design requirement.<sup>g</sup> Significant uncertainties still exist.<sup>h</sup> It is expected that installation of a tritium breeding blanket capable of replenishing at least in part the tritium that is consumed will not be required in a next step experimental fusion facility, at least at the outset. Required breeding blanket technology development will be carried out in a next step device mainly through installation of breeding blanket test modules, introduced through vessel ports specifically allocated and instrumented for this purpose.

mize personnel exposure during venting of the torus for maintenance. Independently of safety limits, control of the in-vessel tritium inventory is also necessary to avoid exhausting the available tritium supply. Tritium retention mechanisms are reviewed in Section 3.5.

Hydrogen and deuterium retention has been measured in several tokamaks, and recently the large tokamaks, TFTR and JET, have provided precise measurements of tritium accounting (Section 4.7.1) and have expanded the technical knowledge base for tritium issues in fusion reactors [200]. Table 5 pro-

vides a list of key quantities related to tritium in existing tokamaks and a next step device [201–204].

Tritium retention and the control of the tritium inventory in ITER and future reactors strongly depend on the choice of plasma facing materials and their operational conditions (e.g. temperature of PFCs, flux density of impinging particles, plasma edge conditions) and geometry effects (gaps, shaded regions, etc.). Recent experimental results (Section 4.7.1) and modelling (Sections 5.3 and 5.6) show that as long as some carbon is used in the machine to clad the divertor plates, the dominant mechanism

for hydrogenic retention will be co-deposition with carbon, and there will be a need to mitigate/control tritium accumulation via co-deposition in the torus. Retention by other mechanisms such as implantation and surface adsorption, which may be significant for small short pulse machines, is expected to rapidly reach saturation in ITER.

Laboratory measurements have shown that co-deposited films start to decompose when exposed to air at temperatures  $>520$  K, releasing tritium (Section 4.7.2.1) [205–209]; so they are considered to be risky under ITER accident conditions, and their accumulation needs to be strictly controlled on safety grounds. The released hydrogen is mainly in the form of water [210]. A precautionary operating limit of 1000 g was set for mobilizable in-vessel tritium in the 1998 ITER design, based on safety considerations due to the release from postulated accident sequences (more than a factor of two lower, i.e. about 350 g, is set for the design of the smaller ITER-FEAT). Upon reaching this limit, operation needs to be discontinued and dedicated cleaning techniques/procedures (discussed below) applied to reduce the torus tritium inventory. The frequency of cleaning intervention will strongly depend on the rate of co-deposition.

It is clear that the rate of tritium buildup observed in JET and TFTR (Section 4.7.1) is much too high for a next generation fusion device. However, there are still large uncertainties in quantifying the in-vessel tritium inventory in next step devices. The tritium retention fractions in terms of throughput experienced in existing machines cannot be simply applied to ITER. The fraction of tritium retained in a tokamak depends on the amount of eroded carbon, which in turn depends on the machine geometry, plasma edge conditions, wall material and temperature, fuelling and heating methods, etc. Thus, detailed modelling, including these effects and validated in existing tokamaks, is necessary to predict tritium retention in ITER in a reliable way. Modelling has been performed for typical plasma edge scenarios (Section 5.3) [3, 154, 158, 211] to predict the tritium inventory in ITER. The estimated tritium co-deposition rates are relatively high (i.e. in the range of 2–20 g/pulse), although the projected retention fraction is lower than that observed in present day tokamaks (TFTR, JET [201, 204]). Although these estimates are still uncertain, mainly because of the uncertainties of the plasma edge physics parameters and material erosion properties, including the effects resulting from mixing of materials, the results are nonetheless useful to illustrate

trends and to guide the current material selection (Section 2.4).

### 2.3.3.2. *Tritium removal from co-deposited layers*

Interruptions of plasma operations, as often as weekly, to remove tritium will be necessary in a next step device with carbon PFCs. In JET and TFTR (Section 4.7.1), tritium removal took place over several weeks, i.e. considerably longer than the approximately 1000 s cumulative total time of high power DT discharges [202, 204]. This would not be adequate in a fusion facility such as ITER, where the tritium removal rate will need to be orders of magnitude higher in order to support the operational schedule of the reactor.

Although several alternatives are being considered for the removal of the T rich co-deposited layers, their removal from a next step machine remains a major unsolved problem. Techniques involving exposure to oxygen (e.g. thermo-oxidative erosion at temperatures above 570 K, or oxygen plasma discharges) have been found to be most effective in laboratory experiments to remove tritium from tritium containing films (Section 4.7.2). Major drawbacks of techniques using oxygen, especially at elevated temperature, include potential damage of other in-vessel components, and wall conditioning recovery time for normal plasma operation. No practical method of localizing the oxidation to the area required (and avoiding oxygen exposure elsewhere) has been developed, although various ideas are being explored. In addition, processing of the DTO exhaust generated is costly. Alternatively, high temperature baking ( $>900$  K) under vacuum is sufficient to remove the trapped tritium, but is technically very difficult to achieve in the torus. Finally, solutions to mechanically move T bearing flakes to an ex-vessel reclamation facility (e.g. by using a conveyor [212]) are also being investigated.

Further development and optimization of the divertor design, based on information provided by future experiments in existing tokamaks, would be useful to control and to mitigate the extent of the co-deposition problem. From design perspectives, initial considerations are being given to solutions that could mitigate co-deposition in critical areas of the divertor (Section 2.5).

If carbon based materials were to be eliminated from the divertor of a next step device, the situation as far as tritium inventory is concerned would be radically different and the control of the tritium

inventory could be much better manageable (see, for example, the experience gained for of Alcator C-Mod (Section 4.7.1.3) [213]). New design solutions using tungsten instead of carbon for high heat flux regions are being explored (Section 2.5). However, the ability of tungsten to withstand high heat flux transients without suffering damage through melting is unclear and may make disruption mitigation a necessity (Section 6.6).

#### 2.3.3.3. *Fuel Isotopic tailoring*

Efficient plasma fuelling is very important for any DT fusion device as the tritium supply is limited and expensive. Only a fraction of the tritium is ‘burnt’ in the plasma, and minimizing the tritium throughput reduces the cost of reprocessing of the plasma exhaust and the potential for losses into the environment [31].

The tritium fractional burnup (see glossary) in JET and TFTR was low (i.e.  $10^{-4}$  in TFTR). However, in a device such as ITER, the tritium burnup fraction is expected to be  $\approx 1\%$  [31], and up to 30% under very optimistic conditions in future reactors (ARIES-RS [214]; see glossary). The high tritium burnup fraction in ARIES-RS is due to the anticipated higher power density; basically, more tritium is burnt before it can be transported from the plasma core. A tritium fuelling rate of at least 0.1–0.2 g/s will be needed to fuel a 1000 MW reactor with a burnup fraction of 1%.

Tritium rich pellets could fuel an optimal 50:50 D:T mix in the core plasma, while deuterium rich gas puffing would lead to a reduced tritium fraction in the edge plasma [215]. Because of the improved particle confinement associated with the deeper tritium core fuelling component, comparable core densities of deuterium and tritium can be maintained even when the edge deuterium fuel source is much larger than the core tritium fuel source. This isotopic tailoring of the deuterium and tritium density profiles can lead to reduction in the tritium inventory accumulating in PFCs. Modelling with the DIFFUSE code [215] showed that the tritium inventory retained in the torus could be decreased by about a factor of two by isotopic tailoring of the fuel sources, reducing the time needed for tritium removal (Section 2.3.3.2).

#### 2.3.3.4. *DT neutron effects and tritium self-sufficiency*

Although usually not considered in the context of PMI phenomena, the production of energetic

(14 MeV) DT neutrons generated in a reactor scale plasma raises important issues concerning the design and operation of PFCs [216]. The neutrons activate PFCs, and shielding is necessary to limit neutron damage and exposure to personnel and public. A dedicated volume neutron source is envisioned in the future to study DT neutron effects on materials and qualify materials for a commercial fusion reactor [217, 218]; these issues will not be further discussed here. On the positive side, neutrons enable the breeding of tritium fuel, a prerequisite for DT fusion power. However, the margin of tritium breeding is low, and tritium self-sufficiency issues have a direct bearing on the choice of plasma facing materials in future DT reactors and pose stringent limits on the maximum permissible retention of tritium.

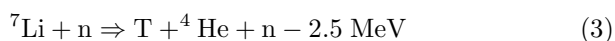
In a tritium self-sufficient reactor, neutrons are used to breed the tritium to replace that consumed in the DT reaction. The tritium burnup rate in a reactor of fusion power  $P_F$  (MW), fuelled with a 50–50 DT mixture, is given by

$$\dot{\Lambda}_T(\text{g/s}) = 1.77 \times 10^{-6} \times P_F \text{ (MW)} \quad (1)$$

A 1000 MW device will burn  $\approx 6.5$  g of tritium per hour of continuous operation. For a typical duty cycle of 0.3, the tritium consumption will be  $\approx 46 \text{ g}\cdot\text{d}^{-1}$ . The tritium consumption and fuelling requirement for the 1500 MW 1998 ITER design have been quantified in Ref. [119]. During the Basic Performance Phase, that was expected to last about ten years, approximately 27 kg would have been burned (averaging about  $5 \text{ kg}\cdot\text{a}^{-1}$  in the last five years of operation when operation was anticipated to become more oriented towards technology testing). These tritium requirements were derived from an operational plan, which specified a total number of  $\approx 9000$  DT pulses with a typical pulse length of  $\approx 1000$  s, corresponding to a neutron fluence of about  $0.3 \text{ MW}\cdot\text{a}\cdot\text{m}^{-2}$ . A subsequent ten year Engineering Performance Phase was planned with the primary objective of raising the neutron fluence to about  $1.0 \text{ MW}\cdot\text{a}\cdot\text{m}^{-2}$ . In this phase, tritium would have been partially produced in the reactor by using a breeding blanket with a breeding ratio of 0.8. The remaining  $1.7 \text{ kg}\cdot\text{a}^{-1}$  would have come from external sources. The reduced size ITER design currently under consideration would have a lower total tritium consumption (e.g.  $\approx 22$  kg of tritium for a fusion power of about 500 MW, and a neutron wall loading of  $\approx 0.5 \text{ MW/m}^2$ , with a total fluence of  $\approx 0.3 \text{ MW}\cdot\text{a}\cdot\text{m}^{-2}$ ). However, it will probably not have a breeding blanket so that all its tritium will have to be provided from external sources.

Present supplies of tritium are generated by neutron irradiation of deuterium in heavy water reactors, but the availability of the tritium supply, and hence the time window for fusion energy development, is not unlimited [219]. Tritium production from the Canadian CANDU reactors is expected to decrease to near zero in the early 2030s. Delays in the advance towards a DT next step device such as ITER would risk a significant penalty in the additional cost of developing alternate supplies of tritium once the CANDU supply is exhausted or lost by radioactive decay.

The supply of tritium will determine the future introduction of fusion power reactors. In power reactors, the tritium fuel will be bred via nuclear reactions in blankets containing lithium breeder materials surrounding the burning plasma:



One can see the possibility of energy gain in reaction (2) and net tritium breeding through secondary neutrons produced in reaction (3). Neutron multiplication is also possible through nuclear reactions in beryllium. The margin for tritium breeding is relatively low. Lithium provides the highest local tritium breeding ratio of 1.86 and a neutron energy multiplier of 1.27 [220]. Tritium production, via breeding reactions (2) and (3), in liquid and ceramic lithium based breeder materials, and tritium extraction have been demonstrated through capsule irradiation in fission reactors [221–223]. In practice, only a fraction of the neutrons produced can be used to breed tritium. The net tritium breeding ratio (TBR) (see glossary), which is the product of local breeding ratio and blanket coverage, is estimated by 3D neutronics codes [224, 225] and needs to be at least 1.07 [226]. An implicit benefit of efficient isotopic tailoring (Section 2.3.3.3) is the reduction of the required tritium breeding ratio due to the increase in the tritium burn fraction. As is shown in Ref. [225], a factor of two increase in the tritium burn-fraction can have a significant effect on the tritium breeding ratio required for tritium self-sufficiency, reducing it from values of  $\approx 1.15$  to about 1.05. This will benefit an engineering test facility such as ITER by reducing costly tritium startup inventories and also has significant implications for an electricity grid based on fusion power reactors.

To convert a significant fraction of electricity generation to fusion power, it is anticipated that the

number of fusion reactors would have to be doubled every 1–5 years. Each new reactor would need a startup tritium inventory [227]; furthermore, the tritium inventory decays radiologically at a rate of 5% per year, requiring replacement. For these reasons, there is a premium on minimizing the tritium inventory in a DT reactor. The development work in this area [228] has made significant progress in this direction by reducing the required site inventory for ITER to about 4 kg. The maximum tolerable tritium loss rate (including both the tokamak and the tritium plant) depends on both the fuel burnup fraction and the fuelling efficiency. Continuous retention or loss as low as 1% of the fuelling rate would imperil tritium self-sufficiency because of the relatively low tritium breeding ratio [229]. Carbon PFCs, which might be required in the ITER divertor design to survive disruption erosion, will not be usable in commercial fusion power reactors because of erosion lifetime and tritium co-deposition considerations (Sections 3.5.3, 4.3, 4.7, and 5.3). Metal (e.g. tungsten) PFCs are not expected to continuously retain tritium once an initial inventory has been built-up in the implantation layer, and so are likely to be preferred. Elimination or mitigation of disruptions to permit the use of metal divertor and first wall components is a necessary condition for practical fusion reactors.

#### 2.3.4. Control of the in-vessel dust inventory

Dust is produced inside the vacuum vessel of a tokamak by interaction of the plasma with the components of the first wall and the divertor. In the past, this has received little attention within the fusion community, mainly because dust is neither a safety nor an operational problem in existing tokamaks. However, the ITER design has highlighted the fundamental need to deepen the understanding of the production of dust in tokamaks since this may directly affect the safe operation of a next step device. The safety issues associated with tokamak dust [230–233] include radiological hazard (tritium and activation products) (see glossary), toxicity and chemical reactivity with steam and air.

A variety of ‘undesired’ products result from PMIs (e.g. films, flakes, debris, dust), and it is not clear how many of these should be considered a ‘dust’ hazard. Small amounts of dust have been collected in various tokamaks during scheduled vacuum vessel vents [234, 235] and have been analysed (Section 4.8). Flaking and breakup of films, resulting from redeposition of eroded and vaporized material, is expected

to be the primary source of dust in a device such as ITER. Arcing, which tends to release micron size particulates, may also play an important role, but investigations are needed to better quantify the effects (Sections 3.3 and 4.4). If redeposited carbon layers are susceptible to arcing, released particulates will be saturated with deuterium–tritium, presenting safety and operational issues (Section 4.8).

The radiological hazard and/or toxicity of the dust depends on the specific dust material, on how much is produced and how well the dust is confined. Confinement depends on the dust particle size (e.g. particles larger than  $\approx 100 \mu\text{m}$  will not be transported to the environment). The activation products of tungsten are radiologically hazardous while the radiological hazard of beryllium and graphite is not due to activation products, but rather to the tritium present in the dust.

In vacuum vessel breach situations, dust can also react chemically with steam and air, and materials such as beryllium, tungsten or carbon oxidize, producing hydrogen. In particular, accident scenarios that result in water or steam exposure of hot plasma facing materials (e.g. during loss of coolant accidents) are of concern for fusion reactor designs such as ITER that include beryllium as the first wall material. Steam interactions with hot beryllium can produce significant quantities of hydrogen [236], which in the presence of air can lead to explosion. The amount of hydrogen produced depends on the specific material, temperature, exposure time, and, in particular on the effective surface area. The large surface area associated with dust can greatly amplify its chemical reactivity [237]. The location where the dust settles will determine its temperature and, consequently, its chemical reactivity.

For these reasons, it is envisaged that the dust inventory should be limited in a device such as ITER: (a) to ensure that chemical reactivity is adequately controlled in order to avoid the hazard of hydrogen or dust explosions [238, 239], and (b) to be compatible with the given radioactivity confinement requirements based on environmental release limits [240].

Dust limits in the ITER design for carbon and beryllium stem primarily from chemical reactivity concerns. The tungsten dust limit is determined by both chemical reactivity and activation hazards. Two different dust limits are currently considered. First, a restrictive limit, on potential chemical reactions for beryllium dust residing mainly in the grooves of the tungsten armour of the divertor PFCs (e.g. dome and baffle); (Section 2.5). These grooves or castellations

in the tungsten armour are an essential feature of the design of PFCs to relieve stresses during cyclic high heat flux loading, thus maximizing the fatigue life-time of the armour to heat sink joint. This dust can be subject to overheating and steam exposure during long term decay heat driven and short term non-decay heat driven incidents. The administrative limit for the inventory of particles (typically,  $\ll 10 \mu\text{m}$  that are highly reactive because of their relatively large surface area) in the grooves is of the order of 10 kg. The second limit is the overall amount of dust that can be mobilized during an accident and, hence, escape into the environment causing a radiological hazard. This is set at a few hundred kg. Within a machine the scale of ITER, these limits represent values that will be difficult to diagnose or guarantee.

The present design of the ITER PFCs is being optimized to minimize dust accumulation by decreasing the number and dimensions of the grooves on the plasma facing surfaces in the critical areas. The rest of the dust and flakes is expected to collect in and beneath the divertor, where sufficient space is available for introducing dust handling systems that can either remove dust on-line or during intervals between pulses.

Simply measuring the in-vessel dust inventory was demonstrated to be a challenge in existing machines, and there are still large uncertainties associated with dust production mechanisms and rates and extrapolation from present machines to the next generation of tokamaks. Research into dust production mechanisms and rates and the appropriate dosimetric limits for personnel exposure has just begun [241–243] (Section 4.8).

## 2.4. Selection criteria for plasma facing materials

Operation experience in existing fusion devices has centred around the use of carbon, mainly because of its high thermal shock resistance and tolerance to off-normal events (ELMs, disruptions) without melting, thereby avoiding surface irregularities (Section 1.3.2). A notable exception is the use of Be in JET, both at the wall [101] and at the divertor (Mk-I) [244]. Experiments in ASDEX-Upgrade [245] with tungsten in the divertor and, more recently, at the inner wall [117], and the use of molybdenum in Alcator C-Mod [156, 246, 247], have also shown that high Z materials might be acceptable in fusion devices with divertors that can produce low plasma edge temperatures ( $\approx 10 \text{ eV}$  or less).

**Table 6.** Identified advantages and shortcomings of candidate armour materials that are considered for the design of the ITER reactor.

Advantages	Shortcomings	Required R&D
<b>Carbon-fibre composites (CFCs)</b>		
<ul style="list-style-type: none"> <li>• Good power handling, good thermal shock and thermal fatigue resistance (low crack propagation)</li> <li>• Does not melt (but sublimates) and preserves its shape even under extreme temperature excursions;</li> <li>• Low radiative power losses with influx to plasma due to low <math>Z</math>;</li> <li>• Well established joining technology;</li> <li>• Broad tokamak operational experience;</li> <li>• In existing tokamaks, C erosion plays a beneficial role because of the reduction of the target power by radiation cooling of the divertor plasma. C radiates efficiently for temperatures down to <math>\sim 5</math> eV.</li> </ul>	<ul style="list-style-type: none"> <li>• Requires conditioning;</li> <li>• Chemical erosion leads to reduction erosion lifetime;</li> <li>• Chemical erosion leads to co-deposition of tritium with eroded carbon;</li> <li>• Possible high erosion under disruption loads due to brittle destruction;</li> <li>• Generates dust;</li> <li>• Physical and mechanical properties deteriorate substantially under neutron irradiation</li> </ul>	<ul style="list-style-type: none"> <li>• in situ removal of tritium from co-deposited films on plasma facing surfaces with minimal impact on machine availability;</li> <li>• C mixed materials effects;</li> <li>• Chemical erosion yield of carbon at relevant plasma edge conditions;</li> <li>• Investigation of ‘brittle destruction’ under relevant disruption loads.</li> </ul>
<b>Beryllium</b>		
<ul style="list-style-type: none"> <li>• Good oxygen gettering ability;</li> <li>• Some tokamak practice (mainly JET);</li> <li>• Because of low <math>Z</math>, low risk of plasma contamination due to impurities and low radiative power losses;</li> <li>• Repairability by plasma spraying;</li> <li>• Well established joining technology;</li> <li>• Low tritium inventory.</li> </ul>	<ul style="list-style-type: none"> <li>• Reduced power handling capacity and resistance to disruptions because of the low melting temperature and high vapour pressure;</li> <li>• High physical sputtering yield;</li> <li>• Toxic — requires controlled handling procedures;</li> <li>• Co-deposition of tritium with beryllium could be significant if the level of oxygen as impurity is large or in the presence of carbon mixing effects;</li> <li>• Properties of thick BeO layers from gettering) are not known.</li> <li>• Neutron induced brittleness</li> </ul>	<ul style="list-style-type: none"> <li>• Removal of tritium from thick oxidized layers;</li> <li>• C–Be mixed materials effects;</li> <li>• Demonstration of in situ repairability;</li> <li>• Saturation of gettering capability due to the buildup of thick oxide layers;</li> <li>• Continue dedicated experiments with Be clad PFCs in tokamaks (e.g. Be first wall experiment in JET).</li> </ul>
<b>Tungsten</b>		
<ul style="list-style-type: none"> <li>• Low physical sputtering yield and high sputtering threshold energy;</li> <li>• No chemical sputtering in H plasma;</li> <li>• Tritium inventory is expected to be small. W does not co-deposit with H isotopes;</li> <li>• Repairability by plasma spraying;</li> <li>• Well established joining technology.</li> </ul>	<ul style="list-style-type: none"> <li>• Low limit for plasma contamination due to high radiative losses;</li> <li>• Chemical erosion due to oxygen impurity;</li> <li>• Limited but promising recent tokamak experience (see Section 4);</li> <li>• Melts under anticipated thermal quench disruption loads Type I ELMs at divertor plate;</li> <li>• Unknown behaviour of melt layer under disruption loads;</li> <li>• Recrystallizes (embrittles) at temperatures <math>&gt;1500</math> K;</li> <li>• Low plasma edge temperatures required for low sputtering;</li> <li>• High activation and generation of radioactive waste.</li> </ul>	<ul style="list-style-type: none"> <li>• Properties and behaviour of melt layers under ITER disruption and ELM thermal loads;</li> <li>• Continue development/testing of W target featuring high heat flux capability</li> <li>• C–W mixed materials effects;</li> <li>• Expand coverage of W clad PFCs and gain operation experience in tokamaks;</li> <li>• Study chemical erosion due to O in combination with H.</li> </ul>

The selection of the armour materials for the PFCs of a next step experimental fusion reactor is a compromise between multiple requirements derived from the unique features of a burning fusion plasma environment. The factors that affect the selection

come primarily from the requirements of plasma performance (e.g. need to minimize impurity contamination and the resulting radiation losses in the confined plasma), engineering integrity, component lifetime (e.g. need to withstand thermal stresses, acceptable

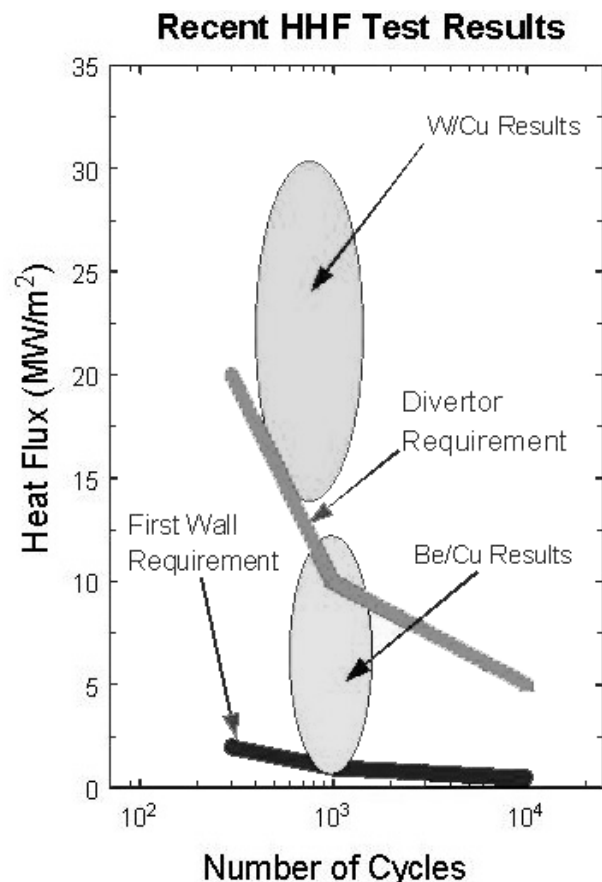


**Figure 7.** High heat flux test results: heat flux versus number of cycles for prototypical W/Cu and Be/Cu high heat flux components. (Figure provided by M. Ulrickson, Sandia National Laboratory [256].)

erosion), and safety (e.g. need to minimize tritium and radioactive dust inventories). In this respect, erosion/redeposition and tritium retention are major factors in the choice of plasma facing materials for a next step reactor.

In the ITER design, beryllium is the primary candidate material for the first wall, whereas tungsten is the preferred material for the divertor, except for the area near the strike points. Each of these three candidate materials has some inherent advantages and disadvantages (see Table 6), and their application depends on the specific operational requirements. The rationale for this selection is thoroughly discussed elsewhere [17–19]. The choice of carbon for the parts of the divertor where the SOL strikes the vertical target and energy deposition from disruptions and ELMs will occur is mainly due to its good power handling and thermal shock resistance; it does not melt (but is subject to sublimation) and preserves its shape even under extreme temperature excursions.

In this region, beryllium would have an inadequate lifetime and tungsten would vaporize during high power transients and could pollute the plasma. Furthermore, with a full tungsten target, there are concerns regarding the formation and the properties of a thick melt layer (up to few hundred  $\mu\text{m}$  thick) during a thermal quench and Type I ELMs (Sections 2.3.1.3 and 5.4), and the generation of surface irregularities that might later form hot spots in normal steady heat flux operation. Because of its low physical sputtering yield and high threshold energy for physical sputtering, W is foreseen in regions where the significant flux of hydrogen neutrals, predominantly of low energy, can lead to large sputtering and unacceptably short lifetimes for materials such as carbon and beryllium. However, with the above material selection the co-deposition of tritium with carbon remains a primary concern. The Fusion Ignition Research Experiment (FIRE) design study [248] (see glossary) has forgone the use carbon PFCs for this reason, the first wall is covered with Be tiles and divertor uses W rods on a Cu backing plate.

An extensive research and development (R&D) programme has been conducted on cooling technology [249] and on the development of joining technologies between armour (beryllium, tungsten and CFCs) and copper alloys/stainless steel [250–252]. Robust engineering solutions of actively cooled high heat flux components clad with CFCs have been developed and tested successfully for up to several thousand cycles at heat fluxes of the order of  $20 \text{ MW}\cdot\text{m}^{-2}$  [253, 254]. Recently, substantial progress has also been made on the development and testing of water cooled high heat flux components clad with beryllium and tungsten [250]. Figure 7 [256] shows the ranges of operational requirements for first wall and divertor components, and the results of high heat flux tests with water cooled Be/Cu and W/Cu components. W armoured prototypes already promise to be as reliable, at similar heat fluxes, as their carbon armoured counterparts [253–255]. This requires, particularly for materials such as tungsten, the use of ‘discrete’ structures (e.g. castellated, brush type) of the type portrayed in Fig. 8. However, there are some remaining concerns of possible PMI effects resulting from the use of such geometrical configurations. These include the interaction of the sharp edges with the plasma, resulting in possible enhanced erosion, arc initiation from the corners, and plasma contamination. Other effects include: the formation of ‘bridges’ across the gaps in case of melting; change of thermomechanical behaviour; the accumulation of



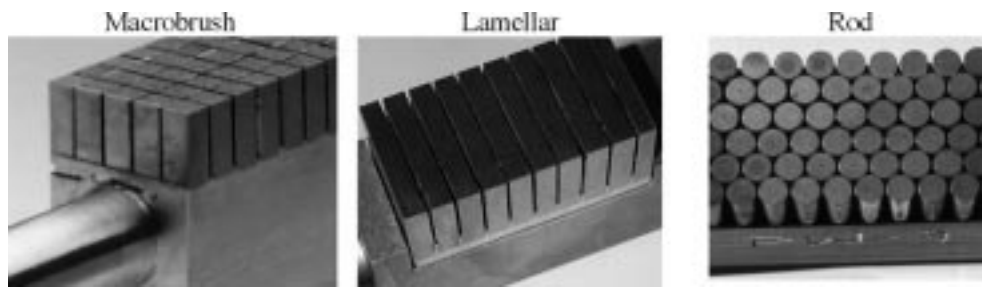


**Figure 8.** Castellated armour concepts for tungsten armoured high heat flux components. (Figure provided by Vladimir Barabash, ITER JCT.)

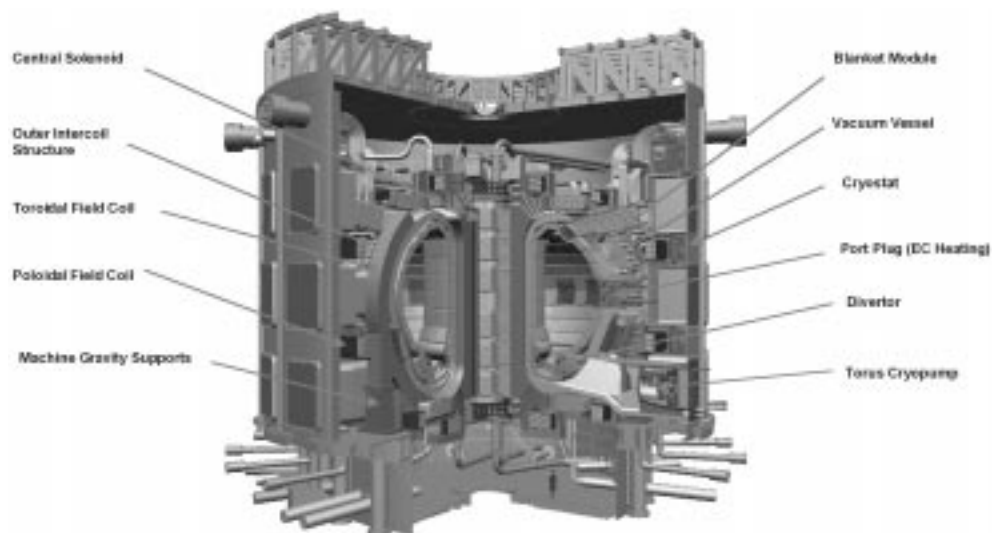


**Figure 9.** A cutaway of the ITER-Feat tokamak.

large amounts of erosion products (dust, tritium co-deposits) in cold regions where they may be difficult to remove; and possible copper substrate erosion due to the presence of gaps.

The primary shortcomings of W that should be addressed in the coming years are the lack of operational experience and the dearth of experimental data regarding formation of melt layers (and their properties) during disruptions (Section 6).

The present strategy in ITER is to initially install carbon as armour on the targets and to maintain the option to switch to more reactor relevant all-tungsten armoured targets before DT operation, when the tritium inventory becomes an issue. The decision to make this change will depend on the progress made in controlling the plasma, in particular, on the frequency and severity of disruptions and, on the other hand, on the success achieved in miti-

gating the effects of tritium co-deposition. Removal and exchange of divertor cassettes will require remote handling capabilities, as will be discussed in Section 2.5.

## 2.5. Overview of design features of plasma facing components for next step tokamaks

A cutaway view of the ITER-Feat tokamak [134, 258, 119] is illustrated in Fig. 9 and is used here, together with the 1998 ITER design [119, 257], as examples to point out some of the characteristic features of the design of a reactor scale experimental facility. The design operation parameters and heat, particle, and neutron fluxes on the PFCs are summarized in Table 7. The in-vessel components are

**Table 7.** Estimated operation parameters used for the design of the ITER PFCs [119, 134]. Parameters of the 1998 ITER design [118] are also included in parentheses. Design specifications for off-normal events are summarized in Table 4.

Component/armour material/ area/main design loads	Peak heat flux <sup>a</sup> (MW · m <sup>-2</sup> )	Particle flux <sup>a</sup> (DT · m <sup>-2</sup> · s <sup>-1</sup> )	Energy (eV)	Fast neutron flux <sup>b</sup> (n · m <sup>-2</sup> · s <sup>-1</sup> )
First wall/Be ~680 {~1000} (m <sup>2</sup> ) – charge exchange neutrals ( $E_{av} < 100$ eV); – radiative power from bremsstrahlung; – localized thermal, particle and electromagnetic loads during disruptions, VDE, runaway electrons <sup>††</sup> .	0.5	10 <sup>19</sup> –10 <sup>20</sup>	100–500	$\leq 1.3 \times 10^{18}$ { $\leq 2.3 \times 10^{18}$ }
Startup limiter/Be ~10 (m <sup>2</sup> ) – direct plasma interaction and high thermal power during plasma startup and shutdown.	~8 <sup>c</sup>	10 <sup>21</sup> –10 <sup>22</sup>	—	$\leq 2.3 \times 10^{18}$ { $\leq 2.3 \times 10^{18}$ }
Divertor target (strike-points)/C ~55 {~75} (m <sup>2</sup> ) – high thermal power and flux of particles; – deposition of energy during disruption, ELMs; – electromagnetic loads during disruptions.	<10 <sup>d</sup> –20 <sup>e</sup>	<10 <sup>24</sup>	1–30 (plasma temp.)	(2–3) × 10 <sup>17</sup> {(4–6) × 10 <sup>17</sup> }
Divertor side wall (baffle)/W ~50 {~200} (m <sup>2</sup> ) – charge exchange neutrals ( $E_{av} < 100$ eV); – direct interaction with SOL plasma; – radiative power from X point (e.g. MARFes); – possible deposition of energy during ELMs; – reradiated energy during disruptions; – electromagnetic loads during disruptions.	3	10 <sup>20</sup> –10 <sup>22</sup>	>30 (plasma temp.)	$\leq 1 \times 10^{18}$ { $2 \times 10^{18}$ }
Divertor dome/W ~30 {~85} (m <sup>2</sup> ) – charge exchange neutrals ( $E_{av} < 100$ eV); – radiative power from X point (e.g. MARFes); – deposition of energy during VDE; – electromagnetic loads during disruptions.	3	10 <sup>21</sup> –10 <sup>22</sup>	>30 (plasma temp.)	$\leq 9 \times 10^{17}$ { $1.1 \times 10^{18}$ }
Divertor private region (liner)/W ~60 {~90} (m <sup>2</sup> ) – radiative power dissipated in the divertor; – reradiated energy during disruptions; – electromagnetic loads during disruptions.	<1	<10 <sup>23</sup>	<1	$\sim 2 \times 10^{17}$ { $4 \times 10^{17}$ }

The pulse duration in the ITER-FEAT design is 400 s, while for the 1998 ITER design was 1000 s. For the first wall no replacement is anticipated during operation (~40 000 pulses) and up to three replacements for the divertor.

<sup>a</sup> Design values.

<sup>b</sup>  $E > 0.1$  MeV.

<sup>c</sup> During startup. During flat-top burn the limiter will experience the same load as the primary first wall;

<sup>d</sup> Peak load expected during normal semidetached conditions.

<sup>e</sup> Peak load expected during slow high power transients (10% frequency, ~10 s duration).

<sup>††</sup> Protection of the first wall against VDEs and runaway electrons could also be achieved by introducing a series of poloidal protection limiters.

cooled by pressurized water at  $\approx 370$  K. The maximum water baking temperature of the PFCs is limited to  $\approx 510$  K because of the 4 MPa maximum pressure that can be allowed in the water cooling pipes.

There may be a possibility of baking the divertor to higher temperatures with hot gas (e.g. He), but the time required to completely remove water, introduce gas, and then reintroduce water will limit such

enhanced temperature baking to major commissioning and decommissioning periods.

*Vacuum vessel and blanket:* The ITER vacuum boundary is formed by a double walled vacuum vessel made of stainless steel SS 316L(N)-IG, ITER Grade: 0.06 to 0.08% nitrogen (60 mm plates for the outer and inner shells, and 40 mm stiffening ribs), which is supported against gravity by the toroidal field coil structure, and which contains the blanket and divertor systems [259, 260]. The basic functions of the vacuum vessel are to provide a suitable vacuum in the plasma chamber, to support the in-vessel components, to assist in the nuclear shielding of the coils and to constitute the first safety boundary. To this end, the vessel cooling system has to provide radioactive decay heat removal by natural convection, even when the vacuum vessel and the blanket cooling loops are not functioning (no pumping action). The shielding, in particular from neutron radiation, has to be sufficient to stay below critical nuclear heating levels in the coils and to allow limited hands on maintenance inside the cryostat.

The shielding blanket is composed of modules, which are attached to a thick backplate in the case of the 1998 ITER design, and in the ITER-FEAT design are instead directly supported by the vacuum vessel. The shielding modules are water cooled steel blocks, which are effective in moderating the 14 MeV neutrons, with a water-cooled copper mat bonded to the surface of the modules on the plasma side, and protected from interaction with the plasma by an armour material. To limit the thermal stresses in the vacuum vessel and to provide sufficient shielding to limit the He production in the vacuum vessel inner shell (due to the interaction of energetic neutrons with various isotopes present in steel either as element e.g. nickel, or as impurities, e.g., boron) below 1 atomic part per million (appm), the blanket modules have a minimum thickness of 450 mm and consist, on average, of  $\approx 80\%$  steel and 20% water (cooling channels). During later phases of operation, some of the blanket shielding modules may be replaced by tritium breeding modules with a design similar to the one described in Ref. [119].

*First wall:* The first wall design is generally less demanding than the design of the divertor high heat flux components (see below) because of lower steady state heat loads, originating mostly from radiation. However, a longer lifetime is required ( $\approx 40000$  discharges) than for the divertor components. This results in a significantly larger total neutron fluence for the first wall than for the divertor, favouring the

choice of stainless steel for the first wall structure and the associated cooling tubes. The first wall design is based on 1 mm thick 10 mm diameter SS cooling tubes with a pitch of  $\approx 20$  mm, embedded in a Cu alloy layer of  $\approx 15$  mm thickness (DS-Cu or CuCrZr). The plasma facing material is a 10 mm thick Be layer [259, 260]. The first wall incorporates the startup limiters [261], which need to absorb several MW of power (up to  $\approx 8 \text{ MW}\cdot\text{m}^{-2}$ ) during the limiter phases of each discharge (i.e.  $\approx 100$  s during plasma startup and  $\approx 100$  s during plasma current rampdown). The limiters are located in two ports at the equatorial plane of the machine. The main loading conditions for these components are summarized in Table 7.

With the aim to reduce cost and nuclear waste, design options are currently being investigated for a modular and separable first wall. This new design approach would allow damaged or eroded blanket modules to be repaired inside the hot cell either by replacement of first wall panels or plasma spraying.

*Divertor:* During the past few years, progress towards the understanding of divertor physics, through experiments, modelling (Section 5.2) and model validation in existing divertor machines, has been significant. On the basis of the available knowledge, the currently proposed divertor for ITER [13] utilises a ‘vertical target’ geometry. A key potential advantage of the vertical target configuration is enhanced recycling. The neutrals recycling in the outer part of the SOL are reflected toward the separatrix near the strike point rather than away from the separatrix (Fig. 1), thus increasing the level of recycling. Detached or partially detached plasma regimes can accomplish the required peak heat flux reduction by spreading the power over a larger surface area of the divertor chamber walls and the first wall by enhanced radiation from the plasma edge. The access to such regimes depends on the divertor configuration, the level of heating power, the impurity level, the edge confinement mode and the edge density (Section 2.3.1 and glossary). Although the techniques employed for power handling in the present ITER design are based on validated scaling laws and models, the design allows for some flexibility to accommodate unforeseen effects. For this reason, the ITER divertor is being designed to be very versatile, with components mounted onto removable and reusable cassettes (to minimize activated waste) so that they can be easily replaced.

The divertor is installed in the vacuum vessel in segments or cassettes (e.g. 54 in ITER-FEAT), where they are supported on a pair of concentric toroidal

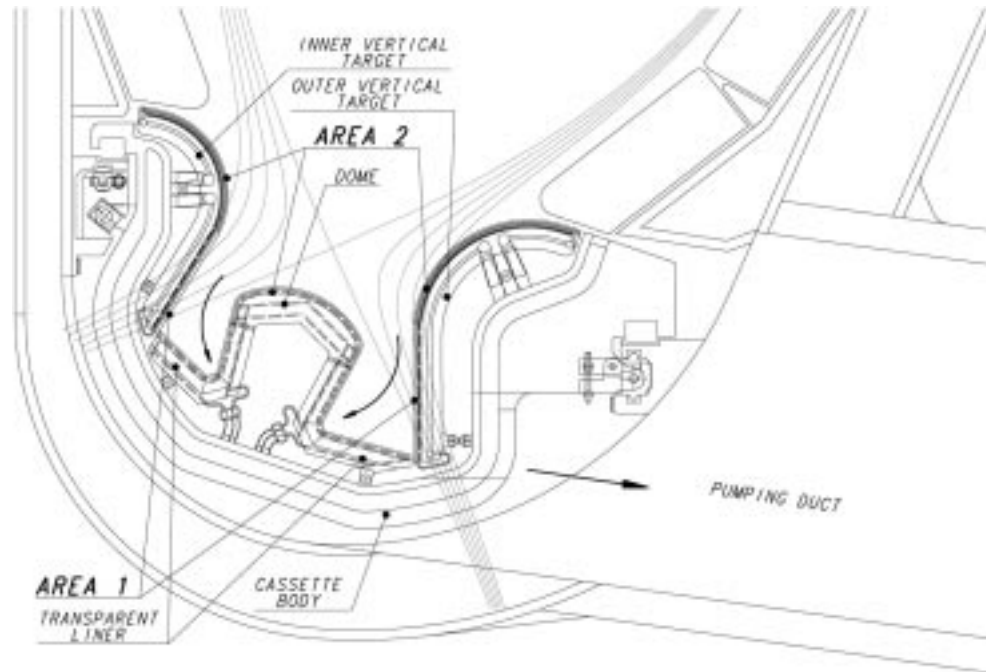


**Figure 10.** Poloidal cross-section through the divertor of the ITER-FEAT design. Area (1) at the divertor strike zones receives high thermal power and flux of particles, deposition of energy during ELMs, high thermal (direct plasma impact) and electromagnetic loads during disruptions. Area (2), which consists of the baffle, the dome and the liner in the private flux region, receives low heat flux and high charge exchange neutral fluxes. Some parts are subject to direct interaction with the SOL plasma, radiative power from X point and possible deposition of reradiated energy during disruptions and mechanical loads due to eddy and halo currents (see glossary).

rails that form part of the vacuum vessel (Fig. 10). The main PFCs of the divertor system are the inner and outer vertical targets, which are the high heat flux components, in their lower part (Area 1 in Fig. 10), interact directly with the SOL plasma and in their upper part (Area 2 in Fig. 10), act as baffles for the neutrals. The private flux region PFC (Area 2 in Fig. 10), consists of a dome, located below the separatrix X point, that baffles neutrals and is exposed mainly to radiation and charge exchange neutrals, and a semi-transparent liner that protects the cassette body from direct line-of-sight of the plasma, while allowing He and other impurities to be pumped away. The design operation parameters and material selected are summarized in Table 7.

The divertor design is being further developed and optimized, on the basis of information provided by modelling and dedicated operation experience in existing tokamaks and laboratory simulations (focused on understanding the chemistry of hydrocarbon deposition [262, 263]), with the scope of elim-

inating or, at least, mitigating the problem of co-deposition. Several design options are currently being investigated to minimize the formation of films in specific areas (e.g. by ensuring that regions of probable deposition are kept ‘hot’ during operation, leading to reduced tritium retention [264]), or by enhancing deposition in specially designed ‘cold traps’ for the hydrocarbons ( $\approx 70$  K) [265], which could be periodically heated to recover the tritium in the form of stable gas molecules. Detailed evaluations of these designs are on-going, however, the complexity of including such a system is to be avoided if at all possible.

The solution shown in Fig. 10, for example, achieves high operating temperatures on the surface of divertor in the private flux region (see glossary), by using the radiated power from the divertor channel to heat radiatively cooled tungsten tiles [264]. The tiles are shaped in such a way as to prevent or minimize line-of-sight from the plasma to the cassette body and to create a labyrinth through which

the helium ash, hydrogen isotopes and other impurities are pumped from the divertor channels, while providing a sufficient length for the hydrocarbons entrained in the gas stream to undergo many collisions with the hot surface of the liner. This could minimize the co-deposition of tritium with carbon by dehydrogenating the carbon and/or recombining most of the active radicals to convert them into stable volatile molecules, which are pumped away without residual deposits. There is also particular concern for the remaining fraction of radicals with relatively low sticking coefficient that could form thin, soft, hydrogenated films on the relatively cold ( $<420$  K) large structures behind the liner [263]. In this case, an ancillary ‘cold’ catcher plate, strategically located, could be used to condense the remaining hydrocarbons. The tritium trapped on this plate could be reclaimed by occasional heating.

### 3. Review of physical processes and underlying theory

#### 3.1. Introduction

Controlling PMIs in current tokamaks and predicting their effects in next step fusion reactors require a detailed understanding of physical mechanisms involved. Many of the underlying physical processes such as sputtering, implantation, diffusion and trapping of hydrogen have been studied for many years and are fairly well understood. However, the development and validation of reliable models to simulate the effects of PMIs in tokamaks are still in progress. This section introduces the main physical processes involved in PMIs and the plasma-material models describing these processes. Section 5 describes how these models are used together with plasma edge models to simulate the effects of PMIs on the plasma, and on PFCs, in present tokamaks and next step fusion reactors. Selected data are presented to illustrate some of the processes and models discussed. Sputtering erosion/redeposition is the subject of the following section. Section 3.3 discusses erosion processes during off-normal plasma events and finally Section 3.4 discusses hydrogen recycling and retention mechanisms in plasma facing materials.

#### 3.2. Sputtering erosion/redeposition processes

Erosion due to energetic particle bombardment depends on the mass ratio of incident particles to

surface atoms, the particle energy and flux density, the surface temperature and other factors. The physical understanding of erosion mechanisms in fusion devices, together with supporting data from laboratory experiments, will be presented below.

##### 3.2.1. Physical sputtering

Physical sputtering is due to elastic energy transfer from incident particles to target atoms. Surface atoms can be ejected if they receive enough energy to overcome the surface binding energy  $E_s$ , be it directly from bombarding ions or through a collision cascade involving other target atoms. The sputtering yield is proportional to the energy deposited in elastic collisions within a near surface layer. At low ion energies, where the transferred energy to surface atoms is comparable with the surface binding energy, the sputtering yield decreases strongly and becomes zero below a threshold energy. For plasma facing materials such as Be, C, and W erosion data exist for H, D and He in the energy range from 10 eV up to 10 keV [266, 267]. The data are extended to higher energies and to T by computer simulation [267, 268].

Physical sputtering is a well understood erosion process, and a sound physical theory exists for it [269, 270]. For light ions incident on heavy materials, the threshold energy,  $E_{th}$ , is determined by the energy which can be transferred to target atoms and analytically approximated by:

$$E_{th} = \frac{(M_1 + M_2)^4}{4M_1M_2(M_1 - M_2)^2} E_s \quad (4)$$

where  $M_1$  and  $M_2$  are the incident particle mass and target mass, respectively, and  $E_s$  is the surface binding energy [268]. For elements considered to be plasma facing materials the surface binding energy varies only within a factor of 2.5, while the atomic masses range from 9 to 184. This makes the threshold energy for light ions strongly dependent on the target mass [271].

The energy dependence of the yield,  $Y$ , at normal incidence can be described by the following expression:

$$Y = QS_n(E) \left(1 - \frac{E_{th}}{E}\right)^2 \left(1 - \left(\frac{E_{th}}{E}\right)^{\frac{2}{3}}\right) \quad (5)$$

where  $S_n(E)$  is the function for the energy dependence of the energy deposited in elastic collisions [272]. Values for the fitting parameters  $Q$  and  $E_{th}$  are tabulated for many ion-target combinations [267].

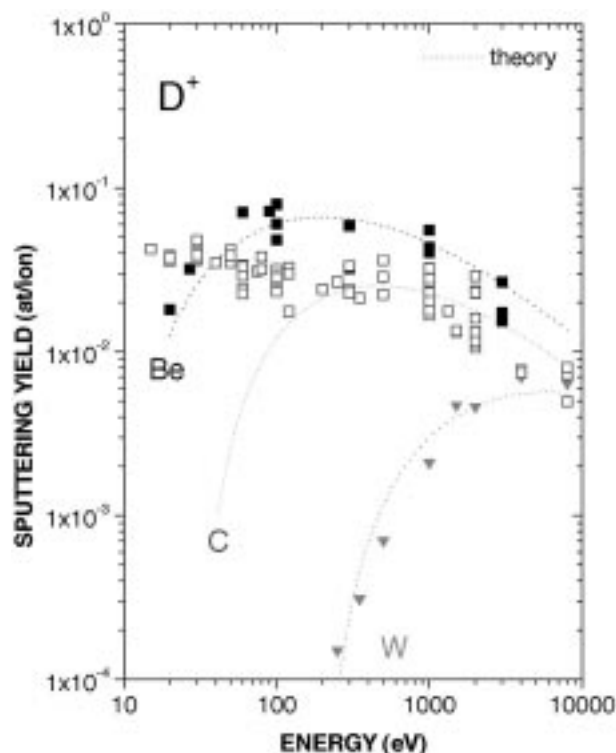


**Figure 11.** Comparison of measured values for the sputtering yield at normal incidence for Be (closed squares), C (open squares), and W (closed triangles) by deuterium ions with results from analytic modelling of physical sputtering [267] (dotted lines). The experimental data were obtained from the weight loss of polished samples after ion bombardment. The divergence between experimental points and modelling for carbon at low energies is due to chemical effects not included in the model.

The strong dependence of the sputtering yield on  $E_{th}$  leads to a pronounced dependence on the atomic target mass for light ions and energies below 1 keV [271]. At grazing incidence the erosion yield is enhanced relative to the yield at normal incidence, as more energy is deposited within the near surface layer. The dependence on the angle of incidence is well described theoretically for light ions [273], and parameter fits exist for light and heavy ions [267]. Surface roughness tends to reduce the pronounced dependence of the sputtering yield on the angle of incidence. This has been demonstrated and interpreted in Monte Carlo simulations for different kinds of graphite materials [274] and beryllium [275]. Physical sputtering does not depend on surface temperature [276]. The energy distribution of sputtered atoms has been evaluated by Thomson [277] and shows a mean value equivalent to  $E_s/2$ . As the value

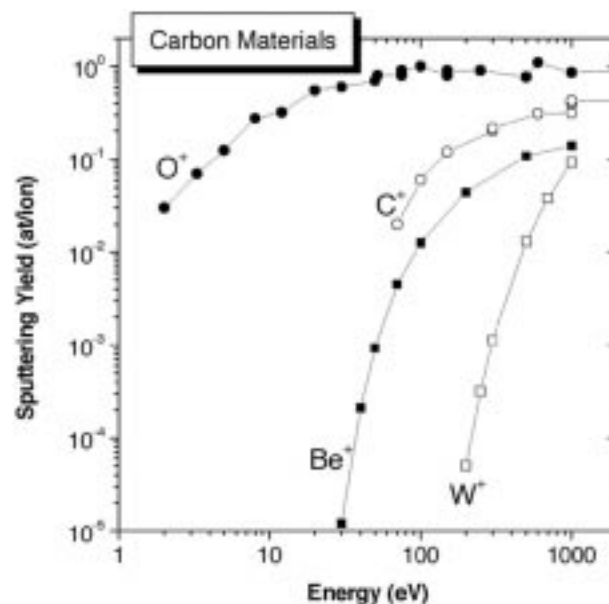


**Figure 12.** Sputtering yields of carbon materials by typical impurity ions: measured values for  $O^+$  [282] and  $C^+$  [283] and TRIM-SP computer simulations for  $Be^+$  and  $W^+$  [281].

for  $E_s$  does not vary much for the considered choice of plasma facing materials, the energy of sputtered atoms does not depend strongly on the material.

For Be and W, experimental data and the fit for the sputtering yield at normal incidence are shown in Fig. 11 for D ions as a function of the incident particle energy. Physical sputtering data are available for both materials from energies close to the threshold energy (9 eV for D on Be and 200 eV for D on W) up to the high keV range [267, 278, 279]. Similar data exist for H and He ion bombardment. All data shown were obtained from the weight loss of polished samples after ion bombardment. In the case of Be, clean surfaces could only be obtained at temperatures above 900 K where Be diffuses through the surface oxide layer [280]; at lower temperatures, oxidation from the residual gas reduced the erosion yield [267]. For carbon based materials, physical sputtering is only dominant for non-reactive ion bombardment, e.g.  $He^+$  or  $C^+$ . For reactive species such as hydrogen and oxygen, the formation of hydrocarbons, CO and  $CO_2$  leads to enhanced erosion yields, even at room temperature (Sections 3.2.3 and 3.2.4). The high threshold energy for sputtering of W reduces the yields drastically at energies below 1000 eV. Ion energies in the divertor are expected to be in the 20 to 100 eV range, and charge exchange neutrals have their maximum below 20 eV. Even for

the low  $Z$  elements carbon and beryllium, the threshold energy is high enough to reduce physical sputtering by deuterium strongly.

However, the situation is different for heavier incident ions such as Be, C, O or W that can transfer almost all their energy onto target atoms. In this case, the threshold energy is determined by the energy loss in inelastic stopping of atoms inside the target [270] and is about 30 eV for carbon, of the order of the surface binding energy  $E_s$ .

Additionally, the incident impurity ions in a fusion device will be multiply charged, e.g., a charge state of 4 can be assumed for Be, C, O, and even higher for W ions. The increased acceleration of these ions in the sheath potential of a divertor plasma with  $T_e = 10$  eV will result in incident energies of around 200 eV, well above the threshold energy.

Measured and calculated data for the sputtering yield of impurity ions such as C, O, Be and W ions, for C based materials are shown in Fig. 12 [281–285]. No experimental data are available for Be and W bombardment. The erosion processes for  $C^+$ ,  $Be^+$  and  $W^+$  are predominantly due to physical sputtering. Chemical effects may contribute through the reaction with oxygen. In the case of carbon, CO formation enhances the erosion yield (Section 3.2.4).

Carbon bombardment, in general, leads to the deposition of protective surface layers (Section 4.3.4). Only in conditions where carbon self-sputtering exceeds unity, i.e. at grazing incidence or at temperatures above  $\approx 1800$  K, could a few yield data points be obtained for clean W surfaces.

### 3.2.2. Non-recycling impurities

At high fluences, metal and carbon impurity ions can form a solid layer on top of the substrate, protecting it from further erosion. While for low coverage the sputtering yield of the deposited atoms is influenced by the substrate material, the conditions for steady state erosion or deposition depend on the self-sputtering yield of the incident ions. At ion energies or angles of incidence where the self-sputtering yield increases above unity, this protecting effect disappears and erosion continues, being only partially reduced by dilution in the implanted layer [284, 285]. For the case of sputtering of W by C ions, Fig. 13 shows the weight change of the sample, as a function of fluence, for different angles of incidence. While after an initial weight loss a continuous weight increase is observed for normal incidence, at angles of incidence larger than  $40^\circ$  continu-

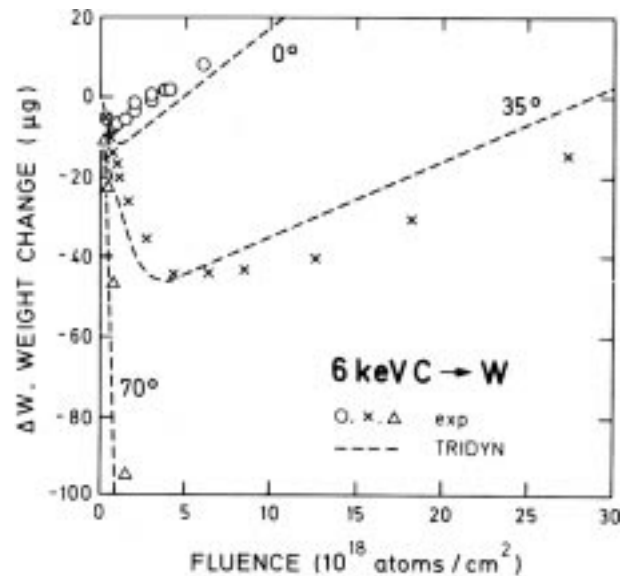


**Figure 13.** Fluence dependence of the weight loss of a W sample bombarded by 6 keV  $C^+$  at different angles of incidence. The dashed lines are the predictions of a Monte Carlo code, TRIDYN. (Reproduced with permission from Ref. [285].)

ous erosion occurs [285]. This angle of  $40^\circ$  is just the angle of incidence where the self-sputtering of carbon increases above unity [283]. The conditions in which net erosion turns into net deposition may further be complicated by changes of surface temperature and hence self-sputtering yield, by RES or by the diffusion and surface segregation of implanted impurities. In a tokamak, particles incident on a divertor plate, for example, have ranges of incident angles and energies, and this complicates predictions of erosion/net deposition (Section 3.2.6).

The erosion properties of layers formed during bombardment with non-recycling ions and effects due to simultaneous bombardment with different ions will be discussed in Sections 3.2.6.2 and 3.2.6.3.

### 3.2.3. Chemical erosion due to hydrogen isotopes

For carbon, chemical reactions with incident hydrogen ions lead to the formation of volatile hydrocarbon molecules or to loosely bound hydrocarbon precursors which can be sputtered with a much lower threshold energy. Chemical erosion is a complicated multistep process that depends on particle energy and flux, surface temperature and material properties such as crystalline structure, and may be influenced by impurity atoms in the lattice. Chemical erosion with hydrogen isotope ions dominates at low ion energies, i.e. below 100 eV, and at elevated

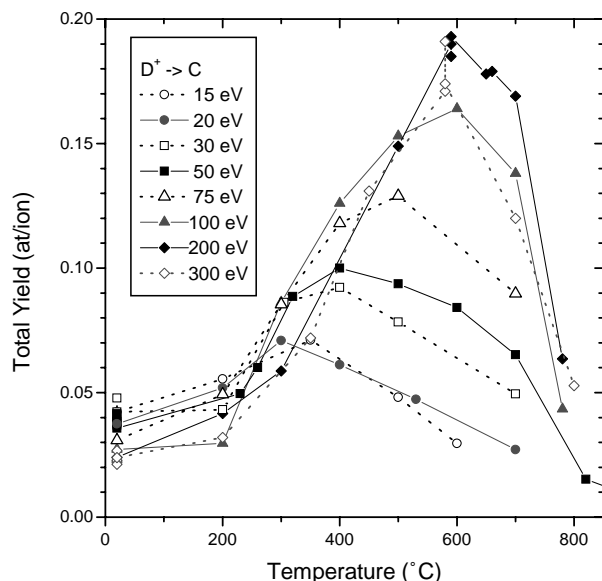


**Figure 14.** Temperature dependence of the erosion yield of pyrolytic graphite by deuterium ions at different ion energies as measured by weight loss [292].

temperatures. It is also found during simultaneous bombardment with inert gas or self-ions and thermal atomic hydrogen atoms. The process has been reviewed recently [282, 286, 287], and only a short discussion will be presented here. Chemical erosion data have been compiled recently in a comprehensive report [288].

Carbon interacts with thermal atomic hydrogen over a broad temperature range, extending down to room temperature forming mainly  $\text{CH}_3$ , and a wide range of higher hydrocarbons [289, 290]. Surface atoms not embedded in a perfect crystal lattice will be hydrogenated up to  $\text{CH}_3$  with one remaining bond to the graphitic lattice. At room temperature the reaction yield with thermal atomic hydrogen is small, but sputtering of this fully hydrogenated surface by low energy hydrogen ions proceeds with a much reduced threshold energy of about 2 eV [287, 291]. Increasing the surface temperature above 400 K results in a thermal release of hydrocarbons, especially  $\text{CH}_4$ , but heavier hydrocarbons are also observed.  $\text{CH}_3$  hydrocarbon precursors neighbouring a free carbon atom may be emitted by simultaneously reforming a graphitic carbon-carbon bond [289]. At temperatures above 600 K, hydrogen molecular recombination occurs before complete hydrogenation of the surface, thus reducing the chemical erosion reaction. The combined processes lead to the pronounced maximum of the thermal chemical erosion with surface temperature.

Figure 14 shows a typical temperature dependence of the total chemical erosion yield, measured via weight loss, of pyrolytic graphite for energies ranging from 15 to 300 eV [292]. Similar plots have been obtained for the various hydrocarbon yields [293]. Upon comparison of the mass loss data [292] and the mass spectroscopic data (sum of hydrocarbons measured in the residual gas) [293], we note two key differences. (i) At energies below  $\approx 100$  eV, the mass loss data are generally higher, possibly because of sticking of emitted hydrocarbon radicals to the analysis chamber wall before they can be measured (RGA signals are reduced [292]). For 15 eV  $\text{D}^+$  impact at 300 K graphite temperature, the difference is about a factor of four (Fig. 15) and is probably due to this effect. (ii) The total chemical erosion yields due to  $\text{H}^+$  and  $\text{D}^+$ , measured by mass spectroscopy, differ by less than a factor of two, while mass loss measurements, show a factor of four to five difference, with  $\text{D}^+$  being higher in both cases [293]. The question remains why more D containing radicals are produced and why the D containing molecules stick more efficiently to the chamber walls.

Chemical erosion by thermal atomic hydrogen, with a maximum yield around 600–800 K, is strongly dependent on the crystalline structure of the surface. The erosion yield ranges from  $10^{-3}$  for pyrolytic graphite to  $10^{-1}$  for amorphous hydrogenated car-

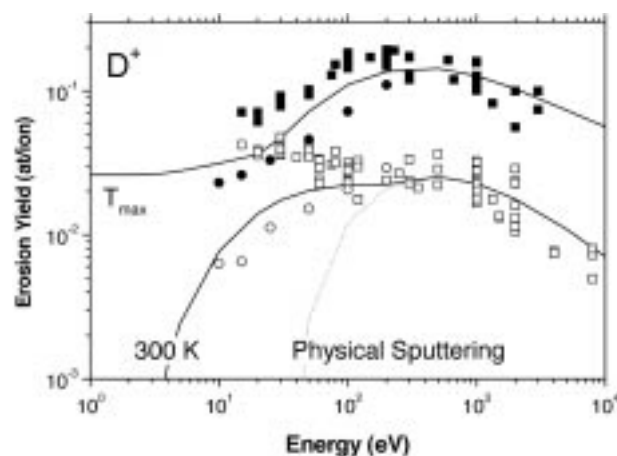


**Figure 15.** Energy dependence of the erosion yield of carbon by deuterium ions at room temperature (open symbols) and at the maximum temperature for chemical erosion,  $T_{\max}$  (solid symbols) (see Fig. 14). Squares are weight loss data collected in [292], circles are total erosion data from mass spectroscopy [293]. Solid curves are from an analytic model [287]. Physical sputtering is also shown (dotted line.)



bon layers, a-C:H [290, 294]. This dependence on the surface structure vanishes for ion energies above 30 eV where radiation damage amorphizes the graphite lattice and enhances the yield [293]. The combined effect of thermal atomic hydrogen and energetic inert ions can lead to chemical erosion yields equivalent to energetic hydrogen bombardment [282, 295].

The chemical erosion yield has been described by analytic equations, with the full parameter dependence taken into account [291, 296]. This work has recently been improved by new data on low ion energy [293] and high flux yields [287]. The models developed for energetic ion impact on carbon [291, 296] are extensions of the thermal atom impact model of Horn et al. [289]. Experimental erosion yields for D ions from weight loss and mass spectroscopy are compared to the calculated energy dependence at room temperature and at the temperature where chemical erosion is a maximum,  $T_{max}$ , in Fig. 15. The room temperature data show a much lower threshold energy than for physical sputtering, possibly owing to an ion induced desorption of loosely bound hydrocarbon precursors [297].

During the past two years, chemical erosion studies have concentrated on the investigation of the dependence of chemical erosion on hydrogen flux, which ranges from about  $10^{20} \text{ m}^{-2} \cdot \text{s}^{-1}$ , for charge exchange neutrals at the wall, to  $10^{24} \text{ m}^{-2} \cdot \text{s}^{-1}$  at the divertor plate. The mechanism involving hydrogenation of carbon atoms, thermal release of hydrocarbon radicals and hydrogen molecule recombination [289] inherently shows a pronounced shift of the temperature of maximum yield,  $T_{max}$ , with ion flux [296], but no strong decrease of the yield at  $T_{max}$ . However, as the flux exceeds  $10^{22} \text{ m}^{-2} \cdot \text{s}^{-1}$  and  $T_{max}$  reaches 900 K, no further increase of  $T_{max}$  occurs, and an apparent decrease in  $Y_{max}$  is observed. Several mechanisms have been proposed for this flux dependence [287, 296]. While the available models provide insight into the mechanisms leading to hydrocarbon formation, a major shortcoming at present is their inability to predict the flux dependence. Attempts have been made, however, to incorporate flux dependence by adding a flux sensitive term as discussed in Ref. [287]. This will be discussed in more detail in Section 4.3. For many years, only scattered yield data were available from tokamaks or plasma simulators [282], where the emission of hydrocarbons was observed spectroscopically from the C–D band intensity, always showing much smaller yields than for low flux ion beam irradiation. However, remaining uncertainties in the determination of the inci-

dent hydrogen flux and energy, as well as the uncertainties in the emitted hydrocarbon flux, made firm conclusions impossible. In particular, the complicated ionization–dissociation chain in the breakup of hydrocarbon molecules to the finally detected CD radicals led to large uncertainties of the excitation to dissociation ratio, D/XB.

Systematic studies of the flux effect of the chemical erosion yield have only recently been undertaken in plasma simulators [298, 299] and in the tokamak edge plasma [300–302]. Also, new attempts have been made to measure and calculate D/XB values as a function of plasma electron temperature [302, 303] and electron density [299]. Still, considerable systematic errors may exist, as the variation of ion flux often correlates with variations in plasma edge temperatures and ion energies [300]. The extent to which parameters other than flux (e.g. energy, redeposition, photon efficiency and viewing geometry in spectroscopic measurements) affect the observed erosion rates needs to be determined. However, these new data (Fig. 16) constitute a new quality in precision, and, in particular, the relative errors within one particular set of data (given, where available, by the error bars in Fig. 16) are small enough to make the interpretation in terms of a flux dependence possible. In Fig. 16, the erosion yield data, as a function of ion flux, are collected for room temperature (Fig. 16(a)) and for a temperature close to the maximum of the temperature dependence curve,  $T_{max}$  (Fig. 16(b)). Included in Fig. 16 are curves giving the predictions of an analytical model based on low flux ion beam data [296], and a refined model taking a possible flux dependence at high fluxes into account [287]. While most of the data show a decreasing trend with flux at high fluxes, this is not the case for the PISCES results [299]. It is also important to note that most of the spectroscopic yield data from tokamaks and laboratory plasma devices are based on the assumption that the methane photon efficiency for the CD band emission also applies to heavy hydrocarbons (i.e.  $\text{C}_x\text{H}_y$  with  $x \geq 2$ ). It is anticipated that in situ photon efficiency calibration for heavy hydrocarbon might affect the derived yields [304]. Therefore, the flux dependence of the chemical erosion yield of graphite at high fluxes is still an open question.

In Fig. 16(a), spectroscopic data from ASDEX-Upgrade [301] are shown for temperatures near room temperature in comparison with ion beam data measured by weight loss and mass spectroscopy [292, 293, 305, 306]. Under low energy and room tem-

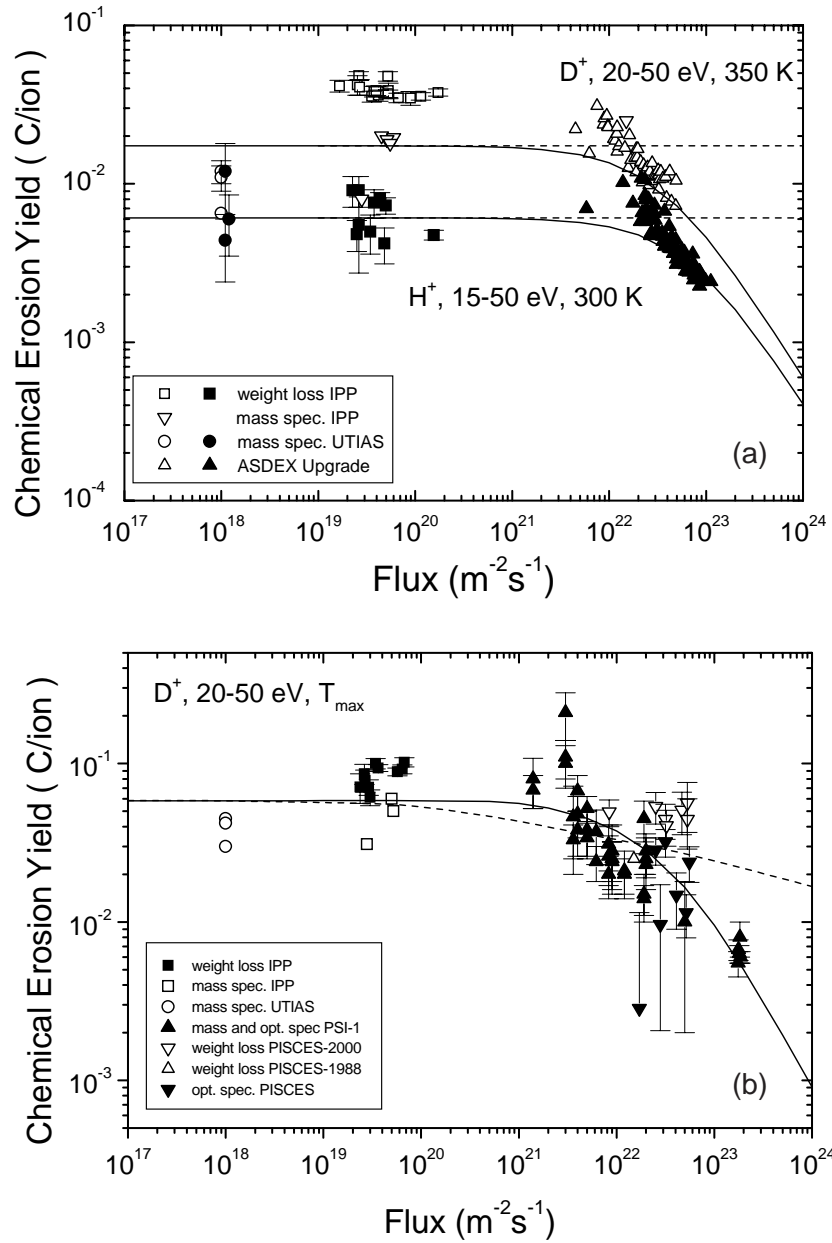


**Figure 16.** Flux dependence of the chemical erosion yield of carbon with deuterium ions near (a) room temperature and (b)  $T_{max}$ . The data combine weight loss and spectroscopic measurements from ion beam experiments [292, 293, 305, 306], spectroscopic measurements from plasma simulators [298, 299, 307, 308] and from the ASDEX-Upgrade divertor [301]. The curves are fits to the data using the models described in Refs [287, 296].

perature conditions, the previous modelling [296] of chemical sputtering did not predict any flux dependence. In contrast, the high flux data clearly show an apparent erosion yield decrease at fluxes above  $10^{22} m^{-2} \cdot s^{-1}$ . Within the error bars of the data a flux dependence close to  $\Gamma^{-1}$  can be deduced.

Figure 16(b) shows a similar comparison of ion beam data [292, 293, 305, 306] with high flux results from the plasma simulators PSI-1 [298, 307] and PISCES [299, 308] (see glossary) for elevated temperatures close to  $T_{max}$ . Again, the data appear to be relatively insensitive to the ion flux up to a

flux of  $10^{22} \text{ m}^{-2} \cdot \text{s}^{-1}$ , in accordance with the weak flux dependence from the previous model [296]. At higher fluxes, the yield appears to decrease steeply (except for the PISCES mass loss data), reaching values below  $10^{-2}$  at  $2 \times 10^{23} \text{ m}^{-2} \cdot \text{s}^{-1}$ . The fact that both the room temperature and high temperature data show the same apparent yield decrease with flux indicates that rehydration of the surface atoms after the release of a hydrocarbon molecule is the rate limiting process, as both the low and the high temperature processes rely on a fast rehydration of the surface [286]. The fact that the onset appears at about  $10^{22} \text{ m}^{-2} \cdot \text{s}^{-1}$  suggests a reaction time constant of the order of 1 ms [287]. Time constants for hydration of surface atoms of this order are actually deduced from the dependence of the hydrogen incorporation in the deposition rate during the growth of a-C:H layers [309].

### 3.2.4. Chemical erosion due to oxygen

The oxygen impurity concentration in today's tokamaks is typically reduced to levels below 1% by beryllium evaporation and boronization. If Be is used to protect the first wall of a next step device, such as in the ITER design, it can be expected that the large Be surface area will getter oxygen effectively, resulting in a relatively low oxygen concentration.

Oxygen ions will interact chemically with the divertor surfaces clad with C based materials. CO and CO<sub>2</sub> formation, and total C removal yields of the order of unity, without strong energy or temperature dependence, have been reported [282, 286, 310, 311]. The energy dependence of the O<sup>+</sup> induced C erosion yield (collected in Ref. [282]) is presented in Fig. 12 for comparison with the physical sputtering yields of other impurity ions. In the case of simultaneous H<sup>+</sup> and O<sup>+</sup> impact on carbon, a small amount of water is also produced, with a temperature dependence similar to that of CH<sub>4</sub> formation, with peak yield at  $\approx 800 \text{ K}$  [312]. The total yield was reported to be in good agreement with the sum of the yields due to individual O<sup>+</sup> and H<sup>+</sup> impact.

For Be, an increase of the surface binding energy occurs under oxygen bombardment, leading both to a decrease of the sputtering yield and to a shift of the threshold energy for sputtering to higher energies according to Eq. (4). The data for deuterium sputtering of a fully oxidized BeO surface are given in Refs [313, 314].

For W, the formation of oxides with high vapour pressure and consequently low surface bind-

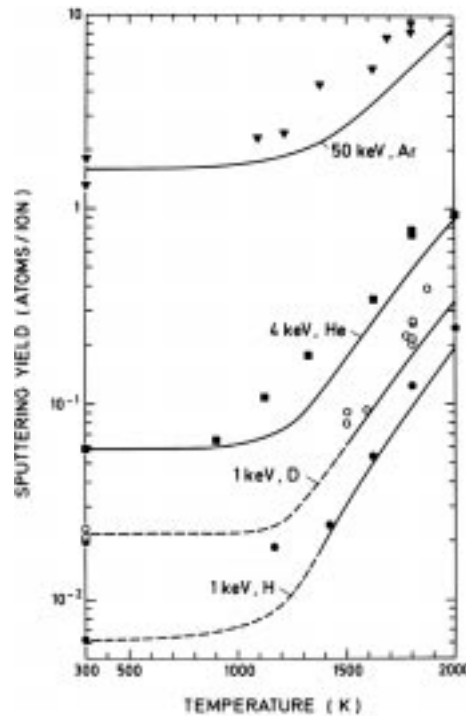


**Figure 17.** Temperature dependence of the sputtering yield of pyrolytic graphite by H<sup>+</sup>, D<sup>+</sup>, He<sup>+</sup> and Ar<sup>+</sup> in the temperature range of RES. Solid curves are from the model described in Ref. [333]. (Reproduced with permission from Ref. [333].)

ing energy, such as WO<sub>3</sub>, is well known. However, the enhanced erosion due to WO<sub>3</sub> appears to be a small effect that could not be observed during oxygen ion sputtering even at temperatures of up to 1900 K [315]. Sputtering by hydrogen isotopes near the sputtering threshold energy results in such small yield values that the additional release of oxide molecules during simultaneous impact of hydrogen and oxygen can be observed [316]. This effect results in measurable erosion yields even below the threshold energy for sputtering of clean tungsten.

### 3.2.5. Radiation enhanced sublimation (RES)

Another erosion process, unique for carbon — radiation enhanced sublimation (RES) — has been observed in ion beam experiments [317, 318]. RES results in the release of carbon atoms with a thermal velocity distribution [319] under ion irradiation. RES has recently been reviewed in Ref. [320].

During ion irradiation, not only surface atoms are displaced from their lattice sites but atom displacements also occur throughout the ion range when energies higher than about 25 eV are transferred

in elastic collisions. In graphite, carbon atoms are very mobile between graphitic planes, and atoms that escape recombination with vacancies can reach the surface and evaporate freely. A detailed analytic model taking defect production, diffusion, recombination and evaporation into account accurately reproduces the observed temperature dependence of the erosion yield [321]. Although RES exists already at room temperature [322], its yield is smaller than the physical sputtering yield below about 1500 K. At higher temperature, radiation induced vacancies become mobile, and an increasing number of displaced carbon atoms escape recombination and reach the surface. The erosion yield increases monotonically with surface temperature until above 2000 K normal sublimation dominates the erosion. Figure 17 [333] shows a collection of erosion data in the RES temperature regime. Attempts to reduce RES by doping the carbon material with impurities showed a shift of RES to higher temperature but, in general, no complete suppression has been achieved [323, 324]. Only in one case, that of Ti doped carbons, has complete suppression of RES been reported (e.g. Ref. [325]), but independent confirmation of this finding is required.

The theoretical model of this process predicts a  $\Gamma^{-0.25}$  decrease with increasing flux [321, 322, 326, 327], somewhat steeper than ion beam data suggest [321, 328, 329]. Carbon influx measurements in tokamaks, such as TFTR, JET [108] and Tore Supra [330], have been interpreted as RES. The observation that the RES process could not be observed in a spectroscopic investigation at the TEXTOR test limiter [331] up to temperatures where thermal sublimation sets in, may be due to a possible decrease of RES with ion flux. Recent data from a high flux plasma source [332] indicate a stronger flux dependence,  $\approx \Gamma^{-0.27}$ , than is observed in ion beam experiments, giving some support to the validity of the model.

### 3.2.6. Erosion under tokamak conditions

Energetic particle bombardment in fusion devices will not be monoenergetic as in laboratory simulations, but will have a broad energy distribution. For example, in the case of charge exchange neutrals impinging on the vessel wall with energies ranging from below 20 eV to keV's, an estimate of the effective sputtering yield can be obtained by integrating over the whole energy distribution. Also, it is rare that only one ion species will impinge on a wall com-

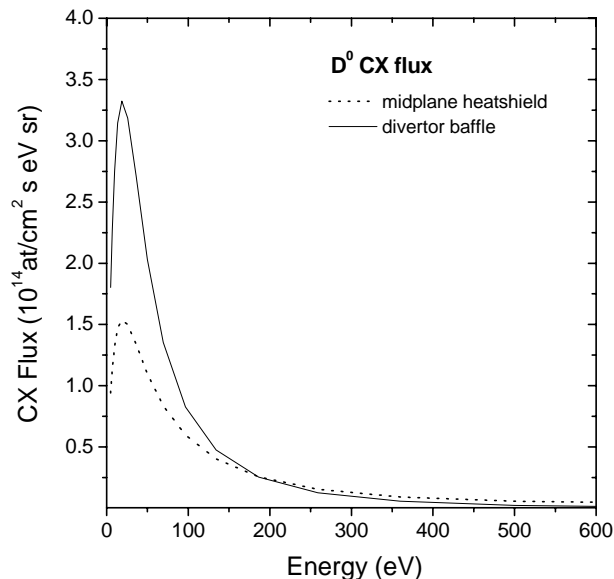


**Figure 18.** Energy distribution of the charge exchange neutral flux to the inner heat shield and the divertor baffle of ASDEX-Upgrade as calculated by using the B2/EIRENE code [157].

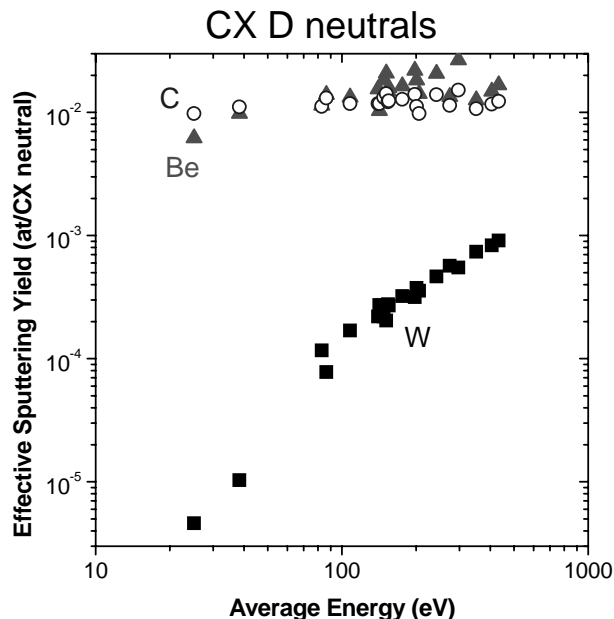


**Figure 19.** Dependence of the effective sputtering yield of Be, C, and W by deuterium charge exchange neutrals on the average energy of the neutrals [157].

ponent, and therefore the effect of multiparticle bombardment has to be taken into account. Erosion properties of deposited layers and mixed material layers also have to be considered.

### 3.2.6.1. Erosion due to charge exchange neutrals at the main chamber wall

Physical sputtering by energetic hydrogen isotopes dominates the erosion of metal PFCs (e.g. Be, W) at the main chamber wall and divertor baffle of a device such as ITER. Redeposition on these surfaces is negligible.

To evaluate the erosion by charge exchange neutrals, an effective sputtering yield has to be calculated which takes the energy distribution of the charge exchange neutrals into account [157, 334–336]. The energy distribution will differ strongly for different wall areas. The charge exchange neutral energy distribution has been measured at a few locations in some tokamaks. Erosion by charge exchange neutrals at other locations and for other plasma conditions can be estimated by using charge exchange neutral energy distributions from plasma edge simulation codes such as B2/EIRENE (see, for example, Ref. [157]). In Fig. 18 the calculated energy distributions are shown for the charge exchange neutral particles incident on the inner vessel wall and the baffle region in ASDEX-Upgrade. Typically, the energy distribution of charge exchange neutrals peaks at low energies and decreases monotonically with increasing energy. Clearly, the high sputtering threshold energy of about 200 eV for W, compared to 9 eV for Be, will result in a drastically reduced effective erosion yield as most of the charge exchange neutrals have energies below 200 eV and only the high energetic tail contributes to sputtering of W. On the other hand, for Be the effective erosion yield is determined mainly by the large flux of low energy neutrals, and the high energy tail does not contribute strongly. In ASDEX-Upgrade, a large variety of charge exchange neutral energy distributions have been measured for different plasma conditions. Figure 19 shows the effective sputtering yields for C, Be and W, calculated by integrating over the whole energy distribution, plotted versus the average energy. For W, the yield increases strongly with increasing average energy, while for Be and C, the low energies dominate and the effective yield becomes insensitive to average energy. Chemical erosion of carbon tiles used in today's tokamaks as cladding of the main plasma chamber by charge exchange neutrals, together with sputtering by edge plasma ions is the origin of a large carbon influx into the plasma [157, 337]. For conditions of low average energies, such as at the divertor baffle or in the divertor chamber, high Z materials show erosion yields orders of magnitude lower than that seen for low Z

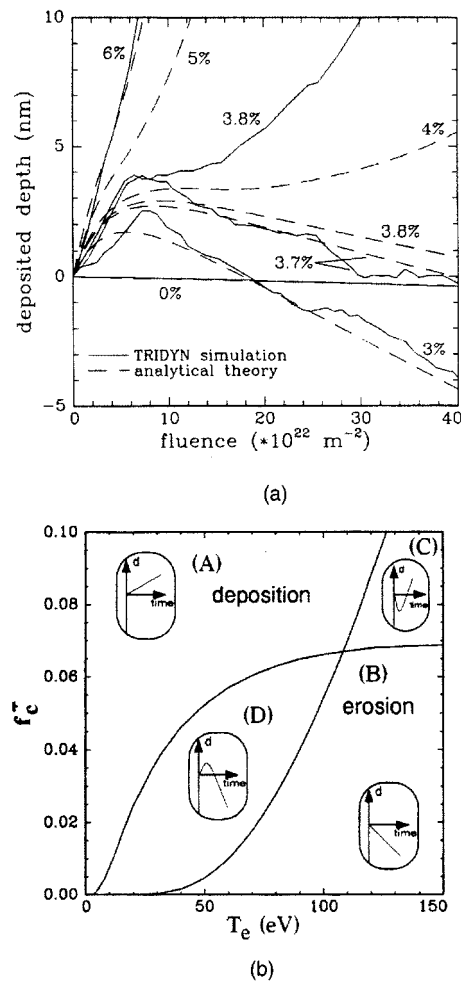


**Figure 20.** (a) Fluence dependence of the deposited depth for W bombarded with deuterium ions from a 20 eV divertor plasma with various levels of carbon impurities; (reproduced with permission from Ref. [338]). (b) Boundaries of erosion and deposition conditions for W bombarded with deuterium ions depending on plasma electron temperature,  $T_e$ , and carbon impurity content,  $f_c$ . The four possible time developments (A–D) are schematically indicated in the figure in their region of validity (Reproduced with permission from Ref. [338].)

materials. For the high average energies at the main vessel walls, this erosion advantage of high Z materials is reduced (Section 1.3.2).

### 3.2.6.2. Synergy between incident impurity and plasma ions

A further complication arises from a consideration of the simultaneous impact of plasma ions together with small amounts (few per cent) of impurities.

Both an increase and a decrease of the erosion yield is possible.

In the case of W erosion, the threshold energy for deuterium sputtering is about 200 eV. At plasma temperatures of 10 eV, typical for divertor conditions, no sputtering by deuterium occurs. However, at the same plasma temperatures, carbon ions, especially those multiply charged, do lead to W sputtering. At high carbon concentrations, carbon will form a protective layer on the W surface, while at low carbon concentrations, the simultaneously impinging deuterons can remove carbon from the surface, leaving W exposed for sputtering by carbon ions. The transition between erosion and redeposition now depends not only on the ion energy, i.e. the plasma temperature, but very sensitively also on the concentration of C in the incident plasma flux. Figure 20(a) shows the transition of erosion to deposition as a function of plasma fluence with different carbon concentrations as the parameter for a fixed plasma temperature of  $T_e = 20$  eV [338] calculated by the dynamic Monte Carlo Code TRIDYN. In Fig. 20(b) this transition boundary is shown in the plasma temperature versus carbon concentration plane. The calculation for the divertor conditions during the ASDEX-Upgrade W experiment [339], with a typical  $T_e = 10$  eV, predicts a transition for about 1% C ions. This prediction will be compared to spectroscopic measurements of W erosion in Section 4.3.1.

The balance of erosion/redeposition is obviously a complex multiparameter process. For the system Be–C–W, Hirooka [340] made predictions of flux ratios and ion energies at which sputtering or deposition will occur on the basis of calculated sputtering yields and reflection coefficients of the pure materials. The analysis, performed only in terms of energy dependent yields, neglects the process of implantation and surface modification. The qualitative findings are, however, in good agreement with experimental evidence at PISCES (Section 4.3.1).

### 3.2.6.3. *Erosion data of mixed materials*

The database for erosion processes on mixed materials is still scarce, although investigations are in progress.

Studies of binary systems include the erosion due to non-recycling or only partially recycling ions previously presented in Fig. 12 for C, and in Fig. 13 for W. In the case of O and C bombardment, the surface will change its composition, and oxides or carbides

may be formed. For O bombardment, saturation will eventually be reached in the stoichiometric oxide. No protective oxygen layers can be built up, and erosion, although reduced, prevails. Continued carbon irradiation, however, will lead to the buildup of carbon layers and a change from erosion to deposition.

Ternary systems cover the simultaneous sputtering by different impurity ions or the erosion by deuterium with simultaneous impurity ion bombardment. The systems  $C^+$  and  $CO^+$  on Be [341] and  $C^+$  and  $CH_3^+$  on W [342] have been investigated in some detail. Figure 21 shows the fluence dependence of deposition and erosion for both systems. In Fig. 21(a), the influence of the simultaneous impact of oxygen together with carbon is demonstrated for Be. The deposition of carbon was measured as a function of the fluence of  $C^+$  and  $CO^+$  ions. While for pure carbon bombardment a continuous increase of the deposition occurs, the simultaneous impact of oxygen prevents the buildup of a protective layer, and deposition reaches a saturation [341]. Actually, weight change measurements show a continuous loss of material, implying that Be erosion continues in steady state. In similar experiments investigating the formation of surface layers on Be, the transition from erosion to deposition was documented as a function of carbon concentration in a deuterium plasma beam [343].

A similar behaviour was demonstrated for simultaneous bombardment of W with carbon and hydrogen (Fig. 21(b)).  $CH_3^+$  bombardment at 3 keV ion energy simulates the simultaneous impact of 2.4 keV  $C^+$  ions (25%) and 200 eV  $H^+$  ions (75%). While the hydrogen ions with energies below the threshold energy cannot sputter W atoms, they can remove carbon atoms and prevent the buildup of a protective layer. Incident carbon ions continue to sputter W; weight loss occurs in steady state. The effect is more pronounced at elevated temperatures as shown in Fig. 21(c), either as a result of the diffusion of carbon into W [342] or the enhanced chemical erosion of carbon by hydrogen ions [344], both effects leaving the W surface unprotected to sputtering.

One important parameter is certainly the carbon concentration in the incident ion flux [338]. The transition from erosion to deposition occurs at lower ion energies as the carbon concentration decreases (Section 3.2.6.2). This transition concentration has recently been investigated for the conditions in PISCES for W erosion as a function of surface temperature [345]. For ion energies around

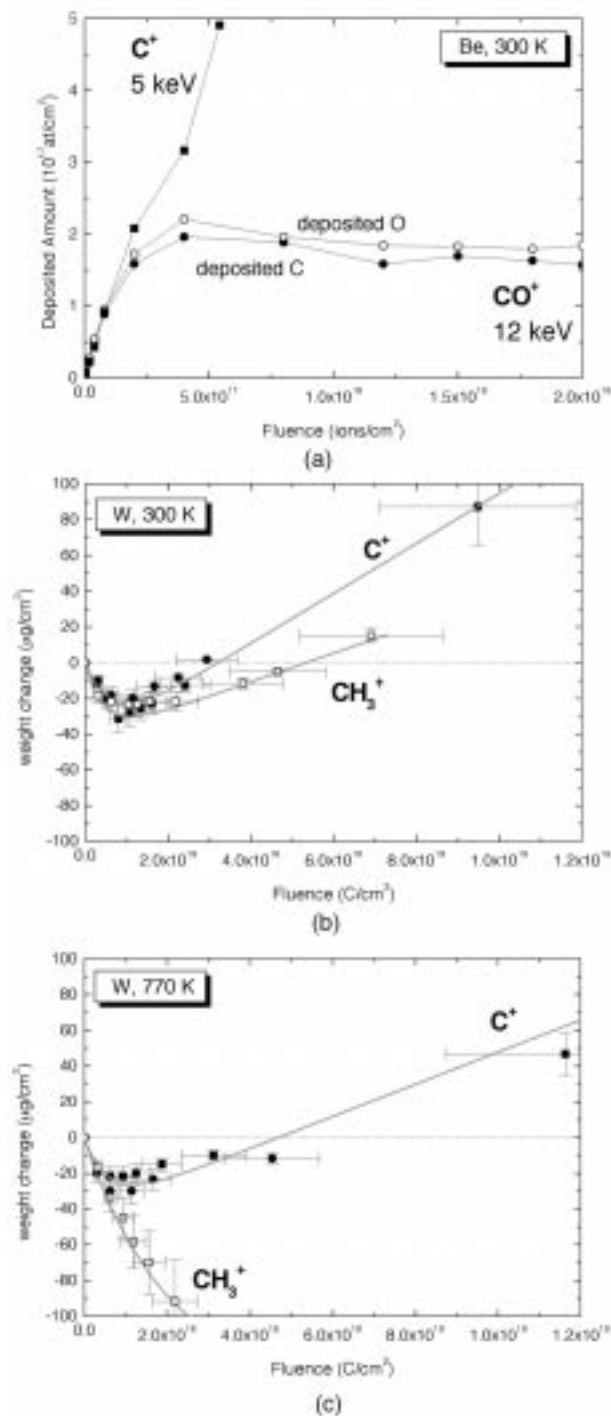


**Figure 21.** (a) Fluence dependence of the deposited amount of atoms during the bombardment of Be with 5 keV  $C^+$  or 13 keV  $CO^+$  [341]; (b) fluence dependence of the weight loss during the bombardment of W with 3 keV  $C^+$  or 3 keV  $CH_3^+$  [342] at 300 K; and (c) same as (b), but at 770 K.

100 eV, the transition for both  $C^+$  and  $H^+$  occurs at concentrations of about 5% in good agreement with

estimates from TRIM.SP calculations [338]. A weak decrease of the transition concentration was found with increasing temperature.

The parameter space for erosion/deposition in ternary systems is large, and only a few laboratory results are available. More experiments are needed to validate computer code calculations, especially as additional thermal effects, such as diffusion, phase formation or surface segregation may occur.

#### 3.2.6.4. Properties of deposited layers

Redeposited material is often considered to be similar to the bulk substrate material as far as erosion and hydrogen retention properties are concerned. However, especially in the case of redeposited carbon materials, these properties may depend strongly on the deposition conditions. Depending on local plasma temperature influencing the incident ion energies, the deposits may vary from hard coatings with an H/C ratio near 0.4 to more polymer like layers with H/C ratios near unity (Section 4.3). There is evidence from laboratory experiments that chemical erosion of hydrogenated co-deposits due to thermal hydrogen atoms is drastically enhanced compared to bulk graphite [294]. The thermal desorption of hydrocarbon molecules from co-deposited layers is strongly dependent on the film structure [346].

In the case of polymer like films, the release of  $H_2$ ,  $CH_4$  and  $C_2H_4$  commences at a temperature of  $\approx 500$  K, whereas for ‘hard’ a-C:H films, only  $H_2$  and  $CH_4$  desorb, and this occurs at temperatures above 700 K. Moreover, thermal decomposition of polymer like films leads to the release of a large amount of  $C_xH_y$  species with  $x \geq 2$ . Indeed, molecular fragments containing up to 7 C atoms have been detected [347]. On the other hand, simultaneously deposited metal atoms may reduce the chemical erosion rate [348]. Chemical erosion reduction has been observed in laboratory experiments for doped graphites [349, 350].

### 3.3. Erosion by arcing

Electrical arcs are short duration ( $< 1$  ms), high current density ( $\approx 10^{12}$  A·m<sup>-2</sup>) localized ‘discharges’ that can occur between the plasma and a PFC. The PFC material is evaporated and eroded quickly ( $> 1$   $\mu\text{m}$ ) due to the significant local heating by the arc. The signatures of electrical arcing between the plasma and the first wall have been seen since the first tokamak experiments were performed (e.g. T-2 [351]). Plasma exposed components show tracks,

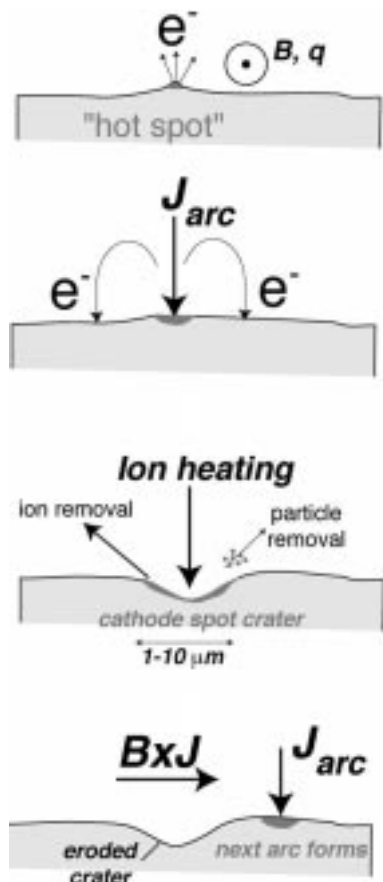


**Figure 22.** Schematic of typical arc history at the plasma facing wall of a tokamak.

scratches or pits caused by the intense local arc erosion that are visible to the naked eye (Section 4.4). The macroscopic nature of the arcing phenomena has made it a natural candidate for PMI investigation. The resemblance of the arc erosion on a PFC to the spots observed on the cathodes of vacuum arcs has been long recognized and has provided a large part of the understanding of arcing in tokamaks [74, 352–354]. The most basic condition that must be met to initiate an arc is that the driving potential at the material surface must surpass the arc voltage threshold,  $U_{arc} \approx 10\text{--}30$  V. This is typically achieved in the laboratory by placing a potential between two probes or plates. In a plasma, a sheath potential arises between the plasma and the material surface to equalize ion and electron fluxes. A temperature  $T_e > 3\text{--}10$  eV provides sufficient sheath potential to initiate an arc, a condition easily met in tokamak edge plasmas. These arcs are called ‘unipolar’ since they have one solid ‘electrode’, namely the wall that acts as a cathode, while the plasma performs the function of an anode.

The other key to arc initiation is the presence of small surface protrusions (Fig. 22) that provide a localized emission source or ‘hot spot’. Several factors at the spot reinforce the ‘seed’ arc current formation. Large electric fields reside there, tending to enhance the local heat flux to the surface and the electron emission. Also, the spot heats up quickly because of its reduced thermal conductivity towards the bulk material. It has also been suggested that ionization of the material within the sheath, which allows additional electron emission into the sheath, may play an important role in initiating the arc [355]. Eventually, these self-reinforcing, current forming and heating mechanisms make the tip evaporate, providing the needed material and current to sustain the fully formed arc. Emitted electrons are accelerated towards the plasma, reducing the local sheath potential, while the return path of the current is through energetic electrons returning to an area much larger than, and adjacent to, the cathode spot. The current channel of the arc contracts as a result of its self-magnetic field, resulting in a small cathode spot ( $\approx 10\text{ }\mu\text{m}$ ) and large current densities ( $\approx 10^{12}\text{ A}\cdot\text{m}^{-2}$ ). The cathode spot is heated via ion impact and cooled by melting and evaporation, the source of the material erosion.

In the presence of an external magnetic field,  $B$  (typically parallel to the PFC surface), an arc with current  $J$  (normal, into the surface) is acted upon by the Lorentz force,  $J \times B$ . However, the retrograde motion of the arc (i.e. in the opposite  $B \times J$  direction) is well established experimentally in both laboratories and tokamaks [356]. This is apparently due to the enhancement of arc density and heating from the alignment of the external and arc caused magnetic field on the retrograde side of the arc [357]. This favours the creation of a new arc on the lip of the initial crater. Thus, the arc appears to hop from one spot to another in the  $B \times J$  direction, causing the common scratch like signature of arcing (typically, several millimetres in length). The motion of the arc across the surface greatly extends the effective area over which the arc erodes material (as compared to a stationary arc that only affects a region of several micrometres in diameter).

The erosion rate of arcing is characterized by the amount of material per coulomb of arc charge and ranges from  $10\text{--}100\text{ }\mu\text{g}/\text{C}$ . Most elements (including carbon and tungsten) show a remarkably similar ratio of eroded ion current to total arc current ( $\approx 10\%$ ) [354]. Erosion losses from neutrals can enhance this by up to a factor of two over a wide



range of arc currents. Neutral eroded material is typically via particles of the order of a micrometer in size, ejected by high pressure vapour produced by the arc. These particles may vaporize and contaminate the plasma or remain as dust in the vessel (Sections 2.3.4 and 4.8).

Figure 22 follows the typical arc cycle seen in tokamaks. The shallow angles of incidence of the heat and particle flux incident on a tokamak first wall make even very small protrusions prone to excess heating. The initial arc is established (through the mechanisms described above), erodes the cathode spot and jumps to a ‘fresh’ location in retrograde direction. Typical arc tracks from limiters and divertors have dimensions of  $10\text{ }\mu\text{m}$  in depth,  $10\text{--}100\text{ }\mu\text{m}$  in width, and  $5\text{--}10\text{ mm}$  in length, resulting in  $10^{17}\text{--}10^{18}$  atoms of eroded material per arc event.

Uncertainties in characterizing the nature and quantity of surface protrusions makes predictive modelling of arcs quite difficult. In contrast to sputtering, which occurs constantly over the surface wetted by the plasma, arcing happens discretely. Arcs are initiated by ever changing surface conditions such as surface roughness, gas loading [358] and thin film formation. The implications of these dependencies will be further discussed in Section 4.

### 3.4. Erosion during off-normal plasma events

Here, we provide a brief overview of the physical processes involved in the deposition of intense energy delivered to PFCs during off-normal plasma transients in tokamaks (disruptions, etc.). Experimental data for disruption erosion, mainly from disruption simulators, are discussed in Section 4.5. Modelling of disruption erosion and the design implications for a next step device are discussed in Section 5.4.

#### 3.4.1. Physical processes

Plasma facing surfaces are rapidly heated during plasma instabilities (e.g. disruptions) by the direct impact of energetic plasma particles and radiation. Energy deposition in the target material is calculated using models that include physics of energy loss by plasma ions and electrons. The deposited energy flux can be high enough to melt and vaporize the surface material rapidly. The thermal response of the material is calculated by solving a time dependent heat conduction equation, with moving boundaries, i.e. the receding eroded surface and the solid–liquid interface, with boundary conditions including heats

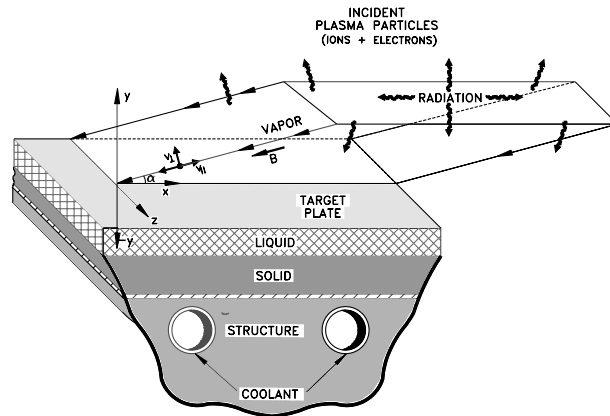


**Figure 23.** Schematic illustration of different interaction zones during a plasma disruption. (Reproduced with permission from Ref. [360].)

of melting and vaporization as described by Hasanein [359].

Initially, the neutral vapour emitted from a solid or liquid target surface expands freely across magnetic field lines in the direction normal to the surface. As the cold vapour is heated by incident plasma particles, it becomes ionized and expands following the direction of the oblique magnetic field lines. The parameters and the dynamics of the target plasma depend on the energy flux and the type of target material. A low  $Z$  target plasma (e.g. C, Be) expands to larger distances from the surface, whereas vapour shields formed from higher  $Z$  materials (e.g. W, Mo) stay closer to the surface. The incoming plasma particles are completely stopped in the vapour plasma, and the plasma energy flux is converted to photon radiation. Although reduced from its original value, the net energy flux to the target surface (dominated by photon radiation) is large enough to cause melting and further erosion of metallic components.

Figure 23 from Ref. [360] is a schematic illustration of the various interaction zones that are currently included in the models to simulate the effects of the thermal quench of a disruption on a PFC.

The melt layer developed during a disruption is exposed to various forces such as electromagnetism, gravitation, mechanical vibration, plasma momentum, surface tension and ablation recoil [361]. For metallic components such as beryllium and tungsten, the erosion lifetime due to these off-normal events will be controlled and dominated by the evolution and the hydrodynamics of the melt layer during disruption, and the resulting loss of liquid material from the surface. In contrast, C based materials do not melt and, therefore, do not erode by these processes.

This is a major motivation for the choice of graphite and carbon fibre composites for some PFCs in existing fusion machines and in the ITER design (Sections 1.2.3 and 2.4). However, C based materials can suffer from different erosion mechanisms, as will be discussed later.

The detailed vapour motion above the exposed surface is calculated by solving the vapour magnetohydrodynamic equations for the conservation of mass, momentum and energy under the influence of a magnetic field [362]. The vapour cloud, if well confined, is predicted to greatly reduce the net energy flux to the surface, resulting in a reduction of erosion by evaporation of one to two orders of magnitude [363, 364]. The magnetic field lines are initially frozen into the surface of the liquid metal layer owing to the high conductivity of the liquid. However, as more vapour is emitted from the surface, the expanding dense ionized vapour will sweep and distort the oblique magnetic field lines. Near the upper vapour boundary, the magnetic field lines become almost parallel to the vapour surface. Such a situation of distorted magnetic field distribution results in a flute type MHD instability (see glossary) in the vapour plasma [365]. As a consequence of the loss of vapour confinement, the turbulent diffusing hot vapour may then deposit its energy on nearby components, causing more erosion. The overall net erosion rate and resulting damage will depend on the disrupting plasma parameters, the size of disruption spot, the design configuration and the type of plasma facing material [366].

In addition, hot plasma incident onto the cold plasma of the vapour shield gives rise to electric fields [367]. The electric field may cause lateral  $\mathbf{E} \times \mathbf{B}$  drifts, which can result in significant deflection of either the vapour shield plasma [368] or the incident plasma [369], or both, but these effects have not yet been demonstrated experimentally.

Photon radiation transport in a vapour plasma is an important part of predicting disruption erosion of PFCs. Opacity and emissivity parameters vary significantly in the developed vapour plasma since it contains very cold and dense plasma regions near the target surface and very hot and less dense plasma regions where the disrupting plasma ions and electrons deposit their energy. The models contained in the HEIGHTS package, developed by Hassanein et. al. [366], and the code FOREV-2 [370] allow for the treatment of non-local thermodynamic equilibrium (non-LTE) of the vapour cloud gener-

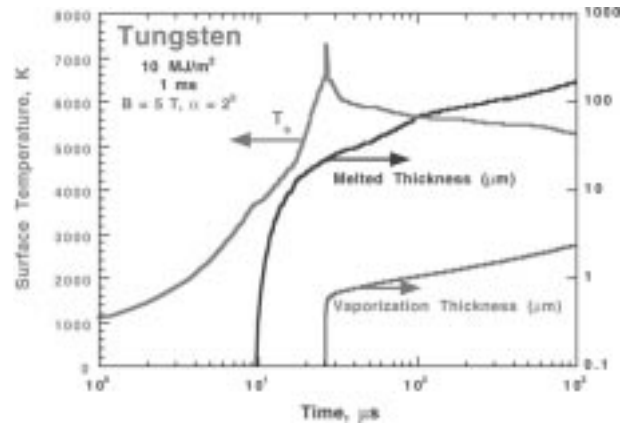


**Figure 24.** Time evolution of tungsten surface temperature, melt layer, and eroded thickness following a plasma disruption predicted by the A\*THERMAL-S code [366].

ated plasma, multigroup and multidimensional analysis of the produced photon spectra, as well as self-consistent kinetic models for both the continuum and line radiation generated in the vapour cloud.

### 3.4.2. Erosion of metallic plasma facing materials

Surface vaporization losses of metallic plasma facing materials are generally small (only a few micrometres) over a wide range of plasma conditions during short (i.e.  $\ll 1$  s) plasma instabilities [371]. The thickness of the melt layer on metallic components can be one to two orders of magnitude higher than surface vaporization losses [372, 373]. This is illustrated in Fig. 24 (taken from Ref. [366]) that shows the time evolution of a tungsten surface temperature, melt layer thickness (see glossary), and vaporization losses during a disruption for an incident plasma energy of  $10 \text{ MJ}\cdot\text{m}^{-2}$  deposited in a disruption time of 1 ms as predicted by the A\*THERMAL-S code (part of the HEIGHTS package) [366]. An initial magnetic field strength of 5 T with an incident angle of  $2^\circ$  is used in this calculation. The sharp initial rise in surface temperature is due to the direct energy deposition of incident plasma particles on the material surface. The subsequent decrease in the surface temperature is caused by the reduction in absorbed heat flux due to the vapour shield and conduction of heat into the material. The subsequent behaviour is mainly determined by the energy flux from the emitted photon radiation in the vapour cloud, as discussed above, and by vapour electron heat conduction.

Two mechanisms of melt layer loss have been observed experimentally [374]. These are melt splashing due to the formation of vapour bubbles inside the liquid layer, and growth of hydrodynamic instabilities due to plasma impact momentum ('plasma wind') at the liquid surface and forces generated by current decay in the liquid metal layer. As a result, hydrodynamic instabilities such as the Kelvin–Helmholtz instability will arise and form liquid droplets that will be carried away by the plasma wind.

The amount and rate of melt layer loss is difficult to predict and expected to depend on many parameters, such as heat flux, impurity and gas content, material properties and disrupting plasma parameters.

### 3.4.3. Erosion of carbon based materials

Because of the shielding layer effect discussed above, erosion by vaporization of carbon is limited to  $<10\ \mu\text{m}$  for a wide range of disrupting plasma conditions. This is about one to two orders of magnitude lower than it would be if no vapour shielding existed [372].

However, in many cases, graphite and C based materials have also shown large erosion losses significantly exceeding those due to surface vaporization. A phenomenon called brittle destruction has been observed in various disruption simulation facilities (Section 4.5). The physical mechanisms causing brittle destruction of C based materials are not yet clear. One potential reason is cracking caused by thermomechanical stresses developing during the process [375–377]. Another proposed scenario is that material is ejected by the sharp rise in pressure of gas trapped in the network of pores between intergranular and intercrystallite boundaries [374]. These processes are likely to depend on the material microstructure.

The macroscopic erosion of C based materials depends on three main parameters: net power flux to the surface, exposure time and the threshold energy required for brittle destruction [366]. The required energy is critical in determining the net erosion rate of C based materials and is currently estimated from disruption simulation experiments (Section 4.5). More experimental data and additional detailed modelling are needed to evaluate the erosion of carbon-based materials, e.g., the role of brittle destruction (Section 6.1).

## 3.5. Hydrogen recycling and retention in plasma facing materials

Retention and recycling of hydrogen from PFCs affect fuelling efficiency, plasma density control and the density of neutral hydrogen in the plasma boundary. This in turn affects particle and energy confinement (Section 1.2.3) [378–381]. Tritium inventory and permeation of tritium through the wall or into coolant channels are also concerns for reactors. This section reviews the underlying physical mechanisms for these processes that provide the basis for models of hydrogen retention and recycling to be discussed in Section 5. The implantation of energetic hydrogen into plasma facing materials and its subsequent diffusion, release or immobilization by trapping or precipitation within the material are discussed here. Hydrogen retention via co-deposition is also discussed.

Some laboratory data are included in this section, mainly to illustrate how the various processes influence hydrogen retention in carbon, beryllium and tungsten. The term 'hydrogen' (or 'H') is used in this section generically to refer to protium, deuterium and tritium.

### 3.5.1. Implantation

Implantation of energetic particles into solids is fairly well understood [382]. In tokamaks, plasma facing materials are bombarded by energetic ions and neutrals from the plasma with energies of up to a few keV. As these energetic particles penetrate into a solid they lose their kinetic energy, mainly to electrons, and are deflected by collisions with atoms, thereby transferring kinetic energy to atoms in the solid (see also Section 3.2.1). Some of the incident particles scatter back out of the material with a significant fraction of their initial energy, leaving the surface mainly as neutrals. The fraction of particles which backscatter is higher for lower incident energies and higher Z target materials and can exceed 50% [383]. Particles that do not backscatter eventually reach thermal energies within the material and settle into an atomic configuration, which has a local energy minimum. The depth distribution of these implanted particles depends on the energy and atomic number of the incident particles and on the target material.

Atomic collisions displace atoms from their equilibrium lattice sites. If the transferred energy is less than a few tens of eV, a metal lattice will

relax back to its original atomic configuration. Collisions transferring more energy than this can produce lattice vacancies and interstitials. The maximum energy transferred in a collision is given by

$$E_t = E_0 4M_1 M_2 / (M_1 + M_2)^2 \quad (6)$$

where  $E_0$  is the incident particle energy and  $M_1$  and  $M_2$  are the incident and target atom masses. Light projectiles, therefore, transfer a larger fraction of their energy to light target atoms than to heavy target atoms. Thus, in a plasma–wall environment, such displacement defects are more likely to be produced in low  $Z$  than in high  $Z$  materials. In metals, a vacancy/interstitial pair is dynamically unstable and will recombine if their separation is less than a few lattice spacings. This limits the concentration of displacement defects to less than about 1 atomic per cent, even in the absence of long range mobility [384]. Vacancies and interstitials also migrate by thermally activated diffusion and disappear at surfaces and dislocations. They are annihilated by recombining with each other or agglomerating into less mobile defect clusters. Defect mobility depends on the material and on temperature. Interstitial atoms are mobile above about 100 K in most metals [378]. Vacancies become mobile at an absolute temperature that is roughly a quarter of the melting temperature. Vacancies may also capture hydrogen, as will be discussed later in this section, which may reduce their mobility. The extent to which atomic displacements by energetic hydrogen influence PMIs is not well understood, but these defects are more likely to have a significant effect for low  $Z$  than for high  $Z$  materials. Monte Carlo computer simulations of implantation have been developed which are widely used to calculate depth profiles of implanted atoms and displaced lattice atoms, and the energy and angular distributions of backscattered particles [268, 385].

Hydrogenic ions from a plasma typically have energies in the range from tens to hundreds of eV after acceleration through a sheath potential (Sections 1.2.4 and 3.2). The energy distribution of charge exchange neutrals depends on the density and ion temperature profile in the plasma edge and can extend up to a few keV for hot low density plasmas (Fig. 18). In low  $Z$  materials such as C or Be, the depth of implantation of hydrogen with energies of 0.1 to 1 keV is about 3 to 30 nm [386]. At a given energy, the depth of implantation of hydrogen into high  $Z$  materials is less than in low  $Z$  materials.

### 3.5.2. Hydrogen behaviour in metals

#### 3.5.2.1. *Hydrogen diffusion in metals*

Hydrogen implanted into metals will predominantly come to rest at interstitial solution sites. From there the hydrogen may hop to neighbouring solution sites, thus undergoing thermally activated diffusion. The fate of implanted hydrogen strongly depends on its mobility through the lattice, hence on the temperature. In most metals, hydrogen diffuses at room temperature and above [387, 388]. In this case, the time dependent distribution of hydrogen in the material can be described by the diffusion equation:

$$\frac{\partial C_s(x, t)}{\partial t} = D \frac{\partial^2 C_s}{\partial x^2} + \Phi P(x) - \sum_i S_i \quad (7)$$

where  $C_s(x, t)$  is the concentration of hydrogen in solution per host atom (i.e. atom fraction) and  $D$  is the diffusion coefficient for hydrogen in solution. The second term on the right hand side is the source term for implanted hydrogen, where  $\Phi$  is the flux and  $P(x)$  is the depth distribution. Source/sink terms  $S_i$  describe other processes, which add to or subtract from the concentration of hydrogen in solution. Such processes include trapping and internal precipitation into gas or hydride phases. In addition, a boundary condition at the surface is required. Release of hydrogen from a metal surface normally occurs by the desorption of hydrogen molecules. The direct thermal desorption of atomic hydrogen from the surface normally occurs at a slower rate because of the higher energy barrier for this process, but can be significant at high temperatures. For release by molecular recombination at the surface, the outgoing flux (atoms per unit area and time) is

$$\Phi_0 = -D[\partial C_s / \partial x]_{x \rightarrow 0} = 2K_r [NC_s(x \rightarrow 0)]^2 \quad (8)$$

where  $C_s(x \rightarrow 0)$  and  $[\partial C_s / \partial x]_{x \rightarrow 0}$  indicate the value and the gradient, respectively, of the concentration of hydrogen in solution just beneath the surface,  $N$  is the atomic density of the host and  $K_r$  is a rate coefficient for molecular recombination.  $K_r$  can be determined in experiments which simultaneously measure hydrogen concentration and release rate [389], and theoretical models exist which give  $K_r$  values from first principles for bare metal surfaces [389–391]. A schematic diagram illustrating the main mechanisms for hydrogen transport and release at the surface of a metal is shown in Fig. 25. Monolayer coverage of surfaces by contaminants such as oxygen can reduce  $K_r$  by orders of magnitude [389, 392]. Dissociative absorption of hydrogen from gas phase into

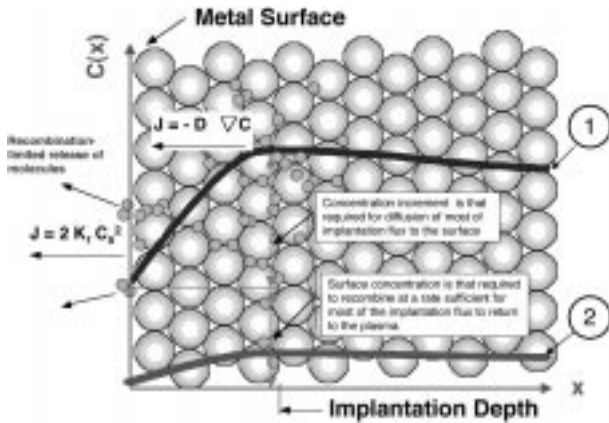


**Figure 25.** Schematic diagram showing main transport mechanisms for hydrogen migration and release at a surface of a metal subject to implantation of energetic particles. The concentration profile is also shown for two cases: (1) with a high near surface concentration resulting from a sluggish re-emission from the surface, and (2) with a lower near surface concentration resulting from an enhanced re-emission of implanted flux to the plasma. This, in turn, means a reduced driving potential for diffusion into the bulk. (Figure provided by G. Longhurst, INEEL, Idaho Falls.)

solution in metals is similarly hindered by surface impurities [392]. This sensitivity of hydrogen uptake and release to surface contaminants often strongly affects permeation and thermal desorption experiments. Controlled experimental permeation studies of the effects of the surface state on  $K_r$  [389, 392–395] and the deposition of thin metal films on permeating substrates [396–398] to control  $K_r$  have been performed, and results are available for palladium, iron, tantalum and copper. Models for permeation of hydrogen in metals are also discussed in Ref. [381].

Analytical solutions to the hydrogen transport equation have been developed [399, 400] for evaluating the hydrogen inventory, recycle and permeation rate and recycle time, under steady state conditions, where hydrogen is being implanted at flux  $\Phi$  to a depth  $R_p$  and release is controlled by diffusion and surface recombination. The flux of implanted hydrogen creates a concentration of hydrogen in solution at depth  $R_p$  given by  $\Phi = -D \partial C_s / \partial x = -DC_s / R_p$  for diffusion limited release or by  $C_s = (\Phi / K_r)^{1/2}$  for surface recombination limited release. In each case, a near surface concentration of mobile hydrogen is established from which hydrogen may diffuse beyond the implantation depth. The steady state flux

of hydrogen permeating through a slab is

$$W = (R_p / D)(K_r / \Phi)^{1/2} \quad (9)$$

when release is diffusion limited at both the front and back surfaces and the depth of implantation  $R_p$  is much less than the thickness of the slab  $x$ . When release is recombination limited at both front and back surfaces with recombination coefficients  $K_f$  and  $K_b$ , respectively, the steady state permeating flux is

$$\Phi_p \cong \frac{\Phi}{1 + K_f / K_b} \quad (10)$$

Diffusing hydrogen can become bound at traps. The concentration of trapped hydrogen can be determined from the concentration of mobile hydrogen, i.e. hydrogen in solution, as will be discussed below. The diffusing hydrogen may also precipitate into gas or hydride phases. Trapping and precipitation can be described by appropriate source/sink terms  $S_i$  in the transport equation as described below. The amount of hydrogen in solution, trapped and precipitated states will depend on the incident flux of hydrogen. This can lead to dynamic pumping effects where hydrogen accumulates in the material during implantation and is released after the implantation ceases. Modelling of hydrogen recycling effects is discussed in Section 5.5.

### 3.5.2.2. Hydrogen trapping in metals

Trapping of hydrogen at lattice defects can strongly affect the behaviour of hydrogen in materials. Here we define traps as sites where hydrogen is atomically bound, which do not interact with each other and where the hydrogen is in a lower energy state relative to a solution site. Examples of such sites are lattice vacancies, adsorption onto internal (i.e. void) surfaces and interfaces with embedded particles such as oxides. Figure 26 illustrates the relative energies of hydrogen in various states in a metal host and the barriers for thermally activated transitions between states.

The condition for thermodynamic equilibrium between hydrogen in traps and hydrogen in solution is obtained by equating the chemical potentials of hydrogen in these two states. For static traps, in which one hydrogen atom can be accommodated in each trap, statistical mechanics gives the equilibrium condition

$$C_s / z = C_t / (C_T - C_t) \exp(-Q_t / kT) \quad (11)$$

between the concentration of hydrogen in solution,  $C_s$ , and the concentration of hydrogen in traps

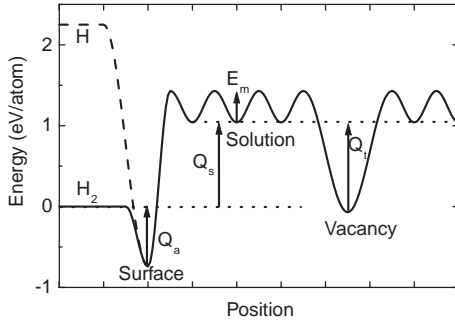


**Figure 26.** Potential energy diagram for hydrogen in tungsten. Enthalpy of solution  $Q_s = 1.04$  eV [407], activation energy for diffusion  $E_m = 0.39$  eV [407], binding enthalpy of hydrogen to a vacancy  $Q_t = 1.1$  eV [404, 405], enthalpy of adsorption  $Q_a = 0.7$  eV [408, 409]. The activation energy for detrapping is  $Q_t + E_m$ .

$C_t(x, t)$ , where  $C_T(x)$  is the concentration of traps,  $Q_t$  is the difference in enthalpy between hydrogen in a trap and at a solution site,  $k$  is Boltzmann's constant,  $T$  is the temperature and  $z$  is the number of solution sites per host lattice atom. This expression assumes that the fraction of solution sites occupied by hydrogen is small and that the non-configurational or vibrational part of the entropy difference between trapped and untrapped hydrogen is small. The source/sink term,  $S_t$ , describing the effect of static traps on hydrogen transport can then be formulated as

$$S_t = \partial C_t / \partial t = \Gamma [C_s(C_T(x) - C_t) - zC_t \exp(-Q_t/kT)] \quad (12)$$

where  $\Gamma$  is the rate at which local equilibrium between hydrogen in traps and solution is approached. The first and second terms on the right hand side are the trapping and detrapping rates, respectively. In equilibrium, these terms are equal, and  $\partial C_t / \partial t = 0$ . The rate coefficient can be expressed as

$$\Gamma = 4\pi NDR \quad (13)$$

where  $R$  is the reaction radius, i.e. hydrogen–trap separation at which reaction occurs, which is about one lattice constant [401]. Solutions to the transport equation usually depend only weakly on the value of the equilibration rate  $\Gamma$ . More critical is the condition for thermodynamic equilibrium (Eq. (11)). This is because features of interest usually involve longer range transport occurring over time scales long compared to the time to reach local thermodynamic equilibrium.

The case where a material contains more than one type of static trap can be described by including additional source/sink terms as given by Eq. (12), each with its own trap concentration and binding enthalpy. If multiple states or types of traps with different H binding enthalpies are present, and the H can exchange among them so that the various states are in thermodynamic equilibrium, then the states with the lowest energy will be occupied first. As more H is added to the system (increasing its chemical potential), the lowest energy states eventually will be filled and the higher energy states can become occupied. Generally, in transition metals H adsorbed on a surface is one of the most strongly bound states. Adsorbed H will therefore tend to saturate the surfaces of internal voids if these are present, before gas begins to precipitate within the voids and before H begins to occupy other weaker traps.

Appropriate source terms for Eq. (7) have also been derived for situations where each trap may accommodate multiple hydrogen atoms, for example, adsorption sites on the surface of internal cavities or multiple hydrogen atoms in a vacancy [380]. This formalism has also been extended to include the case where multiple types of traps are themselves diffusing and interacting with each other to describe hydrogen interacting with mobile displacement defects in nickel [402].

Here, we briefly discuss two special cases of trapping in a material with uniform concentration of traps, where the concentration of mobile hydrogen in solution near the surface is fixed at a value  $C_{ss}$ . In the first case, the concentration of traps is larger than the concentration of H in solution ( $C_T \gg C_{ss}$ ) and trapping is strong such that the concentration of hydrogen in solution in equilibrium with the traps is  $C_{eq} \ll C_{ss}$  until the traps are nearly full. In this case, the traps will be full at depths less than  $x = (2DtC_{ss}/C_T)^{1/2}$  and empty at greater depths. H uptake in this case proceeds through the increase in thickness of a layer in which the H concentration equals the trap concentration. This gives a delay before the onset of permeation through a slab. Secondly, consider the case where the trapping is weaker such that the fraction of occupied traps is still small in equilibrium with hydrogen in solution at concentration  $C_{ss}$ . In this case, the traps may be considered as another type of solution site, and the flux of diffusing hydrogen can be expressed as

$$J = -D\partial C_s / \partial x = -D^* \partial C_s^* / \partial x \quad (14)$$

**Table 8.** Values of binding enthalpy (eV) of H to vacancies relative to a solution site ( $Q_t$  shown in Fig. 26) at low occupancy in several metals obtained both from experiments and from first principles calculations.

Metal	Experiment		Effective medium theory
	Internal Redistribution	Positron Annihilation	
Al	0.52	0.53	0.52
Fe	0.63		0.83
Ni	0.44	0.58, 0.44	0.52
Cu	0.42	0.4	0.37
Zr	0.28		
Mo	1.03	1.4	0.96
Pd	0.23		0.16
Ta	0.42	1.2	
W	1.04 <sup>a</sup>	1.16 <sup>b</sup>	1.15 <sup>c</sup>
Be			1.65 <sup>d</sup>

<sup>a</sup> Thermal desorption [404].  
<sup>b</sup> Perturbed angular correlation [405].  
<sup>c</sup> Ref. [403].  
<sup>d</sup> Density functional theory [406].  
Sources for values not referenced here are given in Ref. [380].

with an effective diffusivity

$$D^* = D/[1 + C_T/zexp(-Q_t/kT)] \tag{15}$$

and an effective concentration

$$C_s^* = C_s + C_t = C_s[1 + C_T/zexp(-Q_t/kT)] \tag{16}$$

In both of these cases, the steady state rate of permeation of hydrogen through a slab of material is not affected by traps; however, the time to reach steady state and the inventory of hydrogen in the material do depend on the trapping.

Trapping of hydrogen at vacancies and on surfaces of internal cavities has been extensively studied in many metals, both theoretically and experimentally, by several methods. Experimental methods include studies of internal redistribution of deuterium between traps at different depths, equilibration of trapped deuterium with gas phase deuterium with known chemical potential, thermal desorption, positron annihilation and perturbed angular correlation gamma emission. Much of this work for metals is reviewed in Ref. [380]. A critical parameter for describing hydrogen trapping is the binding enthalpy of hydrogen to the traps. Table 8 [380, 403–406] gives values of binding enthalpy of H to vacancies relative

**Table 9.** Binding enthalpies (eV) of hydrogen to helium bubbles in metals.

Metal	Experiment		Effective medium theory	Chemisorption minus solution enthalpy
	Internal redistribution	Gas phase equilibration		
Al	0.52		0.52	
Fe	0.78	0.81	0.91	0.73
Ni	0.55	0.52	0.66	0.6
Mo	1.15		0.98	1.3
Pd	0.29		0.35	0.35–0.43
Ta	0.53		0.69	
Stainless steel	0.42			
Inconel	0.45			
W			1.15 <sup>a</sup>	1.8 <sup>b</sup>

<sup>a</sup> Ref. [407]  
<sup>b</sup> Refs [403, 408, 409]  
Sources for values not referred here are given in Ref. [380].

to a solution site ( $Q_t$  shown in Fig. 26) at low occupancy in several metals obtained both from experiments and from first principles calculations.

Trapping of hydrogen at helium bubbles produced by implantation of helium into metals has also been studied extensively. This is relevant to fusion plasma environments where helium bubbles may be formed by implantation of fusion alpha particles, by tritium decay or by neutron induced transmutation, e.g. in materials such as beryllium. These studies show that helium bubbles in metals trap hydrogen even more strongly than vacancies. Table 9 summarizes binding enthalpies of D to helium bubbles relative to a solution site, in several metals obtained from experiments and theory.

Trapping of hydrogen at helium bubbles is essentially the same mechanism as chemisorption onto a surface as can be seen from the fact that binding enthalpy of hydrogen to helium bubbles is similar to measured enthalpy of chemisorption onto external surfaces relative to hydrogen in a solution site. The high density of helium in the small cavities does not significantly influence hydrogen trapping on the cavity surfaces.

As shown by Tables 8 and 9, the binding enthalpies of hydrogen to vacancies and helium bubbles calculated by the ‘effective medium’ theory are generally in good agreement with the experimental values. The central concept behind the effective medium theory is an embedding function which yields the energy to insert an initially isolated atom,

for example, hydrogen or helium, at a particular site in terms of the unperturbed local electron density at that site before inserting the atom [410, 411]. This function depends on the type of embedded atom but is independent of the host. The approximate energy obtained from the embedding function is then refined by incorporating host specific perturbation terms. Figure 27 shows the embedding functions for hydrogen and helium. A significant feature for hydrogen is the energy minimum at finite electron density which reflects its chemical reactivity, whereas the embedding function for helium, which is chemically inert, has no such minimum. For most metals the local electron density at the interstitial hydrogen solution site lies well above the minimum; hence any local dilation of the lattice will produce a trap for hydrogen by lowering the local electron density. Furthermore, the more open the defect the greater the binding enthalpy, with large voids and external surfaces providing the asymptotic limit. For example, mono-vacancies trap hydrogen substantially more strongly than dislocation strain fields or stacking faults, but somewhat less strongly than voids [380]. Trapping of hydrogen at substitutional impurities in metals is observed to be weak ( $Q_t \leq 0.1$  eV typically) [412] as expected since these do not create open volume. Metals with large endothermic heats of solution (i.e. low solubility) should have large values of  $Q_t$  for trapping at vacancies and surfaces since the enthalpy difference between solution and trap sites will be larger, as is illustrated in Fig. 26. For example, molybdenum and tungsten have large endothermic heats of solution (0.68 and 1.04 eV, respectively [407, 413]) and large binding enthalpies (1.03 and 1.1 eV, respectively [404, 405, 414]) for hydrogen trapped at vacancies. The combination of low solubility and strong trapping means that small defect concentrations can strongly influence hydrogen content and mobility, which makes measurements of hydrogen solubility and diffusivity susceptible to errors due to trapping.

Because of its high atomic density, beryllium has one of the highest interstitial electron densities of any metal [415], and thus might be expected to represent an extreme case of low solubility and strong trapping for hydrogen. Density functional theory calculations predict a large endothermic heat of solution (0.8 eV) and strong binding of hydrogen to vacancies (1.62 eV) in beryllium [406, 416]. Experiments to measure hydrogen solubility in Be have found low concentrations of hydrogen in solution but often also small endothermic heats of solution [417] (see also Section 3.5.2.4). This combination suggests that

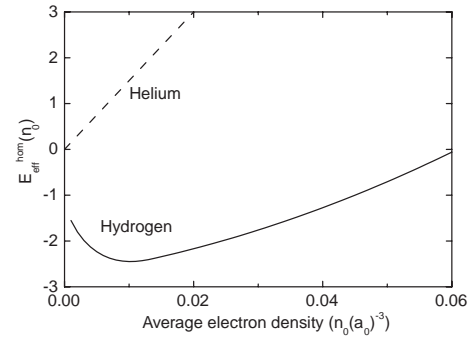


**Figure 27.** The binding energy of a hydrogen or helium atom in a homogeneous electron gas as a function of average electron density in units of electrons/ $a_0^3$ , where  $a_0$  is the Bohr radius.

these solubility studies might be measuring occupation of hydrogen sites other than bulk solution in Be metal. The powder metallurgy process normally used to fabricate beryllium leaves many small beryllium oxide inclusions, typically at volume fractions of 1%, which could provide trap sites at the metal/oxide interface or lower energy solution sites within the BeO particles. Although trapping of H at BeO inclusions in Be has not been studied, H is observed to be strongly trapped by such oxide inclusions in aluminium [418].

### 3.5.2.3. Hydrogen precipitation in metals

If hydrogen in solution encounters an internal void it will precipitate as molecular hydrogen. If the void volume is connected to an external surface the gas will escape the material. Otherwise, the gas pressure in the void will increase as hydrogen flows into it. Net flow ceases when thermodynamic equilibrium between solution and gas phases is reached, i.e. when the chemical potentials of the two phases are equal. This gives

$$C_s/C(P_0) = (P^*/P_0)^{1/2} \quad (17)$$

when the fraction of solution sites occupied by hydrogen is small, where  $C_s$  is the concentration in solution.  $P^*$  is the fugacity of the gas, which for an ideal gas equals the gas pressure. The solubility

$$C(P_0) = C_{s0} \exp(-Q_s/kT) \quad (18)$$

is the concentration of hydrogen in solution in equilibrium with gas at some reference pressure  $P_0$ , small enough for the gas to behave ideally,  $Q_s$  is the enthalpy of solution and  $C_{s0}$  is a solubility prefactor. Implantation of hydrogen into materials may produce concentrations of hydrogen in solution, for



which the equilibrium gas pressure is very high. The fugacity and chemical potential  $\mu$  can be obtained from the equation of state [419] relating the gas pressure  $P$  to the molar volume  $V_m$  by integrating

$$\ln(P^*/P_0) = (\mu - \mu_0)/kT = (kT)^{-1} \int_{P_0}^P V_m(P) dP \quad (19)$$

Precipitation of hydrogen into static cavities can be included in the transport equation through a source/sink term of the form

$$S_g = \partial C_g / \partial t = \Gamma_g [C_s - C_{eq}(C_g, V_c, T)] \quad (20)$$

where

$$C_{eq} = (P^*/P_0)^{1/2} C_{s0} \exp(-Q_s/kT) \quad (21)$$

Here,  $C_{eq}$  is the concentration of hydrogen in solution in equilibrium with the gas in the cavities, which depends on temperature and molar volume of gas in the cavities, and therefore on  $C_g$ , the quantity of hydrogen in the cavities and on  $V_c$ , the volume of cavities per unit volume of material since

$$C_g = 2V_c/V_m \quad (22)$$

The rate coefficient is

$$\Gamma_g = 4\pi D R_c N_c \quad (23)$$

where  $R_c$  is the cavity radius and  $N_c$  is the number of cavities per unit volume.

The flow of hydrogen into cavities may lead to gas pressures high enough to cause the cavity volume to increase. The two principal mechanisms for growth of small cavities are absorption of vacancies and production of dislocations. Growth by emission of single interstitial atoms is energetically unfavoured, compared to the collective process of dislocation production, except possibly for very small cavities approaching atomic dimensions. Absorption of vacancies produced by atomic collisions during implantation can contribute to cavity growth, although absorption of interstitial atoms that are simultaneously produced will have the opposite effect. At high temperatures, mobile vacancies are present in metals in thermal equilibrium. In this case the cavities will absorb and emit vacancies until the internal gas pressure balances the surface energy of the cavity

$$P_{eq} dv = \gamma da \quad \text{or} \quad P_{eq} = 2\gamma/R_c \quad (24)$$

where  $v$  and  $a$  are the volume and surface area of a cavity, and the surface tension  $\gamma$  is the energy per

unit area to create a new surface. This condition gives higher gas pressure and concentration of hydrogen in solution at smaller cavities than at larger cavities, leading to a net flow of hydrogen from smaller to larger cavities, i.e. to a coarsening of the cavity size distribution. The equilibrium gas pressure given by Eq. (24), which is the minimum for cavity growth, can be very high for small cavities. For example, a surface tension typical of metals of  $\gamma = 1 \text{ joule}\cdot\text{m}^{-2}$ , gives  $P = 0.4 \text{ GPa}$  (4 kbar) for 10 nm diameter cavities. At this pressure, the molar volume of hydrogen gas approaches that of solid materials and the equation of state departs significantly from ideal gas behaviour [419]. When the gas pressure has the equilibrium value given by Eq. (24), the forces on the cavity surface due to internal pressure and surface tension balance each other, and there is no net stress in the lattice around the cavity. In the absence of mobile vacancies, the gas pressure in the cavities can rise above the equilibrium value given by Eq. (24), as H flows into the cavity, producing a stress field localized around each cavity. The internal gas pressure required for bubble growth by dislocation loop production is

$$P = (2\gamma + \mu b)/R_c \quad (25)$$

where  $\mu$  is the shear modulus of the material and  $b$  is the dislocation Burgers vector [420]. Typically, this occurs when the internal gas pressure is about an order of magnitude higher than the equilibrium value given by Eq. (24). When bubbles grow by dislocation production the gas pressures are higher when the bubbles are smaller.

The microstructure that results from precipitation of implanted hydrogen depends on the nucleation of cavities. If the implanted hydrogen and displacement defects are very mobile, their concentrations will remain low, the hydrogen chemical potential will also be low, and hydrogen precipitation is likely to occur only at pre-existing open volume sites such as grain boundaries or foreign inclusions. In this case, for low energy, i.e. shallow implantation, most of the hydrogen will escape from the surface, and the fraction retained by precipitation into cavities will be small. If it is less mobile, the implanted hydrogen may buildup to higher concentrations in solution in the implanted layer, giving a higher chemical potential, which will eventually induce cavity nucleation. The production of displacement vacancies could assist initial nucleation and growth of cavities since agglomeration of vacancies along with trapping of hydrogen in them could create nuclei for gas precipitation. In this case

a dense dispersion of very small cavities may develop in the implanted layer and the fraction of implanted hydrogen retained in the material may be close to 100% initially. As the implanted dose increases, the content of hydrogen and the volume fraction of cavities increase. When the volume fraction of cavities is high enough, typically about 0.3, they become interconnected. Hydrogen implanted in beryllium at temperatures below 500 K [421] and in stainless steel below 150 K [422, 423] behave in this way. If the implantation profile ( $P(x)$  in Eq. (7)) peaks beneath the surface, cavity coalescence will lead to blistering and exfoliation of the overlying layer. In a plasma–wall environment, the broad distribution of energies and angles of incidence are likely to produce a hydrogen implantation profile that is highest at or very close to the surface. In this case, metals in which implanted hydrogen has low mobility and solubility will develop a surface layer with interconnecting porosity connected to the surface. This results in H retention that increases with fluence until the near surface porosity develops, after which H retention saturates. This opening of porosity at the surface results in an enhancement of recombination and re-emission of particles back to the plasma and reduced uptake.

Hydrogen dissolves exothermically in some metals, and in this case high concentrations of hydrogen in solution can have low chemical potential and, hence, low equilibrium gas pressure. In such metals, hydrogen precipitates as an ordered metal–hydride phase rather than as gas bubbles. In many cases, the concentration of hydrogen in solution in thermodynamic equilibrium with the hydride phase can be approximated by

$$C_{eq} = C_{h0} \exp(-Q_h/kT) \quad (26)$$

where  $Q_h$  is the enthalpy of formation of hydride from the solution phase, and  $C_{h0}$  is a temperature independent prefactor. Hydride precipitation can be included in the transport equation, Eq. (7), through a source/sink term which incorporates the equilibrium concentration in solution (Eq. (26)) and which stops the hydride dissolution and formation reactions when the local volume fraction of hydride reaches 0 or 1, respectively [380].

The system of coupled partial differential equations given by Eqs (7), (12) and (20) can readily be solved in most cases by discretizing the spatial co-ordinate and then propagating the resulting system of ordinary differential equations forward in time from a specified initial condition using an integrat-

ing algorithm for stiff problems [424]. Several computer codes implementing numerical solutions to the hydrogen transport equation have been developed [380, 425–429]. Some of these will be discussed further in Section 5.6.

#### 3.5.2.4. Hydrogen retention in Be and W

The use of tungsten and beryllium as plasma facing materials in tokamaks has prompted many experimental studies of retention and emission of hydrogen implanted into these metals from ion-beams or plasmas. References and discussions of these studies can be found in reviews [379, 430–432]. Here, we present selected highlights from these studies which are relevant to H retention in Be and W in a fusion plasma environment.

Two basic parameters for understanding H retention are the hydrogen diffusivity and solubility. Studies of solubility and diffusivity are reviewed in Refs [432, 433]. Figures 28 [407, 417, 434, 435] and 29 [407, 435–437] show experimental values for hydrogen solubility and diffusivity in W and Be. For Be there are significant differences between results from various studies. These differences may be due to effects of traps and surface oxide layers. The presence of bulk traps tends to increase the measured values of solubility and to decrease the measured values of diffusivity as was discussed above (Eqs (15) and (16)), especially under conditions where the concentration of hydrogen in solution is smaller than the concentration of traps. For this reason, studies done on materials of higher purity and crystalline perfection, and at higher temperatures and with higher concentrations of hydrogen in solution, tend to give more reliable results. The porosity and oxide inclusions present in beryllium produced by powder metallurgy are also likely to lead to inconsistent results in measurements of hydrogen solubility and diffusivity. The values of solubility and diffusivity reported for W [407] exclude effects of traps. In the Be experiments, the effects of traps were not characterized and may be dominant. One firm conclusion is that the solubility of hydrogen is very low in both Be and W.

Many studies have been done of the retention and emission of H implanted into materials to provide data needed to predict H retention in fusion reactor environments. Figure 30 shows the retention of 1 keV deuterium implanted into Be at 300 K versus incident fluence, measured by thermal desorption [438]. D retention in Be was close to 100% at low fluences but saturated at high fluences. Earlier

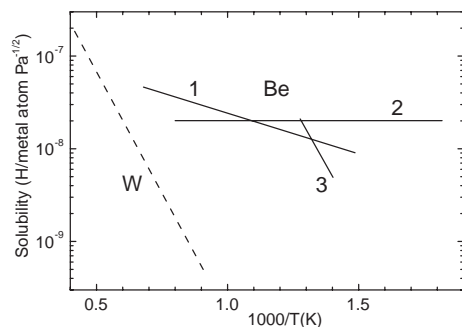


**Figure 28.** Measured solubility of hydrogen in tungsten (dashed line [407]) and beryllium (solid lines 1 [417], 2 [434] and 3 [435]).

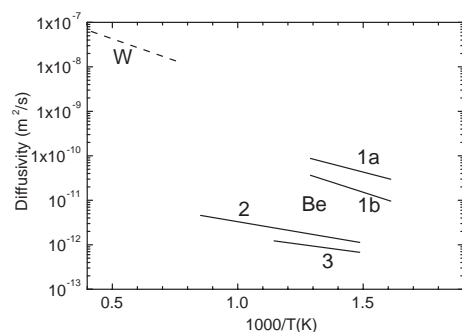


**Figure 29.** Measured diffusivity of hydrogen in tungsten (dashed line [407]) and beryllium (solid lines 1a&b [436], 2 [434] and 3 [437]).

nuclear reaction analysis (NRA) measurements of D retained in Be within  $\approx 1 \mu\text{m}$  of the surface gave very similar results [439]. This saturation behaviour indicates that D implanted into Be at 300 K does not diffuse, but accumulates to a saturation concentration of  $\approx 0.3$  to  $0.4$  D/Be within the implantation zone. At high fluences the implanted zone becomes porous allowing additional implanted D to escape. This saturation mechanism is confirmed by electron microscopy, which shows bubbles and porosity in the implantation zone after high fluence H implantation [421]. Saturation of retention by the same mechanism is observed for D implanted into stainless steel at 150 K where the D is not mobile [422]. H retention in Be increases with increasing ion energy and decreases with increasing sample temperature [431, 440]. The retention of 1 keV deuterium implanted into W at 300 K (shown in Fig. 30) also saturates at high fluence. At high fluences deuterium retention in W is higher at 500 K than at 300 K [441]. Comparison between total retention measured by thermal desorption spectroscopy (TDS) and near surface retention measured by NRA indicates that in W much of

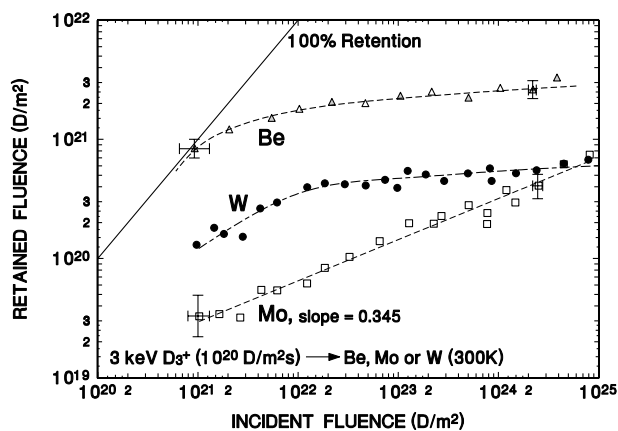


**Figure 30.** Retention of 1 keV deuterium implanted into Be and W, at 300 K versus incident fluence, measured by thermal desorption. (Reproduced with permission from Ref. [438].)

the D is retained beyond the range of implantation [430, 442]. Retention of H implanted in W is due to trapping at defects and precipitation into bubbles.

Figure 31 shows retention of deuterium and tritium as a function of incident particle fluence from a set of high fluence experiments in which Be specimens were exposed to laboratory ion beams (INEEL, UTIAS), linear plasma devices (SNL/LANL-TPE, UCSD-PISCES-B), a tokamak divertor plasma (DIII-D-DiMES), and a neutral beam (NB-JET). In some of these studies carbon deposition or formation of carbide or oxide surface layers occurred, which is likely to affect D retention. The figure shows the D retention in Be observed under a wide range of exposure conditions. The high fluence saturated retention tends to be lower at higher temperatures.

Fusion neutrons will create vacancies and interstitials in plasma facing materials. For metals at reactor wall temperatures, these defects will be mobile and will annihilate at sinks (e.g. surfaces or grain boundaries), recombine, or agglomerate into defect clusters. Vacancy agglomeration may also lead to the formation of voids. In beryllium, neutron induced nuclear reactions produce helium and tritium (Section 5.6.1), which may be trapped at defects or precipitate as gas bubbles. These defects, resulting from neutron irradiation, will increase the retention of hydrogen from the plasma, by increasing the concentration of sites where diffusing hydrogen can precipitate as gas or become trapped as atoms. The effect of neutron irradiation on hydrogen retention in metals is complex, but, in principle, this can be modelled by the formal-

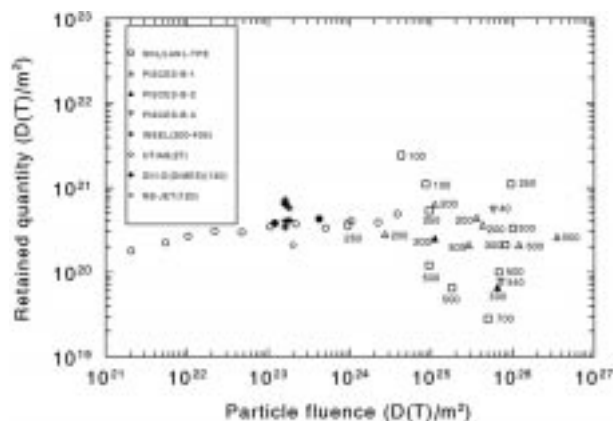


**Figure 31.** Retention of deuterium and tritium in Be as a function of incident particle fluence [431]. For purposes of comparing results from different experiments using different ion energies, the data have been scaled to correspond to an equivalent 100 eV deuterium ion energy. Numerical values next to the symbols and in the legend are specimen exposure temperatures, in degrees Celsius. (Reproduced with permission from Ref. [431].)

ism described above, provided the material parameters are known, such as hydrogen diffusivity, solubility, trap binding energy and defect microstructure produced by the neutron irradiation. For many metals, most of these parameters are known well enough to attempt such modelling. For beryllium, however, uncertainties in solubility, diffusivity and trapping of hydrogen make such modelling of hydrogen retention difficult.

Tungsten might be especially susceptible to hydrogen retention at lattice defects due to neutron irradiation. However, there have been few experimental studies of this because of the intense radioactivation of tungsten upon neutron exposure. The activation energy for diffusion of H in W is low enough (0.39 eV [407]) for H to diffuse to the defects at temperatures where the defects themselves are immobile [443]. Furthermore, because of its low solubility in W, diffusing H will precipitate or be strongly trapped if it encounters open volume defects (see Tables 8 and 9 and Fig. 26). Retention of H at lattice damage in W will depend strongly on the temperatures of neutron irradiation and H exposure. H retention in W should decrease at temperatures above  $\approx 600$  K, where H is thermally released from vacancies and vacancies become mobile [443].

The rate at which tritium is scattered by collisions with neutrons is by far too small to affect permeation. The scattering rate is the product of the cross-section and the neutron flux. The total cross-

section for scattering of energetic neutrons by tritium or deuterium is less than  $3 \times 10^{-28} \text{ m}^2$  [444, 445]. The flux of fast neutrons in ITER is predicted to be less than  $10^{18} \text{ m}^{-2} \cdot \text{s}^{-1}$  (Table 7). The scattering rate is therefore less than  $3 \times 10^{-10} \text{ s}^{-1}$ . The tritium will decay to helium before it is scattered even once by a collision with a neutron.

### 3.5.3. Hydrogen retention in carbon

Carbon differs from metals in the behaviour of implanted hydrogen, mainly because of the C–H chemical reactivity. Implantation of hydrogen into carbon creates broken carbon bonds where hydrogen can be strongly bound through the formation of C–H chemical bonds. At low doses, hydrogen implanted into carbon is nearly all retained near the end of its implantation range. As the dose increases, the local hydrogen concentration increases until it reaches a saturation value that is about 0.4–0.5 H/C for carbon at room temperature and for incident H energy more than a few tens of eV. The saturation level decreases with increasing temperature [446, 447]. Additional hydrogen, implanted into a region already saturated, will either be released or transported further into the bulk via ‘surface diffusion’ of H atoms along internal porosity [448] as illustrated in Fig. 32 [207]. Figure 33 shows an example of the saturation behaviour in the implantation zone [449]. The areal density of implanted hydrogen retained in the carbon therefore depends on the dose and energy as shown in Figs 34 and 35, as observed by NRA and TDS measurements, respectively [449–451]. At low doses, the non-reflected hydrogen is all retained. At high doses, the H retention saturates at a value determined by the saturation concentration and the thickness of the saturated layer and, therefore, by the incident energy of the hydrogen.

Saturation of hydrogen retention also occurs in other materials which form strong covalent bonds with hydrogen, for example boron and silicon [452]. Similar saturation of hydrogen retention is also observed in metals at low temperatures where the implanted hydrogen cannot diffuse [422, 423]. Retention of hydrogen isotopes from tokamak plasmas implanted into carbon components typically saturates at coverages near  $10^{21} \text{ atoms} \cdot \text{m}^{-2}$ .

#### 3.5.3.1. Bulk transport of hydrogen in carbon

The issues of bulk trapping of hydrogen and permeation of hydrogen into graphite beyond the range of implantation have also been examined. The

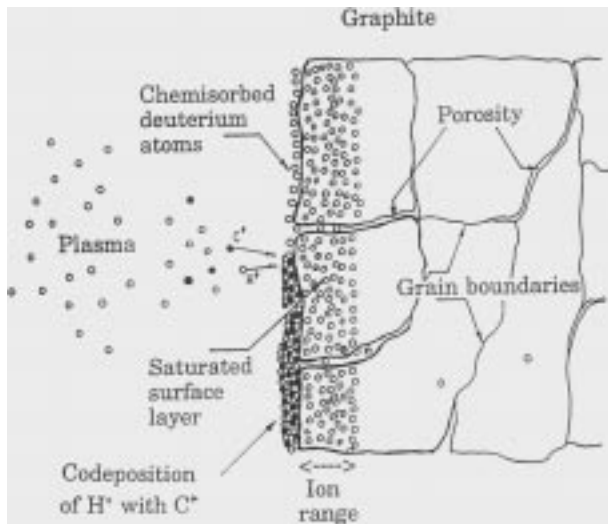


**Figure 32.** Illustration of hydrogen retention and transport in graphite. (Reproduced with permission from Ref. [207].)

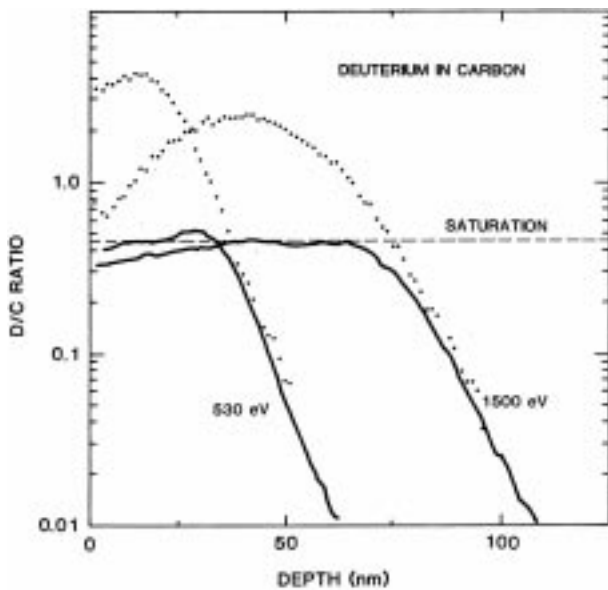


**Figure 33.** Depth profiles measured by secondary ion mass spectroscopy (SIMS) of deuterium implanted at 530 and 1500 eV into carbon at room temperature at fluences of  $10^{22} \text{ D}\cdot\text{m}^{-2}$  (solid lines) and  $10^{20} \text{ D}\cdot\text{m}^{-2}$  (dotted curves). For comparison, the low dose curves are scaled up by a factor of 100. (Reproduced with permission from Ref. [449].)

permeation depends strongly on the microstructure of the graphite [207, 453–455] (Fig. 35). In high density monocrystal graphite, there is essentially no permeation of hydrogen beyond the implantation zone, and the fluence dependence of H retention is essentially flat once the implantation zone

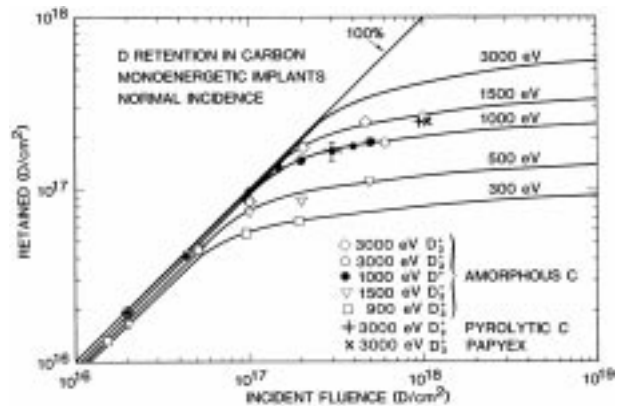


**Figure 34.** Areal density of implanted deuterium retained in carbon versus incident fluence for different energies, measured by NRA (symbols) and calculated (curves) using implantation profiles and a saturation concentration of  $\text{D}/\text{C} = 0.44$ . (Reproduced with permission from Ref. [449].)

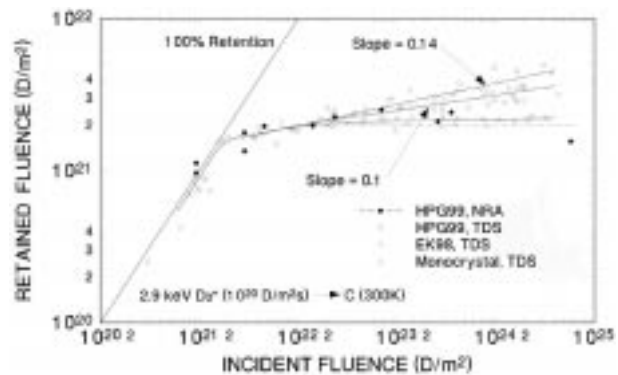


**Figure 35.** Retention of deuterium implanted in various types of graphite versus incident fluence. (Reproduced with permission from Ref. [451].)

is saturated [207, 455]. In high density pyrolytic graphite, some increase in H retention with increasing incident fluence beyond the saturation fluence is observed, which indicates hydrogen transport further into the bulk [207, 453, 455]. As the graphite density decreases and porosity increases, bulk trapping increases [207, 453, 455, 456] (see, for example, EK98 in Fig. 35). Long range diffusion — beyond the implantation zone — due to bulk concentration gradients is unlikely to occur in porous graphites such as EK98 [455] and POCO AXF-5Q [453], because the H will encounter microporosity or crystallite boundaries where it will exit the graphite lattice before it can diffuse very far. The observed uptake of hydrogen into porous nuclear graphites from low energy plasmas, can be accounted for by thermally activated

atomic diffusion along internal surfaces of pores and grains within the material, which gives retained concentrations on the order of 10 appm [453, 456] and may extend several millimetres into the material [457].

Some studies conclude that short range atomic diffusion of hydrogen through the graphite lattice occurs at high temperatures ( $>1270$  K) mainly along the basal planes [453, 458]. Recent measurements of CFC tiles from the JET divertor showed surprisingly large fractions of tritium in the bulk [459].

### 3.5.3.2. Trapping of hydrogen in carbon

In a reactor, fusion neutrons will cause atomic displacements in graphite, which may create traps for tritium. Trapping of hydrogen at lattice defects in graphite was therefore investigated in a series of experiments in which graphite was first irradiated with carbon ions to create traps, and then exposed to deuterium gas at 1470 K to load the traps with deuterium [454, 460–463]. Irradiation produced strong traps, with binding energies consistent with C–H bond formation ( $\approx 4.5$  eV), and whose concentration saturated at about 1000 appm at damage levels above about 1 displacement per carbon atom (dpa). For comparison, the concentration of strong traps in graphites as manufactured, i.e. before ion irradiation, was typically in the range from 10 to 20 appm. An H451 graphite sample damaged by neutron irradiation had about the same D retention as graphite damaged by carbon ion irradiation, demonstrating that lattice damage by ion or neutron irradiation has similar effects on H trapping. Irradiation of graphite by fusion neutrons can thus be expected to produce strong traps that bind hydrogen even at high temperatures. However, the quantity of H retained in such traps in a fusion reactor will depend on whether the H is able to reach the traps. In general, more H will be trapped in graphites in which open porosity provides easier access of H to traps. Furthermore, for H to reach traps within the graphite lattice, it must diffuse into the graphite grains which can only occur at high temperatures ( $>1270$  K).

### 3.5.3.3. Thermal release of hydrogen from carbon

The concentration at which H retention saturates decreases when the carbon is at higher temperatures during the implantation [207, 446, 464] as shown in Fig. 36. This figure also shows the thermal

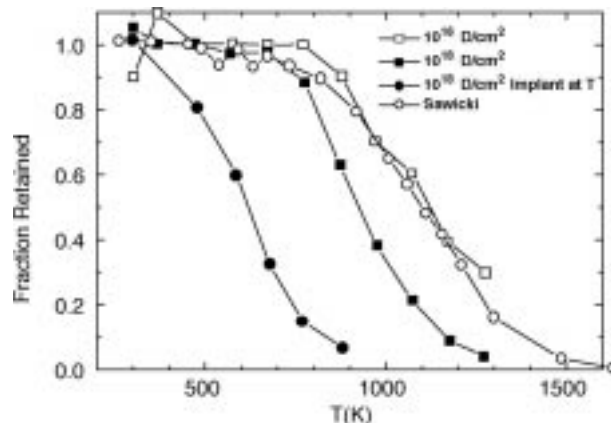


**Figure 36.** Relative D retention in carbon versus temperature measured by NRA [446]. Squares show D retained after implantation at room temperature to doses of  $10^{20}$  D·m $^{-2}$  (open) and  $10^{22}$  D·m $^{-2}$ ·s $^{-1}$  (filled) followed by five minute anneals at each temperature. The dots show relative retention of D implanted to saturation at the indicated temperature. The open circles show release of implanted tritium during isochronal annealing reported by Sawicki et al. [465]. (Reproduced with permission from Ref. [446].)

release, due to isochronal annealing (see glossary), of deuterium implanted into carbon at room temperature [446, 465]. H implanted in graphite is thermally released at temperatures above about 800 K in form of molecules. At wall temperatures above 1300 K the hydrogen is released mainly in the form of atoms [466]. The temperature at which hydrogen is thermally released from carbon films deposited by plasmas may be lower, depending on the incident ion energy during deposition. For low energy deposition (ion energy less than tens of eV) the films contain more hydrogen and the hydrogen is thermally released at lower temperature, compared to films deposited with ion energies of a few hundred eV or more [467] (Section 3.2.6.4). Measurements of D retention by NRA and by TDS show similar deuterium retention levels at low fluences (Fig. 36) on temperature of implantation [207], confirming that the fraction of D retained beyond the range of the NRA analysis ( $\approx 1$   $\mu$ m) is small for the fluences shown in the Fig. 36. This is consistent with localized D retention in the implanted region as shown in Fig. 33. For fluences  $>10^{22}$  D·m $^{-2}$ , TDS measurements may be higher than the NRA integrated measurement in the near surface (Fig. 35), depending on the type of graphite.

#### 3.5.3.4. *Isotope exchange of hydrogen in carbon*

Experiments have shown that one isotope of hydrogen implanted to saturation into carbon can be displaced by subsequent implantation with another isotope [446, 452, 468, 469]. The implanted hydrogen competes locally with other hydrogen atoms already present for the limited sites. In saturation, the total incoming and outgoing fluxes are equal, but the isotopic mixture of the outflux is determined by the hydrogen isotopic composition of the saturated layer, not by that of the influx. This isotope exchange has been modelled by local mixing [452] or local recombination [456, 464] models. In tokamaks with large areas of carbon facing the plasma, this isotope exchange process strongly affects the plasma composition when the injected isotope is abruptly switched, for example from deuterium to tritium. Initially, tritium injected into the plasma is implanted into deuterium saturated carbon surfaces, where it exchanges with deuterium, which flows back into the plasma. Since the inventory of deuterium in the wall is much larger than the amount in the plasma, it takes many discharges for the plasma to become mainly tritium (Section 5.5). Similarly, tritium in saturated layers on plasma facing surfaces may be replaced with deuterium by deuterium fuelled plasma operation.

#### 3.5.3.5. *Ion induced release of hydrogen from carbon*

Energetic particle bombardment also causes release of hydrogen from carbon by processes other than isotope exchange (Sections 4.6.3 and 5.5 for discussion on wall recycling). Carbon implanted to saturation with hydrogen releases hydrogen when bombarded by non-hydrogenic ions such as helium or carbon, even when the ions are sufficiently energetic to pass through the saturated layer [456, 470–472]. The fundamental mechanisms involved in ion induced release are not well understood, but the process can be modelled by a transport equation with a fixed concentration of traps. The model includes terms for trapping, thermal detrapping and an ion induced detrapping rate that depends on the energy deposited into atomic collisions by the bombarding particles. This release process appears to occur via local (i.e. internal) molecular recombination followed by rapid escape of the molecules, possibly via interconnected microporosity [456, 464, 471, 473, 474]. In metals at temperatures where H can diffuse through the lattice, ion induced release of H by internal recombination is unlikely since molecular recombination would only occur at the external surface. In

the metal case, however, ion induced desorption of H adsorbed on the surface might occur, through a process closely related to sputtering.

Helium discharge conditioning or high power low density helium fuelled plasmas remove hydrogen from tokamak walls by ion induced release [472]. After such conditioning, the hydrogen content of the wall is below saturation, and the wall has the capacity to retain or pump incident energetic hydrogen until it becomes again saturated. Retention of charge exchange neutrals over large areas by this mechanism reduces the neutral density at the plasma edge. The wall pumping capacity can be large and persist for many shots since moderate particle fluxes over large areas are involved.

#### 3.5.3.6. *Co-deposition*

In a tokamak, physical and chemical sputtering will produce an outgoing flux of carbon atoms and C/H containing molecules/radicals from carbon plasma facing surfaces. In general, there will also be an incoming flux of carbon atoms. If the outgoing exceeds the incoming carbon flux, the surface will undergo net erosion. In tokamaks, the flux of energetic hydrogen onto such surfaces is usually high enough for the surface to remain saturated with hydrogen as it erodes. In this case, the hydrogen coverage remains constant. However, if the outgoing carbon flux is less than the incoming flux, net deposition of carbon occurs. The deposited carbon becomes part of the hydrogen saturated layer, which now increases in thickness with time. This leads to a hydrogen coverage, which increases linearly with exposure time. This process, often referred to as ‘co-deposition’, is the dominant process for long term retention of hydrogen isotopes in tokamaks with carbon PFCs (Sections 4.7 and 5.6). The H content of the co-deposited material depends on the energy of the incident particles and on the substrate temperature during the deposition. Near room temperature hard films with  $H/C \approx 0.4$  form if the incident particle energy is high ( $\geq 100$  eV) that are similar to carbon implanted to saturation by energetic H. Deposition from low temperature plasmas where the incident particle energies are low ( $\ll 100$  eV) gives softer low density polymer like films with higher H content  $H/C \approx 0.8$ –1 [467]. In tokamaks, such low density films may be deposited from low temperature detached plasmas in the divertor. Compared to the hard films, the soft films are less stable and decompose at lower temperatures and under ener-

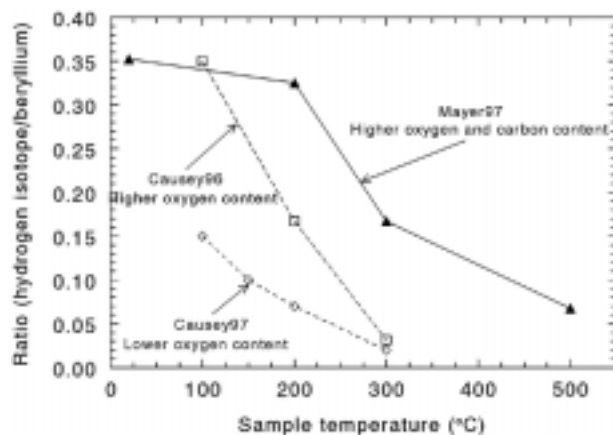


**Figure 37.** Comparison of hydrogen isotope retention in beryllium films produced by collecting sputtered Be from plasma and ion beam exposed Be targets. Data correspond to experiments with the TPE simulator (Causey [476]), and experiments with an ion beam (Mayer [477]). (Reproduced with permission from Ref. [431].)

getic particle bombardment [475]. A key difference between hydrogen retention by implantation and co-deposition is the thickness of the hydrogen containing layer, which is unlimited for co-deposition but is limited to the ion range (tens of nanometres, depending on the ion energy) for implantation.

Co-deposition of hydrogen with redeposited metal atoms has also been examined. Figure 37 shows deuterium retained in redeposited beryllium films, produced by collecting sputtered Be from plasma and ion beam exposed Be targets [476, 477]. The collecting surfaces were exposed to energetic deuterium at fluxes sufficient to saturate D retention in the deposited material. D concentrations were measured using NRA, and impurity concentrations were measured using proton backscattering analyses. In Be with low oxygen content, the retained D concentration is much lower than in co-deposited carbon films. However, in Be with higher oxygen and carbon content, the concentration of retained D is relatively higher and approaches that of carbon.

## 4. Existing experimental database on plasma–material interactions in tokamaks

### 4.1. Introduction

This section is devoted to reviewing the rich experience of PMIs gained in present and past tokamaks and other devices. The section starts with a brief

survey of the diagnostic tools (Section 4.2) used to provide data on PMIs. Erosion of the wall material due to plasma flux, arcing and disruptions is the primary driver for PFC lifetime and for the influx of impurities into the plasma; it will be the subject of the following three sections. Recycling of hydrogen isotopes between the plasma and the wall has a major influence on the plasma behaviour and is reviewed in Section 4.6. Co-deposition of hydrogen isotopes with eroded carbon, tritium retention and removal issues are the subjects of Section 4.7. Flaking of co-deposited layers and dust generation issues are discussed in Section 4.8.

### 4.2. Measurements of plasma–material interactions

Boundary plasma diagnostics are highly developed and have been reviewed in numerous books and articles (e.g. Refs [478–480]). However, diagnostics to characterize the surface of PFCs during a discharge have not received the same attention by the plasma physics community, in spite of the powerful effect the wall conditions have on plasma performance [481].

Diagnosing the full range of PMIs in tokamaks presents a formidable challenge. The physical processes under examination cover several orders of magnitude in time (e.g.  $10^{-4}$ – $10^{-3}$  s for an ELM, to  $>10^8$  s of exposure in an operating reactor) and scale length ( $10^{-10}$  m per monolayer, to  $10^{-2}$  m thick target plates). This range has provided a clear division in current tokamak PMI studies between instantaneous interactions (e.g. sputtering) and long term effects (e.g. net erosion of target plates). From the point of view of the plasma physicist, the instantaneous effects are of greatest interest since they determine the local and global plasma performance via impurity radiation losses and core fuel dilution. Conversely, the engineer's primary interest is the macroscopic viability of the PFCs against net erosion or neutron damage. There has been greater focus on in situ instantaneous measurements since these yield the most vital information for current operating tokamaks. However, any substantial advances by tokamaks toward power production will necessitate the inclusion and integration of both fields of study.

The two most common methods to assess instantaneous PMIs are optical emission spectroscopy and mass spectroscopy. Optical emission spectroscopy involves measurement of neutral and low ionization states of atoms and molecules entering the plasma after being sputtered from the wall. This has the



benefit of being a remote, non-intrusive method that only needs a line-of-sight to the area of interest. It also provides unambiguous discrimination between atomic and/or molecular species. At its simplest, it provides a relative measure of particle loss from the surface. By including the particulars of the atomic physics (ionization, excitation, etc.), it can provide in situ impurity densities or efflux from surfaces; [482, 483] and an evaluation of sputtering yield when combined with simultaneous measurements of incident flux. CD molecular band emission is related to hydrocarbon efflux from surfaces; however, uncertainties over photon efficiencies of CD band emission as a function of plasma density and temperature have hampered efforts to obtain unambiguous data (Section 3.2.3) [304, 484, 485]. Spectroscopy is also used to assess the core plasma's impurity contamination [486].

Mass spectroscopy is universally used to assess vacuum wall 'conditioning' (i.e. hydrogenic wall loading, leak rates, etc.), but is usually accomplished 'off-line' (without plasma or during low density discharge cleaning). Sniffer probes [487] provide localized mass spectroscopy at limiting surfaces and have been used to measure the instantaneous chemical erosion yield (Fig. 38), while recently developed Penning gauge spectroscopy allows real-time monitoring of tritium release from the walls [488].

Almost all PMI measurements need simultaneous high quality edge plasma diagnosis in order to obtain reliable, quantitative results. This is indeed the greatest limitation to PMI studies since, unlike the toroidally and poloidally symmetric core plasma, the edge plasma conditions vary considerably poloidally (and even toroidally). Few quantitative data are available from experiments for the species composition and energy distribution of the particle flux impacting on surfaces [489], despite the existence of suitable instruments for some time (e.g. Refs [490, 491, 481]). Measurements of the total flux by Langmuir probes are open to interpretative difficulties because of the lack of knowledge of the average charge state of the impacting ions. The assumptions on the edge plasma (uniformity, quiescence, etc.) that are used to simplify interpretation are often too restrictive. For example, the transient effects of ELMs are usually ignored although ELMs may represent a substantial portion of the heat flux incident at the wall (Section 2.3.2.3). Rapid events, such as ELMs, and short plasma scale lengths at regions of intense PMI (e.g.  $\approx 1\text{--}5$  cm at the divertor strike points) further complicate complete diagnosis

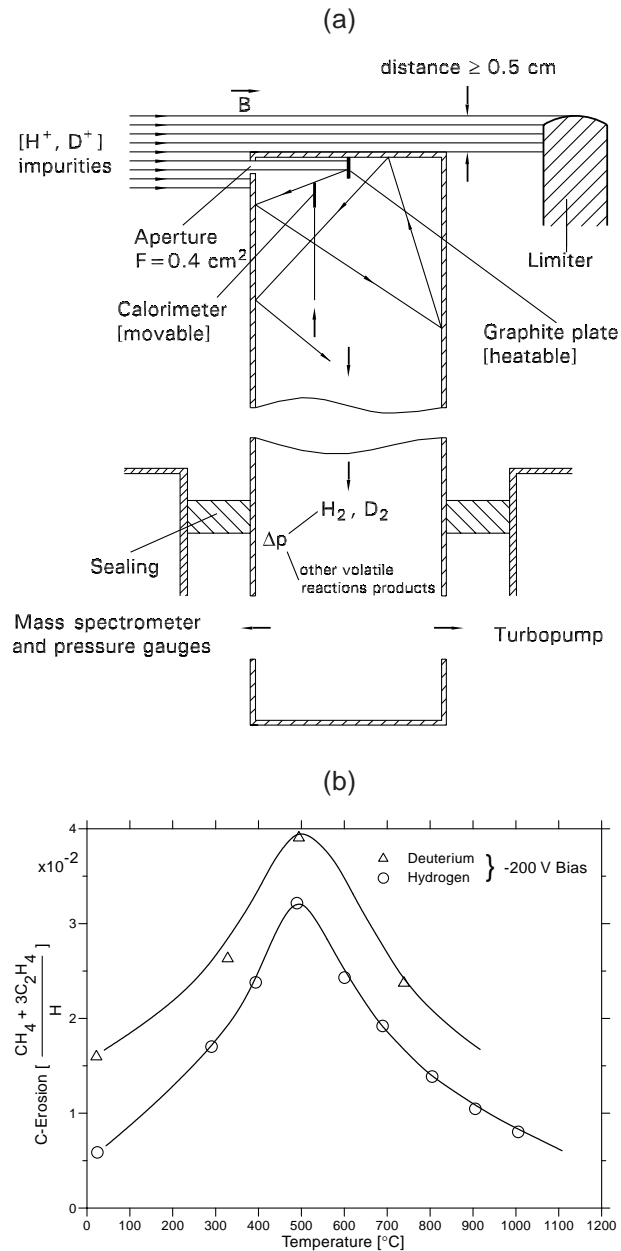


**Figure 38.** (a) Schematic of sniffer probe used on TEXTOR; (b) measured chemical erosion yield in TEXTOR for deuterium and hydrogen versus sample temperature. (Reproduced with permission from Ref. [487].)

by the standard edge measurements, such as Langmuir probes [492]. Also, the experimental nature of present tokamaks leads to large variations in plasma shape, power density and heating scenarios, while little experimental time is dedicated to PMIs exclusively. Hence, data from PMI diagnostics, such as an element's atomic line intensity or partial pressure, are usually interpreted with little knowledge of the specific plasma-wall conditions that caused them.

This qualitative interpretation of PMI data has led to each tokamak dealing with their PMI issues in an anecdotal fashion, increasing the difficulty of extracting a consistent physical picture of PMI from the collection of tokamak experiments. Ironically, many of the dramatic improvements of tokamak performance are linked to improvements in PFC conditioning (e.g. H mode, VH mode, supershots; see Sections 1.2.3 and 4.6). This clearly points out the need for dedicated PMI studies in existing tokamaks (Section 6.4.1).

The most common method of measuring net PMI changes in current tokamaks is an *archaeological* one. A material component is inserted at the wall and removed for study at the next vacuum break, which is typically several months of calendar time and hours of plasma exposure (e.g. Refs [493–496]). Sophisticated surface analysis tools are brought to bear, and detailed and important information on the composition and physical structure of the components is gained. However, the wide variety of conditions experienced during a typical campaign makes it difficult to link such archaeological data to plasma performance. As with the instantaneous PMI measurements, this technique suffers greatly from a lack of experimental control and plasma diagnosis. This makes direct extrapolation of archaeology results (e.g. tritium retention, erosion rates) to reactor class tokamaks very doubtful.

Remote manipulation systems for material samples have been used to obtain better controlled net PMI data in both limiter (TEXTOR [497]) and divertor plasmas (JET [498], DIII-D [110, 499], ASDEX-Upgrade [500]). These usually involve controlled exposures to well diagnosed plasmas for short durations. Exposed materials are designed such that post-exposure analysis provides details about small net changes to the material (e.g. depth markers can provide  $<1$  nm resolution).

Both archaeological and retractable samples rely heavily on ex situ ion beam analysis techniques to measure the net changes in the surface properties. For example, Rutherford backscattering spectroscopy (RBS) of implanted depth markers can provide  $<10$  nm resolution for net changes in sample thickness and  $<1$  monolayer sensitivity of high Z deposited elements [501]. NRA can measure the near surface ( $<10$   $\mu\text{m}$ ) quantity of co-deposited hydrogenic fuel species. There are two principal limitations for the use of retractable probes. The first is the limited geometric access and coverage available for the probes. The second is the very temporary nature of the sample materials in the vessel (which in some

sense, provides the temporal resolution) means that they do not exactly reflect the material properties of intrinsic wall components. This is especially important in a device with multispecies PFCs, such as in the ITER design, where the surface composition can be substantially altered by material mixing.

Measurements of erosion and deposition are nevertheless becoming more sophisticated. Several optical techniques, offering the promise of remote, real time monitoring of net erosion/redeposition, have recently been developed (see Table 10; colorimetry, ellipsometry, speckle interferometry). However, colorimetry and ellipsometry are limited to measuring small net changes ( $<1$   $\mu\text{m}$ ) and depend on the optical properties of the eroding/depositing material, making interpretation of multispecies components difficult.

In situ diagnosis for the quantity of co-deposited/trapped hydrogenic species in wall components is complicated by the need to invoke the release of the trapped gas from the material. This involves some bulk or surface heating of the material, making the techniques complicated mechanically.

Of all PMI diagnostic techniques listed in Table 10 [110, 111, 113, 204, 356, 358, 481–483, 487, 493, 499, 500, 503–536], only emission spectroscopy and infrared thermography are universally used in existing tokamaks. Most tokamaks contain a small subset, or have only temporarily installed, these ‘dedicated’ diagnostics. This situation has necessarily hindered the maturation of PMI diagnostic techniques. Embedded thermocouples, although used for decades in tokamaks, have recently been used to provide measurements of incident power flux in regions of co-deposition [502], overcoming problems associated with IR thermography in these areas and helping to determine the power split between ion and electron channels (as derived from target probes). Solid state microsensors have been used [490, 491] to determine the fluence and energy distribution of the hydrogenic particle flux to surfaces but further improvements, such as measurements of the species composition of the impacting flux, will require development of new diagnostics.

Remote sensing of net PMI changes holds perhaps the greatest promise for future devices, but these have been rarely implemented in tokamaks as ‘routine’ diagnostics [481]. Optical methods of assessing the net change of PFCs in situ could in principle be used for real-time assessment of net erosion/redeposition. Also included in this category are remote electronic devices such as the quartz electronic deposition monitor that can assess the net gain

**Table 10.** Summary of tokamak PMI diagnostic (symbols: t is the time resolution or cw (continuous operation). Scale: \* signifies spatial resolution, otherwise depth resolution).

Diagnostic	Technique	t (s)	Scale (m)	Advantages	Limitations
<b>Instantaneous measurements</b>					
Sputtering rate and/or yield	Emission spectroscopy of atoms/molecules released into plasma [482, 483, 503]	$>10^{-3}$	$* >10^{-2}$	Optical access Element discrimination	Depends on plasma parameters/uniformity & atomic rates
	Sniffer probe molecular spectroscopy [487, 504, 505]	†	$*10^{-3}$	Element discrimination	Access for probe
	Laser induced fluorescence of sputtered atoms [506–509]	0.1–1	$*10^{-3}$	Spatial resolution Known excitation rates	Laser access Choice of transitions
Power loading	Infrared thermography [510, 511]	$>10^{-4}$	$*10^{-2}$	Optical access Toroidal/poloidal resolution	Depends on material emissivity and heat conduction
	Thermocouples [512, 513]	$>10^{-2}$	—	Material independent	Spatial resolution Time response
Arcing	Arc photography [356, 514, 515]	$>10^{-4}$	$* >10^{-3}$	Arc movement	No arc quantification
	Electrical probes [516, 517]	$10^{-6}$	$* \sim 10^{-2}$	Measures arc current Time resolution	Probe access
Fuel wall loading	Mass spectroscopy and particle balance [505]	$>1$	—	Ease of implementation	No spatial resolution Sensitive to first few monolayers
	Penning gauge spectroscopy [518]	0.2	—	Time resolution	
<b>Net measurements</b>					
Net erosion/re-deposition rate	Retracting sample probes [110, 499, 500]	$>10$	$>10^{-9}$	Controlled short duration exposure to plasma	Probe access Needs nm resolution for depth marking
	PFC height change and sticking probes [481, 493, 499]	$>10^3$	$>10^{-6}$	Direct measurement	Access limited to vacuum breaks No exposure control
	Material coupons [113, 520]	$>10^3$	$>10^{-9}$	Material selection	Access limited to vacuum breaks No exposure control
	Speckle interferometry [521–523]	cw	$>10^{-6}$	Remote access	Laser and optical access Never implemented
	Ellipsometry [524, 525]	cw	$>10^{-9}$	Remote access Very sensitive	Laser access Sensitive to material's optical properties and vibrations
	Colorimetry [111, 526–528]	cw	$10^{-8}$ – $10^{-6}$	Remote access Sensitivity	Depends on material's optical properties Limited to $\sim 1 \mu\text{m}$
	Quartz crystal deposition monitor [529, 530]	cw	$10^{-9}$ – $10^{-7}$	Sensitive to small changes in thickness Remote access	No species discrimination Temperature sensitive Limited range
	Spectroscopy markers [531]	cw	$\sim 10^{-6}$	Remote access	Erosion only Depends on sputtering yield of marker versus E
Fuel (D/T) wall inventory	Thermal desorption spectroscopy [532]	$>10^3$	—	Complete inventory measured	Need $>1270$ K baking for in situ measurement Poor depth resolution
	Laser desorption spectroscopy [533, 534]	$>10$	$<10^{-6}$	Controlled release of D/T	Limited to near surface Laser access
	Gas balance [204, 535]	$>10$	—	“On-line” monitoring	Difference of two large numbers
PFC activation and/or neutron damage	In situ sample exposure and activation measurement [536]	$>10^3$	—	Integrated measurement	Limited neutron fluence No time resolution
Arcing	Profilometry [358]	$>10^3$	$\sim 10^{-6}$	Shows net effects	Needs vacuum break

† determined by vacuum time constant

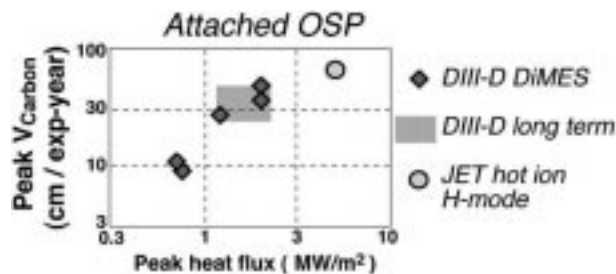


**Figure 39.** Summary of peak net carbon erosion rates  $V_{\text{carbon}}$  (cm/exposure-year), at the divertor strike point versus strike point heat flux on JET and DIII-D. JET data [111] and DiMES at  $1.5 \text{ MW}\cdot\text{m}^{-2}$  [528] were obtained with colorimetry. All other DiMES data come from depth marked insertable probes [487, 537]. The DIII-D long term results are from net changes in divertor tile height after 9 months of operation [498]. (OSP in the figure means outer strike point). (Reproduced with permission from Ref. [537].)

or loss from a PFC. Quartz crystal microbalances to monitor deposition/erosion in tokamaks were pioneered at TdV [529] and have recently been installed on ASDEX-Upgrade [530]. These devices are capable of measuring the growth of co-deposited films on a shot by shot basis. Several other new diagnostic techniques, providing data complementary to that of microbalances, are also receiving attention at the moment [481]. High power pulsed lasers are being targeted at regions of film growth in JET to desorb and study co-deposited material [534]. Similar laser ablation experiments were done at the ASDEX-Upgrade central column for spectroscopic measurement of erosion and of penetration probabilities [117]. So called ‘sticking probes’ are also being tested on JET and other devices [519]. Although technically a long term sample, this diagnostic has the unique ability to discriminate between the efflux to the wall of different hydrocarbon radicals, providing information on the production, transport and redeposition of hydrocarbon molecules.

Although, in general, much tokamak PMI diagnosis remains qualitative, reliable quantitative results have been obtained when several methods were focused on a single issue of interest to the fusion community. One such example is measurements of the rate of net erosion at the carbon divertor plates near the divertor strike points of DIII-D and JET (Fig. 39) [537]. This was a topic of interest due to the selection of carbon for the divertor plates of ITER. Net erosion of attached ( $T_e > 10 \text{ eV}$ ) plasmas was found to increase with incident heat flux, and good agreement was obtained between the various measurement tech-

niques (colorimetry, insertable probes and archaeological measurements of tile thickness changes). Not only does this result show the possible severity of divertor erosion in a long pulse device, but it also accentuates the need for further collaborative efforts in obtaining high quality PMI diagnostic results in current tokamaks.

The implementation of PMI diagnostics in a next step device faces several challenges due to very difficult access and the harsh radiation environment [13]. New techniques such as laser range finding [538] have been developed to measure sub-millimetre scale erosion. Diagnostics to detect disruption precursors such as locked modes will be important to avoid off-normal events that will reduce the lifetime of PFCs. The cumulative flux of charge exchange neutrals and debris from the plasma will limit the useful lifetime of optical mirrors and windows and innovative solutions will be needed to preserve key diagnostic capabilities such as spectroscopic impurity monitoring. Techniques to measure the dust inventory, particularly in hidden areas, will need to be developed to assure compliance with regulatory limits (Sections 2.3.4 and 4.8). A novel technique is described in Ref. [539]. Another potential technique based on infrared thermography was recently identified in Tore Supra [540]. The infrared spectral emission deviates from black-body behaviour because of the presence of dust and flakes. Dust particles were identified by their spectral emissivity falling off with the square of the wavelength. Flakes were identified by their fast cooldown times. These results offer a potential technique for real time monitoring of dust and flakes.

### 4.3. Review of tokamak erosion/redeposition experience

#### 4.3.1. Divertor erosion/deposition

In ITER type divertor machines the most intense interaction of the plasma will occur at the strike point of the separatrix with the divertor target plate. The plasma power crossing the separatrix in the main plasma vessel will be guided by the magnetic field onto the divertor plate, thus concentrating the power onto an area of about  $10\text{--}20 \text{ m}^2$ , resulting in ion fluxes of up to  $10^{24} \text{ m}^{-2}\cdot\text{s}^{-1}$ . In this section, the tokamak divertor experience will be discussed in terms of various plasma regimes. In particular, we shall consider the dependence of erosion/redeposition on electron temperature and density in the divertor plasma, for cases of a high recycling divertor (see glossary) with  $T_e$  between 10 and 50 eV and for a partially

detached divertor with  $T_e < 10$  eV [154]. Erosion due to vaporization and melting during disruptions and ELMs is discussed in Sections 4.5 and 5.4.

The high recycling divertor, with moderate electron densities and electron temperatures of up to 50 eV, has been investigated in a large number of tokamaks, such as ASDEX, ASDEX-Upgrade, DIII-D, JET, Alcator C-Mod and JT-60U. Owing to the high electron temperatures, the ion energies range above the threshold for physical sputtering for most candidate divertor materials. Chemical erosion for carbon based materials is also high, especially at elevated surface temperatures.

Erosion studies have been performed by using marker erosion experiments in ASDEX-Upgrade [500, 541, 542] and DIII-D [110, 501, 543] to evaluate the most useful divertor materials. The measured erosion rates for materials with different atomic number, are shown in Fig. 40, together with Mo erosion in Alcator C-Mod [113]. In spite of the differences in divertor plasma parameters and the comparison of long term exposure [113, 541, 542], with single discharge erosion [110, 111, 500, 501, 543], the data are in good agreement, showing a strong decrease of the erosion rate with the atomic mass of the target material. The erosion rate decreases by more than an order of magnitude from Be to W, in general agreement with expectations from physical sputtering for light ions in the threshold energy regime (Section 3.2.1). However, melting and evaporation increased the Be erosion rate at high power loads in JET [544]. The large scatter of results for carbon divertor materials can be attributed to different divertor plasma conditions due to different central plasma densities and auxiliary heating power. The net erosion rate for carbon increases with the incident heat flux for the attached plasma conditions of Fig. 39 [500, 537]. At heat fluxes  $> 5 \text{ MW} \cdot \text{m}^{-2}$ , the erosion rates of  $20 \text{ nm} \cdot \text{s}^{-1}$  would correspond to about 1 cm peak erosion after 1000 ITER discharges lasting 400 s each.

A similar scatter of data exists for W erosion but here no correlation with the heat flux is evident. The contribution of H and D ions to W erosion is negligible in the temperature range  $T_e < 50$  eV since the incident energies are at or below the threshold for physical sputtering. In contrast, low Z impurity ions with charge state of 3 and more are accelerated to higher energies in the sheath potential and dominate the sputtering of high Z materials: in Alcator C-Mod, predominantly B after boronization [113]; in the ASDEX-Upgrade W divertor experiment, C from

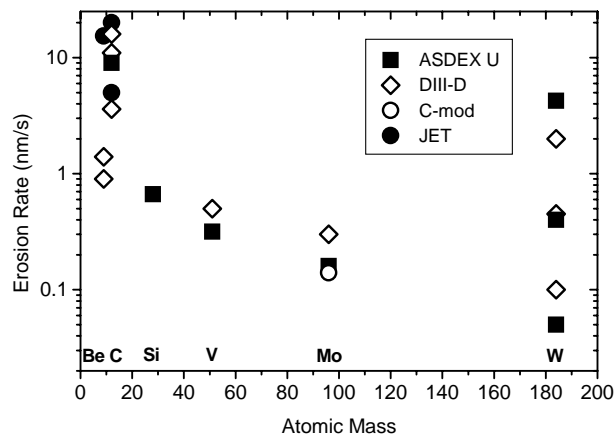


**Figure 40.** Erosion rate of different divertor materials as a function of atomic mass. While most of the data were obtained from marker erosion experiments, Be, C and W have been used as bulk materials in widely differing divertor conditions [110, 113, 500, 501, 541–543].

vessel wall erosion [115]. However, impacting C ions will be implanted into the W surface leading to a gradual decrease of the W sputtering yield until a stationary level is reached where the carbon deposition is balanced by erosion. For a given carbon impurity concentration, this balance is strongly dependent on plasma temperature (Sections 3.2.2 and 3.2.6.2), and below a threshold temperature of the order of 10 eV, there will be net deposition of carbon protecting the W surface from erosion. Fig. 41 shows the measured erosion yield of W in the ASDEX-Upgrade divertor, as a function of divertor electron temperature compared to calculated sputtering yields for  $\text{D}^+$ , 1%  $\text{C}^{4+}$ , and both ion species including C deposition [115]. It can be seen that  $\text{D}^+$  sputtering is negligible, and the erosion rates are well explained by taking the erosion due to 1%  $\text{C}^{4+}$  into account.

This situation is different for low Z divertor materials. The low sputtering threshold and, in the case of carbon, chemical erosion effects lead to a high yield due to deuterium ion impact (Fig. 11) already at divertor temperatures around 10 eV. This high yield is slightly increased, especially at high divertor density and electron temperatures below 10 eV by taking self-sputtering into account for carbon impurity concentrations in the per cent range. Oxygen impurity ions with an effective sputtering yield near unity (Section 3.2.4) contribute according to their concentration in the divertor plasma [545]. Data for eroded C fluxes in ASDEX-Upgrade are included in Fig. 41 as a function of divertor temperature; they agree well with estimates from sputtering calculations [115].

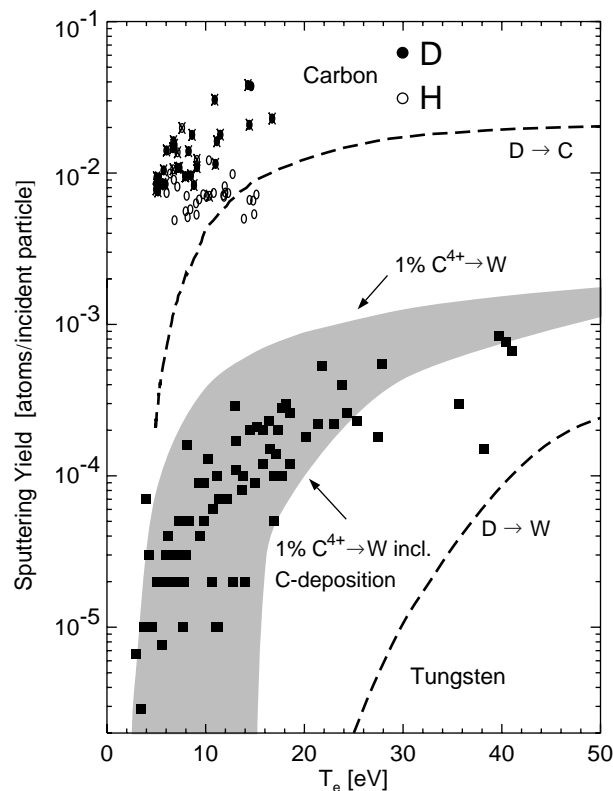


**Figure 41.** Sputtering yield of C and W as divertor materials in ASDEX-Upgrade, as a function of the divertor electron temperature as measured spectroscopically. The data are compared with computer calculations (shown as dashed lines) for physical sputtering. For the case of W, sputtering due to 1%  $C^{4+}$  impurity ions is included. The grey region indicates variations of the sputtering yield due to different degrees of surface coating by carbon deposition [115, 484]. (Figure provided by K. Krieger, IPP Garching.)

The chemical erosion for carbon under divertor conditions is a topic of investigation in most current divertor tokamaks. Although it is often stated that the carbon erosion, as determined from spectroscopically measured  $C^{2+}$  fluxes (see glossary), can be essentially accounted for by physical sputtering [111, 500, 545], the spectroscopic observation of CD bands (see glossary) in all tokamaks indicates the presence of chemical erosion [302, 484, 537, 546]. Also, the increase of carbon plasma impurity content for different surface temperatures, such as observed in JET in going from the Mk-I to the Mk-II divertor, was attributed to the temperature dependence of chemical sputtering [111]. The reason for the large uncertainty [286] in the contribution of chemical erosion of carbon to

the observed erosion rates in tokamaks appears to result from difficulties in decoupling the energy and flux dependences of the chemical erosion yield, as well as uncertainties in the derived hydrogen and hydrocarbon fluxes. Experiments specifically aimed at studying the flux dependence of chemical erosion at high fluxes ( $>10^{21} \text{ D}\cdot\text{m}^{-2}\cdot\text{s}^{-1}$ ) have also been performed in plasma simulators (Section 3.2.3), where the parameters can be controlled independently. In Fig. 42 the dependence of the chemical erosion yield on ion flux obtained from plasma simulator experiments [298, 299, 307] is compared with data from high flux conditions in different tokamaks [300, 304, 484, 487, 547–551], for cases of elevated surface temperatures, near the temperature where chemical erosion is maximum,  $T_{max}$ , and different plasma electron temperatures. In Fig. 42(a) data are collected for incident ion energies between 20 and 50 eV and in Fig. 42(b) for energies between 200 and 300 eV.

The large scatter of the data may be due to a number of causes, including: (i) different ion energies due to different plasma parameters, (ii) experimental uncertainties in the determination of the incident hydrogen and CD fluxes, (iii) uncertainties in translating the CD intensities into  $CD_4$  or  $C_nD_m$  fluxes using the ionization/dissociation sequence [552], (iv) the ionization length, which is determined by the ionization cross-section, (v) the use of different carbon based materials with different surface conditioning, and (vi) different surface contaminations from deposited impurities. In spite of all these uncertainties, the trend in the data for ion fluxes  $>10^{22} \text{ D}\cdot\text{m}^{-2}\cdot\text{s}^{-1}$  indicates a decreasing chemical erosion yield towards an absolute yields at  $T_{max}$  below  $10^{-2}$ . Taking into account that physical sputtering of carbon has a threshold around 30 eV, in low temperature divertor applications the total carbon erosion yield will be controlled by chemical erosion. In view of the above uncertainties, further studies are needed to clearly establish the flux dependence of the chemical erosion at high fluxes (Section 6.1).

Net erosion rates, as shown in Figs 39 and 40, are not only determined by erosion yields as given in Figs 41 and 42 for W and C, but also by the extent of redeposition. Erosion yields multiplied by ion fluxes result in ‘gross erosion rates’, which may be considerably reduced because of the redeposition of the eroded material, leading to the observed ‘net erosion rates’. Sputtered atoms will penetrate into the divertor plasma, become ionized and some will redeposit on the divertor plate together with the plasma flux

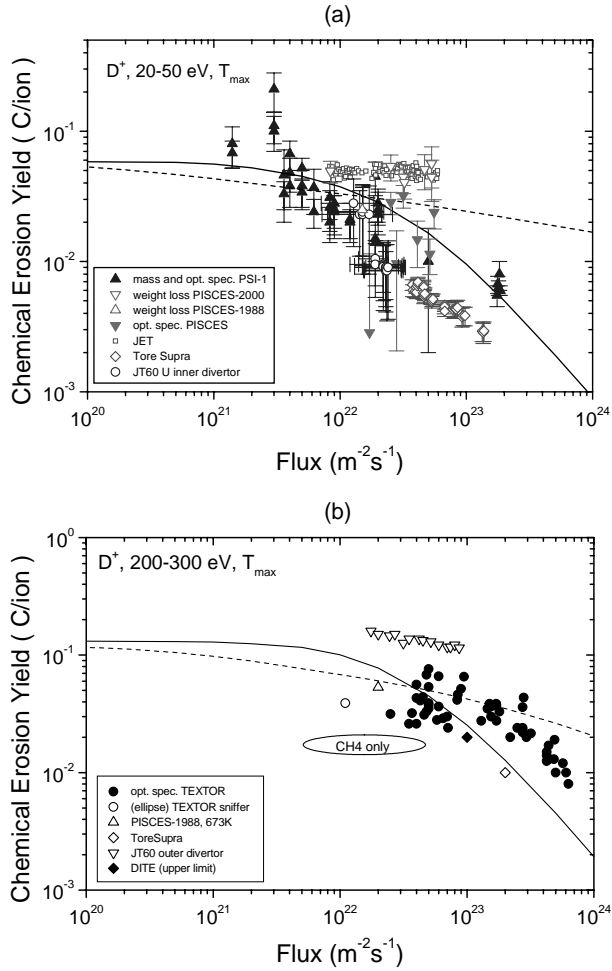


**Figure 42.** Comparison of the flux dependence of the chemical erosion yield of carbon at  $T_{max}$  measured in plasma simulators and in tokamaks for (a) incident ion energy between 20–50 eV [298, 299, 304, 307, 549, 550] and (b) between 200–300 eV [300, 308, 487, 547, 548, 551]. The curves are analytic fits to the data using the analytic model [287] (see also Fig. 16).

(Section 5.3). For cases where the ionization length of sputtered atoms is smaller than, or comparable to the gyroradius of the ions in the local magnetic field, redeposition occurs within the first gyration, and the gross erosion rates are drastically reduced [542]. This is especially true for sputtered atoms of heavier masses since the ionization length is proportional to the velocity and the gyroradius is proportional to the product of velocity and mass. Thus, the ratio of both is a decreasing function of mass. For heavy target materials, such as W, the prompt redeposition within the first gyration is partly responsible for the very small net erosion rates observed, reduc-

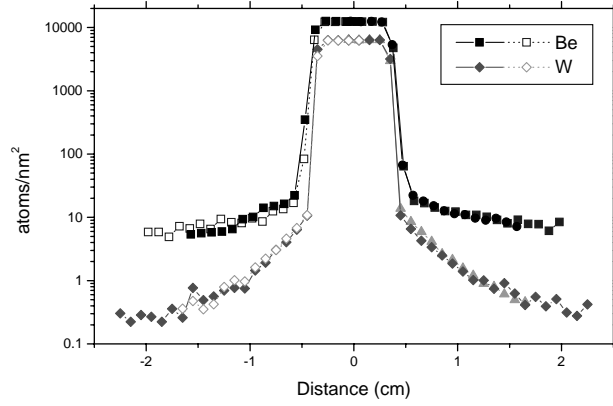


**Figure 43.** Deposition pattern of local redeposition of eroded material from Be and W markers in the DIII-D divertor [501]. Two sets of data are shown for each material at slightly different positions on the same divertor probe. The magnetic field direction is from left to right. (Plasma parameters:  $n_e = 4 \times 10^{19} \text{ m}^{-3}$ ,  $T_e = 70 \text{ eV}$ , power =  $7 \times 10^5 \text{ W} \cdot \text{m}^{-2}$ , ion fluence  $8 \times 10^{22} \text{ m}^{-2}$ ).

ing the gross erosion by factors of up to ten, especially under high density conditions with short ionization lengths [115]. Direct evidence of the prompt redeposition was obtained in marker experiments in ASDEX-Upgrade [541] and DIII-D [110, 501, 543]. The combined action of magnetic field and electrostatic sheath potential leads to a large transport of eroded materials toroidally, in the direction of the magnetic field. In this direction, the decay length of light materials, such as Be and V, was found to be of the order of centimetres, while for W the decay lengths were consistently a factor of three to four shorter. One exception from this general tendency is the light impurity Li, which has a high ionization cross-section at low energy and is likely to be ionized and redeposited more easily than carbon (ionization potential = 11.26 eV) [553]. Figure 43 presents a comparison of the marker redeposition in DIII-D [501] for Be and W, showing clearly the increasing contribution of prompt local redeposition. Modelling of redeposition (including prompt redeposition) gave good agreement with the measured deposition profiles [542, 556].

For the case of carbon based materials, chemical erosion contributes to the gross erosion rates and leads to new channels of redeposition. First, the chemically eroded hydrocarbon molecules [293] are assumed to have kinetic energies only of the order of the temperature of the target plate, and, consequently, very short ionization lengths. Second, within the complex ionization/dissociation chain from CD<sub>4</sub>



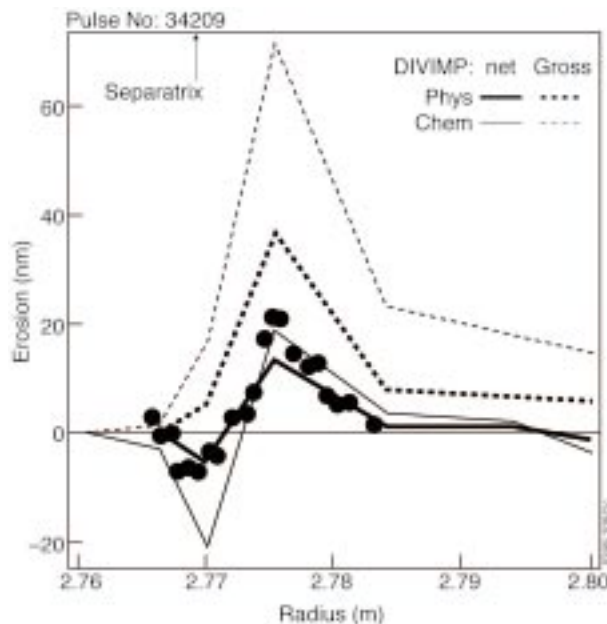


**Figure 44.** Radial distribution of erosion of a deposited carbon layer and redeposition onto the JET divertor plate as measured from colorimetry measurements (solid points) and DIVIMP calculations of net and gross erosion (solid and dashed lines respectively). (Reproduced with permission from Ref. [111].)

to  $C^+$  [552], several neutral radical states occur, especially at low  $T_e$ , and neutral radicals are not confined by the magnetic field. Both effects lead to a relatively efficient local redeposition. A typical example for the comparison of measured net erosion and deposition in the JET Mk-I divertor with calculated gross erosion and redeposition is shown in Fig. 44.

The erosion/redeposition rates at the divertor target have been measured in situ, between two discharges [111, 554], using the method of colorimetry [555] during the JET Mk-I campaign. The erosion rates are strongly dependent on the power deposition on the targets. For an ELMy H mode discharge with 10 MW of neutral beam heating at moderate density, a net erosion of  $\approx 5 \text{ nm}\cdot\text{s}^{-1}$  was measured. At high power, much higher erosion rates have been observed (Fig. 39). For a typical ELM free hot ion H mode discharge with 22 MW heating for a duration of 1 s, the net erosion rate reaches about  $20 \text{ nm}\cdot\text{s}^{-1}$  near the strike point (Fig. 44). The detailed simulations using the DIVIMP/NIMBUS (Section 5.2) codes suggest that the net erosion is predominantly caused by physical sputtering. The codes predict that the gross erosion resulting from chemical sputtering is comparable to that from physical sputtering. However, the chemically produced carbon has lower energy so

that it redeposits promptly back to the target, thus showing little contribution to the net erosion. A very similar conclusion was reached in the modelling of carbon erosion using the DIII-D divertor probe [556].

To reproduce the net erosion rates and the carbon profiles along the JET divertor target, a yield reduction factor of 30–50% had to be used over the low flux chemical sputtering yields [293, 557]. This could be due to the breakup efficiency of hydrocarbons, which is not taken into account in the simulation, or to the flux dependence of chemical yields (Section 3.2.2).

The balance between carbon erosion and redeposition depends strongly on the divertor plasma temperature and geometry. For most of the current divertor experiments, the electron temperature at the inner divertor strike point is lower than at the outer divertor strike point. Frequently, this leads to detachment in the inner divertor and results in deposition at the inner strike point and erosion at the outer strike point. Figure 45 shows a comparison of the D retention due to co-deposition with low Z impurities for different divertor experiments [337]. The long term erosion/redeposition pattern integrated over a whole discharge period is very similar for the DIII-D divertor, the JET Mk-I divertor and the ASDEX-Upgrade Div. I divertor and shows that erosion dominates in the outer divertor. A very similar erosion/deposition pattern has been reported from both JT-60U [558] and Alcator C-Mod [113] with thick deposits of low Z elements at the inner divertor; on Alcator C-Mod macroscopic erosion in the outer divertor was also observed. However, this delicate balance between erosion and redeposition has been altered by the changes in the divertor geometry of the ASDEX-Upgrade divertor. In the new LYRA divertor with vertical targets, the outer divertor is also fully deposition dominated as can be seen from the comparison in Fig. 45 [559]. In this geometry, the outer divertor plasma temperature, averaged over a whole discharge period, has decreased to 7 eV (from 17 eV in the Div. I geometry). For a typical carbon impurity concentration of 1% this decrease in electron temperature leads to a transition from erosion to deposition conditions as was discussed in Section 3.2 (Fig. 20(b)). Similarly, in DIII-D the outer divertor changed from a region with net erosion to net deposition in discharges with partially detached divertor plasmas [537]. In these cases, the whole divertor is deposition dominated, indicating that the erosion dominated areas must lie outside the divertor, most probably at the vessel walls or the protection limiters.



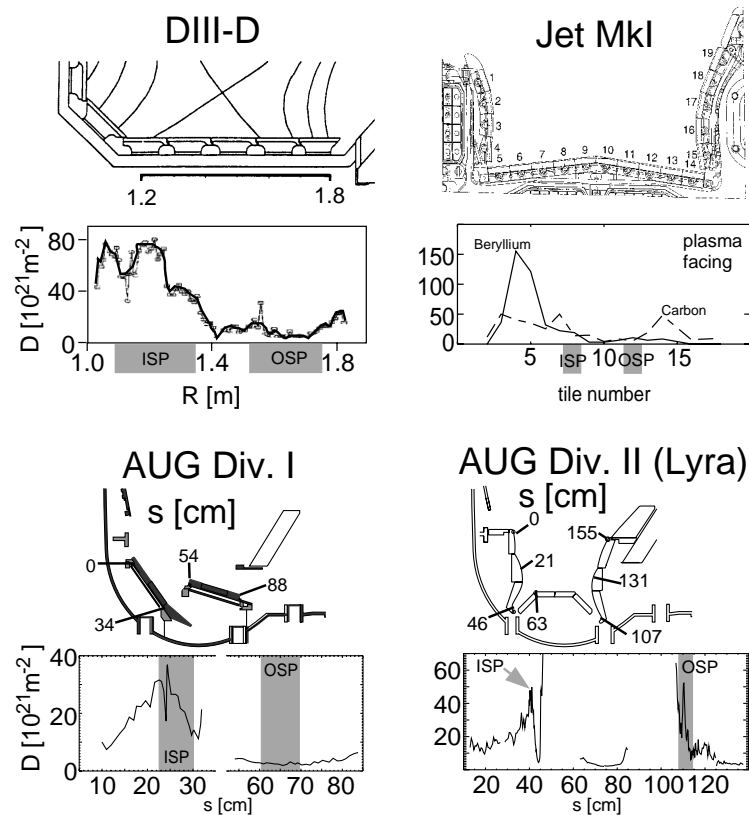


**Figure 45.** Redeposition pattern of carbon onto the divertor plates of DIII-D, JET Mk-I, ASDEX-Upgrade Div. I and Div. II LYRA, as documented by the D co-deposition pattern [64]. The inserts show the different divertor geometries.

The redeposition of carbon will strongly depend on the sticking of the hydrocarbon radicals to the target surface. The radicals that lead to surface deposition may be synthesized in ion–molecule reactions in the divertor plasma, or alternatively, may also be produced by chemical reaction on the surface, or via thermal release from deposited polymer like a-C:H films [346, 347, 543]. These species and their fragments after dissociation in the plasma [154, 560] may be deposited as neutrals with just the energy received during breakup or as ions accelerated in the sheath potential in front of the surface. The majority will have energies between 1 and 10 eV and have a high probability of surviving the impact with surface atoms without breakup.

A plausible scheme for the observed carbon deposition in current divertor experiments (JET [235], ASDEX-Upgrade [530]) is erosion of carbon from the vessel walls followed by deposition as polymer like films on the target plate. This polymeric structure is the stable form of C:H layers if the ion energy is low

(<30 eV) or a high flux of atomic hydrogen leads to a continuous hydrogenation of the  $sp^2$  carbon groups in the film [467, 561]. Both conditions hold for many plasma exposed surfaces inside a fusion reactor. At elevated temperatures, during plasma exposure,  $C_2H_x$  molecules/radicals are released. The deposition of such molecules/radicals on cooler surfaces ( $T < 500$  K) can lead to the formation of thick hydrogenated layers.

A striking feature, which is seen in many tokamaks, is the intense co-deposition of carbon and deuterium in regions which are shaded from ion flux but lie near carbon surfaces receiving high ion flux (Section 4.7). Examples of this are surfaces facing the inner pumping port in the JET Mk-IIA divertor and regions shaded by adjacent tiles (JET and ASDEX-Upgrade), and on the sides of tiles (TFTR and DIII-D). Since ions cannot reach these shaded surfaces, this carbon deposition can only be due to neutral carbon atoms or molecules. Sputtered atoms are unlikely to return to the surface as neu-

trals; instead, they will be ionized and return to surfaces intersecting field lines. However, hydrocarbon molecules leaving the surface can dissociate yielding energetic neutral fragments, including hydrocarbon radicals and atoms. Cross-sections for the production of  $\text{CH}_3$  and  $\text{CH}_2$ , by electron bombardment of methane, peak at electron energies between 20–30 eV [562]. In this energy range, dissociation into neutrals, rather than dissociative ionization, is mainly responsible for the production of molecular radicals [563]. Furthermore, erosion of graphite from hydrogen impact occurs mainly through production of methane and heavier hydrocarbons for hydrogen energies below 100 eV [293]. Therefore, it is likely that carbon surfaces exposed to high fluxes of hydrogenic ions, such as divertor strike points, will be a strong source of hydrocarbon molecules into the plasma. A large fraction of this carbon will promptly return to nearby surfaces as energetic neutral carbon or hydrocarbon radicals. Chemical erosion followed by molecular dissociation will, therefore, result in intense recycling of neutral carbon and hydrogen back and forth between the plasma and the surface. This flux of neutral carbon can deposit on surfaces shaded from the plasma. In contrast, the same mechanism would not occur for metal atoms since metals are eroded by physical sputtering as atoms, not as molecules. The eroded metal atoms will be ionized and redeposit on surfaces intersecting field lines. The ability of carbon, but not metal atoms, to redeposit in shaded regions is consistent with the observation in JET that on the Mk-I beryllium divertor the heavy deposits were predominantly carbon and not beryllium, and that the regions exposed to ion flux, i.e. of net erosion, consisted mainly of beryllium with little carbon. Beryllium and carbon would both be eroded from the plasma contacting regions, but only the carbon would be deposited as neutrals into the shaded regions. This process might be used to advantage to localize deposition of carbon in regions where it can be removed or heated to thermally release tritium (Section 2.3.3).

#### 4.3.2. Limiter erosion/deposition

Investigations in divertor tokamaks such as ASDEX-Upgrade [564] and Alcator C-Mod [565] have shown that, even at several decay lengths outside the separatrix, moderate ion fluxes can reach limiter structures and lead to characteristic erosion/deposition patterns (see, for example, Ref. [213]). Originally, JET was built as a lim-

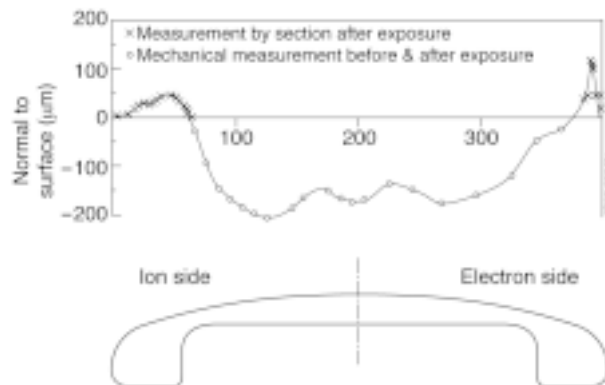


**Figure 46.** Erosion and redeposition pattern (over a campaign of many discharges) across the carbon JET rail limiter. (Reproduced with permission from Ref. [567].)

iter machine with discrete outboard rail limiters and a large area inner bumper limiter. Net erosion/deposition at the discrete limiters that JET used during the 1986 campaign was determined by measuring the tiles with a co-ordinate measuring machine before and after the campaign (Fig. 46) [566, 567]. Additional implanted  $^{13}\text{C}$  markers served as quantitative erosion/deposition indicators. Maximum net erosion of 200  $\mu\text{m}$  was observed at either side of the tangency point, with deposition of up to 120  $\mu\text{m}$  found on the flanks of the tile, deeper into the SOL. The erosion corresponds to an average of 60 nm per pulse over the 3200 discharges in the campaign. In the same campaign, a special erosion probe was inserted into the SOL to within 10 mm of the LCFS for two 20 s discharges with flat-tops of 5 MA for 4 s. The erosion rate in the SOL varied from 60 to 2000 nm per 20 s pulse, while the deposition rate was factors of 25 greater [567, 568].

Erosion/deposition processes at large area bumper limiters were investigated in detail in TFTR [495]. Measurements of the TFTR bumper limiter, by in situ beta back scattering [490], showed areas of net deposition of material (metals and D) at the lower left and upper right and at the midplane of each limiter sector. Relatively clean areas appear to correspond to regions of high plasma flux and net erosion. The deposited material was mainly carbon with 20 at.% D, 6 at.% oxygen and 1 at.% metal atoms with a depth of several micrometres. The main mechanism for D retention was co-deposition rather than implantation. The TFTR bumper limiter was lined with graphite tiles having  $\sim 3$  mm gaps. Removed tiles showed thick (up to several micrometres) carbon deposits  $\sim 2$  cm down the side faces of the gaps. Theoretical and experimental

simulations indicate that sputtered carbon can be transported deep into the gap by multiple reflections off the faces of the gap [569]. Scans along the side edges of removed limiter tiles indicate that the edges retain high levels of deuterium [570]. Deposition in the gaps was more pronounced on the tiles which were erosion dominated on their plasma facing surfaces, indicating local redeposition. More information on deuterium and tritium retention in TFTR and JET is given in Section 4.7.

Erosion/redeposition modelling in TFTR [571] yielded results consistent with the above experimental measurements. Flaking of co-deposits after termination of operations was observed [572, 573]. Analysis of tiles that experienced DT plasmas showed relatively high concentrations of tritium at the top and bottom of the bumper limiter [574], as predicted by earlier BBQ modelling [201].

In TEXTOR, a well diagnosed mushroom type test limiter was used to investigate erosion processes such as RES and chemical erosion (Section 3.2), the behaviour of different limiter materials and erosion/redeposition transport issues. Under typical limiter conditions, the electron temperatures are high enough ( $T_e \approx 30\text{--}80\text{ eV}$ ) that even incident hydrogenic ions have energies above the threshold for physical sputtering for high Z materials. However, under the plasma boundary conditions of TEXTOR with about 2%  $C^{4+}$  and 1%  $O^{4+}$ , the observed emission of W or Mo from limiters made of these materials, respectively, is predominantly due to impurity sputtering [575, 576]. The transition from carbon erosion at the limiter tip to carbon deposition at the limiter rim is very sharp, indicating the change from erosion to deposition dominated areas as the electron temperature decreases below a critical limit (Fig. 20(b)).

#### 4.3.3. Main chamber wall erosion

When erosion in the divertor is suppressed, for example during operation with detached divertor plasmas, the main chamber wall can become the dominant source of impurities to the plasma. In general, the first wall is not a homogeneous surface. Typically, the inner wall is covered by well aligned carbon tiles (ASDEX-Upgrade, DIII-D, JET, JT-60U, TFTR, TEXTOR, Tore Supra) or molybdenum tiles (Alcator C-Mod), while the outer wall houses components such as ion cyclotron resonance heating (ICRH) and lower hybrid (LH) antennas, passive stabilization coils, protection limiters and has

ports and openings for diagnostics and NBI. Often, large areas of the unprotected metal walls have direct line-of-sight to the core plasma. This complicated structure, with a variety of surface materials, is often protected by periodic coating with low Z elements, such as boron (ASDEX-Upgrade, TEXTOR, Alcator C-Mod, Tore Supra, JT-60U, MAST, NSTX), silicon (ASDEX-Upgrade, TEXTOR), beryllium (JET), or lithium (TFTR) (Section 1.3.2). The fluxes to the first wall components are poorly diagnosed (Section 6.4). Protection limiters, positioned several decay lengths behind the separatrix, are subject to ion fluxes, but at much lower intensity than divertors. The large area of the vessel wall behind protection limiters receives charge exchange neutral fluxes. Charge exchange diagnostics typically only measure neutrals with energies above 1 keV. However, the charge exchange neutral fluxes responsible for impurity production are mainly below 300 eV [335] (Section 3.2), and are difficult to measure. Charge exchange neutral fluxes were measured in ASDEX [577] using the change in resistance of thin carbon films calibrated in ion beam experiments [578, 579]. It could be shown that the fluxes were of the order of  $10^{20}\text{ m}^{-2}\cdot\text{s}^{-1}$ , and the estimated sputtering rate correlated with the impurity influx determined from central impurity concentrations [577] for different plasma parameters. For some cases, the energy distributions between 20 eV and 2 keV were measured by using a time of flight method [157, 580–583]; they were used for the estimation of sputtering rates. As the direct measurement can only be done at a few special locations around the plasma vessel, the available data have to be extrapolated to the rest of the vessel wall by code simulations. This has been done by using the B2/EIRENE code (Section 5.2) at ASDEX-Upgrade [157], and Fig. 47 shows the distribution of the sputtered atom fluxes for a W and C first wall due to charge exchange neutral sputtering. The neutral fluxes range from  $10^{18}$  to  $10^{20}\text{ m}^{-2}\cdot\text{s}^{-1}$  and are more than three orders of magnitude smaller than the maximum ion fluxes to the divertor plates. The calculations consider only recycling from the divertor as the main neutral gas source (and do not consider main vessel sources due to cross-field diffusion [584] of plasma to protection limiters, ICRH antennae or gas puffs), which lead to a toroidally non-uniform charge exchange neutral distribution [585]. Owing to the high fraction of neutrals at low energies, high Z materials with high threshold energies for sputtering show a strongly reduced erosion rate compared to low Z materials, especially

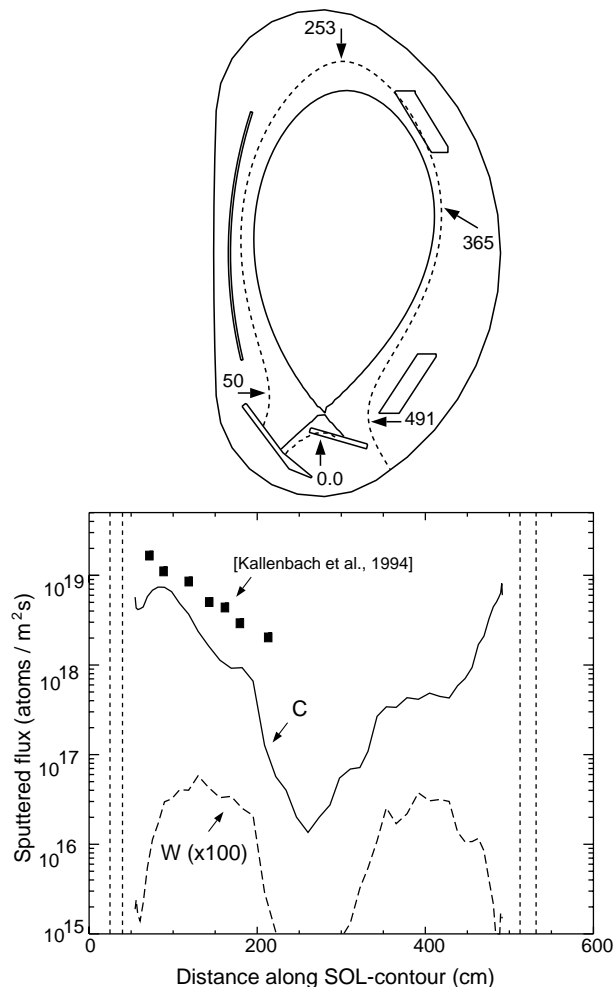


**Figure 47.** Distribution of the sputtered atom flux from the ASDEX-Upgrade vessel wall for a carbon and tungsten wall material due to charge exchange neutral sputtering as calculated from B2/EIRENE code calculations [157]. The carbon values can be compared to spectroscopically measured fluxes from the inner heat shield shown as solid squares [337]. The conditions in the divertor during erosion are: experiment —  $D_2$ ,  $\langle n_e \rangle = 3 \times 10^{19} \text{ m}^{-3}$ , calculations —  $H_2$ ,  $\langle n_e \rangle = 8 \times 10^{19} \text{ m}^{-3}$ .

for high density plasmas with low edge temperatures. The prediction that carbon influxes result predominantly from the lower part of the inner heat shield was directly corroborated by quantitative spectroscopic measurements of the CD band intensity [337] (Fig. 47).

Measurements were also made of the energy and flux of charge exchange neutrals to the wall at the outer midplane in TFTR by using carbon resistance probes, which sense neutrals with energies above 30 eV [490]. The mean charge exchange neutral energies were compared for ohmically heated and neu-

**Table 11.** The mean energy and flux of charge exchange neutrals at the outer midplane of TFTR during ohmically heated (OH) and neutral beam heated portions of the discharge, with the wall saturated with deuterium and unsaturated by ‘supershot’ conditioning [490].

	Mean energy (keV)		Flux ( $10^{20} \cdot \text{m}^{-2} \cdot \text{s}^{-1}$ )	
	OH	NB	OH	NB
Deuterium saturated	0.4	1.5	0.7	1.4
Supershot conditioned	0.3	2	0.06	0.3

tral beam heated portions of discharges. Low density helium fuelled plasmas were used in TFTR to remove deuterium from the limiter and wall to reduce fuel recycling at the plasma edge. The resistance probe study showed that this conditioning dramatically reduced the flux of charge exchange neutrals to the wall but had little effect on their energy, and that neutral beam heating increased both the energy and flux of the charge exchange neutrals (Table 11).

In general, direct spectroscopic determination of the sputtered fluxes from the vessel walls is difficult due to the small erosion rate per unit area, while the total impurity influx is important because of the large area of the vessel wall. Therefore, direct determination of the wall erosion has to be done by long term surface probes integrating over several discharges or whole campaigns. Erosion probes used in ASDEX collected the eroded Ni atoms on Si collectors and could be analysed sensitively using electron induced X ray spectroscopy [586]. In JET, long term probes with evaporated films or implanted depth markers were installed and analysed before and after the exposure for full experimental campaigns [587, 588]. Erosion/deposition at the JET vessel walls was investigated in 1985 by means of 12 long term samples distributed poloidally around the wall and into which  $^{13}\text{C}$  had been implanted at depths of 30 and 450 nm [587]. The overall erosion was much greater than the implantation depths and was not consistent with sputtering by the expected charge exchange neutral flux. Either the flux was larger, or there was an additional ion flux to the walls [587].

Erosion/deposition at the vessel walls was investigated during the Mk-I divertor phase of JET [588, 589] (April 1994 to June 1995.) During this period, the vessel walls (made of Inconel 600 — see glossary) were protected from direct contact with

ions by poloidal rings of carbon (graphite and CFC tiles), but were exposed to charge exchange neutral fluxes. The inner wall was coated periodically with Be evaporated from four heads close to the outer wall at the midplane; parts of the outer wall were also coated with thicker Be layers, while other areas were shielded from the evaporation by the poloidal limiters. Long term samples of different materials were attached to the walls. Detailed measurements of spatial and energy distributions for charge exchange neutrals in JET are not available; however, scaling charge exchange neutral measurements in ASDEX-Upgrade to JET led to reasonable agreement with the erosion rates of the different materials by the likely charge exchange fluxes (Fig. 18) [157]. The net erosion for the Ni sample at the JET inner wall was  $\approx 0.8 \times 10^{19}$  at.  $\cdot$  m $^{-2}$ . Assuming toroidal symmetry, this indicates that about 70 g Ni + Cr + Fe was eroded from the inner wall, in addition to the sputtering of the evaporated Be; about 55 g Be was sputtered from the outer wall. In JET and ASDEX-Upgrade, deposition was found to be minimal, and in most cases this deposition was due to the periodic wall conditioning.

Although eroded atoms from protruding components with direct sight to the vessel wall have a chance to be deposited at the wall without being ionized in the plasma edge [590], the majority are ionized in the SOL and are transported along field lines to limiters or divertor plates [591]. In contrast, the outer stainless steel vessel wall of TFTR experienced net co-deposition. Approximately, half of the deuterium and tritium inventory was found to be deposited on the outer wall (Section 4.7.1.1.) [574]

#### 4.3.4. Impurity flow pattern in divertor tokamaks

As a result of the detailed investigations of erosion and redeposition in tokamaks, a schematic flow diagram of impurities can be constructed. This has been done in ASDEX [592] for the case of Cu divertor plates and a carbon vessel wall, for ASDEX-Upgrade [593] with W as divertor plate material, and for JET [589] using the Mk-I carbon divertor, a carbon inner heat shield and beryllium coated outer walls. As an example, the impurity flow pattern for ASDEX-Upgrade is shown in Fig. 48 for the W divertor. The first wall is the erosion dominated zone, with chemical sputtering of carbon being the dominant erosion process. Sputtering is mostly due to charge exchange neutral fluxes, but there is an indication that ion fluxes to the inner heat shield also contribute to ero-

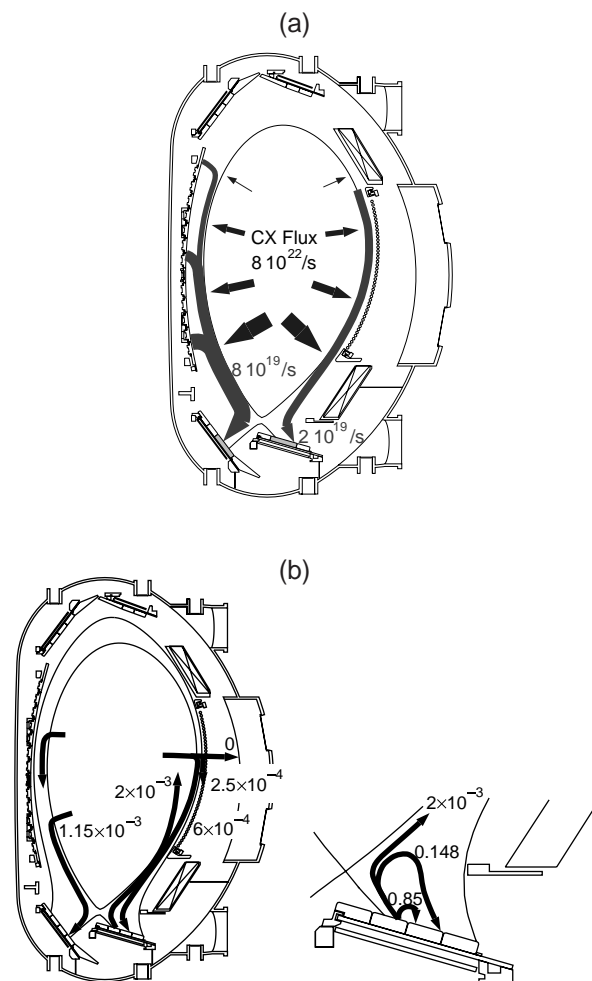


**Figure 48.** (a) Schematic erosion/redeposition pattern of carbon wall material in the ASDEX-Upgrade divertor tokamak. For a total charge exchange neutral flux of  $8 \times 10^{22}$  D  $\cdot$  s $^{-1}$ , the calculated C impurity flux is of  $8 \times 10^{19}$  C  $\cdot$  s $^{-1}$  at the inner divertor and  $2 \times 10^{19}$  C  $\cdot$  s $^{-1}$  at the outer divertor. (b) Schematic of the erosion/redeposition pattern of divertor material in a divertor tokamak as obtained from the ASDEX-Upgrade W divertor experiment. (Reproduced with permission from Ref. [593].)

sion. About  $10^{20}$  C atoms  $\cdot$  s $^{-1}$  are eroded, depending on the main plasma density, and deposited onto a wetted divertor area of less than 1 m $^2$  (Fig. 48(a).) Deposition rates are in the several nm  $\cdot$  s $^{-1}$  range. In the W divertor, the electron temperature at the inner divertor was typically lower than 10 eV, leading to net deposition, while at the outer divertor, at slightly higher temperatures, erosion dominated [594]. Erosion is due to highly charged impurity ions, such as C $^{4+}$ . The energy of the deuterium ions is too low to sputter W from the divertor plates [115].

W sputtered from the outer divertor plate in ASDEX-Upgrade has a high probability ( $\approx 85\%$ ) to be promptly redeposited (Fig. 48(b), right insert). Another fraction ( $\approx 15\%$ ) will be redeposited without ever entering the confined central plasma. Only a fraction of about  $0.2\%$  escapes the divertor and SOL and enters the confined plasma (Fig. 48(b), left insert). In relation to the originally sputtered amount at the outer divertor plate a fraction of  $1.15 \times 10^{-3}$  is deposited on the inner divertor plate, a fraction of  $6 \times 10^{-4}$  returns to the outer divertor, and a fraction of  $2.5 \times 10^{-4}$  is deposited at limiter like structures in the SOL. No deposition at the vessel wall could be measured. In ASDEX-Upgrade, W atom concentrations in the central plasma reached levels above  $2 \times 10^5$  W/D only in a few exceptional cases, where the disappearance of sawteeth led to impurity accumulation [115]. In the new ASDEX-Upgrade LYRA divertor, even the outer divertor is deposition dominated [559].

In JET, coverage of the cold inner Be divertor with carbon was found [494] and partially detached divertor conditions led to the elimination of gross erosion in DIII-D [537]. The low temperature, high density divertor conditions can lead to deposition of a polymer like hydrogenated carbon film, which is unstable at temperatures above 500 K and decomposes to heavy hydrocarbons and radicals [519]. During plasma exposure at elevated temperatures, the deposited layer will, through chemical sputtering, and/or thermal decomposition, lead to the release of hydrocarbons/radicals, which could be transported and deposited onto cooler areas where the deposited layer is stable - such as the inner louvers of the JET divertor (Sections 4.3.1 and 5.3.1) [235], or the ASDEX-Upgrade divertor bottom [530].  $\text{CH}_3$  radicals have a very low sticking coefficient [595] and may be uniformly deposited on cool areas of the vessel wall and deep into the pump duct.

#### 4.4. Experimental evidence for arcing in tokamaks

The underlying physical processes of arcing are presented in Section 3.3. The occurrence of arcs and arc traces on PFCs has been reported by tokamaks for the past 25 years [304, 352, 515, 596]. However, their relative importance is uncertain, primarily because of the difficulties of measuring the effects of such highly localized and transient events. Arcing, like sputtering, has two possible consequences for tokamak operations: introduction of impurities

into the plasma, and damage to PFCs (e.g. net erosion).

One obvious feature is the discrete temporal nature of arcs compared to the continuous release of wall particles from sputtering. To make a comparison, one must know the average number of released particles per arc,  $N_{arc}$ , ( $10^{17} - 10^{18}$ ) and the steady state arc frequency per unit area of PFC ( $f_{arc}$ , in units of  $\text{s}^{-1} \cdot \text{m}^{-2}$ ). The relative flux from arcing,  $\Gamma_{arc}$ , to sputtering,  $\Gamma_{sputter}$ , of released materials is then simply given by

$$\frac{\Gamma_{arc}}{\Gamma_{sputt}} = \frac{N_{arc} f_{arc}}{Y_{sputt} \Gamma_{inc}} \quad (27)$$

Here,  $Y_{sputter}$  is the sputtering (physical + chemical) yield for the incident plasma flux,  $\Gamma_{incident}$ . This formulation is useful since the quantities ( $N_{arc}$ ,  $f_{arc}$ ) can be deduced from post exposure analysis of the arc tracks that have occurred on a PFC over a given operational period. Note that there is an implicit assumption that both the plasma and surface criteria for arcing are met (Section 3.3). Although the underlying plasma material physics is the same, arcing at limiter and divertor surfaces will be addressed separately in the following sections. In summary, the effect of arcing on next step devices should be small at limiter surfaces. Arcing may be important in the divertor, but insufficient data from current tokamaks exist to reliably extrapolate to an ITER class device.

##### 4.4.1. Arcing at limiter surfaces

Arcing from limiter surfaces was initially viewed as a leading candidate for explaining the impurity content of the plasma [597]. This arose primarily from the visual observation of material loss from arc traces. Although there appeared to be some link of arcing with the type of limiter material and its conditioning, the principal correlation for the presence of arcs was the plasma parameters at the limiter. Time resolved arc measurements (using coincident spectroscopy and current measurements) in several tokamaks (DITE, ISX, PLT and T10) in the late 1970s showed that arcing at limiters occurs predominantly during the initial phases of the discharge [352]. On both DITE [516] and JFT-2 [598], this was clearly correlated with disruptive like MHD activity as rational  $q$  surfaces passed the limiter during the current rampup. Significant arcing was also found during plasma disruptions. The enhanced loss of particle and energy flux to the limiters during these events meets the criterion for arc initiation (Section 3.3),

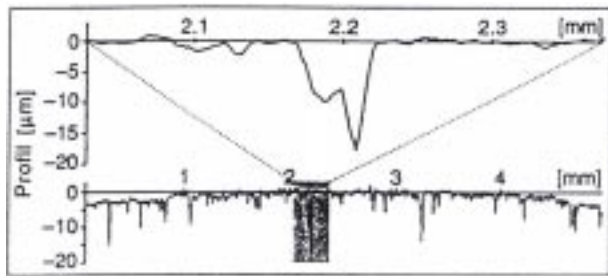


**Figure 49.** Surface profile showing arc traces on a polished graphite tile from the outer divertor of ASDEX-Upgrade exposed to 57 neutral beam heated 1.5 s discharges. Direction of scan is parallel to the magnetic field and therefore perpendicular to the direction of the arc traces. (Reproduced with permission from Ref. [358].)

while quiescent periods do not. It was also found that, although the impurity content of the plasma was increased during arcs, this had little effect on the impurity concentrations during the quiescent, steady state portion of the discharge.

The possibility of arcs at the limiter is more likely during non-quiescent phases such as VDEs when the main plasma moves suddenly into the main wall or limiter (Section 2.3.2). The large energy densities associated with the direct contact of a burning plasma with the limiter surface will certainly meet the criteria for arcing. However, it is difficult in this case to separate arcing from other ablative/melt losses as the principal culprit in damaging the limiter materials.

#### 4.4.2. Arcing at divertor surfaces

Despite the observation of arc traces in the divertor of many current tokamaks (e.g., ASDEX-Upgrade [358], DIII-D [110]), little effort has been devoted to their impact on tokamak operation. The divertor geometry intentionally concentrates heat and particle flux on small regions of the vessel surface. Divertor electron densities and particle flux are typically five to ten times larger than those found at a limiter, while  $T_e$  is usually  $>10$  eV for non-detached divertor plasma regimes. Hence, the plasma conditions necessary for arc formation can be constantly present in the divertor, as opposed to being transiently present at limiter surfaces.

A detailed analysis of the effects of arcing in the divertor has taken place on ASDEX-Upgrade [358, 515]. Post exposure surface analysis of outer divertor graphite tiles showed a localized arc density of  $f_{arc} \approx 5 \times 10^3 \text{ arcs} \cdot \text{m}^{-2} \cdot \text{s}^{-1}$  during the

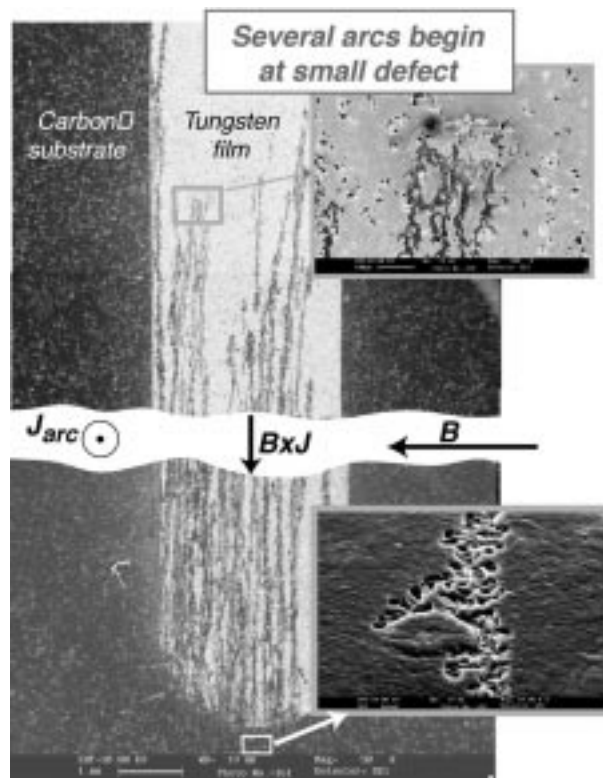
$\approx 100$  s of discharges with neutral beam auxiliary heating ( $\approx 6$  MW). The typical dimensions of the arcs (depth  $\approx 10 \mu\text{m}$ , width  $\approx 50 \mu\text{m}$  and trace length  $\approx 4$  mm) indicated that  $N_{arc} \approx 2 \times 10^{17}$  carbon atoms per arc were eroded (Fig. 49). Therefore, the estimated carbon efflux  $\Gamma_{arc} \approx (1.1 \pm 0.4 \times 10^{21} \text{ m}^{-2} \cdot \text{s}^{-1})$  (Eq. (27)) is comparable to the carbon efflux expected from sputtering,  $\Gamma_{sputter} \approx (1.4 \pm 0.7) \times 10^{21} \text{ m}^{-2} \cdot \text{s}^{-1}$ ,  $\Gamma_{incident} \approx 5 \times 10^{22}$ ,  $Y_{sputter} \approx 2\text{--}3\%$ . Time resolved measurements of the arcing were unavailable. Therefore, it is highly uncertain whether this short exposure reflects the expected steady state arcing frequency or the initial conditioning of the tiles. Significant arc traces have also been observed on DIII-D inner divertor tiles, where the arc traces have removed portions of the deposited carbon layer formed during plasma operations. Arcing was also prevalent at the redeposition dominated inner divertor tiles of ASDEX-Upgrade [358]. Conversely, recent exposures of polished graphite samples to ELMY H mode outer divertor plasmas in DIII-D [110] and ASDEX-Upgrade [500] have shown no signs of arc traces. These results point to the complex role played by the surface conditions in arcing.

Figure 50 illustrates an example of arcing on a  $0.1 \mu\text{m}$  thick film of tungsten on a carbon DiMES probe (see glossary) exposed to ELMY H mode divertor plasmas on DIII-D [110]. In the arc tracks the entire thickness of the tungsten film was removed. Several arcs were initiated at a small defect and then moved in a retrograde direction. At the boundary of the tungsten film, the arcs continued onto the graphite substrate for a short distance. An adjacent beryllium film on this sample had no arc tracks. In contrast, no arc tracks were seen on similar probes exposed at the outer strike point of detached plasmas [599]. Detached plasmas are characterized by  $T_e < 2$  eV; therefore, the local electric field falls below the critical potential necessary for arcing. Despite the diagnosis difficulties, these results raise valid concerns that arcing can play an important role in erosion (at least, transiently) in portions of the divertor.

### 4.5. Disruption erosion in simulation devices and tokamaks

#### 4.5.1. Disruption simulation experiments

The main characteristics of disruptions and other off-normal plasma transients in tokamaks is discussed in Sections 2.3.2. Disruption conditions in next step devices cannot be achieved in existing tokamaks because of the large differences in stored



**Figure 50.** Example of arc traces on a  $0.1\ \mu\text{m}$  W film on a graphite substrate exposed to a divertor plasma in DIII-D.

energy. Laboratory experiments (e.g., laser and electron beams, open plasma traps and plasma guns) are therefore used to study and simulate disruption erosion effects [600]. This section briefly reviews the measurements of erosion in disruption simulators and some effects partially observed during off-normal events in today's tokamak experiments. These experiments are used to validate the theories and the models discussed in Section 3.4, which predict disruption effects in next step devices (Section 5.4).

Table 12 lists the main operation parameters of several disruption simulators, which have been primarily used during the last decade.

#### 4.5.1.1. *Experiments with lasers and high energy electron beams*

Laser [601–606] and high energy electron beam facilities [607–614] have been widely used to test divertor materials, primarily graphite and C based materials. These experiments were mainly carried out in facilities without applied magnetic field and have, typically, shown very high erosion (hundreds of micrometres). A magnetic field can confine the vapour plasma and shield the material surface (Sec-

tion 3.4). In laser beams the beam size is generally very small ( $\leq 2\text{--}4\text{ mm}$ ) and penetrates the expanding cloud of vaporized material with little attenuation. Similarly, in electron beams, because of the high kinetic energy (100–150 keV), electrons penetrate the vapour and the target material more deeply than laser or plasma gun devices. As a result, the vapour cloud is heated to lower temperatures than in plasma gun experiments, and the fraction of incident energy dissipated via radiation in the vapour is much lower [615].

Ejection of macroscopic carbon particles, from carbon based samples, has been observed both in electron beam [603, 612, 616, 617] and laser experiments [618]. The GOL-3 facility of Novosibirsk in Russia [613, 614] combines a combined hot electron beam (low MeV range) and low temperature plasmas ( $\approx 3\text{--}5\text{ eV}$ ) and showed an explosive type erosion of graphite materials [616, 619]. About  $500\ \mu\text{m} \cdot \text{shot}^{-1}$  of graphite were eroded at an energy density of  $30\text{ MJ} \cdot \text{m}^{-2}$  [600]. This high graphite erosion is believed to be due to bulk damage by volumetric energy deposition, and the eroded graphite is emitted in the forms of grains of size ranging between 1



**Table 12.** Some examples of disruption simulators

Facility	Energy density $\text{MJ} \cdot \text{m}^{-2}$	Pulse length ms	Power density $\text{GW} \cdot \text{m}^{-2}$	Parameter $\text{MJ} \cdot \text{m}^{-2} \cdot \text{s}^{-1/2}$	Part. Energy keV	Plasma density $\text{m}^{-3}$	B field T	Plasma stream size m	Can provide useful data on the following
<b>Next step device</b>	10–150	1–10	10–150	$\geq 1000$ $\sim 50\text{--}200$ (ELMs)	20 ions+ electrons	$1 \times 10^{20}$	5	0.2	
<b>MK-200UG</b> <sup>i</sup> Pulsed plasma gun with long drift tube	15	0.04–0.05	300–400	$\sim 70$	1.5 (ion) <sup>1</sup> 0.15 <sup>3</sup>	$2 \times 10^{21\ 2}$	2	0.065 diam.	a, b, c, d, e
<b>MK-200CUSP</b> <sup>i</sup> Long CUSP trap	2	0.015–0.020	150–200	$\sim 15$	0.8 (ion) 0.15 <sup>3</sup>	$(1.5\text{--}2) \times 10^{22}$	2–3	0.005	a, b, c
<b>MKT-U</b> <sup>i</sup> Pulsed plasma gun with 3 m drift tube	1–2	0.03	30–60	$> 6$	1.2 (ion) <sup>1</sup>	$6 \times 10^{20}$	2	$\sim 0.07$ diam.	d, e
<b>QSPA</b> <sup>i</sup> Upgraded quasi-stationary plasma accelerator	5–10	0.25–0.6	10–50	6–20	0.1	$< 1 \times 10^{22}$	0–1	0.05 diam.	d, e
<b>QSPA-Kh-50</b> <sup>ii</sup> Quasi-stationary plasma accelerator	10–40	0.2	37–80	22–90	0.3 (ion)	$(2\text{--}8) \times 10^{21}$	0–2	$\sim 0.04$ diam.	d, e
<b>PLADIS</b> <sup>iii</sup> Plasma gun	0.5–20	0.08–0.5	—	$\sim 15$	0.1 (ion)	n/a	—	0.02 diam.	d, e
<b>VIKA</b> <sup>iv</sup> Quasi-stationary plasma accelerator	2–30	0.09–0.36	20–84	$< 20$	0.2	$> 1 \times 10^{22}$	0–3	0.06 diam.	c, d, e
<b>ELDIS</b> <sup>iv</sup> Electron beam	$< 50$	0.05–0.06	2	$> 100$	120 <sup>4</sup>	$(2\text{--}4) \times 10^{22}$	0–4	—	e
<b>JEBIS</b> <sup>v</sup> Electron beam	2.5	1.5–2	2	$\sim 2$	70 <sup>4</sup>	n/a	0	$> 0.005$ diam.	e
<b>JUDITH</b> <sup>vi</sup> Electron beam	5–10	1–5	2–6	2–10	120 <sup>4</sup>	—	0	$\sim 0.004$ diam.	e
<b>GOL-3</b> <sup>vii</sup> Long mirror trap	8–10	0.01–0.02	1000–1300	$> 50$	1–3 <sup>3,5</sup> (thermal) 20–10 <sup>3</sup> (fast)	10 <sup>21</sup>	2–5	0.06 diam.	b, d, e

<sup>i</sup> TRINITI, Troisk, Moscow, Russian Federation.

<sup>ii</sup> Institute of Plasma Physics, NSC KIPT, Kharkov, Ukraine.

<sup>iii</sup> University of New Mexico, Albuquerque, USA.

<sup>iv</sup> Efremov Institute, St. Petersburg, Russian Federation.

<sup>v</sup> Japan Atomic Energy Research Institute, Naka, Japan.

<sup>vi</sup> Forschungszentrum, Jülich, Germany.

<sup>vii</sup> Budker Institute, Novosibirsk, Russian Federation.

<sup>1</sup> Decreases to 300 eV at the end of the pulse.

<sup>2</sup> Increases up to  $5 \times 10^{21}$  at the end of the pulse.

<sup>3</sup> Electron temperature.

<sup>4</sup> Electrons.

<sup>5</sup> Non Maxwellian distribution function with great contribution of 800 keV electrons.

<sup>a</sup> Vapour dynamics in strong magnetic field at inclined target.

<sup>b</sup> Production of secondary radiation and its interaction with nearby surfaces.

<sup>c</sup> Net radiation power to target surface.

<sup>d</sup> Erosion measurement (vaporization and ablation).

<sup>e</sup> Ablation data (energy of destruction, size and velocity distribution of droplets and macroscopic pieces of graphite).

n/a not available.

and 40  $\mu\text{m}$ . The conditions in this facility, however, may not be fully relevant to disruption conditions in tokamaks.

#### 4.5.1.2. *Experiments with plasma gun devices*

Plasma gun devices [620–627] typically produce low temperature plasmas ( $T < 1$  keV) and a high energy flux (up to 10–20  $\text{MJ}\cdot\text{m}^{-2}$  deposited in a pulsed manner during  $< 1$  ms). They are believed to be more suitable than electron or laser beams for simulating reactor relevant disruption conditions [628]. These facilities are now primarily used to study the underlying physics of the PMIs during disruptions and to quantify the resulting material target erosion. For example, the MK-200UG (Table 12) can produce hydrogen and deuterium plasma streams with a total energy of 50 kJ and ion kinetic energy above 1 keV, in a magnetic field of 2–3 T. Target materials can be tested at perpendicular as well as in an oblique plasma incidence. The main limitation of this facility is its very short pulse duration, i.e.  $\approx 40$ –50  $\mu\text{s}$ , which makes it possible to only simulate the early stages of a disruption in a next step tokamak. Quasi-stationary plasma guns such as VIKA, QSPA, QSPA-Kh 50 and PLADIS (Table 12) generate plasma streams with long pulse duration ( $> 100$   $\mu\text{s}$ ). However, because of the relatively low kinetic energy of the ions ( $E_i \approx 100$ –300 eV), and high plasma densities ( $> 10^{22}$   $\text{m}^{-3}$ ), a shock wave could arise during plasma deposition. This would lead to a deceleration of the plasma stream and to a ‘self-shielding’ effect that mitigates the energy flux reaching the material surface and results in an underestimation of erosion compared to actual tokamak conditions [626].

Several experiments have been performed in various plasma gun facilities primarily to study physical properties and shielding efficiency of plasma vapour shields and the resulting material erosion. In these experiments the plasma temperature and density distributions in the vapour shield are measured together with the lateral leakage of radiation [600, 621, 629–631]. Material damage is generally measured by means of surface profilometry and mass loss. Vapour shielding is seen to reduce erosion, at least to some extent, in all disruption simulation facilities. The dependence of density and temperature of plasma vapour on the incoming plasma flow and the target material are found to be generally in good agreement with theory (Section 3.4).

The incident plasma flows along the magnetic field lines. For perpendicular incidence the target plasma

expands upstream along the magnetic field lines, and transverse motion is inhibited by the strong magnetic field. At oblique incidence, the vapour shield of carbon material was found to drift along the target surface in the direction of the magnetic field lines [621]. This mechanism was found to deplete the shielding properties and increase the erosion of a graphite target by about  $\approx 50\%$ , in agreement with modelling predictions [365].

Recent experiments in MK-200UG [600] have shown collateral damage of nearby surfaces resulting from radiation emitted from the outermost regions in the confined vapour cloud. Graphite erosion of 0.35  $\mu\text{m}\cdot\text{shot}^{-1}$  was caused by a  $\approx 1$   $\text{MJ}\cdot\text{m}^{-2}$  radiation flux from a plasma vapour forming in front of a tungsten target. This erosion is similar to that observed for direct plasma impact (0.4  $\mu\text{m}\cdot\text{shot}^{-1}$ ) at much higher heat flux ( $\approx 15$   $\text{MJ}\cdot\text{m}^{-2}$ ). Modelling [366] confirms that the shielding efficiency under radiation heat loads is lower than under direct plasma impact. The secondary radiation is therefore an important consideration for the choice of divertor materials and geometry in future tokamak devices (Sections 2.4 and 2.5).

For C based materials, high erosion with mass losses that exceed those from surface vaporization have been also observed in plasma gun devices. Experiments in the MKT facility have shown emission of macroscopic particles [632]. Recently, experiments performed in MK-200 UG and QSPA [633, 600] have also revealed macroscopic erosion mechanisms.

Several studies have been also carried out in recent years to investigate macroscopic erosion of metals under disruption conditions. Several mechanisms of metal erosion were described in Section 3.4.2.

Preliminary analysis of the microstructure of the exposed metal surfaces has clearly shown the formation of high volume bubble densities [634] with traces of melted metal droplets of light Z materials (e.g. aluminium) up to a few metres away from the target area. Bubble formation was also found in electron beam experiments [616]. Careful analysis of the irradiated samples has also suggested the possibility of hydrodynamic instability to be a melt layer erosion mechanism, in addition to volume bubble vaporization. Near central areas, where the velocity of the incident plasma stream along the sample surface is close to zero, the bubbles are clearly seen. Near the sample peripheral areas, however, one can see liquid droplets with long tracks formed because of the high velocity of the plasma stream [372].

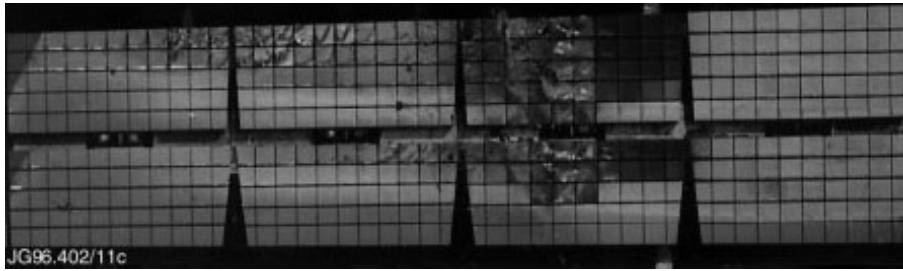


**Figure 51.** JET Mk-I beryllium target plate tiles after plasma operation. A poloidal set of pairs of Be target tiles at the outer strike region are shown at the end of the Be phase. Shown are tiles in row 10 just outboard of the divertor centre line (left of the figure), to tiles in row 13 in the outer SOL (right of figure). The deliberate melting is seen on the tiles in row 12. A small amount of melting is also seen on the tiles in rows 10 and 11, resulting from giant ELMy before the melting experiment. Each tile is  $\approx 75 \text{ mm} \times 40 \text{ mm}$  in size. (Reproduced with permission from JET [639].)

Melt layer erosion of much heavier materials, such as tungsten, was shown to be very low in plasma gun experiments [626] but is more likely to be greater for longer ( $>1 \text{ ms}$ ) heat pulse duration. In experiments conducted in the VIKA facility [635], it was found that for an incident power of  $\approx 100 \text{ GW}\cdot\text{m}^{-2}$ , an appreciable contribution of melt layer loss to the total mass loss of the tested metals (Al, Cu, SS) appears only when the pulse duration exceeds  $0.18 \text{ ms}$ .

Recently, specimens made of several grades of tungsten (e.g. recrystallized W, W-Re, W-Mo cast alloys, single crystal W) were subjected to a number of disruption simulation pulses in MK-200UG (energy density up to  $30 \text{ MJ}\cdot\text{m}^{-2}$  and pulse duration of less than  $50 \mu\text{s}$ ), and then to thermal cycling under steady state heat fluxes up to  $45 \text{ MW}\cdot\text{m}^{-2}$  [636]. Thermal erosion, crack formation, and shallow melting were observed. Crack formation was observed for all studied W grades except single crystal W of proper orientation.

#### 4.5.2. Off-normal events in tokamaks

Erosion data during off-normal events in current tokamaks are scarce and difficult to interpret. Below we shall describe a limited number of cases of interest.

##### 4.5.2.1. JET Be target melting experiment

A dedicated experiment was performed to assess the behaviour of a beryllium target in JET at power fluxes high enough to cause surface melting [244, 637, 638]. These experiments were designed to

test the hypothesis that in ITER a beryllium divertor target would self-protect against excessive, off normal, heat fluxes (i.e.  $>20 \text{ MW}\cdot\text{m}^{-2}$ ) as might occur when radiative divertor operation fails. In this scenario, a highly radiating region produced by evaporating beryllium would reduce the heat flux to the target, preventing significant melting. In a series of JET discharges, the heat fluence to the divertor target was gradually increased, by extending the neutral beam heating duration (to  $\approx 25 \text{ MW}\cdot\text{m}^{-2}$  for  $\approx 6 \text{ s}$ ). Beryllium influxes were seen to rise significantly with target temperature above  $1470 \text{ K}$ , and significant melting of the target was observed with a CCD viewing camera (Fig. 51) [638]. Nevertheless, the radiated power did not exceed 50% of the input power and ELMy H mode operation was retained. In a further series of discharges, without additional gas puffing, but a similar heat flux and heating duration, the radiated power fraction was observed to increase to  $\approx 70\%$  over several seconds. This increase in radiated power fraction is evidence that the evaporated Be flux helped reradiate the incident plasma energy away from the damaged area and may be a sign of self-protection in these experiments. Nevertheless, in this phase of the experiment, melting was observed on both the inner and outer strike points. The total exposure time of the target to the high heat flux was  $\approx 20 \text{ s}$ , and no disruptions occurred during the sequence of pulses which melted the target.

After melting, reference plasma scenarios were repeated with strike points on the annuli of the melted beryllium. The discharges were only marginally worse than the premelt experience. Finally, two long pulse, high power discharges with

sweeping were performed on a different annulus of the target. Beryllium melting was observed, but the radiated power fraction remained moderate ( $<40\%$ ), indicating that self-protection had not occurred. Post mortem examination of the target revealed significant droplet formation in the exposed areas, with droplets forming bridges across the toroidal gap between the tiles. In the most severely melted regions, an annulus approximately 40 mm wide at the outer strike point tiles were eroded to a depth of  $\approx 3$  mm. It can be concluded, therefore, that at heat fluxes  $>25 \text{ MW}\cdot\text{m}^{-2}$ , severe melting of beryllium occurs. While a certain degree of self-protection may have occurred, this was insufficient to protect the tile from melt damage. Melt layer loss may be more severe in a ‘vertical’ target such as envisioned in ITER compared to the horizontal JET divertor (see also oblique magnetic field effects observed in simulators (Section 4.5.1.2)). The damage did not prohibit subsequent plasma operation at JET, but would seriously limit the lifetime of a Be divertor target in long pulse ITER like devices.

#### 4.5.2.2. *DIID-D/DIMES observations on disruptions*

Fast scanning infrared thermography of disruption experiments on DIID-D shows that divertor heat loads for major disruptions and VDE can be significant [174, 640]. For example, in a triggered VDE disruption,  $\approx 80\%$  of the stored kinetic energy of the core plasma (1–2 MJ) can be lost in about 2 ms because of heat convection/conduction to the divertor floor in a 5–10 cm footprint ( $0.5\text{--}1 \text{ m}^2$  total area,  $2\pi R \approx 10 \text{ m}$  for DIID-D). This results in heat loading up to  $1 \text{ GW}\cdot\text{m}^{-2}$  at the divertor floor, with average values  $\approx 0.5 \text{ GW}\cdot\text{m}^{-2}$ . Simultaneous measurements of net carbon erosion/redeposition were made using the DiMES probe [499]. The footprint of the VDE was displaced from the DiMES radial location by about 5–10 cm. It was found that  $\approx 10 \text{ nm}$  of carbon deposition arose from each VDE, indicating significant interactions during the 1–2 ms disruption [641].

An in situ experiment was carried out on the DiMES probe to directly measure the effect of very high heat and particle fluxes on a leading edge of a graphite sample [537, 642]. A DiMES sample with a 0.7 mm vertical lip above the aligned surface ( $\approx 30 \text{ mm}$  radial extent) was exposed to the outer strike point of an ELMing H mode plasma ( $P_{inj} \approx 7 \text{ MW}$ ,  $T_e \approx 30 \text{ eV}$ ,  $n_e \approx 5 \times 10^{19} \text{ m}^{-3}$ ,

heat flux  $\approx 2 \text{ MW}\cdot\text{m}^{-2}$ , incident field line angle  $\approx 2^\circ$ ) for 0.5 s. A parallel heat flux  $\approx 50 \text{ MW}\cdot\text{m}^{-2}$  was incident on an area of  $14 \text{ mm}^2$ , which reached a temperature  $>2800 \text{ K}$ . The graphite part of the sample was seriously eroded after one shot exposure. Localized erosion (pits) depth was as much as  $134 \mu\text{m}$ . Redeposition layers of different structure were formed on the plasma facing surfaces, depending on the impacting heat fluxes and proximity to the erosion region. This experiment was recently repeated to further investigate erosion and dust production from a similar geometry and a parallel heat flux of  $\approx 100 \text{ MW}\cdot\text{m}^{-2}$ . Under these conditions, several  $\text{mm}^3$  of material ablated and production of films and dust in the surrounding areas were observed [641].

#### 4.5.2.3. *Runaway electrons*

The generation of significant levels of superthermal multi-MeV runaway electrons following the onset of plasma disruption is a well known effect in tokamak devices. These runaway electrons persist during current quench disruptions and can produce a current of up to about half of the pre-disruption plasma current in many present experiments, especially at low plasma densities (e.g. TFTR [643], Tore Supra [644], JET [645, 646] and JT-60U [175]). The magnitude of runaway electron generation varies, from none detectable to up to  $\approx 50\%$  of the initial plasma current. Appreciable conversion of the plasma current to runaway electrons is not generally seen in VDEs in divertor tokamaks with non-circular cross-sections (Section 2.3.2.2). In contrast, major conversion is seen in limiter tokamaks with circular cross-sections, in which the post disruption plasma is vertically stable [13]. Data obtained in JT-60U divertor plasmas show that MHD fluctuations [175] and vertical instabilities play key roles in determining the magnitude of runaway electron generation. Disruptions with high levels of fluctuation and vertical instability are essentially runaway free, apparently because the fluctuations produce prompt runaway losses that obviate the buildup of appreciable runaway current. Disruptions or disruption phases with vertical stability and/or lower fluctuation levels produce runaways because current is still inside the core plasma. The level of fluctuation appears to be the factor that determines whether or not runaway electrons develop: vertical instability apparently enhances the fluctuation level. However, the exact mechanism for how vertical instability affects the fluctuation level is not yet clear.

Theoretical considerations suggest that the runaway electrons conversion mechanism — the so-called knock-on avalanche — may lead to potentially worrisome levels of runaway energy deposition in a high current disruption or loss of control VDE, or a pellet injection initiated fast plasma shutdown (Section 2.3.2.4). The impact of runaway electrons with wall components will give rise to localized high heat deposition, leading to significant damage. Although in recent years significant progress has been made in characterizing runaway electrons generation [13, 646], there are still uncertainties in the quantification of material damage.

Present experiments [171] show that runaway deposition is very sensitive to toroidal alignment and that the thermal load deposition is localized. Runaway electrons generated in the current decay following a disruption in Tore Supra [171], pierced the leading edge of an in-vessel tube and caused a water leak. This general vulnerability of modular limiters to runaway electrons was one factor in the move at Tore Supra toward a toroidal ‘floor’ limiter, which eliminates any leading edge.

In a recent investigation of the runaways generated in disruptions in JET [646], detailed time and space resolved X ray images of the runaway beam in flight were obtained for the first time using radiation protected soft X ray cameras. These allowed a detailed diagnosis and analysis of the production and movement of the runaways. The runaways were generated at the vessel centre in a region with small minor radius and they then move to interact with the wall. The interaction zone of the runaways was a small region with a poloidal width of less than 10 cm of the upper or lower vessel depending on the direction of the vertical movement of the beam. The runaway wall interaction varied very rapidly with time and showed a series of very fast spikes. The diameter of the runaway beam at the moment of impact with the wall was 0.8 m. The centre of the beam has a minor radial velocity of  $190 \text{ m} \cdot \text{s}^{-1}$ , and the runaways would therefore all hit the wall in 2.1 ms, in good agreement with the value measured of 2 ms.

In the Frascati Tokamak Upgrade (FTU), the energy content of a high density discharge is relatively high compared to the material area that receives the power released during the thermal and magnetic quenches. This results in very high disruption heat loads on PFCs. This is particularly true in discharges limited by a poloidal limiter. Power loads as high as  $500 \text{ MW} \cdot \text{m}^{-2}$  during the thermal quench and  $200 \text{ MW} \cdot \text{m}^{-2}$  during the current quench



**Figure 52.** Frascati Tokamak limiter of a tungsten coated TZM mushroom type (60 mm in diameter) after plasma transient events. (Figure provided by G. Maddaluno, ENEA, Frascati.)

were recorded by using a single spot infrared detector [647], viewing a limiter zone far from the equatorial plane. Large overall heat loads are expected, because of the plasma column movement during the current quench and/or the runaway electron losses. A power load in excess of  $1 \text{ GW} \cdot \text{m}^{-2}$  was estimated from the amount of molten material found on a tungsten coated molybdenum limiter [648]. A large contribution to the inboard limiter damage was attributed to the electron runaways generated during the fast rise of the loop voltage at the end of the thermal quench. In Fig. 52 a tungsten coated TZM (see glossary) mushroom of the inner half of the FTU poloidal limiter is shown. Severe melting and deep cracks can be observed on the mushroom surface. Recently, the runaway losses during disruptions were investigated by monitoring the photoneutron production [649]. Results suggest that the ‘Dreicer mechanism’ [120] is the primary source of runaway electrons during FTU disruptions and that in high-density clean discharges, this production is reduced to a negligible level. Samples of W+1%  $\text{La}_2\text{O}_3$  exposed to disruptive discharges with negligible runaway production exhibited no evident damage or erosion [650].

Heat pulses due to the thermal quenches accompanying disruptions and ELMs represent a formidable design challenge for a next step reactor. The very high transient heat loads ( $\text{GW} \cdot \text{m}^{-2}$ ) can vapor-

ize the material and, for metals, lead to the formation of melt layers. Transient heat loads impact the PFC erosion lifetime and cause the influx of impurities into the plasma. Long reconditioning of plasma facing surfaces after a severe disruption might be required. There are major incentives to avoid the occurrence of disruptions and to reduce or mitigate the direct and consequential effects (Section 2.3.2.4).

#### 4.6. Control of plasma–material interactions

##### 4.6.1. Introduction

The surfaces of PFCs have a profound effect on the plasma. The number of hydrogenic atoms in the surface layer that interact with the plasma typically exceeds the total number of plasma ions by at least two orders of magnitude. Small changes in wall conditions can strongly affect the influx of hydrogenic atoms or impurities to the plasma edge and thereby determine the boundary conditions imposed on the hot plasma in the core. In turn, the plasma can change the atomic composition of the wall surface, leading to a complex coupled system that is difficult to diagnose and control. However, experience from the earliest days of fusion research has shown that such control is essential for the production of high performance plasmas. Impurity densities must be kept below approximately 1% for low  $Z$  elements and as low as  $10^{-5}$  for high  $Z$  elements such as tungsten to avoid serious radiative losses. In a burning plasma, impurity influx will reduce plasma performance by dilution of the deuteron and triton density. Available wall conditioning tools are (i) baking and/or discharge cleaning to deplete the wall surface of hydrogen isotopes and potential impurities, (ii) film deposition to cover up the wall surface with a more favourable element, and (iii) an in-vessel divertor cryopump to pump hydrogen and volatile impurities.

The currently available database from particle balance experiments in tokamaks reveals marked differences in wall pumping (see glossary) and release behaviour, due to factors such as limiter or divertor configuration, wall material, wall temperature, active pumping by in-vessel cryopumps, etc. [651, 652]. Uncovering the relevant physical processes is arguably more challenging than understanding core plasma physics, because of the large variety of phenomena that are coupled (from solid state physics to plasma transport), and the complex geometry for which simplifying assumptions such as radial symmetry are not possible. Spatially resolved diag-

nostic coverage of the wall/plasma edge region is rather limited or completely lacking. Tokamak operators develop intuitive working hypotheses of recycling phenomena based on their experience of the factors most conducive to optimal performance. This is an area where unambiguous identification of the specific reasons for the different behaviour in different tokamaks is often impossible and anecdotal information on plasma performance is all that is available. The lack of a predictive understanding adds significantly to uncertainty in projections of performance of next step long pulse devices.

In the sections that follow, we discuss the tools available for wall conditioning, the state of the wall surface, and the effects of the wall on the plasma, including density control in long ( $>60$  s) pulses. Wall conditioning requirements in long pulse next step devices are briefly discussed in Section 2.3.1.4 and in Ref. [13]. The physics of hydrogen trapping in materials, including ion induced release of hydrogen from carbon, is treated in Section 3.5. Section 5.5 is devoted to models of recycling, including predictive analysis for next step devices. Wall conditioning techniques aimed at controlling the tritium inventory in a future DT device are discussed in Section 4.7.2. Earlier reviews of hydrogen and helium recycling in tokamaks are in Refs [653, 654].

##### 4.6.2. Wall conditioning

Baking and plasma assisted cleaning are the main methods to remove the ‘adsorbates’ from the surfaces before or in-between plasma operation. Many contemporary fusion devices have the capability of vacuum baking to temperatures in excess of 470 K, including DIII-D, TEXTOR, JT-60U, JET, and reductions in both recycling and impurity influxes are obtained when baking is used. In TFTR direct heating above 423 K was not possible, but the limiter could be heated with intentional disruptive discharges to 573 K [655]. Baking is greatly enhanced by simultaneous or subsequent plasma assisted conditioning. This is done, for example, by running low energy conditioning plasmas such as GDC [36, 37], but various other methods based on RF techniques [38] at the electron cyclotron resonance (ECR) [39, 40, 161] and ion cyclotron resonance (ICR) [41] have been employed. The Large Helical Device (LHD) is limited to wall temperature below 368 K and relies on mild baking combined with ECR discharge cleaning and GDC [40].

Oxygen is present at the material walls in the form of adsorbed hydroxides, water and various metal

oxide compounds, and oxygen influx must be controlled. The original sources of the oxygen contamination are air and water leaks, water vapour that has been adsorbed on the surfaces during vacuum vessel openings, as well as long term diffusion from the bulk to the surface of the in-vessel materials. The cleaning by the plasma is due to the formation of volatile compounds, which are either formed chemically upon the impact of atomic hydrogen or which are released by ion induced desorption due to collisional energy transfer from the impinging particles. Hydrogen plasma impact can reduce metal oxides by forming metal hydroxide surface complexes and finally water molecules, which can be pumped [42, 656]. In addition, adsorbed oxygen can be released in the form of CO and CO<sub>2</sub> molecules by collision-induced desorption in helium conditioning plasmas [657] and also, in hydrogen plasmas, by the chemical reaction of hydrogen with carbon (via a hydrocarbon precursor), and the release of the stored oxygen in the form of CO and CO<sub>2</sub> [312]. The volatile products have to be pumped out and it is essential that the reionization of the reaction products be small so that they are not redeposited on the surfaces. This latter important condition requires a sufficient gas throughput and a low operating pressure of the conditioning plasma. Often, hydrogen GDC is followed by helium GDC to remove hydrogen from plasma facing surfaces [658].

Baking and discharge cleaning are applied routinely in present day fusion experiments, after openings, vacuum or water leaks. They are also of importance after off-normal events such as VDEs or disruptions that can release loosely bound adsorbates from hidden areas, which then are adsorbed on the plasma facing surfaces. As a general trend, low wall temperatures aggravate the consequences of disruptions compared to operation at elevated wall temperatures [658].

In several devices discharge cleaning methods are also used in between plasma pulses. Besides removing impurities, helium glow discharges also induce release of hydrogen trapped in the wall (Section 4.6.3) aiding plasma density control and reducing the frequency of disruptions [657]. In general, oxygen impurities become increasingly deleterious as the density limit of the machine is approached. This is a consequence of the fact that the oxygen sources are located on the entire wall surface. Oxygen can easily be released by either particle impact, by photon induced desorption [659] or by thermal heating. Incident photons produce charge recombination in the bulk, which in turn

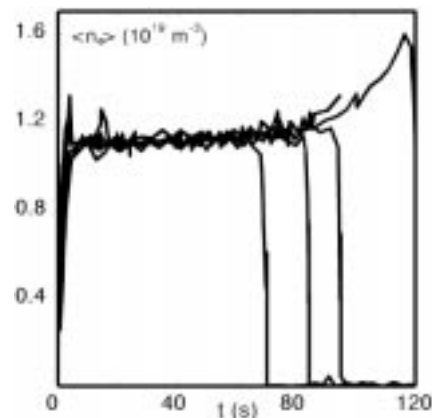


**Figure 53.** Volume average density evolution for very long discharges in Tore Supra. (Reproduced with permission from Ref. [660].)

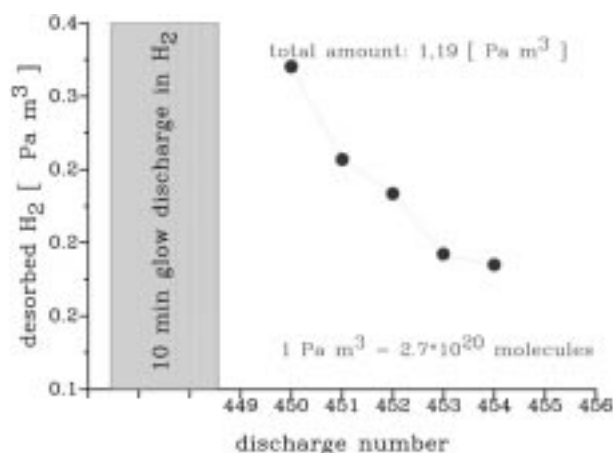


**Figure 54.** Removal of H<sub>2</sub> by ICRH plasmas from the first wall of TEXTOR. 1 Pa·m<sup>3</sup> = 2.7 × 10<sup>20</sup> molecules. (Reproduced with permission from Ref. [41].)

leads to interaction with adsorbates that are bound to the surface by charge transfer, and the release of CO and CO<sub>2</sub>. Since this latter mechanism is proportional to the amount of radiation, an increased oxygen level will lead to even more oxygen influx in a non-linear way. The density rise shown in Fig. 53 is attributed to water desorption induced by wall heating due to the high radiated energy of the plasma (Ref. [660] and Section 4.6.3).

One complication in long pulse devices is that the magnetic field is generated by superconducting coils with a limited number of on/off cycles, so conditioning needs to be done in the presence of the field. While it was possible to generate a glow discharge in the presence of a magnetic field, little release of hydrogenic atoms was achieved [661]. Therefore, new ICRH conditioning techniques have been developed for superconducting devices [41, 662] (Fig. 54).

Deposition of thin films of various materials on the entire plasma facing wall is a more direct way to modify the composition and surface properties of the plasma facing surfaces. Films have been deposited by chemical vapour deposition (CVD), solid target erosion and deposition, and pellet injection, but the technique mostly used is coating by plasma deposition [659, 663, 664].  $\text{H}_2\text{O}$ ,  $\text{CO}$  and  $\text{CO}_2$  partial pressures between discharges, and plasma contamination in subsequent discharges was greatly reduced by titanium evaporation over a large fraction of the vessel surface in ATC [665]. The technique was easy, effective and reliable, but titanium stores large amounts of hydrogen, and after some time the layers of titanium would flake and enter the plasma, sometimes abruptly terminating discharges [666]. Other evaporative getters used include aluminium [84], chromium [667], beryllium [668, 669] and lithium [670] (Table 1). All of these elements are able to reduce oxygen and carbon impurity contamination by chemically binding these species to the wall. The JET tokamak has used beryllium as a getter both by using solid beryllium targets and by frequent evaporation of beryllium onto the inner wall surface. This has reduced the oxygen contamination of the JET plasmas to negligibly small values and has also led to a good control of the plasma density by wall pumping [671] (Section 4.6.3).

In the mid-1980s, work began at the TEXTOR tokamak investigating the effect of a number of plasma deposited surface coatings, including carbonization, boronization and siliconization [663, 672]. All of these techniques involve the use of low temperature discharges (e.g. DC or RF glow discharges) in  $\text{D}_2$  or  $\text{He}$  to dissociate C, B and Si containing gases, (typically, methane, borane and silane, respectively). The treatment usually requires one to a few days, and results in a coating of approximately 100 nm thickness, consisting of a mixture of the respective material, plus deuterium and impurities such as carbon and oxygen. This is highly desirable, since unlike metals, these elements radiate only at the plasma edge [664, 673]. Carbonization, indeed, decreased the concentration of metal impurities in the plasmas significantly and the process is usually repeated when the metal impurities reappear. In the 1990s, this ‘covering up’ of metal surfaces has been taken to an extreme in DIII-D [106] and other tokamaks (e.g. TCV, JT-60U), where >80% of the plasma facing surfaces are now graphite tiles, whether plasma contacting or not. However, carbonization of the walls has proven to be less effective

in controlling the level of oxygen. The use of boron films (boronization), on the other hand, has been found to be much more effective at providing simultaneous control of the metal and oxygen influxes [49, 674–676]. Boronization is now the primary gettering technique in current tokamaks. It is able to keep the oxygen level low for a substantial time and allows rapid recovery from air venting. The boron layers do not react significantly with molecular oxygen up to temperatures as high as 620 K, and their gettering action is due to co-deposition of eroded boron along with oxygen in the SOL regions of the device and the strong bonding of the oxygen in these layers. Thick boron carbide coatings have been proposed for high heat flux areas such as tokamak divertors [677].

Boronization has significantly widened the operational regime towards high density on TEXTOR and other tokamaks. This is exemplified in Fig. 55 [677, 678], which shows the operational space of TEXTOR under different wall coating situations in a Hugill diagram [120]. Siliconized wall conditions were most effective for reaching very high densities in TEXTOR-94, with maximum values of nearly twice the Greenwald density limit (see glossary) [678] and efficient suppression of oxygen impurities [48]. In DIII-D, boronization has led to a very high confinement mode (VH mode) [45]. Boronization in the Mo walled Alcator C-Mod tokamak leads to a considerable decrease of the molybdenum core radiation and better H mode performance [43]. The reduction in radiated power leads to a lower H mode power threshold. However, an improvement in confinement has not been observed after boronization of TEXTOR, ASDEX-Upgrade and JT-60U. This different behaviour is not fully understood and demonstrates the complex link between the properties of the wall, the plasma edge and confinement.

Lithium has been introduced into plasmas by pellet injection [52, 680–682], evaporation [670, 683, 684], lithium borohydride discharge [685], and by laser assisted lithium aerosol injection [164]. It has had dramatic effects on the performance of TFTR (Fig. 2 and Section 1.2.3), greatly increasing the fusion triple product ( $n_e \tau_E T_i$ ) and energy confinement time [53]. However, mixed results have been obtained on other machines (DIII-D, Alcator C-Mod, TdeV, JIPP, TII-U, Heliotron E), in contrast to boronization, which has given similar effects on all machines [686]. Careful preparation is necessary to ensure that the number of free lithium atoms available is equal to the hydrogen fluence to the wall



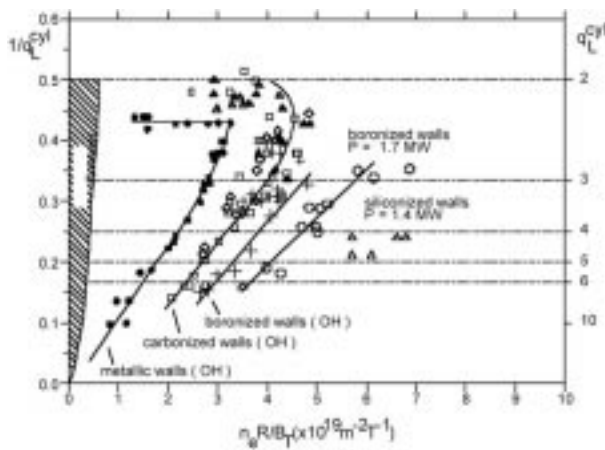


**Figure 55.** Operational density limits for TEXTOR for ohmic (OH) and beam heated plasmas for different surface conditions. Data for metallic walls are for hydrogen operation; all others are for deuterium. Data for carbonized walls include carbonized steel limiters and liners (squares and crosses) or graphite limiters and carbonized liner (other labels). (Reproduced with permission from Ref. [679]). Triangles are data points measured recently with siliconized wall conditions [678].

during the discharge. Prior depletion of deuterium in the wall by ohmic conditioning discharges was an essential step in TFTR. Cases where lithium did not make an improvement may be due to existing impurities that consumed the limited quantity of lithium introduced leaving no *free* lithium available to the plasma [553]. Laboratory studies show that chemical reactions with lithium suppress hydrogen and oxygen impurity influxes [553]. Lithium was found to reduce chemical sputtering of carbon by 25%. Physical sputtering was also reduced. Intercalation (mixing) of lithium into graphite was evident, and lithium was preferentially sputtered over carbon, leading to an order of magnitude reduction in net carbon sputtering yield. Materials mixing in the carbon and lithium systems appears to be a key process to successful lithium wall conditioning [687]. Renewed interest in liquid lithium as a plasma facing material [55] makes these low recycling regimes relevant to fusion reactor studies.

In-vessel cryopumps may be used to control recycling by pumping part of the flux recycled from the wall before it reaches the core plasma. This leads to a decrease of electron density and an increase of electron temperature at the plasma edge. The implantation depth is then changed, and deeper wall implantation occurs leading to an increase in parti-

cle pumping by the walls. Only with active pumping has it been possible for JET to obtain ELMy H mode plasmas of density near or at the Greenwald density limit with acceptable energy confinement time [688]. A pumped limiter or divertor can also be used to control the wall hydrogenic inventory [689–692].

In DIII-D, a cryopump allows pumping of the lower divertor region during discharges [693, 694]. Assessment of the particle balance with the cryopump operating indicated that the wall could actually be unloaded during the course of the discharge, i.e. under certain conditions more particles could be pumped than had been injected into the plasma. The cryopump was found to pump/unload the wall even without helium GDC, resulting in excellent density control and good plasma performance [695].

#### 4.6.3. Hydrogen isotope recycling

Carbon plasma facing surfaces retain hydrogen (H, D or T) energetically implanted from the plasma (Section 3.5.3) and can subsequently release it, affecting plasma density and performance [653, 696, 697]. The capacity of the wall to retain H depends on incident ion energy and wall conditions [654]. The wall conditioning procedures described in Section 4.6.2. can change the hydrogen content and increase particle recovery after a discharge [34, 697, 698]. In the absence of gas fuelling or external active pumping, the wall alone can fuel a low-density plasma [696]. If higher densities are needed, gas injection is used to drive the plasma-wall equilibrium to a higher density. In the presence of carbon walls, the fuelling efficiency of gas injection is low (1–20 %) [31] as most of the injected gas is trapped directly in the walls. With the introduction of Be in JET strong pumping was observed which increased the fuelling required by a factor of 4 [699, 700] and allowed the attainment of a very high ion temperature [101]. A comparison of wall deuterium retention and plasma fuelling requirements in the ASDEX-Upgrade, DIII-D and TdeV tokamaks is reported in Ref. [701].

Recycling fluxes are composed of particles coming out from the wall reservoir and particles from the plasma that are backscattered or reflected directly by the wall (about 20% of impinging particles in the case of carbon [383]). The recycled flux raises the neutral density in the plasma edge and the flux of energetic charge exchange neutrals to the wall. These neutrals carry energy out of the plasma edge, thereby cooling it.

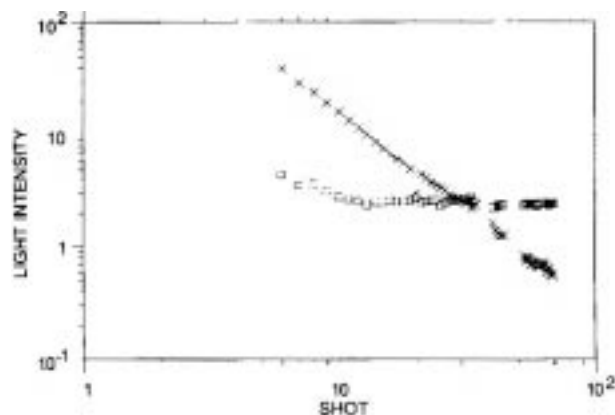


**Figure 56.** Deuterium (×) and carbon (□) influx in helium discharge cleaning pulses following a 1 MA ohmic disruption in TFTR. (Reproduced with permission from Ref. [109].)

In many cases the highest plasma confinement and DD neutron production has been obtained in low-density discharges with low hydrogenic recycling such as negative central shear, supershot, hot ion H mode and VH-mode discharges [702–704]. All these regimes rely on wall conditioning procedures (Section 4.6.2), in order to reduce recycling. In axisymmetric divertor machines, the H mode transition is also strongly related to the control of particle influxes, although the causal linkage is not entirely understood [705–707]. Low recycling fluxes are also needed to obtain reproducible startup conditions and obtain a good plasma current rampup.

A major handicap to a detailed understanding of recycling processes is the difficulty of directly measuring the atomic ratio of H/C on the plasma facing surfaces during a plasma discharge. In TFTR the ratio of  $D_{\alpha}$  to C II emission (see glossary) was used during supershot conditioning as a convenient measure of wall conditions [109] (Fig. 56). A sensitive characterization of the wall was obtained by measuring the tritium concentration in the JET subdivertor during the DTE1 experiments [518]. A predischage estimation of wall saturation status of Tore Supra was derived from the small plasma currents during the initial phase of the discharge when the poloidal coils are energized [708].

In the absence of measurements of H/C in the wall, we can consider only the balance between the particles added to the vessel and those removed, the difference being the number of particles retained in the vessel walls [654, 709, 710]. Such empirical reservoir models are described in Section 5.5.

Recent tritium experiments offered new opportunities to track hydrogen isotopes. Fuelling of the plasma core by recycled deuterium was derived from the DT neutron rate in TFTR plasmas with tritium only NBI [33]. The DTE1 campaign at JET in 1997 allowed a detailed study of hydrogenic isotope recycling and retention in a pumped divertor configuration relevant to ITER. There appear to be two distinct inventories of retained tritium: dynamic inventory and inventory controlled by co-deposition.

The dynamic inventory, i.e. hydrogen (deuterium and tritium) recycling, is governed by implantation and isotopic exchange of charge exchange neutrals in a thin layer over the whole vessel surface area [204]. Since a relatively low particle flux over a large area is involved and the hydrogen content of the wall is large compared to the content of the plasma, modest reductions in the wall inventory produce large wall pumping effects, which persist for many discharges. In some materials the implanted hydrogen may diffuse beyond the implantation depth during the discharge, and this may also contribute to the observed wall pumping [711]. The high tritium retention fraction (>90%) observed in L mode experiments in TFTR was due to isotope exchange with deuterium in the wall (Section 4.7.1.1).

In the second category, co-deposition of hydrogen leads to a continually growing inventory, trapped in co-deposited layers (Section 3.5.3.6). The inventory of co-deposited hydrogen plays a small role in the particle balance of a single discharge, but grows continually and ultimately dominates the hydrogenic inventory. Fuel balance studies of wall pumping in TEXTOR-94 also show these two components to hydrogen retention [712, 713].

From the PMI point of view, long discharges permit us to explore conditions close to a reactor. Control of recycling is important as the current drive efficiency decreases when plasma density increases [660]. Also, control of the radial density profile and, therefore, of the recycling sources is essential for generating non-inductive bootstrap currents, another way to achieve long pulse operation. Today, only two machines have achieved long pulse operation at relatively high plasma density. In JET, 60 s duration discharges showed an uncontrolled increase in density [651]. Discharges of up to 120 s duration were realized on Tore Supra with the help of lower hybrid current drive [125]. The Tore Supra vessel is maintained with a wall temperature higher than 420 K by means of a 3 MPa water loop system. However, an increase of plasma density (which accelerates in time)

was observed (Fig. 53). The higher the injected and radiated powers, the sooner the increase of density appeared. This behaviour was not due to exhaustion of the pumping capacity of the wall. No evidence of wall saturation during these long discharge pulses was found, probably because of the low density operation, which is needed to obtain good current drive efficiency [125, 660, 714]. Instead, the behaviour was correlated with an increase of the oxygen and hydrogen (protium) plasma density. It is attributed to water desorption induced by wall heating due to the power radiated from the plasma. The water originates from surfaces that are far from the plasma and are not baked during the conditioning procedures usually used at Tore Supra [660].

Apart from the limitation on the heat exhaust capability on Tore Supra, the observed increase of the electron density during long pulse discharges is a barrier to achieving steady state operation. This underlines the importance of having an effective steady state particle exhaust scheme for long pulse operation. The Tore Supra Upgrade project 'CIEL' (see glossary) [715] addresses this issue by the installation of a toroidal pumped limiter.

#### 4.7. Database on H isotope retention and removal

Mechanisms of hydrogen retention in metals and carbon have been discussed in Section 3.5. Here, we review experience gained from retention of hydrogen isotopes in various operating tokamaks, with emphasis on the two tritium fuelled devices, TFTR and JET. Global tritium retention and isotope exchange have been studied during tritium fuelled plasma experiments in TFTR and JET, mainly by comparing tritium recovered to tritium input. From the JET data, however, it will be shown that the global retention of T in these short experiments is enhanced by isotope exchange with the pre-existing D inventory. Thus the likely long term retention from sustained operation in DT is best estimated from the D retention. Long term studies of deuterium retention in large tokamaks also provides additional information on where and how retention occurs, how it varies for different plasma facing materials (carbon versus metal), and how it depends on machine geometry (limiter versus divertor) and operating conditions. These comparisons reveal the mechanisms controlling fuel retention and suggests methods to reduce it. The observed magnitude and distribution of deuterium retention in different tokamaks

showed that co-deposition with carbon is the dominant long term fuel retention mechanism in tokamaks with carbon PFCs. This co-deposition often results in the retention of a large fraction of deuterium used to fuel plasmas. The much lower deuterium retention observed in machines with high Z metal rather than carbon PFCs, such as C-Mod with molybdenum and ASDEX-Upgrade with tungsten divertor strike points, indicates a way to substantially reduce fuel retention. Tokamaks fuelled solely with deuterium provide also T related experience since the transmutation of D in the plasma produces equal numbers of 1 MeV tritons and 2.4 MeV neutrons. The probability of the DD fusion reaction is about one-three-hundredth of the DT rate, so the quantity of T produced is quite small. Typically, tritium is present in the exhaust gas, retained in the dynamic wall inventory and incorporated in the deposited layers at a ratio of T:D of  $1:10^6$ – $10^7$  [716].

This section also reviews controlled laboratory and tokamak experiments on the removal of co-deposited H–C layers. The experience gained from studies of hydrogen isotope retention and removal in tokamaks, particularly tritium removal in TFTR and JET, is of paramount importance for understanding underlying mechanisms and for assessing the impact of tritium retention on design and operation of next step devices.

##### 4.7.1. Fuel retention in tokamaks

###### 4.7.1.1. Fuel retention in TFTR, carbon limiter

*Deuterium fuelling in TFTR.* Before tritium fuelled plasma operation in TFTR, there was an extensive evaluation of the anticipated in-vessel tritium inventory and the constraints that this would impose on the DT experimental programme. To establish a basis for predicting future tritium inventory, the in-vessel inventory of deuterium was followed from 1986 through 1991.

An initial comprehensive study of D retention was made following the operational period from November 1985 to July 1987 [495, 717]. During this period TFTR produced 9922 high power plasmas with nearly circular cross-section. The plasma boundary was defined by contact with a limiter of graphite tiles on the inner wall subtending poloidal angles from  $60^\circ$  below to  $60^\circ$  above the midplane with a total area of  $22 \text{ m}^2$ . The base temperature of first wall components in TFTR was normally about 320 K. However, the surface temperature rose during the discharge, with hot spots up to 1070 K or higher.

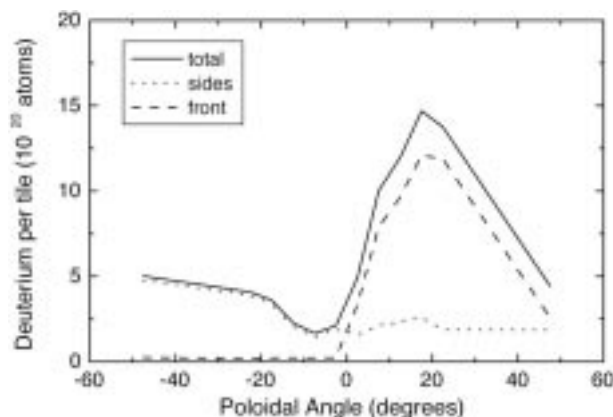


**Figure 57.** Retained deuterium on tiles from the TFTR bumper limiter. Deposition in the gaps between tiles dominates retention in regions of net erosion on the plasma facing surfaces (poloidal angle  $<0$ ).

In-vessel beta backscattering [718] and ion beam analysis of removed tiles showed net erosion occurring over approximately one third of the limiter area and net deposition over the remaining two thirds. The regions undergoing net erosion were also observed to be the regions receiving the highest heat and ion fluxes [719–721].

Optical and electron microscopy on limiter tiles showed a layer of deposited material up to tens of micrometer thick, with a large volume fraction of open porosity on regions of net deposition, [718]. Ion beam analysis showed this deposited material to consist of mainly carbon and deuterium, with small amounts of other elements (several atomic percent of oxygen and about 1 at.% of metal atoms (Cr, Fe, Ni)).

Thick layers of deposited material were also found on the sides of the limiter tiles, i.e. in the gaps between tiles [495, 717], especially on tiles where net erosion of the plasma facing surface was high (Fig. 57). This pattern of deposition shows that on tiles undergoing net erosion, there is a large flux of carbon onto nearby regions shaded from erosion by direct ion flux, such as the gaps between tiles. In TFTR, the deuterium deposited in the gaps between limiter tiles was a significant fraction of the total in-vessel inventory of deuterium (see Table 13).

Hydrogen might also penetrate into porosity common in nuclear graphites, beyond the range of energetic implantation. This was examined in graphite tiles from TFTR [495, 717] and ASDEX-Upgrade [722]. The deuterium concentration (measured by NRA) in the bulk of a TFTR graphite tile was too low to contribute significantly to the in-vessel inven-

**Table 13.** Deuterium retention and fuelling in TFTR.

Year	D retained			D fuelling		% retained
	total (g)	% BL face	% BL gap	% wall	total (g)	
1987	5.3	50	11	39	24	22
1988	5.7	40	33	27	9	63
1989	7.3	57	13	30	18	41
1990	11	55	12	33	22	50
1991	4.3	18	8	74	10	43
Total	33.6	47	15	38	83	40

BL = bumper limiter.

tory of deuterium. A similar result was found in a study of graphite tiles from the ASDEX-Upgrade divertor [722], which examined near surface D retention by NRA, total D retention by TDS and the spatial distribution of D and deposited material. Earlier work [532] concluding that diffusion dominates D retention in ASDEX-Upgrade divertor tiles misinterpreted the large effect of surface roughness on the depth distribution of co-deposited deuterium.

Ex situ ion beam analysis of wall coupons from TFTR gave a detailed picture of deuterium and carbon deposition on the vessel wall. Deposition was fairly uniform toroidally but was several times higher at the top and bottom of the vessel than at the outer midplane because of the proximity of the source of the carbon, which is the graphite limiter. The high D/C ratio of 0.33 indicates that the rate of D accumulation on the wall is determined by the carbon deposition rate rather than by the flux of deuterium onto the wall.

The D retention in TFTR was followed from 1987 through 1991 [717]. Each year, a standard set of limiter tiles and wall coupons were removed and analysed for deuterium accumulated during the preceding run period. Beta back scattering and ion beam analysis showed that regions of net erosion and deposition on the limiter remained similar from year to year.

Table 13 summarizes the deuterium inventory in TFTR determined from these studies and the corresponding plasma fuelling during each run period. These data show the range of variation in D retention observed over several years with changing machine operating conditions. Over the five year period, a total of 33.6 g of deuterium was retained in the vessel and a total of 83 g of deuterium was used to fuel plasmas. Therefore, during this five year period, 40% of the deuterium used to fuel plasmas remained inside

the vessel. Of this retained deuterium, 47% was on the plasma facing surface of the limiter, 15% was in the gaps between limiter tiles and 38% was in the remaining vessel wall.

Deuterium retention in TFTR was also examined by fuel balance methods in which the quantity of deuterium injected into the plasmas as gas or neutral beams was compared with the quantity of deuterium recovered by the vessel pumping system [723]. In deuterium neutral beam heated plasmas the fraction of D retained increased from 25 to 65% with increasing neutral beam power [202]. Higher power input to the plasma appears to cause greater carbon erosion and thus more co-deposition. Also, the C II emission increased with NBI power, indicating a more intense interaction of the plasma with the limiter. Although the short term D retention from fuel balance varied depending on recent operating history, on average, the fraction of D retained was large, consistent with the D inventory estimated from component analysis. In contrast, fuel balance measurements on plasmas, fuelled with helium showed that the fraction of helium recovered was very close to 100%. Energetically implanted helium is retained in carbon, but at lower concentrations than D, and the retained He is thermally released at lower temperatures since it is not chemically bound to the C, i.e. it is less strongly bound than D [724, 725]. The weaker binding of helium in carbon is due to the absence of chemical binding, which makes co-deposition ineffective at retaining helium.

The studies of D retention in TFTR showed that the primary physical mechanism for long term D retention was co-deposition of D together with carbon eroded from the limiter by the plasma. In the period from 1985 to 1991, a total of 33.6 g of D was retained in the vessel, which was about 40% of the D used to fuel plasmas. This D retention was consistent with results from fuel balance studies [723] and accurately predicted the long term tritium retention observed during subsequent tritium plasma operation [535, 726].

The retention of T resulting from DD operation in TFTR has been found to be consistent with the D retention, at about 50% of the T [495, 727].

**Tritium fuelling in TFTR.** TFTR operated with DT fuelling in three separate campaigns in the period 1993 to 1997 [121]. After each campaign there were extensive cleanup programmes to remove tritium retained in the vessel. Over the 3.5 years, a total of 100 g of tritium were processed, including 3.1 g of tritium injected into the plasma via NBI and 2.1

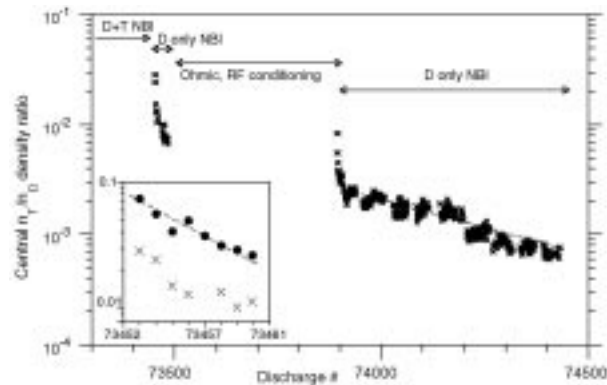


**Figure 58.** The decay, in between periods of tritium injection, of the central ( $r/a < 0.2$ ) T/D density ratio, as derived from the DT/DD neutron ratio. The long term decay (starting at discharge #73950) followed a time constant of 404 discharges. The short-term decay is shown in the inset: (●) is the  $T_\alpha/(H_\alpha + D_\alpha + T_\alpha)$  ratio showing the T influx from the limiter and (×) the central T/D density over 9 deuterium discharges following a sequence of tritium NBI discharges. (Reproduced with permission from Ref. [731].)

g by gas puffs. Deuterium discharges were used to optimize particular plasma conditions before tritium was injected and the overall isotopic fuelling was 3% T/D.

Tritium exhaust was pumped by the liquid helium cooled cryopanel in the neutral beam boxes and/or by turbopumps in the torus vacuum pumping system. The tritium inventory recovered from the turbopumps and cryopanel was measured by parallel plate ion chambers in the gas holding tanks to an accuracy of typically 5–7% [535]. However, much of the torus fuelling was by NBI, and only 4% of the T supplied to the neutral beam boxes entered the torus, the rest being pumped directly by the cryopanel. Thus the error in the measurement of the exhaust is comparable to the amount of T entering the torus, which makes a shot by shot estimate of the retained T difficult.

At the beginning of the DT campaign in TFTR,  $7.47 \times 10^{21}$  T atoms (360 Ci) were injected into the torus by 21 DT neutral beam heated discharges (most of which only used one T beam source) in two batches, interspersed with 55 DD pulses. The maximum T concentration seen from the Balmer alpha profiles in these experiments was 7.5% [728–731]. In the absence of further tritium fuelling, tritium decreased with an initial decay constant of 7.5 discharges, which then slowed down to a decay constant of 404 discharges, as shown in Fig. 58 [731].

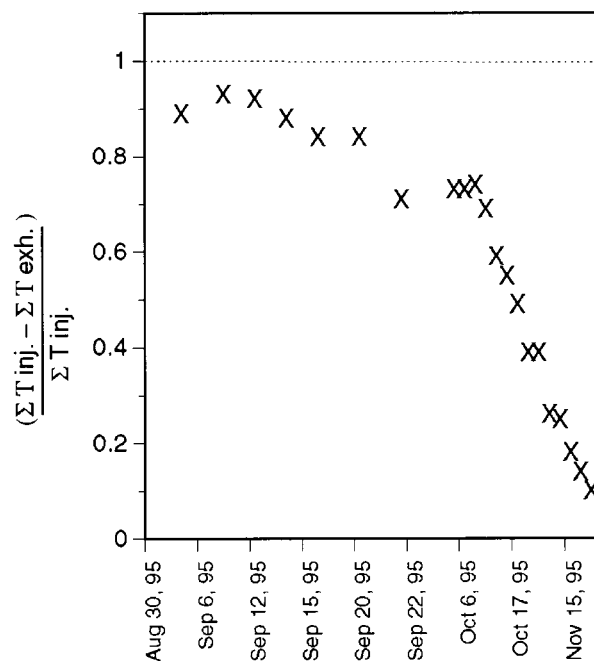


**Figure 59.** High retention during tritium gas puffing into TFTR during September to November 1995. The fractional retention is defined as the ratio of the cumulative tritium injected less the cumulative exhaust, divided by the cumulative tritium injected. (Reproduced with permission from Ref. [535].)

In September 1995, experiments were performed in L mode plasmas on the isotope scaling of transport and on the efficiency of RF heating. These experiments required for the first time significant amounts of T gas puffing. An accurate measurement of the short term retention was made possible by closing off the torus pumping system and reserving one of the four beamlines solely as a pump for the exhaust. The total torus tritium exhaust was estimated as four times that recovered from the reserved beamline. With strong tritium gas puffing the short term retention rose to above 90% and the  $T_\alpha/T_\alpha + D_\alpha$  fraction observed in the Balmer alpha spectrum increased to 75%. In contrast,  $T_\alpha$  was relatively slow to appear in T-NBI fuelled discharges, the maximum  $T_\alpha/T_\alpha + D_\alpha$  fraction was only 11% after 8 T only NBI discharges [732]. The Balmer alpha spectrum reflects the isotopic composition of hydrogen recycled from the limiter [733] and clearly much of the tritium gas puff went to the limiter. A subsequent D fuelled conditioning phase restored the limiter to a low recycling state for ‘supershot’ [703] operations (Fig. 59).

During the three periods of high temperature plasma operations (excluding periods dedicated to

tritium removal), approximately 51% of the tritium supplied to the plasma was retained in the vacuum vessel [201, 734]. Active tritium removal during maintenance periods was successful in removing substantial amounts of tritium and kept the tritium inventory below the 2 g administrative limit [735, 736]. Removal techniques are listed in Table 14. Air ventilation was found to be the simplest and most effective method of T removal. Generally, relatively more T was released as the vessel temperature and/or air pressure was increased. Some T was tenaciously held and not released, an important consideration in assessing consequences of potential accident scenarios (Section 2.3.3). With these techniques, the in-vessel tritium inventory was reduced to 0.85 g by April 1998, i.e. the long term retention (including cleanup) was  $\approx 16\%$  of the tritium input. The outgassing rate was less than  $\approx 0.1 \text{ mg}\cdot\text{day}^{-1}$ , and the radiological decay rate was  $\approx 0.2 \text{ mg}\cdot\text{day}^{-1}$  [734].

Tritium in the outermost  $\approx 1 \mu\text{m}$  of the in-vessel surfaces was detected by configuring the vacuum vessel as an ionization chamber and measuring the secondary electron current resulting from the tritium beta decay [737]. This was performed during the tritium removal phase following the 1997 operations and the technique calibrated by noting the current rise after injecting a known quantity of T as a gas. The current measured prior to the injection corresponded to 1600 Ci (0.16 g-T) about  $\approx 10\%$  of the in-vessel inventory at that time. During the clean-up it appeared that all the near surface T was removed, as the collected current fell almost to zero. This was paralleled by a fall of  $\approx 3500 \text{ Ci}$  (0.35 g) in the inventory, after which the inventory was  $\approx 14\,700 \text{ Ci}$  (1.5 g), all of which was perhaps more than  $1 \mu\text{m}$  from the surface. Even though it can only detect T close to the surface, beta decay, has potential for providing an in situ monitor of the near surface inventory in a tokamak, and this technique may well be useful in future machines [737].

Flaking of co-deposited layers has been observed [573, 738]. This phenomenon was unexpected and occurred after the termination of plasma operations (Section 4.8). Tiles, flakes, wall coupons, a stainless steel shutter and dust samples have been retrieved from the TFTR vessel for analysis [574]. Selected samples have been baked to release tritium and assay the tritium content. The in-vessel tritium inventory is estimated to be 0.56 g and is consistent with the 0.64 g in-vessel tritium inventory derived from the difference between tritium fuelling and tritium exhaust. TFTR experiences co-deposition on the out-

**Table 14.** Summary of tritium removal techniques used in TFTR and JET.

Machine operation:	Comments	
	TFTR	JET
D tokamak pulses	Ineffective	Tokamak pulses in deuterium reduced the In-vessel inventory at end of DTE1 by a factor of 2; T removal by pulses $\approx 10 \text{ mg} \cdot \text{d}^{-1}$ .
He-GDC	Ineffective	Ineffective
D-GDC	Initial removal rate high ( $>18 \text{ mg} \cdot \text{h}^{-1}$ ), falling to $1 \text{ mg} \cdot \text{h}^{-1}$ , from exposed areas. Average removal rate: $1 \text{ to } 30 \text{ mg} \cdot \text{h}^{-1}$ .	Ineffective. Rarely used in DTE1 because of large gas processing load on AGHS. Amount of T released negligible ( $\approx 40 \text{ mg}$ ).
D <sub>2</sub> gas soaks	Ineffective	Ineffective
Outgas	Ineffective	Ineffective
ICRF	Not applied	Pulses with RF heating (ICRF) used in June 1997 before repair of beam box. Removed more tritium than ohmic pulses; ‘sweeping’ strike point also increased T release. Wall inventory reduced from 4.4 to $\approx 2.9 \text{ g}$ in $\approx 120$ pulses
ECRH plasma discharges	Not applied	Gas load on AGHS much smaller but negligible T removal, and no reduction in T fraction
He/O-GDC	Rate: $\approx 5 \text{ mg} \cdot \text{h}^{-1}$ – constant with time	Not applied
N <sub>2</sub> vents	Not applied	Ineffective
Disruptions	Can release T by flash heating of surface. 0.014 g recovered after one major disruption; other times no release seen.	Not quantified
Pulse Discharge Cleaning (PDC)	Heats limiter to $\approx 520 \text{ K}$ . 100 mg T removed over 23 h. Average removal rate: $4 \text{ mg} \cdot \text{h}$ .	Not applied
Boronization	Little tritium released; most near surface tritium previously removed.	Not applied
.....		

**Table 14.** Cont.

Machine operation:	Comments	
	TFTR	JET
Baking divertor surfaces normally cooled	Not applied	Before venting, divertor support structure (normally $\approx 310 \text{ K}$ ) heated to $\approx 410 \text{ K}$ . Small amount (6 mg T) desorbed at high T/D ( $\approx 1.8\%$ )
Vessel venting	Air at 718 torr released 220 mg of T in $<1 \text{ h}$ ; $\approx 24 \text{ h}$ to process the air.	2 g T released in four months air ventilation of torus for post-DTE1 shutdown
Remote tile exchange	Not applied	Divertor tiles, carriers and flakes physically removed (containing) $\approx 0.6 \text{ g T}$ .

board stainless steel vessel wall because of the large carbon source from the TFTR bumper limiter. The average tritium areal density in co-deposits on the outboard wall was  $32 \text{ Ci} \cdot \text{m}^{-2}$ , compared to the average density on the bumper limiter of  $87 \text{ Ci} \cdot \text{m}^{-2}$ . The outboard area is five times larger however, and co-deposits on the outboard wall account for two thirds of the total tritium inventory, consistent with the large contribution from the wall to long term D retention (see Table 13). Relatively high concentrations of tritium were found at the top and bottom of the bumper limiter, as predicted by earlier modelling (Section 4.3.2) [201].

4.7.1.2. *Fuel retention in JET, limiter and divertor, beryllium and carbon*

*Deuterium fuelling in JET.* Long term deuterium retention has been closely followed in JET since 1985 by analysis of components removed after each operational campaign [494, 699, 739–741]. These studies include periods of operation with limiter and with divertor plasma configurations, and with both carbon and beryllium first wall materials. By 1988, 55% of the geometric surface area of the wall was covered with graphite or CFC tiles, including all surfaces exposed to ions traveling along field lines. The carbon components included tiles covering the inner wall, two toroidal belt limiters on the outer wall, and 40 poloidal rings of carbon tiles. After the ‘all-carbon’ campaign completed in May 1988, the total long term D retention in the vessel from about 2500 plasmas was estimated, from hundreds of measurements of D on tiles and long term samples, to be 3.6 g

or about 17% of the D input during the campaign [740, 741]. About 1000 of these discharges were with the 'X point' open divertor configuration in which the upper X point is just inside the poloidal limiters. On the toroidal belt limiter tiles and poloidal X point tiles, regions of net erosion with lower D coverage were seen at locations of highest power flux. Most of the D inventory was associated with relatively small regions of deposited material close to regions of high power flux. During this campaign, the mean daily retention of D in the vessel was estimated from fuel balance to be about 40% of the gas input [700]. The difference in retained fraction from fuel balance and component analysis is largely due to D removed during venting and He glow discharge cleaning, which was not included in the fuel balance analysis. Considering this, the D retention estimated by these two methods is in good agreement.

Beryllium was introduced into JET in two stages. First, Be was periodically evaporated onto the entire inner wall, then a few months later the graphite toroidal limiter tiles were replaced with Be tiles. The introduction of Be did not significantly change the long term average quantity of D retained per pulse. Also, the distribution of long term D retention within the vessel after operation with Be was similar to that for the 'all-carbon' (see glossary) phase of 1988 [741]. However, during operation with Be, the amount of D required to fuel the plasmas increased by about a factor of four compared to fuelling for 'all-carbon' operation [699, 741] (Section 4.6.3). This increased fuelling is due to a larger dynamic wall inventory, as mentioned in the previous section, i.e. D which is absorbed by the wall during discharges and then released between discharges. The presence of Be on, or mixed with C, at a significant proportion of the in-vessel surfaces clearly affects the adsorption properties. The observations are consistent with the model [204] that the dynamic inventory is controlled by implantation of charge exchange neutrals into a thin surface layer over the entire vessel surface area, whereas long term D retention is dominated by co-deposition of D with material eroded by the plasma from localized regions of high power flux. However, the thin evaporated Be film is quickly removed from regions undergoing net erosion at locations of highest heat flux, leaving erosion and redeposition of the carbon, and hence long term D retention, little affected by the Be evaporation.

To improve upper X point open divertor operation, the top of the vessel was fully covered by car-

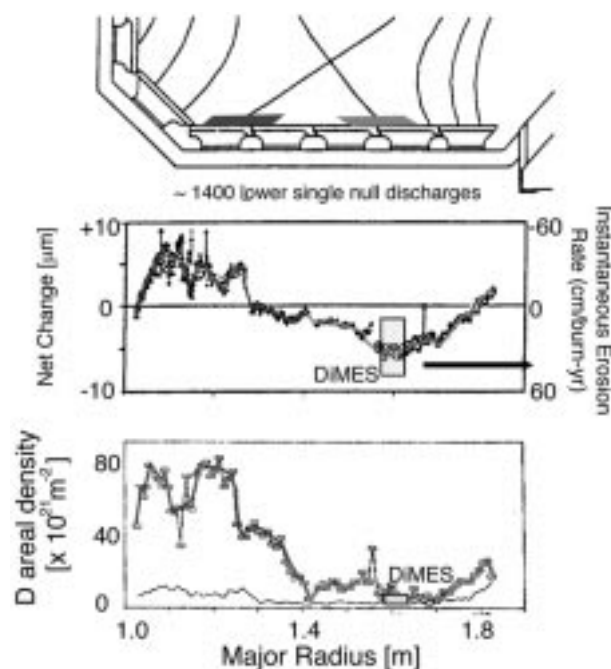


**Figure 60.** Retained deuterium and net erosion on tiles from the DIII-D divertor. (Reproduced with permission from Ref. [743].)

bon tiles early in 1991 and modifications to improve power loading were made in August 1991. The tile shapes provided shaded regions on adjacent tiles, so that no edges would be exposed to excessive heat flux due to imperfect tile alignment. While in the vessel, these tiles were frequently coated with thin Be films of fairly uniform thickness from the sublimation sources. Analysis of D and Be coverage on these X point tiles after the run campaign [699, 740, 741] revealed regions of net erosion, with low D and Be coverage, at locations of highest power flux at the inner and outer strike points. Areas of heavy net deposition with high coverage of D and Be were present on nearby regions of lower power flux, particularly near the inner strike zone and in the private flux region. Also, heavy deposition on shaded surfaces in the strike zones show there was local redeposition of carbon from the plasma onto surfaces shaded from ion flux.

Deuterium retention with open divertor plasma configurations and carbon tiles at the strike points has also been examined in DIII-D and JT-60U. [493, 742]. In DIII-D the pattern of long term D retention was consistent with measured long term erosion/deposition on the divertor as shown in Fig. 60. The long term net erosion at the outer strike point is also consistent with erosion from short



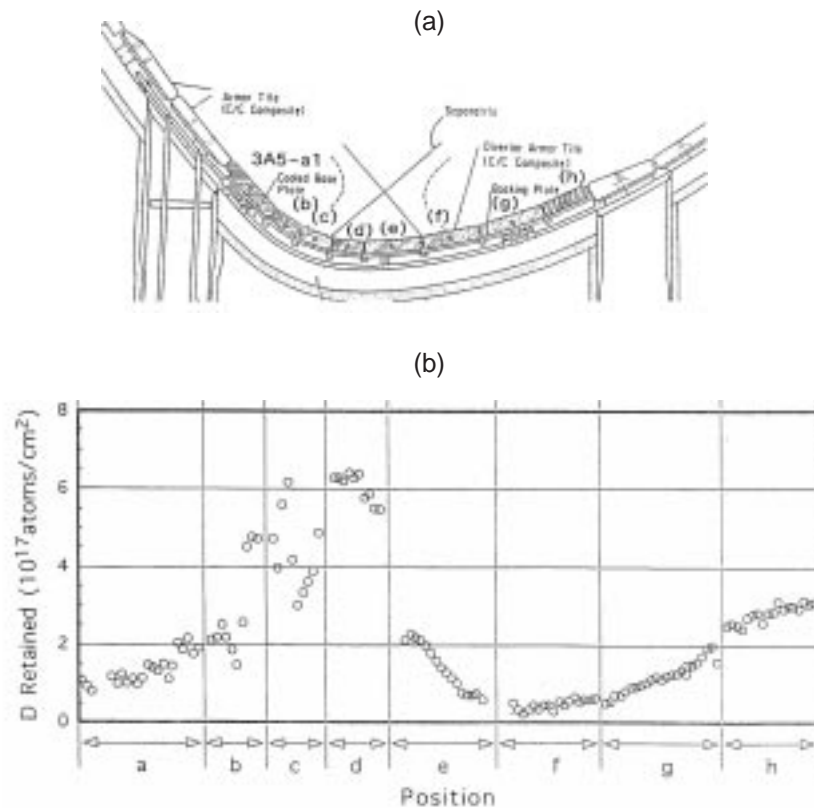


**Figure 61.** (a) Poloidal cross-section of the JT-60U divertor. (Reproduced with permission from Ref. [742].) (b) Retained deuterium on divertor tiles in JT-60U. (Figure provided by K. Masaki, JAERI.)

term exposures to well defined plasma conditions measured using the DiMES facility on DIII-D [743] (Section 4.3.1).

In JT-60U, the lowest D coverage is at the outer strike point, while the highest D coverage is near the inner strike point as shown in Fig. 61 [742, 744].

These results indicate that net carbon erosion occurs from plasma facing surfaces near the outer strike point where the fluxes of power and energetic particles are highest. D coverage remains relatively low on surfaces undergoing net erosion. The eroded carbon is redeposited in the gaps between tiles and onto plasma facing surfaces near the inner strike point where the plasma is often detached and the power flux and particle energies are lower than at the outer strike point. The redeposited carbon incorporates deuterium at concentrations of  $\approx 0.2$  to  $0.4$  D/C. In regions of net deposition the areal density of deuterium, therefore, just depends on the thickness of the deposited layer. Similar patterns of net erosion at the outer strike point and deposition

at the inner strike point are observed on DIII-D, ASDEX-Upgrade and JET [64].

JET operated with a toroidal divertor in the bottom of the vessel with CFC tiles from April 1994 to March 1995, and with Be tiles from April to June 1995. A cross-section of this Mk-I divertor is illustrated in Fig. 62. Tiles were attached to a water cooled support so their ambient temperature was  $\approx 320$  K. In contrast, all PFCs had ambient temperatures of at least 570 K before installation of the Mk-I divertor. Each divertor tile was inclined along the toroidal direction to shade the edge and some of the surface (typically 15 to 50%) of the adjacent tile to protect tile edges from excessive heat flux. Subsequent to these two campaigns, tiles were examined by NRA for near surface D, Be and C [494].

The most striking feature of the distribution of D on the carbon divertor tiles is the heavy accumulation of D in the shaded areas at the strike and SOL regions, i.e. on shaded surfaces adjacent to regions of net erosion (Section 4.3.1). Regions exposed to

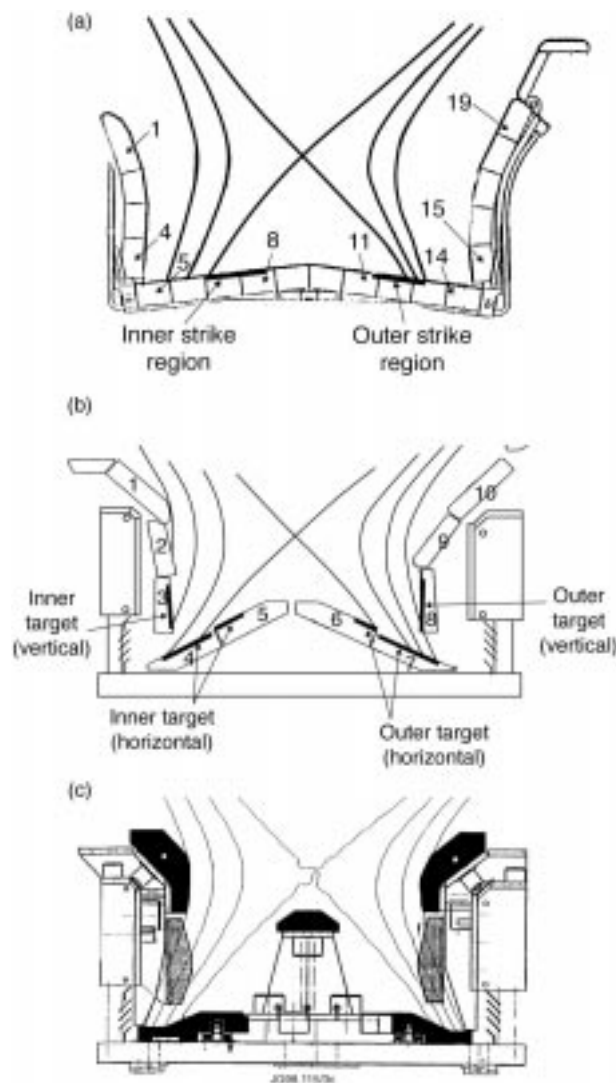


**Figure 62.** Geometry of (a) Mk-I, (b) Mk-IIA and (c) Mk-II Gas-Box JET divertors. (Reproduced with permission from JET.)

ion flux had low D coverage, indicating net erosion. Also, the D coverage was much higher on the inner leg of the divertor than on the outer leg. Similar patterns of heavy deposition in shaded areas were seen on the inner side-wall tiles as well as on the inner floor tiles, but the outer side-wall tiles had low coverage of D. Within the private flux zone, D coverage was low both inside and outside the shaded regions.

The amount and distribution of D on the Be tiles in the inner half of the divertor was similar to that for the graphite tiles, however, on the outer half of the divertor there was much less D retained on the Be than on the carbon tiles. Ion beam analysis showed that the heavy deposits on the Be tiles were predominantly carbon and not beryllium and that the regions

exposed to ion flux, i.e. of net erosion, were mainly beryllium with little carbon. This leads to the conclusion that even with a Be divertor, D retention is largely due to co-deposition with carbon transported into the divertor from the main chamber. For most of the discharges with the Be divertor, the main plasma impurity was carbon, not Be. Furthermore, carbon must be redistributed by local recycling within the divertor until it reaches shaded areas, which act as sinks. The fact that these deposits are predominantly carbon indicates that local recycling transports carbon more efficiently than Be. This may be due to molecular effects, present in carbon for not for Be (Section 4.3.1). Similar low Z deposits were found on the W divertor in ASDEX-Upgrade (Section 4.7.1.3).

Long term samples exposed at the wall of the JET main plasma chamber to  $\approx 940$  discharges between April and June 1995 revealed net erosion of the surface [745], in contrast to TFTR where the wall is an area of net deposition. This difference is probably due to different impurity transport in the SOL for limiter and divertor configurations. Co-deposition and long term retention of D on the JET main chamber wall is restricted to the sides of poloidal limiters. The majority of the main chamber wall is a source of impurities due to erosion by charge exchange neutrals. Graphite components in the main plasma chamber could thus be the source of carbon deposited onto the Be divertor.

The Mk-IIA divertor (Fig. 62) was designed to be more closed than the Mk-I divertor, which it replaced, and to exhaust particles through gaps between the floor and side wall modules at the inner and outer corners making it more like the ITER divertor design. D retention in the Mk-IIA divertor was dominated by co-deposition with carbon beyond the inner corner of the divertor on the louvres and the tile surfaces adjacent to the pumping gap. The pattern of deposition indicated mainly line-of-sight transport from the strike zone or pumping gap many centimetres into regions shielded from ion flux. This indicates that the carbon is transported as neutral atoms or C-containing molecules (Section 4.3.1). The films on surfaces facing the inner pumping gap were measured to be  $\approx 40 \mu\text{m}$  thick and were seen to flake-off from metal surfaces such as the louvres, probably on venting the vessel. Ion beam analysis of the flakes gave D/C ratios as high as 0.8 [235]. It was estimated that this heavy co-deposition inside the inner pumping gap resulted in additional long term retention of at least 6% of the gas fuelling, and this also resulted in higher than expected retention

of tritium during subsequent tritium fuelled plasma experiments.

During maintenance periods in between deuterium operations at JET and, similarly at TFTR, tritium resulting from DD operations was released from the PFCs by isotopic exchange with water molecules [746–748]. Tritium has been found in the exhaust gases from deuterium plasma operations. The percentage of tritium retained (i.e. not recovered in the exhaust) was higher than that of D in both JET [700] and JT-60U [749, 750]. Analysis of tritium in PFCs and exhaust gases shows that 50% or more of tritium produced by  $D(D,p)T$  nuclear reactions in JT-60U, during the period between July 1991 and October 1993, remained inside the vessel,  $\approx 80\%$  of the retained T was in the first wall, and 20% in the divertor region [751]. The content of T from D plasma operation was also measured in DIII-D first wall tiles by collecting DT gas released by baking tiles outside of the vessel at 1270 K [752]. The fraction of T retained was estimated to be 10% or more. Ratios of T/D, measured in DIII-D divertor tiles, were in the range from  $10^{-7}$  to  $10^{-6}$  [753].

Tritium on the first wall of JET was surveyed after the 1986 campaign, and on some components from 1987 [754]. Graphite tiles from the limiters, inner wall and upper X point region were removed from the vessel and analysed, together with graphite coupons bolted to several locations on the inner surface of the vessel wall. The majority of the T retained in the vessel was found in the graphite PFCs. Overall, the largest amount of T remaining in the vessel was present in the inner wall tiles, although the highest concentrations were found locally at the limiters ( $10^{12}$  tritons·m $^{-2}$ ). The T distributions on the tiles match more closely the patterns of retained D, and the overall T inventory indicated a fraction of the T generated in the campaign was retained [754], similar to that of the D fuelling retained [716].

A depth profile for the T in a JET inner wall tile was derived by removing  $\approx 3$   $\mu\text{m}$  slices at the surface using a fine emery paper, and progressively thicker slices into the bulk. The majority ( $\approx 98\%$ ) of the T was present within the first 25  $\mu\text{m}$ , for which the profile is shown in Fig. 63 [754], however, this is less localized than the D, which is almost exclusively in a 3  $\mu\text{m}$  film at the surface. Profiles of tritium (from DD operations) into the surface of tiles from ASDEX-Upgrade were obtained by Accelerator Mass Spectroscopy (AMS) [755]. The maximum T level was located 3 to 5  $\mu\text{m}$  from the surface, with some evidence of diffusion (together with D) into the

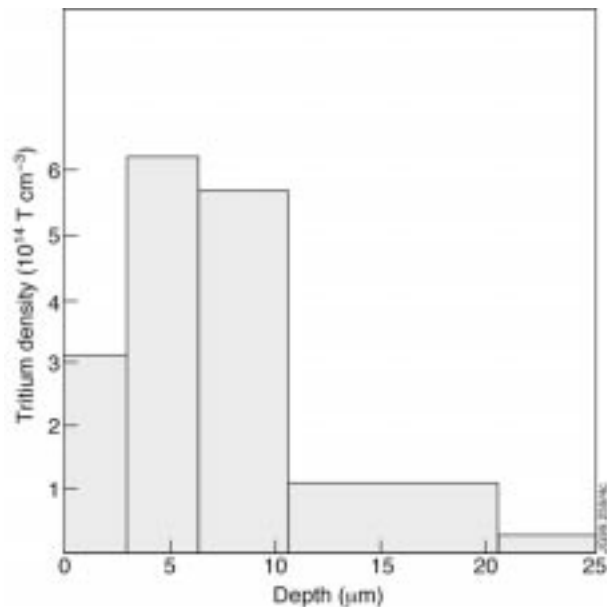


**Figure 63.** The tritium depth profile for the near surface region of the JET midplane inner wall graphite tile. (Reproduced with permission from Ref. [754].)

bulk (see also Section 3.5.3.1 and Ref. [459]). These data, together with the relative fractions of D and T released on venting or to the pumps, suggest that T has a greater mean energy distribution at the wall, and is implanted more deeply into the surface.

*Tritium fuelling in JET.* Experiments with tritium fuelling in JET began with the preliminary tritium experiment (PTE) in 1991. Tritium was introduced into two pulses by injection from two of the sixteen neutral beam sources. This followed a series of discharges when the two sources were fed with a mixture of 1% T in D to check operational procedures, diagnostics, and transport codes for T in D plasmas [756]; the total T entering the torus during these trace tritium experiments was  $\approx 3 \times 10^{19}$  atoms. The JET machine at this time was fitted with two belt limiters, but the plasma contacted special shaped tiles at the top of the vessel, which were used as an open divertor (the so-called ‘X point’ configuration). A total of  $\approx 2 \times 10^{22}$  atoms ( $\approx 0.1$  g) of T were introduced into the NBI system, but only a total of  $(1.10 \pm 0.09) \times 10^{21}$  T atoms were injected into the torus over the two pulses; each source injected  $0.75 \times 10^{20}$  atoms·s $^{-1}$  at 78 keV. The T beams corresponded to 13% of the total beam fuelling, as the remaining 14 sources operated in D, and were on for 3.5 s during a 25 s discharge. T was injected into a plasma fuelled with D, and although the T concentration in the plasma reached  $\approx 10\%$ , the proportion

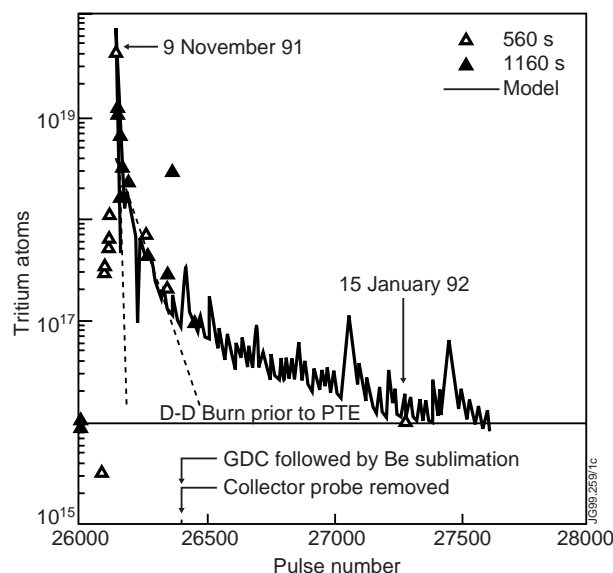


**Figure 64.** Number of tritium gas atoms released from the JET vacuum vessel as a function of pulse number for the PTE campaign and subsequent cleanup. The data are integrated for the first 560 s (open triangles) or 1160 s (closed triangles), and the solid curve is the prediction of a model. (Reproduced with permission from Ref. [756].)

of the total T gas input for each pulse was only 1.3% [757]. The peak fusion power generated during each pulse was 2 MW [716].

Over the weekend following the two high yield PTE pulses,  $(3.7 \pm 0.6) \times 10^{20}$  T atoms were recovered by the Gas Collection System (GCS). Thus, including a small residual amount of T from the setting-up experiments, the remaining torus inventory was  $(7.4 \pm 1.1) \times 10^{20}$  T atoms. Following the next two weeks of clean-up experiments, this retained inventory was reduced to  $(1.5 \pm 1.4) \times 10^{20}$  T atoms. Analysis of a collector probe exposed during the PTE and removed at this time gave an estimate of the retention in the vessel of  $1.8 \times 10^{20}$  atoms, in excellent agreement with the value from the GCS [757]. By the end of operations, three months later (which included an accidental venting to air when  $4 \times 10^{18}$  atoms were released), the retained inventory was reduced to  $(1.0 \pm 1.4) \times 10^{20}$ . Figure 64 shows the gas sample measurements, and the fit to a recycling model described in Ref. [756].

During the shutdown, three months after the PTE, a representative selection of tiles were removed from all parts of the first wall. The tritium content of the tiles was determined by outgassing pieces of the tiles, combusting to form HTO and scintillation counting [758]. The T was distributed round the vessel in a reasonably uniform manner, except for a

higher concentration in the tiles protecting the inner wall from neutral beam shinethrough. The majority of the T remaining on the X point target tiles was contained within deposited layers. From the measurements, the total T remaining in the vessel was estimated to be  $(3.4 \pm 1.7) \times 10^{19}$  atoms, or about 3% of the T fuelling.

During 1997, JET was operated for an extensive period using deuterium–tritium plasmas. This experimental campaign was known as ‘DTE1’, and the main physics results are reported in Refs [122, 123, 759]. The Active Gas Handling System (AGHS) delivered tritium to both the torus as gas fuelling and the NBI systems and was able to provide accurate measurements of the amount of tritium supplied to each system [760]. All the gas exhausted from the torus was returned to the AGHS, where T was separated from other elements and returned to the uranium beds where it was stored. The AGHS thus operates as a complete closed cycle, and since the T inventory is always measured in the same way, the amount retained in the torus is accurately known.

The main difference to the JET in-vessel configuration since the time of the 1991 PTE [756–758, 761] is the presence of the pumped divertor, together with a toroidal cryopump, a cross-section of which is shown in Fig. 62 (Mk-IIA). Pumping slots in both corners of the divertor allow neutral particles to be pumped by the cryopump. The divertor support structure is water cooled, and, as a result, the base temperature of the divertor tiles is 470 K, significantly lower than the ambient temperature of the rest of the torus ( $\sim 590$  K). Water cooled louvres, located in the pumping slots, shield the divertor cryopump and divertor coils from direct line-of-sight with hot surfaces and particles, while allowing the transmission of particles to the cryopump. Conditioning of the vessel is maintained by occasional evaporations of Be from four sources near the outer midplane.

The DTE1 campaign was separated into two phases by an interruption to repair the NBI system. It was necessary to clean up for the repair, and the tritium fraction in the plasma and in the exhaust gas was reduced to  $T/(T + D) \approx 0.01$  in about four days of pulsing in deuterium. Of the deuterium techniques, only tokamak pulses were found to be effective in reducing the T content of subsequent plasmas. Other techniques that were tried are listed in Table 14. However, it was not possible to reduce the tritium inventory to below  $\approx 17\%$  of the tritium input to the torus by plasma operation [203].

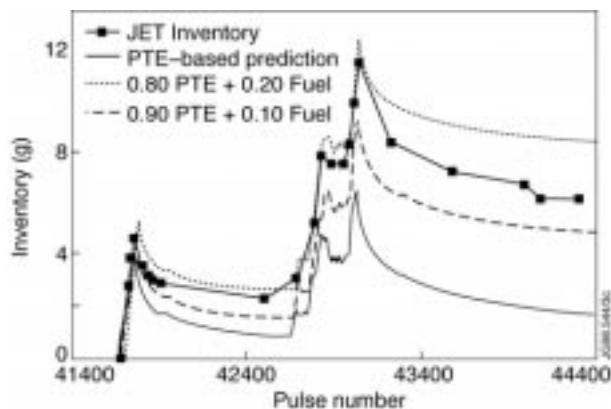


**Figure 65.** Tritium inventory in the JET vessel (measured as the difference between the tritium fuelling and the amount recovered from the vessel) plotted against pulse number for the 1997 DTE1 campaign. Also plotted are predictions of the inventory based on the behaviour during the PTE campaign of 1991, made by (i) merely scaling up the amount of T fuelling, (ii) adding an extra retention equal to 10% of the fuelling, and (iii) adding an extra retention equal to 20% of the fuelling. (Reproduced with permission from Ref. [741].)

Operation was resumed after the NBI repair with about one month of deuterium operation. The plasma tritium fraction during this time fell very slowly and lay in the  $10^{-3}$  range. Then, tritium operation was resumed, this time with both NBI and gas fuelling of the tritium. After the last tritium pulse, operation with pure deuterium plasmas reduced the tritium fraction to about  $T/(T + D) \approx 10^{-2}$ . At this level, approximately 25% of the total neutron production is due to DT neutrons [203, 204].

During DTE1, a total of 100 g of tritium was delivered by the AGHS, of which 65% went to the NBI system at Octant 8. 35 g of tritium was introduced into the torus: 0.6 g by NBI (which has an overall efficiency of  $\approx 1\%$ ), and the remainder by gas puffing. Figure 65 shows the torus tritium inventory [741] as a function of pulse number. The maximum tritium inventory in the torus during DTE1 (just after the last T fuelled pulse) was  $\approx 11.5$  g, i.e. more than half of the 20 g of tritium on site.

The plasma tritium fraction in DTE1 was accurately predicted by comparing with the tritium fraction observed in the exhaust gas following injection of 5 mg of tritium during the PTE campaign. The number of pulses to change over from one isotope to another was very similar to the PTE based prediction, despite the absence of an in-vessel cryopump during PTE. However, as shown in Fig. 65, the in-

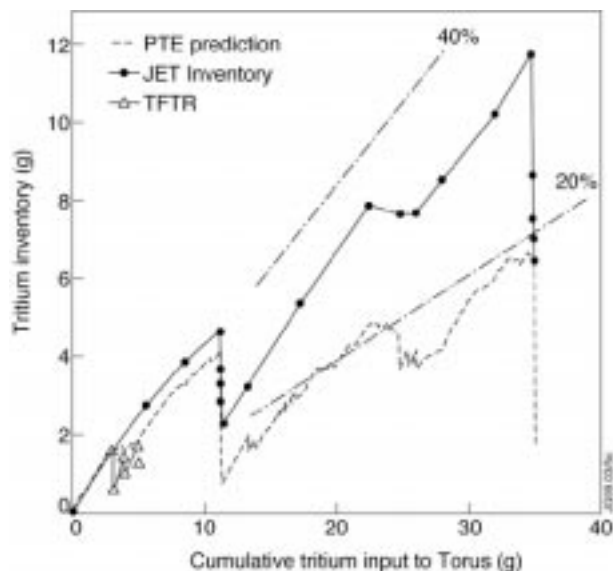


**Figure 66.** Tritium inventory in the torus versus cumulative tritium input during the JET DTE1 campaign. (Reproduced with permission from Ref. [203].)

vessel T inventory is very different in DTE1 compared to the expectation based on the PTE. The tritium inventory in DTE1 could only be reduced by a factor of about two by pulsing in deuterium, whereas in the PTE a much more complete recovery was achieved. By the end of the Mk-IIA divertor campaign, about 6 g of tritium remained in the torus, i.e. 17% of the 35 g input, and this amount was being reduced by only  $10 \text{ mg} \cdot \text{day}^{-1}$ . The tritium inventory is also shown in Fig. 66, but as a function of the cumulative tritium input to the torus [203]. Total gas balance measurements indicate that about 85% of the input gas is recovered, and approximately 15% of the total input is retained [741]. This is consistent with the tritium retention following pulsing in D.

The greater long term retention in DTE1 compared with PTE is due to deposition in regions not in contact with the plasma, which, hence, cannot be cleaned up by subsequent plasma operation. Following a period of operations with the Mk-IIA divertor before DTE1, heavy deposition was found on the water cooled louvres through the pumping slot at the corner of the inner divertor (Section 4.3.1) [235, 741, 762]. The deposits have high D/C ratio ( $\approx 0.7$ ) [762, 763] since they are at low temperature and shaded from the plasma. This deposition appeared to be an extra mode of retention since the time of the PTE (when there were neither water cooled surfaces nor a cryopumped divertor in the vessel). In contrast, no deposition could be seen in the

**Table 15.** Comparison of retention in TFTR and JET

	TFTR	JET
Edge $n_e$ ( $\text{m}^{-3}$ )	$10^{18}$ – $10^{19}$	$10^{20}$
Edge $T_e$ (eV)	200–600	<30
Total $T$ injected, NBI	3.1 g	0.6 g
gas puff	2.1 g	34.4 g
Initial retention during $T$ gas puff fuelling (mostly isotope exchange)	$\approx 90\%$	$\approx 80\%$
$T$ retained during DT operation (excluding cleanup)	2.6 g (51%)	11.5 g (40%)
Longer term retention (mostly co-deposition)	51%	17%
$T$ remaining in torus	0.6 g May 2000	2.1 g Dec 1999
Long term retention	12%	6%

region of the louvres at the outer divertor. Figure 65 also shows predictions if an additional 10 or 20% of the fuelling is retained (for example in deposits not accessible to the plasma). Good agreement with the data is obtained assuming such an additional retention of  $\approx 15\%$ . This is also consistent with the measurements of gas balance referred to in the previous paragraph, and is the origin of the 20 times greater chronic release rate on venting the torus [203, 204].

During the shutdown following DTE1, 2 g of  $T$  were recovered from the purge gas. Bakeout of the JET vessel following this shutdown, and venting in Summer 1999 and the subsequent bakeout, released another 1.25 g of  $T$ . In total, tritium release by these ‘active’ methods (3.25 g) thus reduced the inventory by more than one half, as was also the case for TFTR. The various techniques to reduce the  $T$  inventory in the torus used by JET and TFTR and their effectiveness are summarized in Table 14.

Analysis programmes have been carried out to provide mapping of the  $T$  levels around the vessel, and particularly in the divertor; the results are shown in Fig. 67. Also, a photograph of a section of the louvres with flakes is reproduced in this figure [518]. The total retention in the divertor tiles (which were removed at the end of DTE1) was only  $\approx 0.1$  g  $T$ , with a similar amount remaining in the limiter tiles in the main chamber. Depth profiling measurements have been made on a number of JET tiles exposed during DTE1 [459]. More tritium was found in the

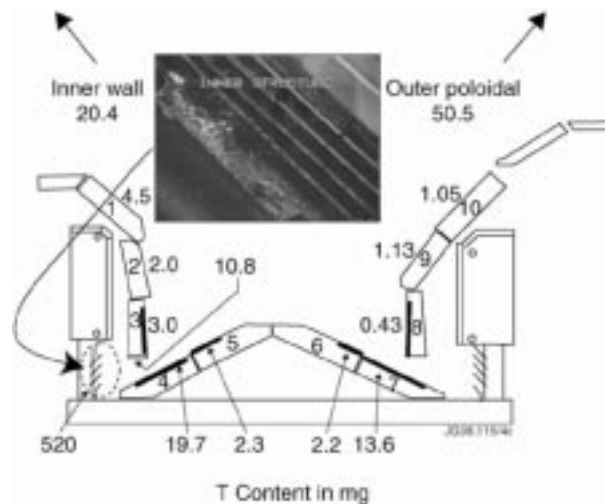


**Figure 67.** Distribution of tritium in the JET vessel in the shutdown following DTE1. The amounts at each location are integrated around the torus. (Reproduced with permission from Ref. [764].). The photograph in the inset shows a typical region of the flaking deposition on the louvres at the inner corner of the JET Mk-IIA divertor. (Reproduced with permission from JET.)

bulk of CFC than graphite tiles, possibly due to migration along the fibre planes. This bulk content would require reduction by a large factor before the tiles could be classified as low level waste. Flaking deposits (154 g) were removed from the vicinity of the inner louvres, containing 0.52 g tritium (measured by calorimetry) (Section 4.8.3) [763]. Taking into account the 3.25 g released by venting and baking, this means there are  $\approx 2$  g  $T$  unaccounted for in the vessel. This  $T$  is believed to be present in the large quantities of flakes that have been seen by remote inspection under the divertor structure, having fallen from the inner louvres [764].

A comparison of tritium and deuterium retention in JET and TFTR shows striking similarities and contrasts. The beginning of tritium gas puffing led to close to 100% retention in TFTR due to isotope exchange with deuterium (Fig. 59). Furthermore, the global retention of  $T$  in JET remained at 40% in the comparatively short DTE1 campaign, and did not saturate [204]. This enhancement is due to isotope exchange with the pre-existing  $D$  inventory. Thus, for JET the likely long term retention from sustained operation in DT is best estimated from the  $D$  retention. Table 15 groups the TFTR and JET operational periods in order to reveal similarities in the retention due to isotope exchange and co-deposition. In both machines the long term retention was dominated by

co-deposition near the principal plasma interaction zones (the inboard limiters in TFTR and the (inner) divertor in JET). Many of the areas of co-deposition are shadowed from the plasma; so their T content cannot be removed by pulsed D operation. After extensive clean-up efforts, the long term T retention in TFTR was 0.6 g (12%) on 3 May 2000 and in JET 2.1 g (6%) on 31 December 1999.

#### 4.7.1.3. *Fuel retention with high Z metal at the strike point*

In Alcator C-Mod, the plasma contacting surfaces are molybdenum tiles. Erosion and deuterium retention are expected to be much lower than in tokamaks with graphite as the main plasma contacting material. Measurements were made of erosion and deuterium coverage on the plasma facing surfaces of a set of Mo tiles exposed to 1090 plasmas in Alcator C-Mod between November 1995 and March 1996 [113, 213]. These measurements give in-vessel deuterium inventories of 0.10 g outside the divertor and 0.0025 g inside the divertor, which are much smaller than those found on graphite limiter and divertor tiles in JET, TFTR and DIII-D. Tritium retention resulting from DD operation in C-Mod was also dramatically lower than that in carbon machines. The fraction of DD tritium retained was determined to be less than 0.2% [213].

Boronization is periodically applied in Alcator C-Mod [43]. The boron thickness is much greater than the range of energetic D from the plasma; therefore, most of the D retention is due to implantation of D into the boron layer, probably via energetic charge exchange neutrals onto the main vessel wall. Retention of D implanted into boron is similar to that of D implanted into carbon. D is retained in the implanted layer until a saturation concentration is reached. The areal density of D retained after saturation depends on the thickness of the implanted layer, and hence on the energy of the D. In tokamaks, D retention by this mechanism should saturate at an areal density in the range from about  $(1-3) \times 10^{21}$  D·m<sup>-2</sup> in agreement with the observed D areal density outside the divertor in C-Mod. Also, measurements of D depth profiles on tiles from the inner wall showed the D to be within the boron film.

The only region of net Mo erosion in Alcator C-Mod was near the outer strike point where  $\approx 0.15$  μm of net Mo erosion was measured and the surface boron layer was absent. Thus, the quantity of eroded material is small. The D depth profile measured by

NRA on a region of net Mo erosion shows that diffusion of D into the Mo gives bulk concentrations too low to significantly impact in-vessel D inventory. The main difference between D retention in Alcator C-Mod and tokamaks with graphite divertors or limiters is that in Alcator C-Mod there was no significant accumulation of material redeposited by the plasma.

In the period between March 1991 to July 1995, ASDEX-Upgrade operated with a lower single-null plasma configuration with a divertor consisting of graphite tiles. During this time, the divertor tiles were exposed to about 1900 plasma discharges. Subsequently, tungsten coated graphite tiles (500 μm plasma sprayed W layer with nearly full toroidal coverage of a region 160 mm wide at both the inner and outer strike point) were installed in the divertor. From December 1995 to July 1996, the W coated tiles were exposed to about 800 plasma discharges. At the end of this W divertor campaign, divertor tiles and components from the main plasma chamber were removed and analysed. These two campaigns provide a unique comparison of low Z versus high Z divertor material with similar geometry (ASDEX-Upgrade Div I in Fig. 45) and plasma conditions.

For the graphite divertor tiles removed in 1995, the peak deuterium areal density was about  $3 \times 10^{23}$  D·m<sup>-2</sup> on the inner divertor and about a factor of 2 lower on the outer divertor [532, 722]. The deuterium was observed to be present in deposited material consisting mainly of carbon, boron, H and D of non-uniform thickness owing to the roughness of the substrate [722]. The total amount of H and D in the graphite divertor tiles was estimated to be about  $7 \times 10^{23}$  atoms or about 2 g [532].

On the W divertor tiles, the highest D areal density ( $\approx 5 \times 10^{22}$  D·m<sup>-2</sup>) was measured in the shaded region of the inner divertor, outside the separatrix. The D areal densities on the W inner divertor plate were several times lower on the unshaded than on the shaded regions. On the outer W divertor plate, the D areal densities were about ten times less than on the inner W divertor and were about the same in shaded and unshaded regions. In the case of the W divertor experiment, more than 50% of the total in-vessel D inventory was on the inner divertor while less than 10% was on the outer divertor [594]. The total amount of D retained on divertor tiles during the W divertor experiment was  $1 \times 10^{23}$  atoms (0.3 g) [765] which is seven times less, or about three times less per shot than during previous operation with a graphite divertor and is about 2% of the D

input [765], whereas during previous operation with a graphite divertor, a major part of the hydrogen and deuterium puffed into the plasma chamber was retained in the divertor [532].

With both the graphite and W divertors, the inner divertor was found to be completely covered by a layer of low Z material a few  $\mu\text{m}$  thick. On the outer divertor the deposition was discontinuous on the scale of the surface roughness [594, 722], and the deposited low Z material was found in microdepressions of the rough surface, which are shielded from re-erosion, whereas adjacent protruding parts of the rough surface undergo net erosion and were not covered by low Z material. The areal density of deposited low Z atoms was about five times less on the outer divertor than on the inner divertor [594], which is sufficient to account for the much lower areal density of retained D by co-deposition. The similar distributions of deuterium and low Z deposition shows that for both the graphite and W divertors the dominant mechanism for deuterium retention is co-deposition of D with low Z elements, mainly carbon and boron, onto the surface. Also, in general, deposition dominates on the inner divertor, while erosion prevails on the outer divertor (Fig. 45).

The D coverage was also measured on graphite PFCs from the main plasma chamber following the W divertor experiment. These surfaces, which do not have direct plasma contact, had areal densities of  $(1\text{--}2) \times 10^{21} \text{ D}\cdot\text{m}^{-2}$ . The observed magnitude and poloidal distribution of this retained D is consistent with a model based on implantation of charge exchange neutrals from the plasma [594]. Even though the area is large, this mechanism does not dominate long term D retention, because retention by this mechanism saturates at a relatively low coverage due to the small thickness ( $<0.1 \mu\text{m}$ ) of the implanted layer.

The observations that the average quantity of D retained per shot, or fraction of D input retained, is about three times less with the W divertor than with the graphite divertor, and that the D is mainly in regions of net deposition on the inner divertor, indicate that with the graphite divertor, D retention is mainly due to co-deposition of D with carbon eroded from the outer divertor. Removing this major source of carbon erosion (with the use of the W divertor) greatly decreased D retention with no adverse effects on plasma conditions.

In 1997, ASDEX-Upgrade began operation with a new divertor geometry (illustrated in Fig. 45 AUG Div II LYRA), which used CFC tiles. In this new

geometry, the strike points are on nearly vertical tile surfaces and the pumping slots are between the strike points, i.e. in the private flux region. Local maxima in D coverage were observed at both the inner and outer strike points, as shown in Fig. 45. Plasma edge modelling indicates that for the Div I geometry the plasma electron temperature is high enough to cause erosion at the outer strike point but not at the inner strike point, whereas for the Div II geometry the electron temperature is below the threshold for erosion at both the inner and outer strike points [559]. In this case, the source of carbon deposition in the divertor is thought to be due to wall erosion [115].

In summary, a large fraction (10–50%) of hydrogen-isotope fuelling of all tokamaks with carbon PFCs is retained in the torus, principally by co-deposition. This will seriously impact the operation or design of next step machines and makes the development of efficient removal techniques imperative (next section).

#### 4.7.2. H isotope removal from C based co-deposited layers

Tritium removal from amorphous tritiated carbon layers, a-C:T, co-deposits in next generation tokamaks, such as ITER, has an important impact on machine operation. If in situ co-deposit removal techniques are fast and effective, both in terms of T removal and plasma performance recovery after cleanup, then the long term T retention/inventory problem could be mitigated.

In principle, tritium could be removed from materials via thermal desorption or ion-induced desorption. However, the temperature requirement for thermal desorption from C based materials is much higher (typically,  $>900 \text{ K}$ ) [456] than the design temperatures for PFCs (typically,  $500 \text{ K}$ ) [3, 211]. Ion induced desorption at room temperature, or ion isotope exchange in the case of H, D, and T, is limited to depths corresponding to the ion range, typically a few nanometres for plasma discharges, and therefore, will not reach the trapped T in the tens of micrometres thick co-deposits. Thus, the removal of T from thick a-C:T co-deposits may require the removal of the co-deposits themselves. This can be done by chemical and/or plasma assisted oxidizing reactions in the presence of oxygen or, alternatively, via abrasive/mechanical techniques.

Oxygen free techniques for tritium removal have been proposed but need further development.  $\text{CO}_2$  pellet blast cleaning is widely used in the semicon-



**Table 16.** Thermo-oxidative and plasma discharge techniques for a-C:T co-deposit removal\*.

Technique	Merits	Shortcomings	Comments
Air/O <sub>2</sub> exposure with hot walls	<ul style="list-style-type: none"> <li>– Good removal efficiency and short cleaning time is expected at wall temperature &gt;520 K;</li> <li>– accessibility of non line-of-sight and shaded regions, gaps, etc.</li> </ul>	<ul style="list-style-type: none"> <li>– Needs partial venting;</li> <li>– ratcheting effects could limit cleaning at 510 K (max. temperature in ITER);</li> <li>– limited tokamak practice (air in TFTR; O<sub>2</sub> in TEXTOR).</li> </ul>	Further R&D is needed (e.g. effects from mixing of materials).
ECR + oxygen	<ul style="list-style-type: none"> <li>– Does not require vent or opening of the vacuum vessel;</li> <li>– some tokamak conditioning experience exists (e.g. JFT-2);</li> <li>– can be applied in the presence of strong magnetic fields.</li> </ul>	<ul style="list-style-type: none"> <li>– erosion is line-of-sight (shaded areas are eroded by neutrals but at much lower rates);</li> <li>– expected low erosion rates;</li> <li>– very limited tokamak practice (Alcator C-Mod; ECR was ineffective in JET).</li> </ul>	Significant R&D is needed.
ICR + oxygen	<ul style="list-style-type: none"> <li>– Does not require vent or opening of the vacuum vessel;</li> <li>– some limited R&amp;D for ITER;</li> <li>– some tokamak conditioning experience (TEXTOR, Tore Supra);</li> <li>– can be applied in the presence of strong magnetic fields.</li> </ul>	<ul style="list-style-type: none"> <li>– Erosion is line-of-sight;</li> <li>– mechanisms are not well understood.</li> </ul>	Significant R&D is needed.
GDC + oxygen	<ul style="list-style-type: none"> <li>– Well established tokamak practice;</li> <li>– does not require vent or opening of the vacuum vessel.</li> </ul>	<ul style="list-style-type: none"> <li>– TF needs to be off; long shutdown;</li> <li>– low film removal efficiency for ITER;</li> <li>– limited access to shaded areas.</li> </ul>	

\* All of these techniques require the introduction of oxygen into the torus and thus will require conditioning to remove the residual oxygen and water to recover plasma operation. Further work with all of these techniques is also required to determine the effects of collateral damage.

ductor and nuclear industries [211]. Preliminary tests using existing equipment at the Sandia National Laboratories [766] did remove the surface layer from a graphite tile from the DIII-D tokamak but also severely eroded the tile. Laser surface heating is an alternative technique [767]. This takes advantage of advances in laser technology to rapidly heat co-deposited layers with a high power scanning laser beam. Recent experimental tests have removed 84% of the tritium on co-deposits on TFTR tiles [766]. This technique offers the potential for tritium removal in a next step DT fusion device without the use of oxidation and the associated deconditioning of the plasma facing surfaces and without the expense of processing large quantities of tritium oxide.

Another possible cleaning technique for use in fusion reactors is cathodic arc cleaning (also known as transferred arc cleaning) [768, 769]. Transferred arc cleaning utilizes a DC plasma torch and a secondary power supply attached between the torch (anode) and the part to be cleaned (cathode). The

torch produces a plasma which becomes the electrical conduction path for the cleaning arc. The arc attachment to the cathode is influenced by the surface shape, the surface roughness and surface contaminant layers (oxide, organic and/or metal film). The cathode contaminant layers are preferential sites for arc attachment. This is caused by ion charge buildup on the contaminants producing an enhanced electric field that increases in strength until breakdown of the film occurs resulting in arcing to the cathode [770]. Joule heating of the cathode causes erosion of the contaminant layer and the bulk cathode material beneath. As the contaminant is removed, electron emission ceases and the arc is displaced to another area with remaining contaminant. This process continues until the contaminants are removed.

Here, we shall review attempts and available results obtained for co-deposit removal using thermo-oxidative and plasma discharge techniques. The merits and shortcomings are summarized in Table 16.

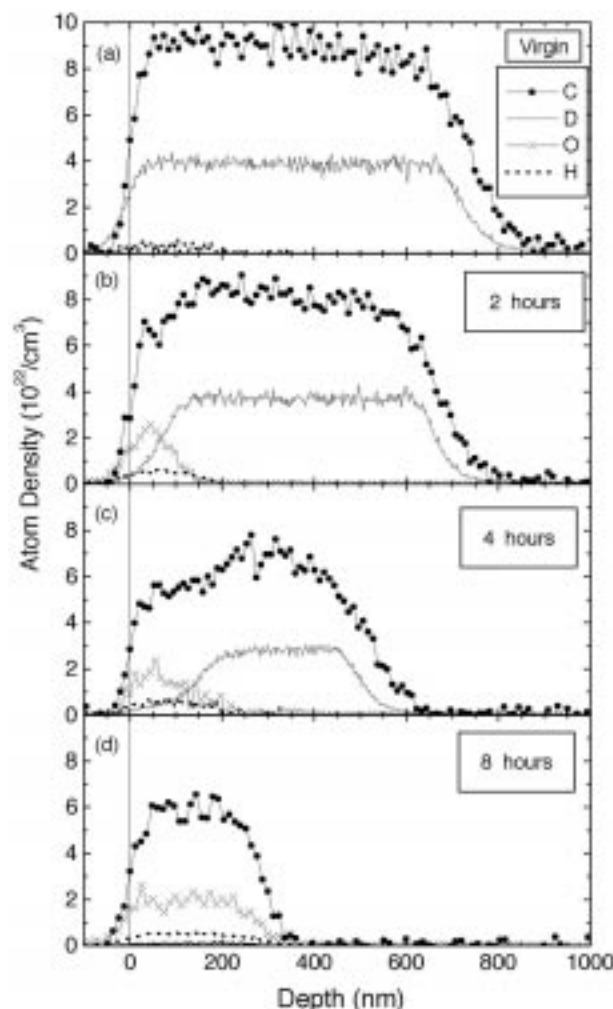


**Figure 68.** Depth profile changes in carbon, deuterium, oxygen and hydrogen in a-C:D films due to air exposure at 650 K: (a) before annealing, (b) after annealing for 2 h, (c) after annealing for 4 h, and (d) after annealing for 8 h. The original film thickness was 730 nm. For each temperature step a fresh sample was used. (Reproduced with permission from Ref. [475].)

#### 4.7.2.1. Laboratory studies on co-deposit removal via high temperature oxidation

Extensive laboratory studies of hydrogen isotope removal rates on exposing co-deposited films and D implanted graphite to air or oxygen have led to the following conclusions: (i) the release of D occurs in conjunction with C erosion [207–210, 475, 771] and (ii) the D removal and C erosion rates depend strongly on the film structure.

The D release rate during oxidation is a critical function of the annealing temperature and is significant even below 900 K, the temperature needed for thermal desorption in vacuum [456]. At a fixed

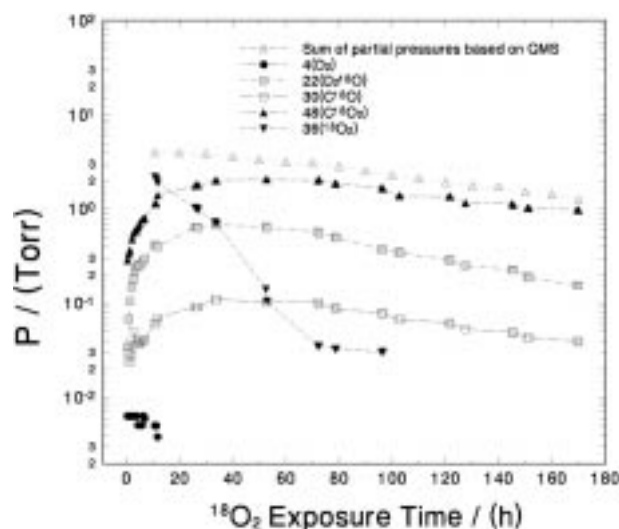


**Figure 69.** Partial pressure of reaction products formed during  $^{18}\text{O}_2$  exposure of an a-C:D film at 470 K. (Reproduced with permission from Ref. [210].)

temperature of 650 K, the erosion of an a-C:D film was measured as a function of the annealing time in air (Fig. 68). Initially, D was released, and the thickness of the deuterium depleted and oxygen saturated layer increased with annealing time until it finally extended throughout the whole remaining co-deposit layer [475]. Further annealing led to a thickness decrease until the complete layer was removed.

From an analysis of the reaction products formed by exposing a laboratory produced a-C:D film to  $^{18}\text{O}_2$  at 470 K, it was concluded [210] that essentially all of the D is removed via  $\text{D}_2\text{O}$  formation, and C is removed by the formation of  $\text{C}^{18}\text{O}$  and  $\text{C}^{18}\text{O}_2$  (Fig. 69). No  $\text{D}_2$  and no methane were observed. Surface analysis of such a-C:D films after  $^{18}\text{O}_2$  exposure using X ray photoelectron spectroscopy (XPS) and secondary ion mass spectroscopy (SIMS) revealed the appearance of carbonyl groups and an increase of hydroxyl groups due to surface oxidation [475]. Thermal oxidation of hydrocarbon polymers provides a plausible reaction mechanism leading to the emission of  $\text{D}_2\text{O}$ ,  $\text{CO}_2$  and  $\text{CO}$ . This mechanism is consistent with the observed surface complexes [475]. Reaction product analysis performed by Alberici et al. [771] of a laboratory produced a-C:D film exposed to oxygen also showed that  $\text{CO}_2$  dominates the C release, and water, not  $\text{D}_2$ , is the dominant D containing reaction product.

Mixed material effects can be important. The threshold temperature for removal of D and C from carbon silicon layers (a-C:Si:D) by heating in air

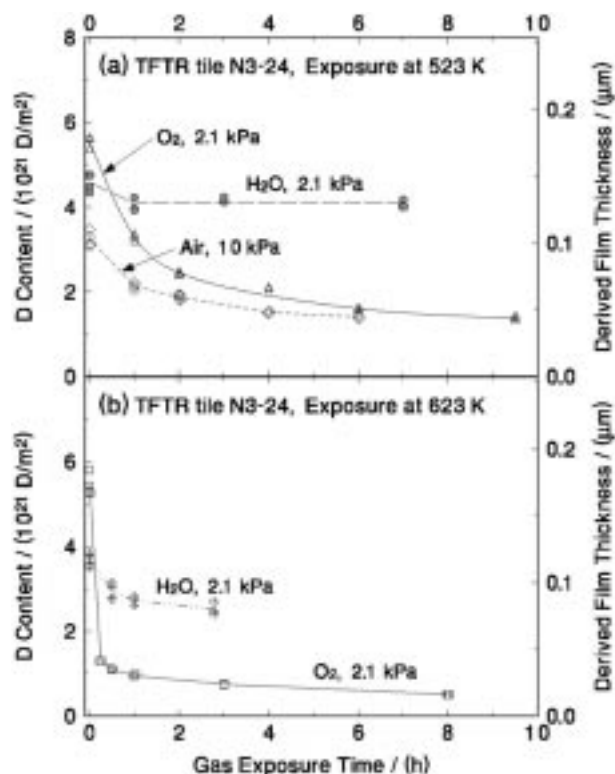


**Figure 70.** D content of TFTR co-deposit as a function of gas ( $\text{O}_2$ ,  $\text{H}_2\text{O}$ , air) exposure time at (a) 523 K and (b) 623 K. (Reproduced with permission from Ref. [209].)

varies with the fraction of Si. For a-C:D layers the removal rate increases strongly above 550 K. With Si concentrations larger than 0.2 Si/(Si + C) the temperature threshold increases to above 650 K [772]. The C removal rate is always lower than the D removal rate and Si is not removed by this method.

D removal from hydrogenated films was also studied under exposure to other atmospheric gases. Nitrogen exposure and heating in vacuum at or below 570 K did not lead to deuterium release from D implanted layers [207]. On the other hand, exposure of D implanted layers [207], as well as TFTR co-deposits [209], to water vapour did result in D removal, but with no evidence of C erosion. It is suggested that D is removed via isotope exchange between the impacting  $\text{H}_2\text{O}$  and the trapped D in the film [207]. Comparing the effectiveness of oxygen and water, oxygen was seen to be considerably more effective in removing the trapped D [207, 209]. While isotopic exchange and reaction of the water with the carbon may occur, the reaction of oxygen directly with the hydrogen and carbon has the greater effect on the release of hydrogen. In the case of the TFTR co-deposit, initial D removal rates in water vapour

were down by factors of four to eight, compared with oxygen under similar conditions (16 torr and 520–620 K). After about 1 h, no further D removal was observed with water, and a considerable amount of D was still left in the specimen [209] (Fig. 70). D removal data obtained in oxygen and air are similar (Fig. 70(a)), indicating that it is the oxygen in air that dominates the film removal process [209].

On the basis of available results, it is evident that the D removal and C erosion rates depend on the film structure and differ greatly for laboratory produced films and co-deposits produced in tokamaks. C erosion rates from laboratory films and D implanted layers are very similar and of the order of a few to tens of  $\text{nm}\cdot\text{h}^{-1}$  at temperatures <700 K [208, 210]. In contrast, measured C erosion rates for tokamak co-deposits are orders of magnitude higher under similar conditions [208, 209]. In Table 17, we show derived C erosion rates and measured D removal rates during oxygen exposure for several co-deposits obtained from major tokamak devices: TFTR, JET and DIII-D. Table 18 contains several measurements for TFTR and ASDEX-Upgrade specimens during water and/or air exposure. We note that C erosion rates in oxygen or air (16 torr) range from  $\approx 0.1$  to  $1 \mu\text{m}\cdot\text{h}^{-1}$  at 523 K to tens of  $\mu\text{m}\cdot\text{h}^{-1}$  at 623 K. The high removal rate for co-deposited films is in part due to their porosity [717] and resulting large surface area available for reaction.

It is evident that tritium can be removed from thick co-deposits of carbon and tritium by heating them in air or oxygen. According to the data in Tables 17 and 18, if a reactor could be heated to approximately 620 K in air, T containing co-deposits of tens of micrometre thickness could be removed within hours. On the basis of these rates, thermo-oxidative removal of co-deposits via air exposure is an option for ITER. Also, the limited experience gained from the controlled oxidation experiments in TEXTOR (see below) and the accidental loss of vacuum in JET [773] shows promising results for post oxidation plasma performance recovery.

It is important to note that two key features of tokamak co-deposits make the thermo-oxidation technique viable for T removal. First, the dominant fraction of retained T in the torus is in co-deposits, and second, the co-deposits erode at rates two to three orders of magnitude higher than the ‘bare graphite’ tiles not covered by co-deposits [774], e.g. walls of current tokamaks and part of the divertor in ITER. Hence, while the co-deposits are eroded — and the trapped T is released —, the thickness of the

**Table 17.** C erosion and D removal rates for tokamak co-deposits during oxygen exposure.

Temp. [K]	TFTR/N3-15 [208, 209] ~5 $\mu\text{m}$ thick ( $\rho \sim 1900 \text{ kg} \cdot \text{m}^{-3}$ ; D/C $\sim 0.35$ ) 16 torr O <sub>2</sub>		TFTR/N3-24 [209] ~0.15 $\mu\text{m}$ thick 16 torr O <sub>2</sub>	
	Erosion [ $\mu\text{m} \cdot \text{h}^{-1}$ ] <sup>a</sup>	D removal [ $\text{C} \cdot \text{m}^{-2} \cdot \text{h}^{-1}$ ] <sup>b</sup>	Erosion [ $\mu\text{m} \cdot \text{h}^{-1}$ ] <sup>c</sup>	D removal [ $\text{D} \cdot \text{m}^{-2} \cdot \text{h}^{-1}$ ] <sup>b</sup>
523	0.8	$5.7 \times 10^{22}$	0.07	$0.2 \times 10^{22}$
573	3.5	$29 \times 10^{22}$		$10 \times 10^{22}$
623	>10	$>70 \times 10^{22}$	>0.5	$1.5 \times 10^{22}$
Temp. [K]	DIII-D# B [209] ~2 $\mu\text{m}$ thick ( $\rho \sim 1300 \text{ kg} \cdot \text{m}^{-3}$ ; D/C $\sim 0.185$ ) 16 torr O <sub>2</sub>		JET divertor 6A [209] ~2 $\mu\text{m}$ thick 16 torr O <sub>2</sub>	
	Erosion [ $\mu\text{m} \cdot \text{h}^{-1}$ ] <sup>a</sup>	D removal [ $\text{C} \cdot \text{m}^{-2} \cdot \text{h}^{-1}$ ] <sup>b</sup>	Erosion [ $\mu\text{m} \cdot \text{h}^{-1}$ ] <sup>c</sup>	D removal [ $\text{D} \cdot \text{m}^{-2} \cdot \text{h}^{-1}$ ] <sup>b</sup>
523	0.23	$1.5 \times 10^{22}$	0.5	$1 \times 10^{22}$
573				
623	3.5	$22 \times 10^{22}$	3.3	$7 \times 10^{22}$

<sup>a</sup> Erosion rate is estimated from measured D content and scanning electron microscopy (SEM) photos of film thickness, assuming constant D/C.

<sup>b</sup> C erosion rate is estimated from measured D content and D/C ratio based on mass-loss measurement.

<sup>c</sup> Erosion rate is estimated from measured D content and an assumed D/C ratio and density based on the TFTR/N3-15 value.

bare graphite is negligibly affected. Further differentiation in the co-deposit and bare graphite erosion rates could be achieved by local heating of the co-deposit regions. Notwithstanding the differences in erosion rates, the bare graphite will also contribute to the overall CO and CO<sub>2</sub> formation in proportion to surface areas and relative erosion rates, impacting on pumping requirements.

Although the thermo-oxidation technique looks promising, its impact on plasma performance recovery, the effects of impurities and mixed materials on co-deposit erosion rates and the collateral effects of oxidation on other in-vessel components need to be investigated. From an engineering standpoint, the pumping and processing of large quantities of DTO in the torus exhaust would significantly increase the cost of the tritium processing plant.

#### 4.7.2.2. Oxidation experiments in TEXTOR

To gain confidence in projecting laboratory results for T removal from tokamak co-deposits to ITER, the T removal techniques need to be tested in current fusion devices. First experiments in a tokamak

using oxygen with hot walls (620 K) to remove co-deposits have been performed in TEXTOR [775]. In the initial tests, the external pumps were closed, and the vessel was filled with <sup>16</sup>O<sub>2</sub> or with <sup>18</sup>O<sub>2</sub> isotopes to pressures ranging from 0.005 to  $\approx 0.2$  torr. At a filling pressure of  $< 0.01$  torr, most of the oxygen was adsorbed on the wall and the remaining 10–20% oxidized the deposits — and C impurities on other wall surfaces — to form CO and CO<sub>2</sub>, which were then released. At higher filling pressures ( $\approx 0.2$  torr), the fraction of oxygen adsorbed decreased by 20–30%, whereas the fraction of CO formation was about constant and the formation of CO<sub>2</sub> increased. This behaviour of the CO<sub>2</sub>/CO ratio is in agreement with laboratory observations [475]. It has been found that the adsorption of oxygen <sup>18</sup>O on the walls leads to the release of C<sup>16</sup>O and C<sup>16</sup>O<sub>2</sub>, C<sup>16</sup>O<sup>18</sup>O molecules by isotopic exchange processes. A significant increase of water partial pressures has been observed by the differentially pumped quadrupole mass spectrometers, but the available experimental results are not sufficient to separate the contributions to the observed reaction products originating from the co-deposits and other internal vessel wall

Table 18. C erosion and D removal rates for tokamak co-deposits during oxygen exposure.

Temp. [K]	ASDEX-Upgrade [475] ~0.75 μm thick (ρ ~ 1900 kg · m <sup>-3</sup> ; D/C ~ 0.43) 760 torr air		TFTR tile edge [205, 206] ~0.50 μm thick 760 torr air	
	Erosion [μm · h <sup>-1</sup> ]	D removal [C · m <sup>-2</sup> · h <sup>-1</sup> ] <sup>a</sup>	Erosion [μm · h <sup>-1</sup> ] <sup>b</sup>	D removal [D · m <sup>-2</sup> · h <sup>-1</sup> ]
523				
623			>50	n/a
650	n/a	3.7 × 10 <sup>22</sup>		
Temp. [K]	TFTR/N3-24 [209] ~0.15 μm thick 76 torr air (P <sub>02</sub> = 16 torr, P <sub>H2O</sub> = 2 torr)		TFTR/N3-24 [209] ~0.15 μm thick 16 torr H <sub>2</sub> O vapour	
	Erosion [μm · h <sup>-1</sup> ] <sup>c</sup>	D removal [D · m <sup>-2</sup> · h <sup>-1</sup> ]	Erosion [μm · h <sup>-1</sup> ] <sup>d</sup>	D removal [D · m <sup>-2</sup> · h <sup>-1</sup> ]
523	0.035	0.1 × 10 <sup>22</sup>	n/a	0.05 × 10 <sup>22</sup>
623			n/a	
650				0.15 × 10 <sup>22</sup>

<sup>a</sup> Thickness recession and C erosion rates are estimated from measured NRA depth profiles of C and D.  
<sup>b</sup> Erosion rate is estimated from measured D content and SEM photos of film thickness, assuming constant D/C.  
<sup>c</sup> Erosion rate is estimated from measured D content and an assumed D/C ratio and density based on the TFTR/N3-15 value in Table 17.  
<sup>d</sup> It is postulated that H<sub>2</sub>O exposure leads to isotopic exchange of H and D, without significant carbon removal.  
n/a not available.

surfaces. A more sophisticated analysis to interpret the signals in terms of hydrogen release from the a-C:D co-deposits is in progress.

Encouragingly, TEXTOR did not experience any long term adverse consequences after the use of oxygen to remove deuterium, and high performance plasma operation could be recovered after 15–30 minutes of GDC in helium and deuterium. The oxygen impurity content was initially two to three times higher than before oxidation, but was seen to decrease shot after shot, indicating a self-cleaning process during plasma operation [775].

4.7.2.3. Co-deposit removal via plasma discharges

Glow discharge cleaning (GDC)

One of the most widely used wall conditioning techniques in tokamaks is GDC (Section 4.6.2). It cannot be applied, however, to machines with superconducting magnets. In the absence of magnetic fields, laboratory experiments using He/O glow discharges have produced rapid, controlled

co-deposit removal with minimal O contamination. Erosion rates of about 1 μm·h<sup>-1</sup> have been observed for co-deposit specimens removed from TFTR [776]. By comparison, He/O GDC performed inside the TFTR vessel resulted in much lower T removal rates [202, 735], possibly because of the redeposition of the reaction products before being pumped out of the tokamak. Laboratory studies have determined this erosion to be a two step process: oxidation, followed by particle induced desorption, with the maximum erosion rate limited by the latter. Temperatures in excess of 500 K are required for rapid thermal desorption of CO from carbon surfaces [776]. Helium ions of a few hundred eV have a high CO desorption yield, typically much higher than for electrons or photons. Rapid, efficient evacuation of the desorbed impurities from the system is also important. Dissociation, which can lead to redeposition, is primarily caused by energetic electrons; thus, electron densities and energies should be kept as low as possible (low electron densities imply low ion flux to surfaces). Conditioning studies with Taylor discharges and ECR support this conclusion. In both cases desorbed impurities were efficiently evacuated

only after the discharge was terminated. Physical sputtering due to the high incident ion energies during GDC may cause undesired deposition of high  $Z$  impurities onto lower  $Z$  components. As with other discharge methods (see below), tritium removal due to ion impact is limited to line-of-sight surfaces.

#### Ion cyclotron resonance discharge cleaning

Tritium removal techniques capable of operating in the presence of magnetic fields are desirable due to the permanent toroidal magnetic field in ITER. Such techniques include ICR and ECR discharges. Co-deposit removal experience with ICR and ECR in tokamaks is rather limited. High hydrogen removal rates have been reported in ICR experiments in Tore Supra with He and D [661] and TEXTOR with He [41]. H removal in these discharges occurs via a combination of processes: chemical erosion due to H/D, physical sputtering, ion induced desorption, and isotope exchange. The first two processes lead to erosion of the co-deposit, while the latter two lead to removal and replacement of hydrogen within the range of ion/charge exchange neutrals. In the Tore Supra experiment the C removal rate was estimated to be  $\approx 4 \times 10^{22} \text{ C}\cdot\text{m}^{-2}\cdot\text{h}^{-1}$  [661]. This corresponds to  $\approx 1 \mu\text{m}\cdot\text{h}^{-1}$  for a TFTR type co-deposit. Although this erosion rate is about an order of magnitude lower than the rate due to thermo-oxidation at 623 K, the fact that this is achieved without oxygen is promising. However, two key limitations remain: no access to shaded areas, and sputtering (due to energetic ions and charge exchange neutrals) of components where no co-deposits exist.

It might be possible to mitigate and possibly overcome these limitations by establishing discharge conditions that suppress ion and charge exchange neutrals induced sputtering and at the same time create reactive neutral atoms that could access shaded areas. Laboratory experiments have been performed at the Sandia National Laboratories to assess the potential of ICR for tritium removal and to evaluate the erosion rate for TFTR like co-deposits using He/O ICR plasmas [777]. Initial results show very efficient formation of atomic O, with little residual  $\text{O}_2$  to permeate into and contaminate graphite pores;  $\text{O}_2$  is readily dissociated in the mixed He–O discharge. C and H removal can occur via CO formation and via desorption of reacted surface CHO species due to energetic He neutrals. As in the case of thermo-oxidation via  $\text{O}_2$ ,

atomic oxygen is expected to preferentially erode the co-deposits compared to ‘bare graphite’.

#### Electron cyclotron resonance discharge cleaning

ECR hydrogen discharges yield low energy and high density plasmas [579, 778]. Early experiments of ECR discharge conditioning in tokamaks date back to the 1980s. The cleaning effect of hydrogen ECR plasmas in JFT-2 [779] and JIPP T-II [780] was found to be similar to that obtained with Taylor discharge cleaning.

More recently, ECR discharges were used in JET to remove tritium from the torus after the DTE1 campaign. No significant tritium removal was detected after 2.5 h of low pressure deuterium ( $\approx 6 \times 10^{-4} \text{ Pa}$ ) discharges [203]. Controlled experiments in C-Mod using deuterium ECR discharges removed a diamond like carbon coating from a stainless steel specimen at a rate of  $\approx 3 \text{ nm}\cdot\text{h}^{-1}$  [161]; however, this material is not representative of what is expected in ITER. The effectiveness of the ECR technique to remove tritium from tokamak co-deposits remains to be further assessed.

Co-deposit removal with ECR discharges has also been investigated in laboratory experiments [781, 782]. The erosion rate was found to depend critically on the film structure at the surface. Among the gases studied, oxygen shows always the highest erosion rates; the relative rates behave as  $\text{O}_2:\text{D}_2:\text{H}_2 \approx 10 : 2 : 1$  [347, 467, 781, 782]. The erosion rates increase with substrate temperature, ion energy, and ion flux. These correlations are true for soft and hard C:H films, although the absolute rates differ significantly. Erosion rates of  $1.7 \mu\text{m}\cdot\text{h}^{-1}$  and  $3.6 \mu\text{m}\cdot\text{h}^{-1}$  were measured at 300 and 620 K, respectively, for hard a-C:H films in oxygen ECR plasmas with surfaces maintained at floating potential. The rates for soft C:H films are roughly a factor of two higher. For discharges in pure oxygen, no large oxygen inventories were found in ex situ analyses of a-C:H samples after plasma treatment. The dominant erosion products, as measured by mass spectrometry, are  $\text{H}_2$ , CO,  $\text{CO}_2$ , and  $\text{H}_2\text{O}$ . Etching by neutral species (most probably atomic oxygen) was demonstrated to occur, but the underlying processes remain unclear [781]. A key question is how much CH is removed by ions and neutral species and whether the ECR discharge needs to be localized in a tokamak (e.g. in the divertor) by localizing the RF power absorption close to the surface to be cleaned. The neutrals may be important to access shaded, non line-of-sight areas. ECR

plasmas should cause little or no physical sputtering because ion energies are below the threshold for sputtering.

In summary, the thermo-oxidation and plasma discharge techniques discussed above have the potential for tritium removal. While oxygen is necessary for thermo-oxidation, it appears that the discharge removal techniques will also require the presence of oxygen to achieve sufficient erosion and tritium release rates. The presence of neutral oxygen atoms is necessary to reach shaded areas, while the energy of ions needs to be minimized in order to prevent sputtering of other in-vessel components. Localizing the discharges in the divertor region may be required. The introduction of oxygen into the torus requires further investigations on plasma recovery, the collateral effects of oxygen in the torus, and processing of DTO. Recently, promising results were obtained by laser heating that would avoid the introduction of oxygen [766].

## 4.8. Dust and flake experience

### 4.8.1. Introduction

Particulates in tokamaks are produced by plasma erosion of plasma facing materials, by plasma disruptions, or by assembly, machining, welding, and operations inside the tokamak. Dust generation in next step fusion devices will increase with the increase in duty cycle and this has important safety implications. Tokamak dust may be toxic, radioactive and/or chemically reactive. The hazard of dust depends on the dust composition, how much dust is produced, and how well the dust is confined [230] (Section 2.3.4). Research into dust production mechanisms and their biological interactions has just begun and the dust production mechanisms and rates are not adequately known at present [241, 242, 783] (Section 6.5). Little is known about dust generation from mixed materials.

Appropriate limits for occupational exposure to tritiated graphite dust need to be established. The micron size typical of tokamak dust will allow it to be trapped in lung alveoli. While the annual limit of intake (ALI) and derived air concentration (DAC) for  $T_2$  and  $T_2O$  are well known, there are few data at present on the biological lifetime of tritiated tokamak dust in the lungs. Expected limits are much lower than for  $T_2O$ , posing a challenge for real time monitoring of airborne tritiated dust. Some data are available on the biokinetics and dosimetry of titanium tri-

tide particles in the lung [119]. Recent studies from JET showed that the dosimetric properties of tritiated dust are quite different to those of HT/HTO [784]. More studies on tritiated graphite dust are needed to provide a technical basis for safety limits, both for occupational exposure and for the general population under accident scenarios.

Although the structural materials for the vacuum vessel, internal cooling systems, etc., are shielded from the confined plasma ions by cladding, such components may be affected by off-normal events such as arcing (Section 4.4) and disruptions (Section 4.5). In a survey of TEXTOR [241], 15% of the dust collected was ferromagnetic even though TEXTOR was an 'all-carbon' machine, in the sense that all ion interaction was with carbon based PFCs. Much of the ferromagnetic material appeared as sections of almost perfect iron rich spheres, suggesting surface melting with the ejection of droplets, which solidify before landing elsewhere in the tokamak.

### 4.8.2. Dust in tokamaks

Measurements of dust concentration, diameter, surface area, porosity, chemical composition and activity have been carried out during the maintenance periods of several tokamaks. The results are diverse and reflect PFC configuration, materials, alignment, plasma conditions and disruption history. Studies were made of dust removed from TFTR in 1987 [746]. Vacuum cleaning of the vessel yielded less than  $25 \text{ cm}^3$  of particulates. The typical size of particles collected on a filter was  $\approx 100 \text{ }\mu\text{m}$ . Analysis of the volatile tritium component (HTO) showed a concentration of  $\approx 8 \times 10^{12} \text{ T atoms}\cdot\text{g}^{-1}$ ; this results from DD reactions, so the D content of the particles is probably  $10^6$ – $10^7$  greater (Section 4.7.1). A similar result was obtained from JT-60U in 1994, with a T activity of the dust of  $3 \times 10^{13} \text{ T atoms}\cdot\text{g}^{-1}$ . Studies were also made in the period 1987 to 1992 of dust collected from JET. Smears taken from in-vessel surfaces showed that the graphite surfaces are friable as a result of damage by plasma interaction. When JET was vented following the PTE campaign in 1991, the ventilation air exiting the vessel was also filtered to measure the resuspended fraction of the dust. An high efficiency particulate (HEPA) filter was used to collect the airborne particles from 97% of the air-flow through the vessel over a twelve-hour period in which time  $600 \text{ m}^3$  of air was sampled (three times the vessel volume) [785]. The suspended particles had a total mass of 2.29 mg, and the median mass aero-

dynamic diameter was about  $4\text{ }\mu\text{m}$ , with a geometric standard deviation of  $1.9\text{ }\mu\text{m}$ . The composition of the particle matrix was 80.3% C, 16.7% Fe, 1.3% Cr, 1.2% Ni, 0.02% Co and 0.03–0.7% Be (H isotopes and oxygen not included). Dust was also collected by swabbing surfaces inside JET with pads of tissue humidified with ethanol [785]. The largest amount of dust was found on the lower (graphite) toroidal limiter, at almost  $4\text{ g}\cdot\text{m}^{-2}$  of which 85% was C and 11% was Be. Elsewhere, Be was normally the main contribution to the composition, with C and the components of Inconel making up the rest, the largest sample (of  $0.7\text{ g}\cdot\text{m}^{-2}$ ) coming from the lower part of the inner wall.  $^7\text{Be}$  was found in all dust and aerosol samples, and in debris collected by vacuum cleaner from the vessel floor. Dust samples contained  $1.33 \times 10^{12}$   $^7\text{Be}$  atoms $\cdot\text{g}^{-1}$ , but the  $^7\text{Be}$  content of the debris was  $3.38 \times 10^9$  atoms $\cdot\text{g}^{-1}$ , and in each case the other radionuclides detected came from activated Inconel.

During the operational campaigns up to 1992, both JET and TFTR were operating as ‘all-carbon’ machines. Both machines were developing high power regimes, which resulted in high power densities in the SOL. Both JET and TFTR experienced tile alignment problems, which resulted in pulses terminating in ‘carbon blooms’, wherein erosion from tile edges increased the carbon concentration in the plasma beyond the stability limit [721, 786]. In JET, many millimetres were eroded from some tile edges by the plasma, and probably this was mostly responsible for the light dusting of carbon based material observed over the interiors of both JET and TFTR at this time. The interior of JET was changed in 1992–94 to incorporate a divertor, and great care was taken with the design of the power handling surfaces to avoid exposed tile edges. As a result, discharges could be run with high power levels for longer periods without impurity problems, and the amount of dust observed in JET since 1994 had been greatly reduced. Similarly, attention was paid to the alignment and shaping of target tiles in TFTR [107], and the amount of dust collected in this machine also decreased. A specific experiment to demonstrate that dust can be formed as a result of plasma impact at tile edges has more recently been carried out on DIII-D [787] (Section 4.5.2.2). In this case, it was shown that the leading edges erode rapidly and form difficult to clean diamond like films in shaded regions. In the area of intense redeposition, the formation of  $5\text{--}10\text{ }\mu\text{m}$  ‘globules’ was also observed.

More recent surveys on dust have been conducted on several tokamaks. The INEEL Fusion Safety

Program has collected dust from major tokamaks (DIII-D, Alcator C-Mod, Tore Supra, ASDEX-Upgrade and TFTR) following typical run periods, and extensively analysed the collected dust to determine the composition, particle size distribution, and specific surface area [231, 234, 788–793]. The tokamak dust is generally submicrometre to micrometre in size. The data can be fitted to a log-normal distribution, similar to many industrial aerosols [794]. Figure 71 contains the results of all the particle size data used to establish the conservative value used in the ITER safety analysis. The data points in the figure represent the count median diameters (CMDs) of the particulates (see glossary) that were measured, and the uncertainty bars in the figure represent the geometric standard deviation (GSD) of the size distributions. The horizontal lines indicate the size range for the  $0.5\text{ }\mu\text{m}$  CMD and a GSD of 2.0 used for the ITER safety case.

The mass concentration of dust varies throughout a tokamak, dependent upon the location. In DIII-D, it ranged from  $1\text{--}10\text{ mg}\cdot\text{m}^{-2}$  on vertical surfaces and  $0.1\text{--}1\text{ g}\cdot\text{m}^{-2}$  on the floor and lower horizontal surfaces. The ranges of mass concentration in the Alcator C-Mod tokamak collected during the March 1998 were an order of magnitude greater, while the dust vacuumed from a  $0.1\text{ m} \times 0.1\text{ m}$  area of the TFTR vacuum vessel floor had a concentration of  $20\text{ g}\cdot\text{m}^{-2}$  [795]. Additional samples were collected in the vessel entry with a hand vacuum cleaner fitted with a slotted nozzle and  $0.2\text{ }\mu\text{m}$  pore size filter [574]. Particles and debris were evident on the floor of the vessel, including flake fragments and debris from a laser-assisted lithium conditioning aerosol device ‘DOLLOP’ [164]. Bay J was particularly dusty and collection from a  $10\text{ cm} \times 10\text{ cm}$  area yielded  $0.46\text{ g}$ . In contrast, the bottom of a neutral beam duct yielded only  $0.06\text{ g}$  from a  $20\text{ cm} \times 60\text{ cm}$  area. The gap between the bumper limiter and poloidal limiter, at Bay K, yielded  $0.07\text{ g}$ .

The specific surface area of tokamak dust is important from a chemical reactivity standpoint. High specific surface areas indicate large surface areas that could react with air or steam during an ingress event. The specific surface area of carbon dust samples retrieved from diagnostic viewing pipes and from the floor of TFTR has been measured by the BET method (see glossary) [795–797] and ranges from  $7$  to  $27\text{ m}^2\cdot\text{g}^{-1}$ . The specific surface areas of various tokamak dust samples are plotted versus the mean volume-surface diameter in Fig. 72. Also shown in the plot are the corresponding theoretical lines for pure



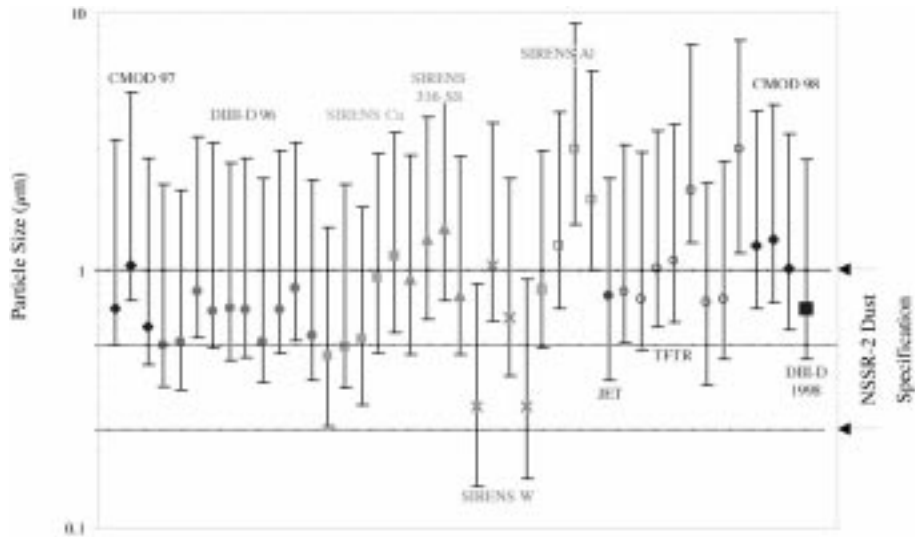


**Figure 71.** Tokamak and plasma gun particulate data used to specify values used in ITER safety analysis. (Figure provided by K. McCarthy and D. Petti, INEEL, Idaho Falls.)

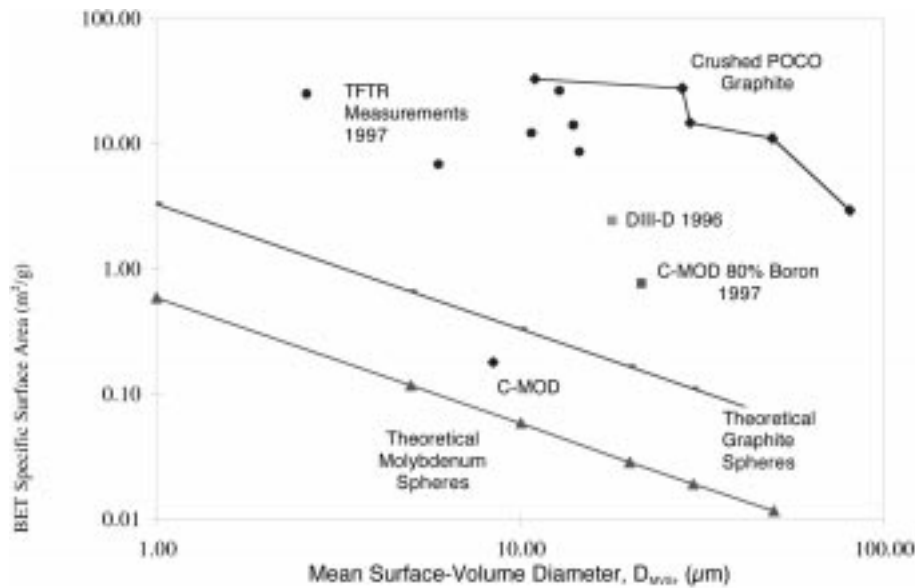


**Figure 72.** BET specific surface area of tokamak dust compared to theoretical carbon and molybdenum spheres. (Figure provided by K. McCarthy and D. Petti, INEEL, Idaho Falls.)

fully dense graphite and molybdenum monodisperse spheres and data on crushed POCO graphite.

The Alcator C-Mod 1998 sample is fairly close to the theoretical line, indicating that the metal is not based on small agglomerated particles or has limited porosity. (The Alcator C-Mod 1997 sample contained 80% by weight boron, which biased the measurement

high relative to the theoretical line for Mo). The carbon based tokamak dust samples show surface areas well in excess of the theoretical values, indicating either significant agglomeration or surface-connected porosity [798].

Dust composition is measured quantitatively using inductively coupled plasma mass spectroscopy

and qualitatively using environmental scanning electron mass spectroscopy. The composition of the dust consists primarily of the first wall material used in the machine, e.g. carbon in DIII-D and TFTR and molybdenum in Alcator C-Mod. Carbon dust samples were retrieved from diagnostic viewing pipes and from the floor of TFTR [795]. Millimetre-size flakes were observed in samples collected from the diagnostic pipes; while by mass, these large flakes are significant, by count they are not, since they are few in number, compared to the smaller particles (Section 4.8.3). The hydrogenic concentration was relatively low with atomic ratios in the range D/C of 0.006 and T/C in the range of 0.0003. The 20:1 D/T ratio is similar to the 30:1 D/T fuelling ratio during the DT campaign in TFTR. In general, dust will also contain material used for conditioning, instrumentation, insulation and diagnostics in the tokamaks. Such materials include boron, stainless steel, aluminium and silicon oxides.

Detailed surveys of dust and other debris in JET were carried out during a break in the Mk-IIA divertor phase in October 1996. JET had operated with the Mk-IIA divertor for 6 months during which there had been 2000 discharges and about  $9 \times 10^{25}$  D atoms were injected. Swab samples were taken from the divertor and also the poloidal limiters and analysed for T activity, gamma activity, particle size, specific surface area and composition [235]. High Be concentrations were measured at areas of the outer wall close to the Be evaporators; elsewhere, the Be was uniformly low at  $\approx 10 \text{ mg}\cdot\text{m}^{-2}$ . One sample contained 40% Ni by weight, but otherwise the swabs gave average concentrations of particulates of  $1.2 \text{ g}\cdot\text{m}^{-2}$ , comprising 97% C, 2% Be and 1% metals by weight (not including H isotopes or oxygen). The radioactivity of the samples resulted from T (varying from  $4 \times 10^{13}$  to  $2.6 \times 10^{15}$  tritons $\cdot\text{m}^{-2}$ ) and  $6.64 \times 10^{10}$   $^7\text{Be}$  atoms $\cdot\text{m}^{-2}$ . The median diameter was  $27 \mu\text{m}$ , with a geometric standard deviation of  $2 \mu\text{m}$ . Specific surface area was measured for only the largest size fraction:  $4 \text{ m}^2\cdot\text{g}^{-1}$ .

In a recent survey of dust collected in TEXTOR [241], three categories of large particles were collected, apart from the ferromagnetic material referred to above. These were pieces of a Si based composition, probably originating from the silicization [799] of the machine, pieces of graphite, and flakes of co-deposited films (see below). Small particles were also collected, many of which were sub-micrometre in size, which themselves were agglomerates of particles of about 100–300 nm in diameter.

The size and structure of these small particles suggests growth in the edge of the plasma or during wall conditioning processes, similar to the nanoparticles formed in process plasmas [800, 801]. Under the conditions of a detached plasma with electron densities of the order of  $10^{18} \text{ m}^{-3}$ , temperatures  $< 5 \text{ eV}$  and hydrogen flux densities of  $\approx 2 \times 10^{22} \text{ m}^{-2}\cdot\text{s}^{-1}$ , the local hydrocarbon concentration near the target surface is  $\approx 10^{18} \text{ m}^{-3}$ . These conditions are close to those of the process plasma where dust formation has been observed by multiple ion-molecule reactions and agglomeration processes.

In addition to collection from operational tokamaks, an experimental system has been developed to study disruption-induced particulate formation using the SIRENS high-heat-flux facility at North Carolina State University [802–804]. Results from the SIRENS experiment are used to understand the basic particle generation and formation mechanisms in tokamaks having high disruption energies as expected in future fusion power plants (Section 4.5). Results of size measurements on particles produced in SIRENS are not significantly different than the dust found in tokamaks. A variety of materials have been tested in SIRENS, including stainless steel, copper, tungsten, carbon, aluminium, and mixtures thereof; photographs of stainless steel and graphite are shown in Fig. 73. Further experiments are ongoing in Russian disruption simulation facilities.

#### 4.8.3. Flakes in tokamaks

Thick layers of eroded first wall material are deposited at points in the SOL, such as at the sides of the limiters, in machines where the limiters are the primary plasma boundary. In many tokamaks, such as JET (pre-1992), TFTR and TEXTOR, these layers may reach  $\approx 100 \mu\text{m}$  in some areas. The typical appearance of films flaking from the sides of limiters in TEXTOR [805] is shown in Fig. 74.

The thick films on the discrete limiters used until 1986 in JET had a fine layer structure, were highly stressed, and did break up on occasions, particularly following venting to air. The analysis of the outermost one or two  $\mu\text{m}$  showed D concentrations of  $\approx 0.1 \text{ D/C}$ , but thick film analysis techniques showed average D concentrations for the film as a whole to be almost two orders of magnitude lower [806]. The surface temperature of the central region of the JET limiters regularly reached over 1300 K, and temperatures at the flanks, where these thick deposits were located, must also have reached temperatures at which co-deposited films start to degas ( $\geq 700 \text{ K}$ ).

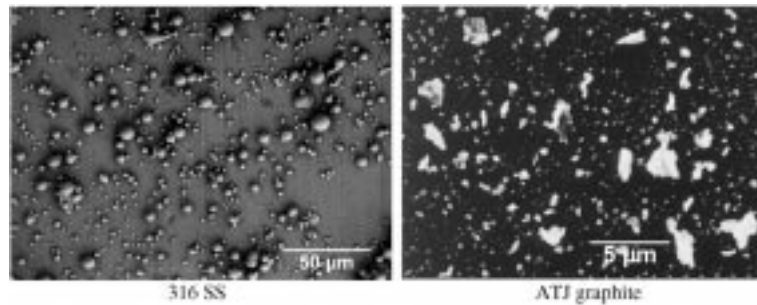


**Figure 73.** SEM photographs of particulates generated from the SIRENS plasma gun. (Figure provided by K. McCarthy and D. Petti, INEEL, Idaho Falls.)

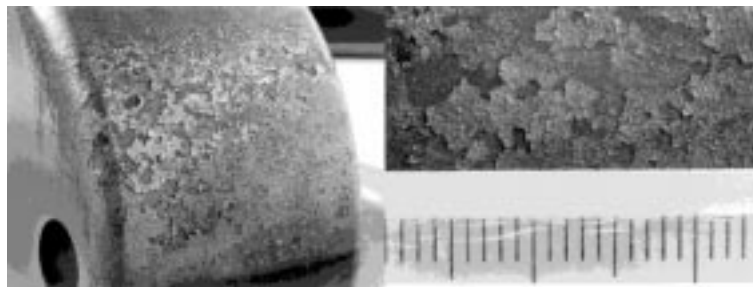


**Figure 74.** Photograph of the heavy deposition at the side of a TEXTOR limiter. The scale is in mm (visible are 23 mm) and refers to the detail of the flaking region shown on the upper right part of the figure. (Reproduced with permission from TEXTOR.)

Recent analysis of poloidal limiters and RF antenna protection tiles from TEXTOR show similar results [496, 807]. As in the case of the JET limiters, these PFCs are normally at 540–570 K, and can reach much higher temperatures during plasma pulses. Films of up to 170  $\mu\text{m}$  thickness were observed, which were loosely bound and tended to peel off as flakes. Flakes of up to 10 mm in diameter were observed, but they were brittle and very easily disintegrated to form much smaller agglomerates of dust particles [496]; scanning electron spectroscopy (SEM) imaging showed that the outer regions of the films consisted of fine granules of up to 5  $\mu\text{m}$  diameter [807]. An SEM section of such a film is shown in Fig. 75. Films of only  $\approx 10 \mu\text{m}$  thickness are seen to blister and peel in other parts of TEXTOR. During the period the tiles were in use in TEXTOR, the mean growth rate for the thicker films corresponded to  $4.5 \text{ nm}\cdot\text{s}^{-1}$  [807].

Thick films (tens of  $\mu\text{m}$ ) are also deposited on the inner bumper limiter of TFTR (Fig. 76). Following the conclusion of the DT phase in April 1997, TFTR

has been held in air at slightly below atmospheric pressure. No spalling of these layers was observed until 18 months after the machine had been vented to air; by two years after the venting, approximately 15% of the inner wall showed some flaking [573, 738] (Section 4.7.1.1). TFTR was operated with the wall at room temperature, and although tiles on which the films are seen were heated during discharges, stresses (and D concentrations) may be different from those at the discrete JET and TEXTOR limiters. Values of D:C at the surface are typically 0.1–0.2 [495]. A 0.24 g sample of the TFTR flakes has been heated in air to 773 K for 1 hour, which released  $1.5 \times 10^{19}$  T atoms. This amount confirms that the flakes are detached co-deposited layers that contain most of the retained tritium. Rutherford backscattering analysis of a TFTR flake showed a D/C ratio of 0.13 on the plasma facing surface, six times lower than the D/C of 0.7 found in JET co-deposits.

When tiles were removed from the JET Mk-IIA divertor in October 1996, a much greater

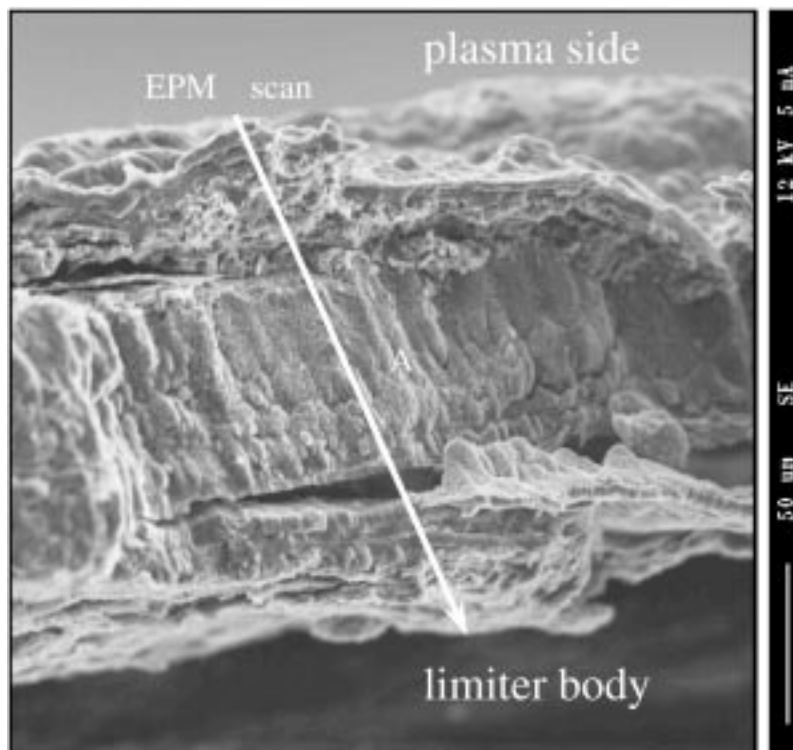


**Figure 75.** An SEM image of a piece of film that has flaked from the side of a TEXTOR limiter. (EPMA = Electron Probe Microanalysis). (Reproduced with permission from Ref. [807].)

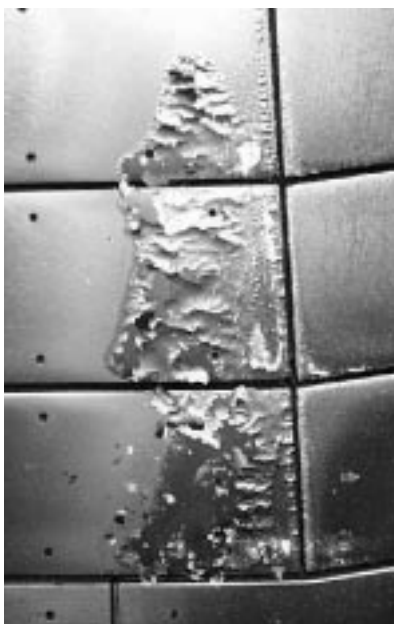


**Figure 76.** Blistering and flake detachment on TFTR graphite tiles at Bay H on February 25, 2000. The vertical height of a tile is 81 mm. (Reproduced with permission from TFTR.)

potential dust problem for large tokamaks was discovered. Flaking deposits were found on water cooled louvres beyond the inner corner of the divertor (Section 4.7.1.2). These deposits were  $40\text{ }\mu\text{m}$  thick, and since they are not exposed to the plasma (and are on cooled surfaces) their D:C ratio is approximately 0.7 [762]. The films exhibit a layer structure (Fig. 77) similar to the films seen on the JET and TEXTOR limiters. The T content of these flakes (from DD operations only) was  $5 \times 10^{15}$  tritons $\cdot\text{g}^{-1}$ , so that flakes resulting from full DT operation are predicted to contain  $\approx 10^{22}$  tritons $\cdot\text{g}^{-1}$ . The flakes comprised 99% C, 0.6% Be and 0.5% metals (disregarding the H isotopes and traces of oxygen). The total amount of D trapped in the films on the louvres corresponded to 4% of the total D fuelling. Since the flakes had been exposed to air before analysis, there may have been considerably more D present in the flakes during operation; following the JET DT campaign in 1997, one third (2 g) of the retained T was released to the air during the shutdown (Section 4.7.1.2). Most of the T retained in the JET vessel during DTE1 was believed to be incorporated in the flakes that formed at the louvres. Over 150 g of flakes were

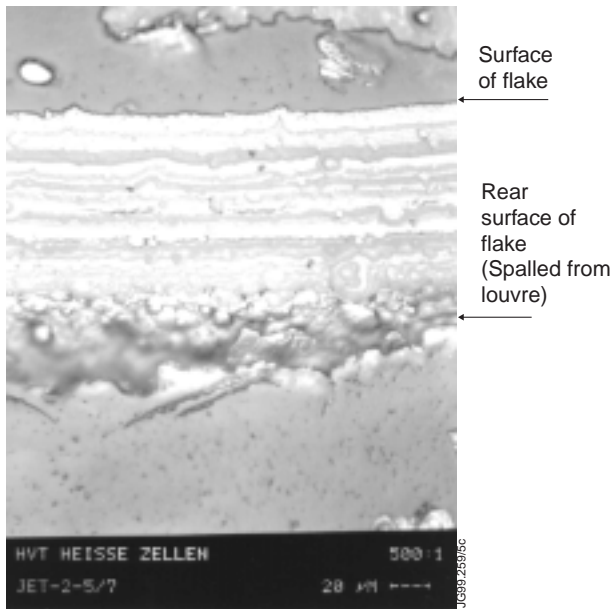


**Figure 77.** Polished cross-section of a flake from the JET Mk-IIA divertor, showing the layer structure. The scale marker on the figure is  $20\ \mu\text{m}$ , which makes the film thickness  $\approx 100\ \mu\text{m}$ . (Reproduced with permission from JET.)

recovered from the vicinity of the inner louvres containing  $0.52\ \text{g}$  of T [763], and, by extrapolation, up to  $\approx 800\ \text{g}$  of flake may remain beneath the divertor structure, which was inaccessible.

Films of up to  $2\ \mu\text{m}$  thickness have been found in the ASDEX-Upgrade divertor region, on the vacuum vessel near divertor slits, and on the structure of the roof baffle [530] (Fig. 78). From the position of the films and shading by structures, it is clear that the deposition is of charged particles following field lines. Much more symmetric deposition between inner and outer divertor structures is found than in JET. The films, which have a tendency to detach to form flakes, are carbon based with  $\approx 40\ \text{at}\%$  D,  $10\ \text{at}\%$  O and  $5\ \text{at}\%$  B (from boronizing the main chamber); an estimated  $5\ \text{g}$  resulted from  $3000\ \text{s}$  of plasma discharges. Modelling predictions for ITER suggest that up to few grams of T may be retained per pulse in C co-deposits analogous to those in JET (Section 5.3). These deposits would spall continually, and the flakes may break up into small pieces of high specific surface area. The implications of this material (which may or may not, be defined as ‘dust’) for next step devices are discussed in Sections 2.3.3, 2.3.4, 6.2 and 6.5.

## 5. Application of models and predictions for next step tokamaks

### 5.1. Introduction

The conditions expected in next step tokamaks are far away from those attained in present and past devices, and thus the extrapolation of current experience requires detailed models. Years of close interplay between experiment and modelling have resulted in models that can reproduce many features of plasma behaviour. Rapid progress in multi-teraflop computational resources continues to facilitate more detailed and comprehensive coverage of plasma-wall interaction phenomena. The next step fusion experiment will require large capital investment, and modelling plays an essential role in finding optimal configurations and reducing the uncertainty in projections of the performance.

The diversity of phenomena has made it difficult to create integrated models of plasmas and wall boundary effects. Experimentally, the powerful effect of the wall conditions on plasma performance is very clear. However, the actual conditions on the wall surface during a discharge are hard to diagnose, and the complexities of wall physics are not consistently incorporated into predictive plasma codes used by machine designers. Databases used to predict machine performance are based on experience in short pulse machines with preconditioned walls, but it is likely that new phenomena will occur as the physical and chemical state of the wall changes in a long plasma pulse. Some work to link the state of the wall to plasma phenomena has begun. For example, the global tritium retention in TFTR has been linked to detailed Monte Carlo models [201, 574]. Quantitative models connecting the dynamic exchange between recycling and the edge/pedestal region (see glossary) have been compared to experimental data from the JET DTE1 experiment [518]. Non-linear simulations of the stabilizing effect of radial electric field shear have uncovered a link between enhanced confinement in TFTR and lithium conditioned low edge densities [61].

The continuing advances in available computational resources clearly lend themselves to constructing and linking codes of increasing complexity. However, one must be careful that the addition of free variables leads to codes that are thoroughly grounded in experimental data. The breadth and depth of diagnostic data from the wall/edge must increase commensurately with the complexity

## Inner Divertor Leg

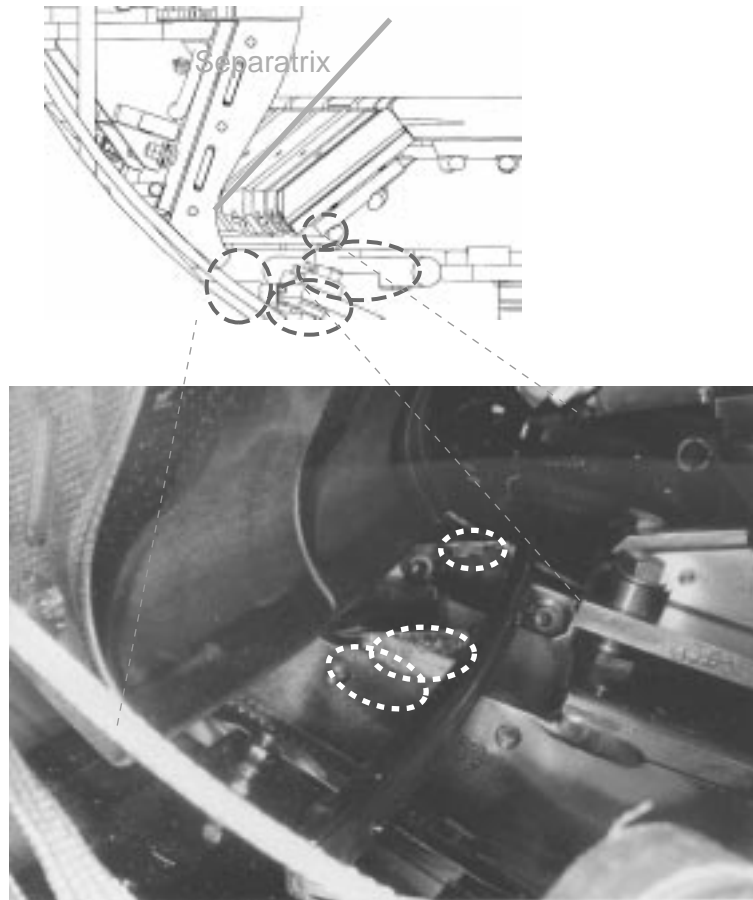


**Figure 78.** Location of flakes and films of carbon in ASDEX-Upgrade. The flakes were found below the divertor, whereas carbon films were found on the divertor structure. They are located at surfaces perpendicular to the magnetic field. (Figure provided by V. Rohde, ASDEX-Upgrade, Garching.)

of the modelling. Experimental data on sputtering, reflection and redeposition under high flux conditions must guide and benchmark integrated models of the edge before a predictive capability can be confidently established. An emerging area with significant safety implications is the modelling and benchmarking of tritium co-deposition and dust generation.

Modelling of PMI effects and the interpretation of the available data are often hampered by the lack of detailed time resolved diagnostics of the edge plasma and wall conditions, and lack of time resolved measurements of erosion/deposition/H retention. To make further progress in this critical area, real time in-vessel diagnostics need to be further developed and more widely implemented with dedicated

run time [481] (Sections 4.2 and 6.4). The detailed data generated will challenge models, lead to a better understanding of the many interacting plasma, atomic and surface phenomena involved and generate more confident predictions in future devices.

General principles of plasma edge modelling by one dimensional analytic and two dimensional fluid modelling are presented in Section 5.2 and illustrated with comparisons to tokamak measurements. A detailed discussion on this subject can be found in Ref. [13]. Two dimensional Monte Carlo impurity modelling is discussed in Section 5.3, which addresses modelling of erosion of and deposition on the PFCs, tritium co-deposition in growing redeposited surface layers, and the contamination of the

core plasma from surface materials. Modelling of erosion of plasma facing materials subject to off-normal events such as disruptions is discussed in Section 5.4. Section 5.5 is devoted to modelling of wall recycling and plasma particle balance. Finally, Section 5.6 discusses models of retention, permeation, and re-emission of hydrogen isotopes in materials exposed to reactor plasmas. The physical processes and underlying theory behind these models were described in Section 3.

## 5.2. Plasma edge modelling

Next step designs, as typified by ITER, call for a device of significantly greater size and power than any earlier machine. To extrapolate to an ITER class device, one must use several models to cover various aspects of edge/surface/boundary physics. Many such models have been developed over the last 20 years, and some have been validated to a certain degree by comparison with experimental data. In general, the plasma models simulate the parallel transport of particles, momentum and energy according to classical prescriptions, but still rely on empirical values for the cross-field transport rates. The inability to predict from first principles the absolute level of cross-field transport is the greatest weakness in modelling work. The relative level of cross-field transport, in comparison with the parallel transport, will determine the width of the SOL, and thus, the power density on the divertor plates (Section 1.2). Codes, for example, typically assume that cross-field transport coefficients are spatially uniform (or vary with the strength of the poloidal magnetic field), something that is almost certainly not correct [27, 808].

Modelling follows three basic approaches: (1) one dimensional analytic modelling; (2) two dimensional fluid modelling; and (3) two or three dimensional, kinetic, Monte Carlo impurity modelling (Section 5.3). The neutral hydrogenic behaviour is modelled separately. Each is dealt with separately below.

### 5.2.1. Simple one dimensional modelling

In most cases, quick and reasonably accurate estimates of the basic plasma conditions in the SOL can be obtained from simple analytic expressions. Such modelling is often called in the literature ‘two point modelling’— ‘two point’, because one usually solves the transport equations at two locations, the divertor plate and some upstream location, typically the outside midplane (see Refs [9, 10]). Basically, the

SOL problem is separated into two one-dimensional heat transport problems, one for cross-field transport and one for parallel field transport. The following is usually assumed in such modelling: (1) the divertor is opaque to recycling neutrals (Section 1.2.1); (2) the transport of heat along the SOL to the divertor is, therefore, through parallel heat conduction (primarily by electrons); (3) plasma pressure is conserved along field lines in the SOL. An exception to the last may be close to the divertor plate, where plasma pressure may be lost by ion–neutral interactions and/or volume recombination when the divertor plasma temperature is low (less than, or approximately equal, to 3 eV).

Under the above assumptions, simple expressions can be derived for many SOL parameters [9, 10]. Figure 79 gives an example of such modelling, where experimental data from the Alcator C-Mod tokamak are compared against results from the two point model with an extension for the neutral particle behaviour [809]. In this case, data are presented for the outer divertor plate, for a flux surface which is 1 mm outside of the separatrix (outside midplane equivalent) — this is assumed to be representative of the SOL (which has a power width of  $\lambda_P \approx 3$  mm). The upstream parallel power density,  $q_u$ , is observed in experiment to be fixed at  $q_u \approx 75$  MW·m<sup>-2</sup>. Two fitting parameters are used in this modelling: the radiated power in the divertor is taken from experiment, and the relation between the upstream density and the line average discharge density,  $\bar{n}_e$ , where the approximation  $n_u \approx \bar{n}_e/3$  is made. Thus, the ‘good fit’ between model and experiment in Fig. 79(a) (b) is artificial.

The analytic modelling readily identifies three regimes of SOL operation (indicated in Fig. 79), which depend on the collisionality of the SOL, or, in other words, the ability of the SOL to sustain temperature gradients along field lines for a given density and power flow. In terms of engineering parameters, the SOL can sustain significant gradients if

$$\frac{n_u^2 L^{\frac{6}{7}}}{q_u^{\frac{8}{7}}} > 2 \times 10^{31}, \text{ in MKS units} \quad (28)$$

where  $L$  is the connection length (see glossary). A similar criterion in terms of plasma density and temperature appears in Ref. [810].

At low values of collisionality, e.g. at low density or high power, the SOL is isothermal, with relatively high values of temperature,  $T_u \approx T_t > 60$  eV. This is known as the ‘linear’ or ‘sheath-limited’ regime. ‘Linear’ because the divertor plate density increases

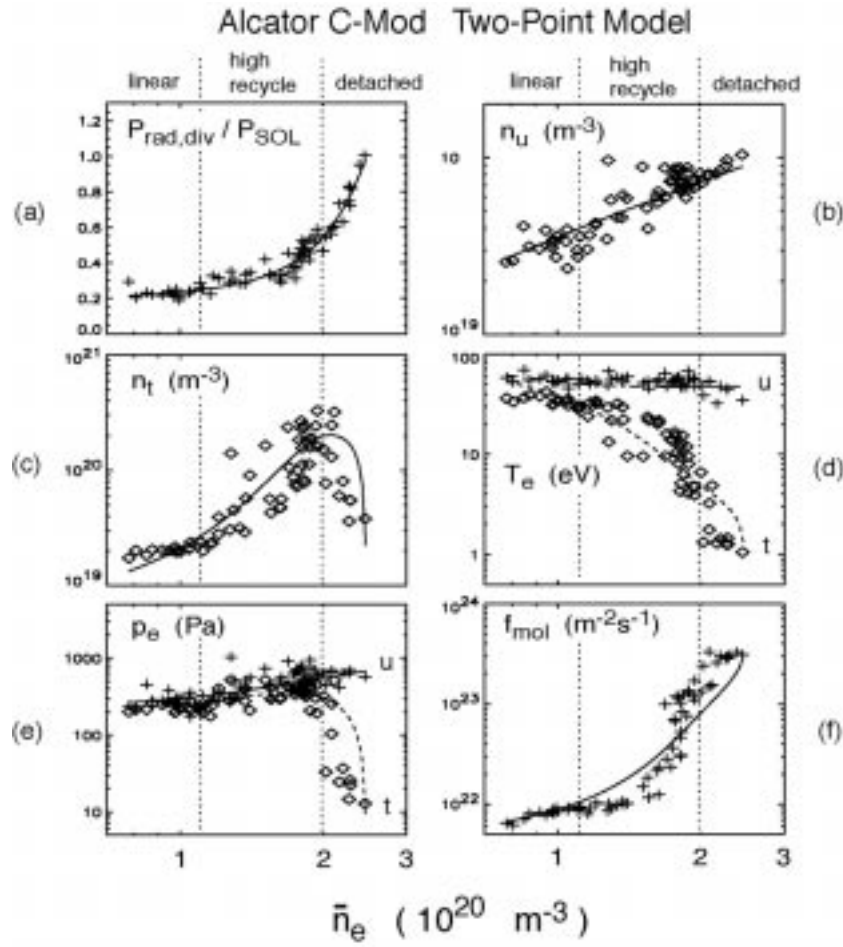


**Figure 79.** Comparison between SOL conditions as measured on Alcator C-Mod (discrete points) with results from the two point model with extensions (lines). Given in the figure is: (a) the relative level of radiation in the divertor  $P_{\text{rad,div}}/P_{\text{SOL}}$ , (b) the upstream density  $n_u$ , (c) the target plate density  $n_t$ , (d) the upstream and target plate temperatures  $T_u$ ,  $T_t$  (ion temperature is assumed equal to electron temperature), (e) the electron pressure upstream and at the plate  $p_u$ ,  $p_t$ , and (f) the molecular flux density of the  $\text{D}_2$  gas in the divertor plenum. In the figure ‘u’ refers to upstream parameters and ‘t’ refers to parameters at the target plate. (Reproduced with permission from Ref. [809].)

in proportion to the upstream and average discharge density, and ‘sheath limited’ because parallel heat flow is limited by the sheath transmission of electron energy at the divertor plate.

At moderate levels of collisionality, i.e. moderate levels of density and power flow, significant gradients along field lines can develop. This regime, known as the ‘high recycling’ (see glossary) or ‘conduction limited’ regime, has low divertor plate temperature and high divertor plate density. In this case, the heat flow along the field lines is limited throughout most of the

SOL by electron heat conduction. Close to the divertor plate, where strong particle recycling occurs and electron temperatures and their gradients are low, parallel particle convection dominates the heat flow. It is assumed that the total plasma pressure adjacent to the plate is approximately equal to the upstream plasma pressure, i.e.  $n_u T_u \approx n_t T_t$ , which is usually the case with  $T_t > 5$  eV.

At still higher values of collisionality, the target plate temperature falls below 3 eV, and the ionization reaction rate for recycling neutral particles in



the divertor becomes small in comparison with the rate of ion–neutral charge exchange and elastic scattering. Under these conditions, first pointed out in Ref. [811], significant plasma pressure loss can occur next to the plate, concomitant with a drop in ion particle flux and plasma density (Fig. 79(e)). The ion flux to the plate can be reduced still further by volume recombination of the ions [812].

This last regime, the ‘detached’ regime, is very desirable from the point of view of power handling at the divertor plate. The parallel power density  $q_t$  the divertor plate is given by

$$q_t = n_t c_{st} (\gamma T_t + \epsilon_{pot}) \quad (29)$$

where  $c_{st}$  is the ion acoustic speed,  $\gamma = 7$  and  $\epsilon_{pot}$  is the potential energy associated with each ion reaching the plate, including the atomic and molecular recombination energies ( $\epsilon_{pot} \approx 16$  eV) [9]. At low plate temperatures, the heat flux is dominated by the last term associated with the potential energy. This can only be reduced to low levels (e.g.  $q_t/q_u < 0.05$ ), for a reasonable level of upstream plasma pressure, if pressure loss due to friction and possibly recombination is present [140, 813, 814], as observed in the experimental data from Alcator C-Mod (Fig. 79(e)) and similar data from several other machines [143, 695, 815].

The neutral molecular flux density,  $f_{mol}$ , adjacent to the divertor plasma is given by Fig. 79(f). One can see that this increases monotonically with discharge density, basically following the divertor plasma density in the linear and high recycling regimes. It continues to increase with discharge density even in the detached regime, and this is expected from simple particle balance given by the extended two point model [9].

### 5.2.2. Two or three dimensional fluid modelling

The two dimensional nature of the SOL has led to the development of two-dimensional fluid models based on the finite difference numerical technique. Typically, the SOL and the outer regions of the confined plasma are mapped out using a curvilinear grid, where one dimension lies along magnetic flux surfaces, and the other, i.e. the radial direction, is orthogonal. In the parallel direction, as with two point modelling, the transport of particles, momentum and energy is assumed classical although in this case the full set of Braginskii equations is used [816]. In the cross-field direction, again, spatially uniform anomalous transport coefficients are used, with typical values for the particle and heat diffusivity ( $D_\perp$

and  $\chi_\perp$ ) being of order of  $\approx 1$  m<sup>2</sup>·s<sup>−1</sup>. The inner boundary of the problem corresponds to a magnetic flux surface inside the plasma, normally in the region of  $r/a \approx 0.9$ . At this boundary, one might specify the heat flux crossing the surface from the confined plasma, the density and temperature. There are now several large plasma fluid codes used to model the edge, with the major ones being B2 [817–819], UEDGE [820–822], EDGE2D [823, 824], PLANET [825], and UEDA [826].

The volume source of ions via neutral particle ionization is a critical quantity in any modelling of the boundary. This determines the plasma flow patterns, the level of heat convection, the transport of impurities, etc. Usually, fluid codes rely on a partner code to model the neutral particle distribution in the boundary. These partner codes attempt to model the transport of neutral particles from their point of entry into the plasma to their eventual ionization. Thus, surface properties such as particle reflection and molecular re-emission must be considered, as well as a large variety of atomic and molecular processes, the most important of which are molecular dissociation, ionization and charge exchange (see review [827]). These neutral particle codes use either a Monte Carlo technique (e.g. DEGAS [733, 828], DEGAS 2 [829], EIRENE [830, 831], NIMBUS [832]) or a fluid prescription [833]. The Monte Carlo technique, essentially a kinetic calculation, is technically more appropriate for tokamak boundaries, but can be computationally demanding in comparison to fluid calculations. Fluid calculations tend to be more valid in the divertor than in the main chamber, particularly in high-density divertors as in C-Mod [833] and expected for ITER because the collisional mean free path (see glossary) of neutral particles becomes much shorter than the typical divertor or grid dimensions.

It is important that plasma edge models include effects of neutral hydrogen on energy and particle transport. The DT neutron rate was used to provide a measure of the deuterium influx into the core of TFTR. Modelling with the DEGAS code was able to relate the deuterium influx to the probability of incoming neutral deuterium penetrating the SOL [33]. A recent study [834] shows that density and temperature gradients in the plasma edge depend strongly on the local neutral hydrogen density owing to effects of charge exchange and ionization on the anomalous inward drift velocity.

In addition to handling neutrals, sophisticated plasma fluid codes can model a large number of

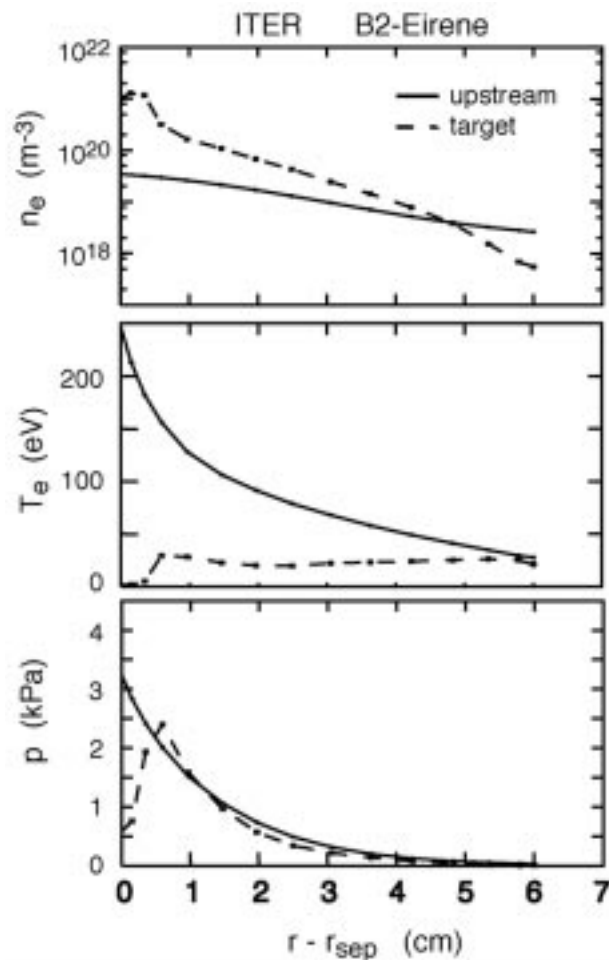


**Figure 80.** Results from a B2/EIRENE simulation of the ITER edge plasma [835].  $r - r_{sep}$  is the distance from the last closed flux surface (outside midplane equivalent). (Figure provided by A. Kukushkin, ITER JCT.)

plasma species including all the charge states of wall impurities and helium ash. A model for the generation of impurities by physical and chemical sputtering is required. Physical sputtering can be represented by a sputtering yield as a function of incident ion energy and angle of incidence. Although the validity of physical sputtering models may be uncertain because of a lack of confirming available data at, for example, near threshold energies, and oblique angles of incidence, the models are nevertheless relatively straightforward [112]. Chemical sputtering may be an important process for carbon surfaces, and there is considerable uncertainty in the appropriate sputtering yield, its dependence on surface temperature, particle energy and flux density (Sections 3.2, 4.3 and 5.3). Further, it is not clear how the hydrocarbon molecules that are released are bro-

ken down in the boundary plasma, ultimately resulting in a source of carbon ions. These uncertainties emphasize the importance of rigorous comparisons between modelling and experiments (Section 6.3). Such hydrocarbon modelling has been in a continual state of development for over ten years.

Figure 80 gives an example of B2/EIRENE modelling of the 1998 ITER design, where the radial profiles of density  $n_e$ ,  $T_e$  and total plasma pressure,  $p$ , at the upstream and target plate are presented [835]. The radial co-ordinate corresponds to the outside midplane location. In this case, 200 MW of power enters the inner boundary of the grid from the core plasma. Approximately 120 MW of this is radiated in the boundary and SOL by impurities, where He, Ne (seeded at 0.2% at the inner boundary) and carbon (primarily chemically sputtered from the divertor plates) are all present and modelled. The assumed cross-field transport coefficients are  $D_{\perp} = 0.3 \text{ m}^2 \cdot \text{s}^{-1}$  and  $\chi_{\perp} = 1 \text{ m}^2 \cdot \text{s}^{-1}$ . The radial e-folding widths for density, temperature and pressure at the outside midplane are approximately 2 cm, 2 cm and 1 cm, respectively. The divertor is significantly colder than the midplane, and consequently the density is much higher in the divertor, rising above  $10^{21} \text{ m}^{-3}$ . The plasma pressure drops in a radial region close to the separatrix and below the X point. This is known as ‘partial detachment’ and is frequently observed in present experiments [9, 143, 695, 815].

An alternative approach to the modelling of impurities in the boundary is to start from a background plasma given, either from detailed experimental measurements or from some other modelling source, i.e. two point or fluid modelling. Impurities are then injected into a 2 D grid of the boundary and their trajectories followed by the Monte Carlo method. Such a technique has numerous advantages over running a full scale multi-fluid code — it is typically easier to write, is numerically stable and in many respects handles the detailed impurity transport better, particularly during the time period before an impurity is ionized and fully thermalized/coupled to the background plasma.

The Monte Carlo approach is ideally suited to handling chemical sputtering (Section 5.3). Carbon enters the plasma ‘grid’ in the form of a hydrocarbon molecule, e.g.  $\text{CH}_4$ , that, through interaction with the plasma is dissociated through a long list of daughter products, some neutral and some ionized. During this process, the fragments are heated and collisionally coupled to the plasma. These processes are not handled in fluid codes, since they are

of a kinetic nature, yet may be critically important in ultimately determining where the fragments are transported. A Monte Carlo handling of this problem, in contrast, is relatively straightforward (although perhaps tedious). There are a number of impurity transport codes using the Monte Carlo technique. These include WBC [836], DIVIMP [837], IMPMC [826] MCI [838] and BBQ [330, 839].

### 5.3. Sputtering erosion and co-deposition modelling

#### 5.3.1. Modelling approaches and validation

The flux of energetic ions and neutrals onto plasma facing surfaces results in sputtering by physical and chemical processes as described in Sections 3.2 and 4.3. At the same time, impurities flow onto these surfaces from the plasma. The net result of these two competing processes can be either removal or accumulation of material at the surface. A significant portion of sputtered material is promptly ionized and returned to the surface near its point of origin, greatly reducing the net erosion rate. The magnitude and spatial distribution of the net erosion depend on the material properties, and on near surface, SOL, and core plasma transport processes. Quantifying these effects in erosion/redeposition/co-deposition models is essential in helping select surface materials and plasma edge regimes, predicting the lifetime of divertor and wall components, evaluating the sources of impurities and the resulting plasma contamination, and calculating the accumulation of tritium in co-deposited layers.

Owing to gradients in plasma density, temperature and flux, impinging energy, sputter yield energy dependence, etc. there can be a rapid change in the net erosion rate along a surface, particularly near a strike point. Erosion on one side of the strike point, for example, can give way to deposition on the other side. This has been clearly demonstrated for divertor machines, and at the limiters of tokamaks without divertors, where deposition occurs further out in the SOL, especially at the sides of the limiters (e.g. Refs [567, 574]). This process also occurs, during plasma startup, at the poloidal limiters in the main chamber of machines with a divertor configuration. Deposition can also occur away from the divertor or limiter, i.e. on the first wall, or adjacent surfaces. The amount and location of the redeposited material is crucial for future devices using carbon, because tri-

tium will be trapped within these deposits by the co-deposition process (Section 3.5.3.6). Co-deposition is important, too, for beryllium, but less so than for carbon because lower H/Be trapping fractions, and is much less important for tungsten and other high Z materials owing to both lower trapping fractions and low erosion rates.

The ITER project has chosen carbon for the divertor target, primarily owing to perceived advantages in disruption response (Section 2.4). Also, the reference ITER divertor plasma is partially detached, with moderate plasma temperature ( $T_e \approx 30$  eV) away from the strike point, and detachment ( $T_e \approx 1-5$  eV) near the strike point. These choices have led to a co-ordinated effort in the fusion community to improve models for low plasma temperature carbon erosion analysis. Ironically, this is by far the most difficult plasma-material combination to analyse, because of the need to model low impingement energy chemical sputtering yields, multispecies hydrocarbon transport, rapidly varying atomic and molecular processes in low temperature plasmas, and low energy carbon/hydrocarbon sticking/reflection at the surface. Other next step fusion designs, notably the FIRE design study [248], have chosen a tungsten divertor surface, in part to avoid problems with high carbon erosion rates. In this section we review erosion/redeposition modelling for surface materials in general, but with a strong focus on carbon.

Experimental investigations of redeposition and net erosion in fusion devices have gained importance in recent years; however, data are limited by restricted access to machines and the lack of experimental methods giving real time erosion information (Sections 4.2 and 6.4). Furthermore, comparison between data and models is sometimes difficult because erosion/deposition processes depend strongly on local plasma conditions that in most cases are not known very well. However, dedicated experiments, notably in DIII-D, with good near surface plasma diagnostics, and in situ and ex situ erosion measurements have verified erosion/deposition models, for several materials and plasma regimes. In certain cases, notably carbon in a detached plasma regime, the present database on net erosion is still in a preliminary state, and much more experimental work is needed (Section 6.1). Thus, the low plasma temperature carbon case suffers both from highly uncertain models and insufficient data.

The general feature of the models/codes is that they use a given background plasma solution, calcu-

late the sputtering rate for the given material (using, e.g. the material erosion properties data as described in Section 4.3), and follow the paths of the particles through the plasma until they are redeposited onto the originating surface or another surface, or enter the SOL/main plasma region. A description of the general modelling techniques can be found in Refs [497, 836, 840–843]. In most cases, boundary plasma conditions are not strongly influenced by impurities coming from the surface. An exception would be in cases where near runaway self-sputtering occurs. The ultimate goal is to model all effects self-consistently, but this capability is not yet available.

Inputs to the erosion/redeposition codes are the measured, or derived by plasma codes, plasma density, temperature, deuterium–tritium ion flux, charge exchange neutral flux, magnetic field profiles and strike point variation with time over the exposure periods. These codes incorporate numerous models and subcodes for sputtering and reflection coefficients, atomic and molecular processes, plasma–impurity collisions, surface temperature and temperature dependent hydrogen isotope trapping ratios, and sheath parameters. Critically important sub-models for detached plasma conditions discussed here include carbon chemical sputtering coefficients at low energies (5–15 eV), rate coefficients for hydrocarbon molecular impact processes with plasma ions and electrons, hydrocarbon sticking coefficients, and the effects of mixed materials, e.g. beryllium and carbon, on sputtering and tritium trapping. Some details of these critical models are given in Section 3.2 and Refs [560, 844].

The REDEP/WBC code package developed by Brooks [840, 841] is a prime example of a current state of the art erosion code package. The WBC Monte Carlo code [836] computes the details of the impurity atom and ion transport at the kinetic description level. This code is relatively time consuming since it is Monte Carlo and follows, in principle, all relevant details of the impurity transport (e.g. charge changing and velocity changing impurity–plasma collisions), with subgyro motion detail. The redeposition parameters computed by WBC can be used as input to REDEP, a finite difference code that is numerically optimized to treat the entire plasma facing surface. With the availability of fast, inexpensive work stations, there is increased use of Monte Carlo codes alone.

To assess the reliability of erosion/deposition predictions for a next step device many compar-

isons of code predictions and observations of erosion/deposition have been performed in current tokamaks, for example TFTR [201, 571, 719, 845], DIII-D [154, 537, 556, 743, 846], ASDEX-Upgrade [542], TEXTOR [843] and JET [111, 847] and on laboratory plasma linear devices such as the PISCES [848] and the PSI-1 [298] facilities.

An extensive effort at code validation has been done using measurements of erosion/deposition in the DIII-D divertor using the DiMES facility [154, 537, 556, 743, 846]. Probes containing carbon, beryllium, vanadium, molybdenum and tungsten were exposed at the strike point to various divertor plasma conditions. Post exposure ion beam analysis determined net erosion/deposition of material resulting from short exposures to steady state divertor plasmas. The plasma conditions needed for modelling erosion/deposition were well characterized by Langmuir probes, Thompson scattering, spectroscopy and neutral pressure diagnostics. The observed erosion/deposition of carbon at the outer strike point with attached H mode plasmas agrees well with Brooks and Whyte REDEP/WBC modelling [537, 556]. In general, comparison of code with experimental results for attached plasmas in DIII-D shows good agreement for erosion profiles, photon emission and core plasma contamination by sputtering.

Results from a long term exposure ( $\approx 1400$  discharges) of DIII-D divertor tiles [743] show a carbon erosion rate at the attached outer strike point of  $\approx 9.5 \text{ nm}\cdot\text{s}^{-1}$  ( $\approx 30 \text{ cm}\cdot\text{burn year}^{-1}$ ), with an equivalent rate of deposition at the inner strike point (where the plasma is usually detached). This erosion rate is the same as was measured during short exposures at the outer strike point in DiMES experiments [743].

The modelling work of Brooks and Whyte for DIII-D described above also included the effect of ELMs on erosion by sputtering. This was modelled for an attached plasma regime in DIII-D [556]. The near surface plasma temperature during the ELM was estimated to be similar to the period between ELMs, but the plasma density, particle flux and hence gross erosion rate are about 20 times larger during the ELM. However, the very high electron density during the ELM decreases the mean free path for ionization of the sputtered carbon atoms by an order of magnitude, causing prompt local redeposition of carbon to approach 100%. Furthermore, the ELM period constitutes only about 3% of the total exposure time. The contribution of the ELM period

to the total net erosion is therefore negligible, and it is the quiescent period that determines the net erosion rate. This prediction was verified experimentally on DIII-D from DiMES net erosion experiments with and without ELMs [556]. Unlike DIII-D, ELMs in ITER will cause erosion by thermal ablation (discussed in Sections 2.3.2.3 and 5.4.3), in addition to erosion by sputtering discussed here.

The erosion/redeposition patterns of sputtered metal atoms deposited onto a graphite DiMES sample, as described above (Fig. 43) [110, 501, 556] and on similar probes inserted into the SOL plasma of JET [842] and TEXTOR [497] have been successfully modelled by Brooks et al., and Naujoks et al., using subgyro-orbit transport codes (WBC [840], ERO [799]), with generally good agreement. Thus, there is reasonably good confidence in the predictive value of the erosion codes for metal surfaces. In general, beryllium and carbon exhibit longer transport distances than those of high  $Z$  metals. The DiMES and TEXTOR results indicate that the near-surface transport of the sputtered high  $Z$  metals is highly determined by ionization lengths and sheath acceleration of the ions. In addition, local radial electric fields have to be considered, which can significantly tilt the redeposition pattern with respect to the magnetic field lines due to  $\mathbf{E} \times \mathbf{B}$  forces [497].

Preliminary comparisons of model predictions with experimental tritium retention measurements in TFTR and JET, with a carbon limiter and divertor, respectively, were made to determine the retention mechanisms during the discharge. The step from single shot erosion/deposition calculations to the net global redeposition is a complex issue that requires knowledge about the relative frequency of characteristic discharge regimes and the effect of off-normal events. For TFTR a set of representative high power discharges of known frequency were analysed, and the BBQ Monte Carlo code of Hogan [330, 839, 849] was used to extrapolate to the global retention. These calculations suggested that known erosion mechanisms (e.g. physical sputtering, chemical erosion and RES) were sufficient to account for the order of magnitude of retention due to co-deposition [201] and predicted that when detailed analysis of TFTR tiles from the tritium campaign is made, significant concentrations of co-deposited tritium will be found near the upper and lower leading edges of the bumper limiter. This pattern was not expected from previous deuterium measurements [495] or earlier modelling [571]. These predictions were borne out by subsequent observations [574].

As mentioned, much less net erosion data and model validation exist for carbon in detached and partially detached regimes, where plasma temperatures are below 10 eV. This is critical for carbon where the principal sputtering mechanism changes from physical to chemical erosion via emitted hydrocarbon molecules, and their dissociation, ionization and transport are strongly changed since electron temperatures are near or below the critical values for ionization. In this regime dissociation of hydrocarbon molecules into neutral fragments (Section 4.3.1) may contribute significantly to local redeposition. Using a newly developed atomic and molecular data set for methane and higher sputtered hydrocarbons, REDEP/WBC modelling [560, 844] predicts that prompt redeposition efficiencies will decrease significantly (e.g. from near 100% to about 90%) for fully detached plasma conditions. This would result in increased net chemical erosion and associated co-deposition, depending, however, on the magnitude of the chemical sputter yields and other factors.

Detached plasma carbon chemical erosion data appear to yield contradictory results. Experiments on JET with detached plasma conditions show very little C II emission, less than calculated with carbon emissions from chemical sources during detachment [111]. Also, detached divertor plasmas in DIII-D caused no net erosion, and the observed intensity of CD molecular optical emission was weak [599]. These data suggest that local redeposition might remain efficient, and/or boron affected the results, or other possibilities. However, there were very large carbon deposits on the inner louver region of the JET divertor, and a correspondingly high amount of trapped tritium, such data tending to imply much higher erosion of carbon than expected. This is discussed further below.

Most divertor experiments show greater deposition at the inner than at the outer target (as discussed in Sections 4.3 and 4.7) [64]. This asymmetric erosion/deposition is in part due to a lower plasma temperature at the inner target, and a tendency for detachment to occur first at the inner target. An extreme example of this asymmetry is in JET with the Mk-IIA divertor, where, as mentioned, heavy deposition was found at cold louvers beyond the inner divertor corner (Section 4.7), with no such effects at the outer divertor.

The peak net erosion rate obtained for the CFC plate of the outer (attached) divertor leg on JET [111] was  $\approx 24 \text{ nm}\cdot\text{s}^{-1}$  ( $75 \text{ cm}\cdot\text{burn year}^{-1}$ ) at  $5 \text{ MW}\cdot\text{m}^{-2}$ . This erosion rate (strike zone) was mod-

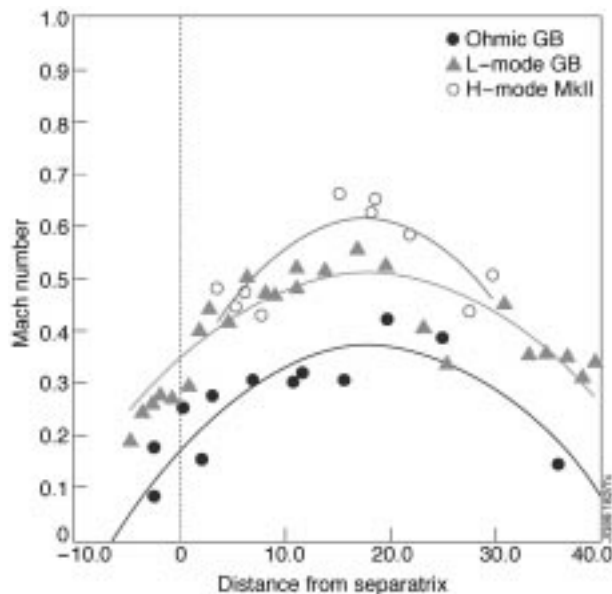


**Figure 81.** Flow in the JET SOL measured for different types of plasma using a Mach probe on the reciprocating probe inserted near the top of the torus. GB in the legend refers to the gas box divertor configuration installed in JET. (Reproduced with permission from Ref. [847].)

elled by using the two dimensional Monte Carlo impurity modelling code of Stangeby et al., DIVIMP [837], and a good match to JET data is obtained if chemical sputtering is included [850].

This JET asymmetry and the absolute magnitude of the carbon deposition ( $\approx 4\%$  of the total ion fluence to the inner divertor leg) is not correctly modelled by DIVIMP or REDEP/WBC using ‘conventional’ values of low-energy chemical sputter yield ( $\approx 1\% \text{ C/D}$ ), sticking probabilities and other parameters. Agreement between observed deposition and DIVIMP modelling was achieved by including three additional mechanisms, which alter deposition patterns in JET by more than an order of magnitude [847]. These mechanisms are: (i) drift in the SOL as has been observed in JET, (ii) additional interaction with the main chamber wall, and (iii) enhanced erosion of the redeposited carbon films at the inner target.

The first required mechanism, drift in the SOL, has been observed in JET [28, 29, 851] and in JT-60U [30]. Drifts peaking at velocities of half the sound speed have been measured in JET, as shown in Fig. 81. Some possible mechanisms have been proposed for these large drifts [29], but these do not fully

explain the data, particularly the reversal of the flow direction when  $B$  is reversed (due to the concomitant reversal of  $B \times \nabla B$  from downwards to upwards in the vessel). Regarding enhanced erosion of the redeposited carbon films, there is speculation that sputtering rates for redeposited carbon in tokamaks may be an order of magnitude greater than laboratory measurements of carbon chemical sputtering yields [294] (see also Section 3.2.6.4). On the other hand, as discussed in Sections 3.2.1 and 4.3.1, there is speculation that a flux dependence could lower chemical sputtering yields at high fluxes.

Another key issue is sticking/reflection coefficients of redeposited carbon/hydrocarbons. High sticking coefficients will obviously tend to minimize erosion, whereas high reflection will have the opposite effect. The key impingement energy range of interest is from about 1–10 eV. There are unfortunately both very limited data and theory for this range. Laboratory data of Von Keudell et al. [519] have shown low sticking probabilities for some hydrocarbons, but these measurements are at thermal energies only. The extrapolation or relevance of thermal data to 1 eV or higher impingement energies is uncertain. Deposition probabilities for injected  $^{13}\text{C}$  labelled methane through a TEXTOR limiter into a 35 eV plasma at  $2 \times 10^{18} \text{ m}^{-3}$  appeared to be only about 5%. This value is significantly smaller than the 60% predicted at these conditions by Kirschner et al., using the Monte Carlo impurity transport model ERO-TEXTOR [497, 843], based originally on the Naujoks ERO code. The reason for the discrepancy is unclear but may, for example, be due to low sticking of deposited carbon, and/or enhanced chemical sputtering.

Von Keudell [519] has also demonstrated high break up rates for certain hydrocarbon molecules (especially of the form  $\text{C}_2\text{H}_x$ ) in some temperature regions relevant to tokamaks. These species can be transported large distances away from the reaction zone, as is necessary to reach the louvres in JET. This process may also account in part for the formation of deposits under the divertor structure in ASDEX-Upgrade [530, 559]. There is currently underway modelling work using, for example, molecular dynamic simulations, to study the carbon/hydrocarbon reflection issue. Overall erosion modelling work is continuing using, e.g. REDEP/WBC to examine above mentioned mechanisms and additional mechanisms to further explain JET data.

**Table 19.** Summary of selected results of divertor erosion and tritium co-deposition analysis of various evolving ITER divertor designs. From analyses by J.N. Brooks et al.

Divertor target material	Design concept/ year	Strike point electron temperature (eV)	Peak gross erosion rate (nm/s)	Peak net erosion rate (nm/s)	Tritium co-deposition rate (mg/s)	References/ comments
Carbon	High recycling (1989)	150	61.5 <sup>a</sup>	8.6 <sup>a</sup>	4.9 <sup>a</sup>	[852]
		60	104 <sup>a</sup>	7.3 <sup>a</sup>	2.8 <sup>a</sup>	
		60	317 <sup>b</sup>	16.5 <sup>b</sup>	4 <sup>b</sup>	
	High recycling (1997)	~30	346	14.6 <sup>b</sup>	2.6 <sup>b</sup>	[560]
	Radiative (1997)	8 <sup>b</sup>	240 <sup>b</sup>	5.7 <sup>b</sup>	1.3 <sup>b</sup>	[560]
	Fully detached (1997)	~1.5	(51–305) <sup>c</sup>	(4.4–37.8) <sup>c</sup>	(12–106) <sup>c</sup>	[560]
Tungsten	high recycling (1989)	40	1.3	<0.03	~0	[852]
	High recycling (1997)	<30	1.6	<0.003	~0	[560]
	Radiative (1997)	~8	<0.2	<0.003	~0	[560]
	Semi detached (1998)	<3		<0.0005	~0	[154] sputtering due to trace O content
Beryllium	High recycling (1989)	60	374	23.1	1	[852]
	High recycling (1997)	~30	475	18.7	3	[560]
	Radiative (1997)	~8	217	10.1	(2–4) <sup>d</sup>	[560]
	Fully detached (1997)	~1.5 <sup>b</sup>	(0–4.4) <sup>d</sup>	(0–4.4) <sup>d</sup>	(0–4.4) <sup>d</sup>	[560]
	Semi detached (1998)	<3		9.5	2	[154]

<sup>a</sup> With physical sputtering only;<sup>b</sup> Includes chemical sputtering;<sup>c</sup> Range of values computed for possible variations in non-thermal D-T molecule chemical sputtering coefficient;<sup>d</sup> Range shown is for variations in He/Be sputter yield and H/Be trapping rate.

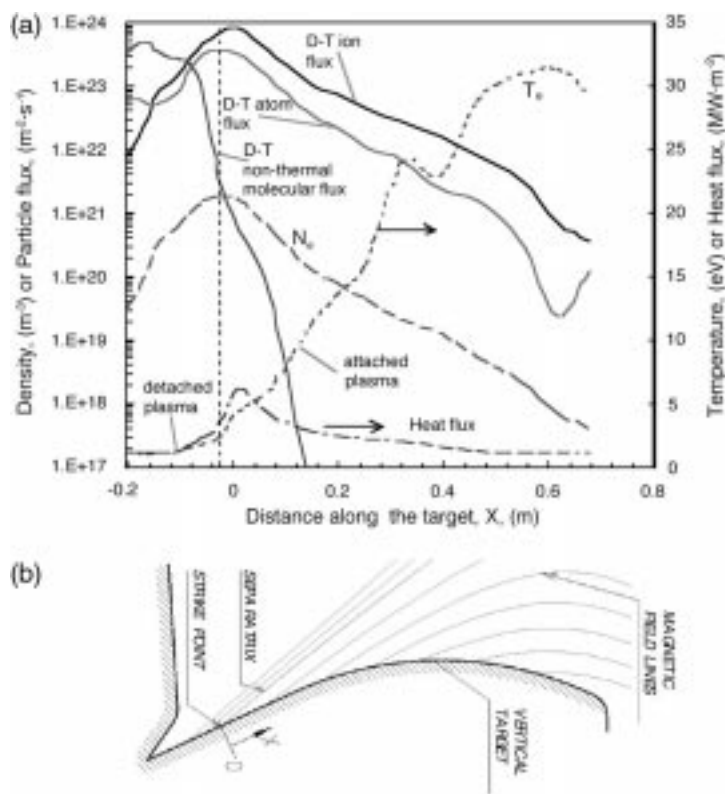


**Figure 82.** (a) Plasma parameters/fluxes along the ITER divertor outer vertical for so-called partially detached plasma conditions (see text); (b) schematic of the ITER divertor outer vertical target. (Part (a) of the figure reproduced with permission from Ref. [154].)

### 5.3.2. Erosion lifetime and tritium co-deposition inventory analysis for ITER

The erosion lifetime and tritium co-deposition for the divertor target of the ITER device have been modelled by Brooks and colleagues, over many years, for various divertor materials, using two dimensional profiles of plasma parameters for various regimes, and temperature dependent hydrogen retention data. A summary of the results obtained with the REDEP/WBC code is shown in Table 19.

For these studies, details of the analysis for a ‘high recycling’ plasma solution are given in Refs [154, 560, 852] and references therein. Because of the resulting high heat loads on the divertor plates, this regime of operation was not deemed desirable for ITER. However, for other devices and possibly ITER as well, high recycling regimes with lower heat loads could possibly be achieved, e.g. by enhancing core radiation. Trends shown in Table 19 should apply to most devices. These trends, for the high recycling and radiative regimes (with enhanced SOL radiation but without full detachment) are high net erosion

rates for the low  $Z$  materials, and low rates for tungsten.

Of primary interest for ITER, as mentioned, are the results of erosion/co-deposition analysis for partially detached conditions. Plasma parameters and fluxes along the outer divertor plate for the plasma solution calculated for the 1998 ITER design [3, 154] are shown in Fig. 82. The plasma density, temperature, heat flux and various particle fluxes along the outer divertor plate of the ITER carbon divertor vertical target are shown. The partially detached plasma is in part created by using a  $\approx 1\%$  neon impurity to radiate much of the incoming power from the plasma core to the boundary. This radiated power is much less spatially peaked than power flowing to the divertor by particle transport. As shown in Fig. 82 there is a rough division between an attached plasma zone of width  $\approx 70$  cm with temperatures  $\approx 3$ – $30$  eV, and a  $\approx 20$  cm detached zone of  $\leq 3$  eV with high density near the separatrix. Similar conditions are also found for ITER-FEAT [158]. Because of the high density, particle fluxes — including a non-thermal (‘fast’) molecular flux — are high in the detached



portion. The divertor geometry and the corresponding plasma solution and detailed neutral flux calculation results [154] are incorporated into the REDEP and WBC codes to compute gross and net erosion rates along the divertor, core plasma contamination, and tritium co-deposited with carbon both on the plates and adjacent regions.

From these studies, it was found that: (1) carbon chemical sputtering in the detached region along each plate is the main source of net carbon erosion and tritium co-deposition; (2) physical sputtering of the entire plate contributes about 20% to the co-deposition; (3) chemical sputtering in the attached regions has essentially no contribution to net erosion (because of  $\approx 100\%$  redeposition); (4)  $\approx 75\%$  of growth/co-deposition occurs on the bottom of the divertor vertical target, and  $\approx 25\%$  occurs in the private flux region. Various plasma parameter sensitivity studies were performed for the co-deposition calculations, as discussed further in Refs [154, 158]. Both beryllium and tungsten sputtering occur primarily or entirely along the attached part of the target. The predicted divertor net sputtering rates for partially detached conditions are very low for tungsten and high, but marginally acceptable, for beryllium and carbon.

Tritium co-deposition with sputtered carbon represents a formidable challenge for ITER (Section 2.3.3). Unless this retention can be drastically reduced without significant interruptions in operation, it is not practical to use carbon as the divertor material in ITER. A further review of tritium co-deposition modelling is given in Ref. [853].

Erosion and tritium co-deposition in beryllium sputtered from the wall and redeposited on the wall and/or divertor have been computed by several authors (see, for example, Refs [154, 158, 854]). Using worst case (coldest) surface temperatures for the critical beryllium deposition zones of  $\approx 500$  K, tritium co-deposition rates for beryllium are estimated by Brooks et al. to be  $< 0.1$  g/pulse, using low oxygen-content, Causey et al. H/Be trapping data [476], or  $\approx 0.6$  g/pulse, using 'carbon corrected' Mayer et al. data [477]. In either case, the wall derived T/Be co-deposition is less than that from carbon sputtering in the divertor. The reason for this is: (1) the quantity of beryllium eroded from the first wall by the charge exchange flux is less than the carbon eroded at the divertor (as predicted for the partially detached regime), and (2) the hydrogen trapping fraction in Be is less than in carbon.

#### 5.4. Modelling of erosion during ELMs and off-normal events

Erosion damage of PFCs in a next step device during ELMs and off-normal events (e.g. disruptions, VDEs, runaway electrons, etc.) represents a major concern for component survivability and lifetime. These events are anticipated to cause surface damage and high erosion losses due to surface vaporization, cracking and spallation, and melt layer loss. Besides, surface damage effects, plasma instabilities of longer duration such as VDEs, or those that deposit energy more deeply (e.g. runaway electrons), can produce significant bulk effects. These include large temperature increases in the armour and heat sink/structural materials and at their interface, causing high thermal stresses, possible structure melting, and material fatigue and failure and high-heat-flux levels in coolant tubes. The result may be coolant burn-out of the tubes (see glossary), leading to significant downtimes for repair and maintenance. The characteristics of ELMs and off-normal events expected in a next step device are described in Section 2.3.2, while the underlying physical erosion processes are described in Section 3.4.

##### 5.4.1. Modelling approach and validation

Several models of disruption plasma/vapour/material interactions have been reported [359, 364, 365, 370, 372, 628, 631, 855–865]. The models included in the more sophisticated code packages (e.g. Refs [366, 370]) integrate several models self-consistently. These include a model for the SOL behaviour during a disruption, a model for plasma interaction with the target material and the developed vapour cloud, and a model for heat transport within the material and mass losses due to various erosion mechanisms. The lifetime predictions largely depend on the uncertainties in the duration of the thermal and magnetic energy quenches and the distribution of the deposited energies onto the divertor and first wall surfaces, and on uncertainties in the magnitude of melt layer loss, and for carbon, the role of brittle destruction.

These codes are being validated against well diagnosed experiments in disruption simulation facilities (Section 4.5). In general, although good agreement is found for some of the cases analysed, there are cases where the discrepancies are still significant and need to be resolved (Section 6.1).

**Table 20.** Vaporization and melting thickness ( $\mu\text{m}$ ) per disruption event [866].

Material	Tungsten				Beryllium				Carbon			
Energy density ( $\text{MJ} \cdot \text{m}^{-2}$ )	10		100		10		100		10		100	
Disruption time (ms)	vap	melt <sup>a</sup>	vap	melt <sup>a</sup>	vap	melt <sup>a</sup>	vap	melt <sup>a</sup>	vap <sup>b</sup>	melt <sup>c</sup>	vap <sup>b</sup>	melt <sup>c</sup>
0.1	1.2	63	2.2	68	1.9	28	3.1	35	6	—	10	—
1	2.5	186	4.5	212	7.4	80	12	91	nc <sup>d</sup>	—	nc <sup>d</sup>	—

<sup>a</sup> Only stationary melt layer thickness (without splashing).<sup>b</sup> Carbon surface vaporization only — no erosion due to brittle destruction is assumed.<sup>c</sup> Carbon does not melt.<sup>d</sup> Not calculated.

#### 5.4.2. Erosion during a disruption thermal quench

The above models predict for ITER that of the order of several micrometres per disruption could be lost from carbon and tungsten owing to vaporization, and that melt layers up to few hundreds of micrometre would form for metals (Table 20) on the divertor plates under a typical disruption thermal quench (e.g.  $10\text{--}100 \text{ MJ} \cdot \text{m}^{-2}$ , in 1 to 10 ms (Section 2.3.2)).

Figure 24 in Section 3.4 shows as an example the typical time evolution of a tungsten surface temperature, melt layer thickness, and vaporization losses during a disruption for an incident plasma energy of  $10 \text{ MJ} \cdot \text{m}^{-2}$  deposited in a disruption time of 1 ms as predicted by the A\*THERMAL-S code [366]. On the basis of these results, for a disruption energy density of  $\approx 10 \text{ MJ} \cdot \text{m}^{-2}$  and a disruption time of 1 ms, the calculated vaporization and melting thickness for a tungsten plate are about  $2 \mu\text{m}$  and  $180 \mu\text{m}$ , respectively. The lifetime for a metal target strongly depends upon the fraction of melt layer lost per event. A sacrificial depth of 20 mm of C would then lead to a lifetime of  $>500$  disruptions, due to vaporization alone (i.e. without including erosion from brittle destruction, whose quantification is uncertain), or a lifetime of 130 to 430 disruptions for W if 50% or 10% of the melt layer is lost for W, for the above disruption energy density and duration. Table 20 gives calculated thickness of vaporized or melted layers for W, Be and C.

It has also been found that, depending on the divertor configuration and design, the transport and deposition of the radiation, generated from the primary vapour cloud, can be high enough to cause

severe melting and erosion of nearby components. The vapour cloud developing on the front of the surface of the nearby component may not be as effective as the primary cloud in protecting adjacent components because of strong vapour diffusion losses, vapour cloud optical properties and geometrical effects [169].

#### 5.4.3. Erosion during ELMs

ELMs deposit a few per cent of the core plasma total thermal energy onto the divertor plate in a time of 0.1–1 ms. The energy density of an ELM in current tokamaks is too low to cause damage. However, in ITER the energy density deposited by ELMs will be an order of magnitude higher and surpass the most severe disruption in current tokamaks. ELMs are expected to occur at a frequency of about one per second during high confinement plasmas in ITER (Section 2.3.2.3). Damage to the divertor plate due to ELMs is therefore a serious concern for ITER.

Material response calculations shown in Fig. 83 [155] give the number of ELMs that will erode a 20 mm thick carbon target and a 10 mm thick tungsten target (assuming no loss of melt layer). The ELM frequency varies inversely as the ELM energy. Assuming that Type-I ELMs transport about 20% [13, 172] of the power crossing the separatrix, that the resulting 18 MW is deposited on  $7 \text{ m}^2$  and that the plates are to withstand 2000 plasma pulses, each lasting 400 s, the product of ELM number and energy,  $N \times E$ , is at least  $2 \times 10^6 \text{ MJ} \cdot \text{m}^{-2}$ . For 0.1 ms to 1 ms duration, the resulting maximum allowable ELM energy density (see intersection of  $N \times E$  with ELM erosion in Fig. 83) is 0.22 to  $0.64 \text{ MJ} \cdot \text{m}^{-2}$  for carbon and 0.54

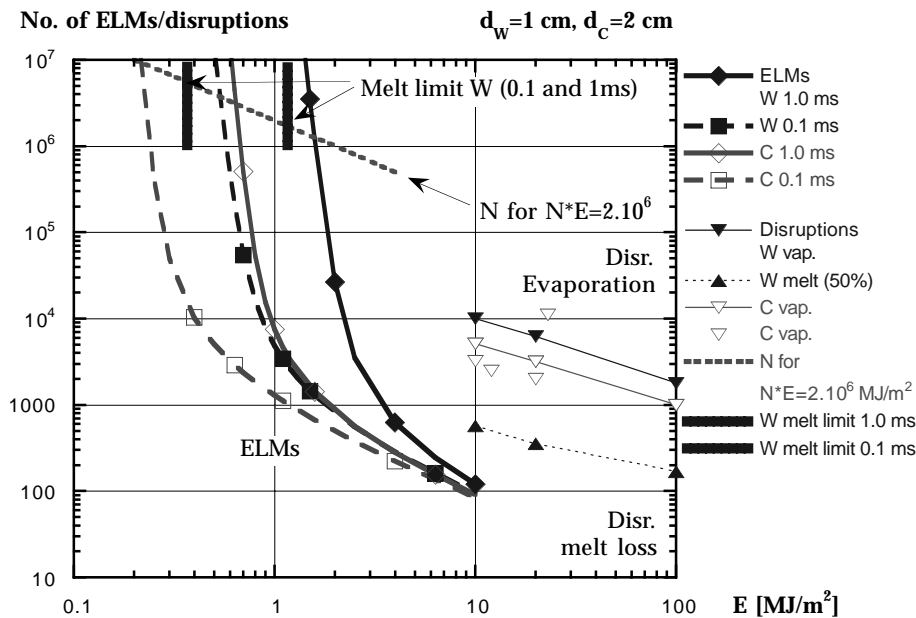


**Figure 83.** Number of ELMs,  $N$ , to erode 1 cm of W (solid symbols) or 2 cm of C (hollow symbols) versus ELM energy per unit area  $E$ , for ELM duration of 0.1 (diamonds) and 1 ms (squares). Melt limit for W is also shown. Disruption evaporation and melt loss numbers with vapour shield (see references in Ref. [155]) are shown for comparison. The product  $N \times E = 2 \times 10^6$  MJ · m<sup>-2</sup> (expected ELM energy deposited in 2000 shots; see text) is also indicated.

to 1.6 MJ · m<sup>-2</sup> for tungsten. To avoid melting of tungsten the ELM energy density must be less than 0.37 to 1.17 MJ · m<sup>-2</sup>. The expected ELM amplitude according to one Type-I ELM scaling [13] is  $\approx 2\text{--}3\%$  of the stored energy, yielding 1.1 MJ · m<sup>-2</sup> in ITER. Methods to lower deposited energy density from ELMs are, therefore, essential for the divertor target plate to survive a large number of shots (Section 2.3.2.4).

#### 5.4.4. Effects of longer plasma instabilities and runaway electrons

Because of their short duration (<10 ms), ELMs, and disruptions have no significant thermal effects on structural materials and coolant channels. In contrast, plasma instabilities, such as VDEs (duration 100–300 ms), and runaway electrons, in addition to causing severe surface melting and erosion, can result in substantial bulk damage to these components. Elevated temperatures and high thermal stresses in the structure can seriously degrade the integrity of the interface bonding, and burnout the coolant channels. Runaway electrons (up to

many MeV) penetrate many centimetres of graphite and directly heat underlying metal structures [867–870]. Disruption mitigation techniques that address the runaway electron issue are described in Section 2.3.2.4.

The erosion due to VDEs in a device like ITER has been modelled by various authors, [139, 364, 871, 872], whereas the results of analysis done to quantify the effects on PFCs resulting from runaway electrons can be found in Ref. [873]. As an example, Figure 84 shows the temperature of a copper surface at its interface with tungsten, beryllium and carbon tiles of 10 mm thickness, over the 5 mm copper substrate during a typical VDE releasing to the surface about 60 MJ · m<sup>-2</sup> in 300 ms [364, 871]. For ITER conditions, the tile thickness is determined by the surface temperature limitations during normal operation. Tungsten and carbon armours of similar thickness usually result in similar and higher copper surface temperature than that of beryllium armour of the same thickness. This is because most of the incident plasma energy is removed by the beryllium's higher surface vaporization rate, which leaves little energy to be conducted through the

**Table 21.** Vaporization and melting thickness ( $\mu\text{m}$ ) per VDE (without any vapour shielding effect) [866].

Material/thick. (mm)	Tungsten/10		Beryllium/10		Carbon/10	
Energy density ( $\text{MJ} \cdot \text{m}^{-2}$ )	20	60	20	60	20	60
Disruption time (ms)	vap	melt <sup>a</sup>	vap	melt <sup>a</sup>	vap <sup>b</sup>	melt <sup>c</sup>
100	0.2	450	nc <sup>d</sup>	nc <sup>d</sup>	98	—
300	$\sim 0$	$\sim 0$	105	1370	$\sim 0$	—

<sup>a</sup> Only stationary melt layer thickness (without splashing).<sup>b</sup> Carbon surface vaporization only — no erosion due to brittle destruction is assumed.<sup>c</sup> Carbon does not melt.<sup>d</sup> Not calculated.

structural material [364]. To reduce the temperature at the copper interface, thicker tiles would be required. Only beryllium tiles of reasonable thickness ( $<5\text{--}10\text{ mm}$ ) or very thick carbon or W tiles ( $>20\text{ mm}$ ) can withstand the acceptable temperature rise in the copper structure for the conditions shown.

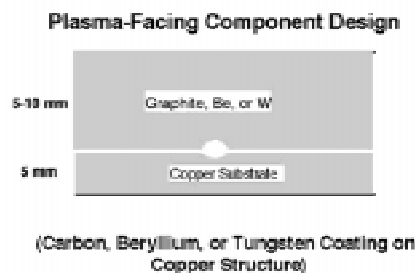
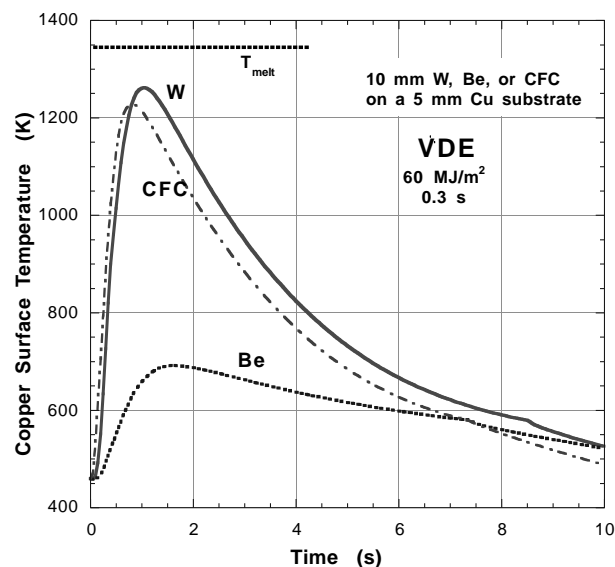
## 5.5. Modelling of particle–wall recycling

### 5.5.1. Modelling approaches

In this section we consider models of particle–wall recycling in tokamaks. The detailed processes involved and the effects of hydrogen recycling at the walls are discussed in Section 3.5 and 4.6.3, respectively. We will discuss three categories of particle wall recycling models: (i) global models — these lack a detailed description of the plasma and wall, but can be written in analytic terms and are particularly useful in dealing (in an empirical way) with time dependent phenomena; (ii) refined plasma edge models — these use a sophisticated treatment of the edge plasma and simple descriptions of the wall properties; and (iii) refined wall models — these constitute the opposite approach, with a sophisticated treatment of the wall, and a somewhat simplified description of the plasma.

#### 5.5.1.1. Global modelling

This approach links the plasma density response to the wall uptake under external fuelling. The method lacks a detailed description of the plasma, and a number of complex physical processes are described by simplified model parameters. However, the calculations become analytically tractable, and this approach is particularly suitable for dealing with

**Figure 84.** Interface copper surface temperature rise during a VDE for different surface coating materials.

time dependent plasma discharge phenomena. The results of these calculations provide some insight into the governing processes involved, and also quantitative results on global parameters such as the global particle recycling coefficient (see glossary),

the fuelling efficiency, and also specific material related properties. Examples and applications of this approach can be found in Refs [653, 654, 874, 875] and are described in Section 4.6.3.

Global modelling of recycling is usually based on particle balance models, in which the particles are assumed to be distributed between different regions. A *multireservoir* model distinguishes between several regions, or reservoirs, i.e. (i) the plasma core, bounded by the LCFS, (ii) the plasma SOL, and (iii) the material surfaces surrounding the plasma. The evolution of the particle distribution in each reservoir is governed by the physics of particle exchange processes, which are in turn affected by particle transport in the plasma and in the materials, respectively.

The basic elements of the global model are described in Ref.[654]. In the model, the particles leave the plasma and encounter the material surfaces of the first wall after an average confinement time,  $\tau_P$ . The particle balance model can be written in its simplest form for a closed system (after fuelling and pumping has been switched off) as

$$\frac{dN_p(t)}{dt} = -\frac{N_p(t)}{\tau_p} + R(t)\frac{N_p(t)}{\tau_p} \quad (30)$$

where  $N_p$  is the total plasma particle (electron) inventory and  $\tau_P$  is the global particle confinement time.  $\tau_P$  depends on plasma transport and the particle source distribution in the plasma. The quantity  $N_p/\tau_P$  represents the total plasma particle flux from the plasma to the surfaces, and  $RN_p/\tau_P$  is the total particle flux from the surfaces back to the plasma.  $R$  is termed the global particle recycling coefficient and includes different kinds of particle release from the surface (re-emission, reflection, etc. [654]). The global recycling coefficient is an average over many recycling processes at various surfaces inside a tokamak. In particular, if the wall pumping capability is very small,  $R$  is close to 1 and the particle flux from the plasma is almost entirely recycled. For a non-recycling species,  $R$  is not precisely known and depends on the wall particle trapping physics. For a more detailed analysis, the effect of the different surfaces in the tokamaks (limiter, divertor, wall) have to be taken into account individually.

A straightforward improvement of Eq. (30) is to introduce a wall reservoir interacting with the plasma [874]:

$$\frac{dN_p(t)}{dt} = -\frac{N_p(t)}{\tau_p} + f_r \frac{N_p(t)}{\tau_p} + \frac{N_w(t)}{\tau_w} \quad (31)$$

$N_p$  and  $\tau_P$  are defined above;  $N_w$  represents the total hydrogen content in the wall surface,  $\tau_W$  is the global particle confinement time in the wall. In this model, the flux out of the wall back into the plasma consists of two terms. The prompt term,  $f_r N_p/\tau_P$  is the recycling flux and is proportional to the plasma efflux, which is kinematically reflected and desorbed. The slow term,  $N_w/\tau_w$ , represents diffusion/recombination in the wall (Sections 3.5 and 5.6). The essence of the slow part is embodied in the global residence time in the wall,  $\tau_W$ , defined in the same way as the global plasma particle confinement time is defined; thus,  $\Gamma_w A_w = N_w \tau_w$ , where  $\Gamma_w$  is the spatially averaged flux out of the wall into the plasma, and  $A_w$  the wall area. One difficulty here is to define clearly what walls are involved.

More sophisticated treatments of the wall reservoir, which include multiple reflection and screening (non-fuelling) processes, are available [654, 875]. In Ref. [876], fast and slow reservoirs are used to explain the two different time constants observed in the rate of change-over from one isotope to another. However, increasing the number of reservoirs leads to a greater number of independent parameters whose experimental characterization is often difficult. In this case, the simplicity of the original model disappears.

#### 5.5.1.2. Refined plasma edge modelling

In these models, the interaction between the plasma and the neutrals recycled from the wall is described by a combination of plasma fluid models (described in Section 5.2) or ad hoc simplifications to describe plasma transport in the core and edge regions, together with a multispecies Monte Carlo neutral transport code. The models calculate the spatial distribution of charge exchange neutral fluxes and energy spectra to the wall.

These models treat the main working gas (i.e. hydrogen species such as D, T, D<sub>2</sub>, DT, T<sub>2</sub>), as well as the prominent intrinsic or extrinsic impurities. They give information on the density and temperature distributions of the edge plasma, which affect plasma processes such as the production of energetic charge exchange neutrals, the plasma power deposition at the divertor target plates, the impurity generation and retention in the divertor plasma. However, in these models the interaction between particles and material surfaces is not explicitly calculated, and an *albedo* parameter is often simply assumed to describe the phenomena at the surface (e.g. recycling coefficient, sticking probability, external pumping) [877].

These ad hoc coefficients have a significant effect on model predictions and, in some cases, can only be derived from other quantitative and testable models (see below). An albedo parameter of this kind will depend on the type of material and its temperature, on the H content of the material, and hence on the location in the machine and the history of operation, as well as on the energy spectrum of the incident H species.

#### 5.5.1.3. *Refined wall modelling*

In this case, the interaction between material surfaces and the plasma is based on detailed validated models for the dynamic exchange between recycling surfaces and the edge plasma. A predictive model must treat the strongly coupled interaction between the edge plasma and the surfaces of wall regions that comprise the active exchange surfaces. This is very difficult, although initial steps have begun [201, 518]. Most of the models are based on established laboratory values for fundamental wall process rate coefficients, but often provide a somewhat simplified treatment of the plasma [714, 878, 879]. In some cases, the study of the interaction with the wall is solved in isolation from the plasma, for characteristic phases of the discharge. This latter approach has been followed to describe features of wall release in tokamaks after a single or a sequence of discharges; see, for example, Refs [651, 652, 697, 711, 756, 880].

It has become increasingly clear that recycling phenomena in tokamaks are strongly dependent not only on several material properties (e.g. temperature, hydrogen content), but also on the conditions in the SOL (plasma temperature and density, neutral density). A detailed treatment of charge exchange reactions in the SOL has become an essential component of recent modelling [582, 881]. Indeed, charge exchange particles determine the saturation characteristics of the wall because they can access the large wall surface area away from the divertor strike points [697]. In addition, energetic particles can be deposited deeply in an unsaturated region and can be retained in the wall for times much longer than the plasma particle confinement time, before recycling back into the plasma.

Various approaches have been followed to model the interaction of charge exchange neutrals with the wall and divertor. For example, a model for the implantation range, derived from TRIM [882], is used in the code WDIFFUSE [878] to relate the

mean energies from an EIRENE [830] analysis to the implantation range for each surface element. In Ref. [878], the one dimensional SPUDNUT code has been used [883] to calculate the energy distribution of charge exchange neutrals, based on measured radial plasma density profiles. In the model described in Refs [714, 884], the time evolution of the plasma density in the core region is calculated by solving self-consistently a plasma transport equation, where the charge exchange implantation source is estimated separately from detailed Monte Carlo calculations [150, 885].

At the wall, deposition, diffusion and emission from the surface can be treated by coupled equations describing the concentrations of trapped and mobile particles [711, 756, 881, 886]. The basic equations for the concentration of mobile,  $C_s$ , and trapped,  $C_t$ , species in the wall can be written as follows:

$$\frac{\partial C_s}{\partial t} = D \left( \frac{\partial^2 C_s}{\partial x^2} \right) + \phi U(0, \Delta_i) / \Delta_i - \gamma C_s^2 - \frac{\partial C_t}{\partial t} \quad (32)$$

$$\begin{aligned} \frac{\partial C_t}{\partial t} = & \frac{1}{\tau_a} C_s \left( 1 - \frac{C_t}{C_{\max 0}} \right) - \frac{1}{\tau_a} \beta C_t \\ & - \sigma \phi U(0, \Delta_i) C_t \end{aligned} \quad (33)$$

where  $D$ ,  $\gamma$ ,  $\beta$ ,  $\sigma$  are the diffusion, volume recombination, thermal detrapping coefficients and particle induced detrapping cross-section, respectively.  $\tau_a$  and  $C_{\max 0}$  are the time constant for the trapping and detrapping process and the maximum trapped concentration in the wall, respectively. Characteristic numerical values of these constants and coefficients can be found in Refs [150, 711, 756], where a detailed explanation of these terms is also given. To estimate the wall deposition distribution, the energy spectrum of charge exchange particles is required. Indeed, the estimation of the penetration depth,  $\Delta_i$ , requires the knowledge of the incident energy of the particles, which can be obtained by solving the plasma energy equation. Alternatively, estimates of  $\Delta_i$  can be made from detailed Monte Carlo calculation of the charge exchange implantation source [150] for the specific experiments to be analysed. This approach has been followed in Ref. [714].

#### 5.5.2. Status of model validation

Tritium experiments on JET and TFTR provided an interesting opportunity to check wall/edge models because the initial tritium fuel was easy to dis-

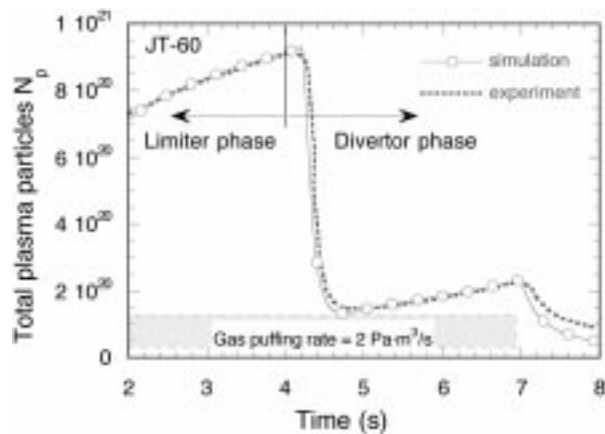


**Figure 85.** Experiments (dashed line) and simulation results (solid line with open circles) for the density behaviour during limiter transition and divertor phases in JT-60. (Reproduced with permission from Ref. [884].)

tinguish from the existing deuterium wall inventory. Examples of the use of modelling for data interpretation are given for JET [204, 518, 651–654, 696, 697, 756, 876, 880, 887–889], Tore Supra [696, 711], DIII-D [879, 881], TFTR [33, 201, 574], JT-60 [884], and ASDEX-Upgrade [890]. The Doppler broadened Balmer alpha spectral line profile was measured on TFTR and compared to Monte Carlo calculations of neutral hydrogenic velocities. Good agreement was obtained under a range of conditions, validating the treatment of charge exchange, molecular dissociation, surface reflection and sputtering in the neutral gas code DEGAS [733] although a residual deficiency in  $H_2^+$  dissociation was noted. Outgassing in JET with all-carbon walls was successfully modelled by assuming a controlled release of trapped particles from a hydrogen saturated layer over a large surface of the first wall, well beyond the main limiter or divertor [697]. A sensitive characterization of the wall saturation status was obtained by measuring the tritium concentration in the JET sub-divertor during the DTE1 experiments [518]. Wall rate coefficients from the Ehrenberg semiempirical model [654] were found to yield good agreement with the observed tritium recycling. This ‘first principles’ description of the tritium pathways in JET coupling the wall, divertor and core/wall transport offers an exciting prospect of a predictive transport model. This work has recently been extended to hydrogen (protium) [891].

Plasma discharges in tokamaks usually startup in limiter configuration; then, by applying a different current distribution to the poloidal field coils,

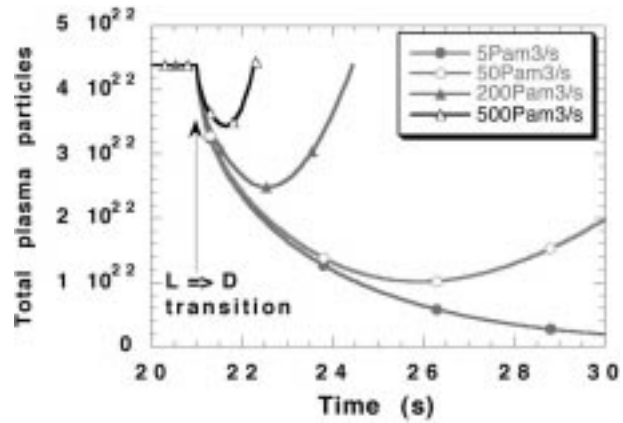


**Figure 86.** Density behaviour of deuterium during a typical limiter to divertor transition in the 1998 ITER design for various values of the fuelling rate. (Figure provided by M. Sugihara, ITER JCT.)

one achieves a transition to a divertor configuration. This transition often causes a strong decrease of the plasma density, due to the large absorption of particles by the wall, independent of the material of the target plates. Figure 85 shows the results of experiments in JT-60, where the plasma was moved from the inboard limiter to the outer TiC-coated divertor [892]. A gas puff of  $2 \text{ Pa} \cdot \text{m}^3 \cdot \text{s}^{-1}$  was constantly injected up to 7 s. During the transition, the plasma density decreases very rapidly owing to strong pumping by the divertor plate and side wall. Further modelling details can be found in Ref. [884].

Similarly, in a large device such as ITER, because of the strong absorption of particles by the wall, the density drop can be very large, which may cause low density locked mode disruptions so that rapid fuelling is needed for proper density control. The requirements for the 1998 ITER design were analysed with the model described in Ref. [714], with feedback control of the fuelling rate. The results are illustrated in Fig. 86 and show that, during the transition phase, a fuelling rate of about  $500 \text{ Pa} \cdot \text{m}^3 \cdot \text{s}^{-1}$ , as specified in the design, allowed an adequate recovery rate of the density.

Wall models have also been extensively used to interpret/describe outgassing of hydrogen from the first wall after discharges. Several studies in tokamaks have shown that the deuterium release rate, as a function of time after a discharge,  $t$ , can be described by a power law proportional to  $t^{-n}$  with  $n \approx 0.5\text{--}1.0$  [652, 697, 893–896]. Reference [697] shows how such a relation may be derived from Eqs (32) and (33) for trapped and solute atoms and

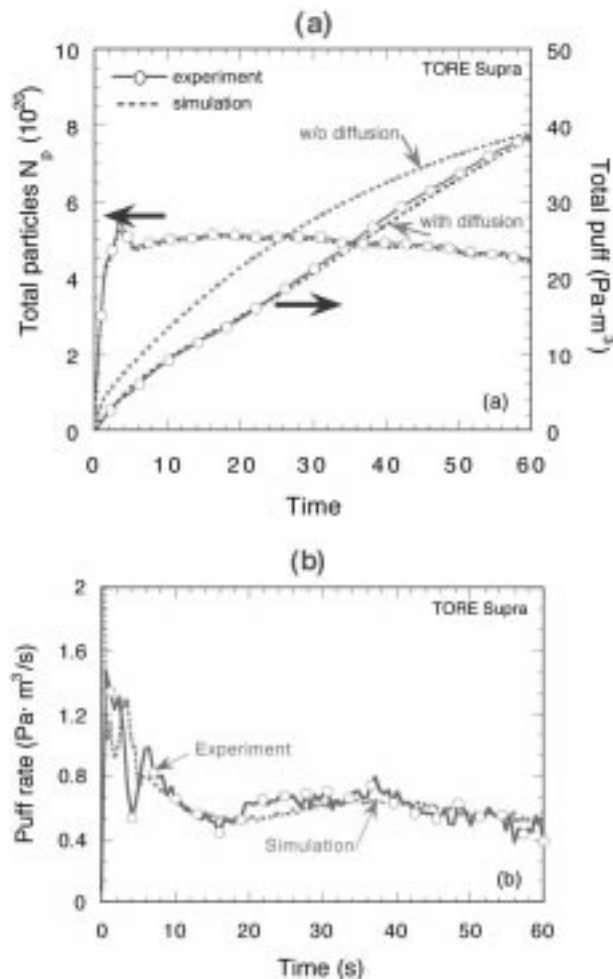


**Figure 87.** (a) Time evolution of the total puffed particles calculated to match the time behaviour of measured density for a long pulse Tore Supra discharge (shot 9016). Experimental results are represented with a solid line with open circles, whereas the results of the simulation are represented with a dotted line for a case with and a case without enhanced diffusion. The initial wall concentration was adjusted to match the total puffed particles at  $t = 60$  s with the experimental value (solid line with open circles). (b) Time behaviour of gas puff rate calculated with enhanced diffusion (dotted line) and the experimental value (solid line with open circles). (Reproduced with permission from Ref. [714].)

how the outgassing rate can decrease by orders of magnitude while the concentration in the material only varies by a factor of two.

Hydrogen transport/retention processes in graphite have also received a great deal of attention (see, for example Ref. [897]), and a large number of models have been proposed, based for the most part on laboratory scale experiments for basic

rates. However, wall recycling data are scarce for other materials such as Be, W, Mo, which are used to a much lesser extent than carbon in existing tokamaks, but are being considered promising candidates for wall protection in a next step device. The increased wall pumping effect observed in JET, upon incorporation of beryllium, is understood to be due to a larger number of empty traps becoming available before the next discharge due to an enhanced outgassing between discharges. However, that model [697] does not quantitatively explain the pumping behaviour of the JET walls during discharges. To explain the long term buildup of hydrogen isotopes in the first wall and divertor, it is necessary to include the effects of diffusion of hydrogen into the bulk of the material, and co-deposition. An interesting observation is that the more the discharges load up the wall with particles, the higher the outgassing rate becomes, particularly at longer times ( $>100$  s). As suggested by earlier studies [898–901], the long term (more than one discharge) depletion or saturation characteristics can be explained in terms of saturation of surfaces, which are irradiated by energetic neutral particles away from the strike points. This is caused by outward diffusion of more and more particles that have penetrated into greater depths of the material during the course of the previous plasma discharges.

Because of their particular relevance to next step tokamak operation, a set of typical long pulse discharges in Tore Supra [125] were analysed in Ref. [714] to identify the dominant wall pumping mechanisms. This discharge used lower hybrid current drive with a boronized first wall. The plasma density was maintained almost constant for  $\approx 60$  s, even under continuous gas fuelling without external pumping so that the walls absorbed all of the fuelled particles. Two plausible mechanisms of enhanced particle absorption were included in the model: (i) diffusion with adsorption along the inner surfaces of the wall, and (ii) co-deposition. The former mechanism had been suggested for the case of a boronized wall to explain the enhanced particle release after the shot [893]. Co-deposition was considered only for the limiter. Figure 87 shows the results of the calculations. The effective diffusion coefficient for the regions of the limiter and first wall and the initial particle concentration in the wall were selected to reproduce the experimental observations. Although the results of the calculations are close to the experimental data, further quantitative examination of the



role of diffusion/co-deposition is necessary to draw firmer conclusions on the actual loss mechanisms (Section 6.3).

### 5.6. Modelling of long term implanted tritium inventory/permeation

Accurate estimates of the long term accumulation of tritium on the surfaces and in the bulk of the materials of the PFCs in a next step device are required for determining the tritium supply requirements, for assessing the radiological hazards from routine operation and from potential accidents. The degree of tritium permeation to the coolant is also important for the design of the water detritiation system.

#### 5.6.1. Modelling approaches

This section describes models for estimating permeation, retention and re-emission of hydrogen isotopes from materials exposed to fusion plasmas. The underlying mechanisms of transport and retention of hydrogenic species in plasma facing materials currently considered as primary candidates for ITER are reviewed in Section 3.5. The modelling of co-deposition is discussed in Section 5.3. The modelling of recycling of hydrogenic species at the wall of tokamaks is discussed in Section 5.5.

Models for the retention of hydrogen isotopes in the implantation layer of graphite and C-based materials (Section 3.5 and Fig. 32) have shown a good fit with experimental data (Figs 34 and 35 and Refs [446, 450, 456, 469, 886, 902]). However, while this saturated region contributes very strongly to recycling and plasma density control in tokamaks (Section 4.6), its hydrogen retention capacity and contribution to the overall inventory are rather small. Modelling of mechanisms of tritium retention inside the geometrical surface of graphite and C-based materials, e.g. on pore surfaces and bulk, is still meagre. The models described in Refs [456, 903], for example, analyse the kinetics associated with the migration of hydrogen isotopes diffusing along the pores and adsorption onto pore surfaces. Much like the saturated layer, the tritium retention on graphite pore surfaces is fairly limited, and the overall effect of the porosity on the tritium retention in a device of the size of ITER is expected to be fairly small compared to co-deposition.

Although tritium migrates in the bulk of carbon only at elevated temperature ( $T \geq 1270$  K), the presence of pores allows the tritium gas to rapidly enter

the graphite, effectively exposing all of the inner porosity to an equal gas pressure, and, therefore, it is not necessary for the tritium to diffuse from the geometrical boundary inward. Success in modelling the uptake of tritium in the bulk of graphite has been obtained [453], assuming each of the graphite grains to be surrounded by the gas.

Models for estimating hydrogen diffusion, retention and re-emission for metals follow similar approaches and are based on physical mechanisms, which are described in Section 3.5 and Refs [378–381, 904]. The main physical processes are illustrated in Fig. 25. Hydrogen atoms in solution diffuse through the metal lattice and can be bound at traps within the matrix. These traps are characterized by a concentration and a binding energy of hydrogen to the trap. At the interfaces between the host structure and the gas or vacuum regions, most models assume that recombination takes place either with other diffusing atoms (second order) or with other populations of atoms (other hydrogen, oxygen, etc., first order). A solution law such as Sieverts' law or Henry's law may also be invoked if the hydrogen in solution and the gas phases are in thermodynamic equilibrium. Implantation is usually treated as a localized or distributed volumetric source. Retention of implanted hydrogen saturates when the hydrogen mobility is low, causing accumulation of high hydrogen concentrations. This occurs in carbon and in metals at low temperatures (Section 3.5). In metals, the hydrogen eventually precipitates into bubbles, and the bubbles grow and interconnect to form channels for rapid release. This limits the driving potential for diffusion deeper into the layer, restricting the total inventory and permeation rate (curve (2) Fig. 25).

Codes that follow this approach include PERI [905], DIFFUSE [426], PIDAT [427], and TMAP4 [906]. TMAP4 also includes heat transfer, fluid flows and chemical reactions in other than the solid state. Other codes such as BETTY [907] and ANFIBE [429, 908] were developed for beryllium. While using the same solid state transport equations, they include bubble formation, which has recently been recognized as a significant process for many materials at high plasma flux densities.

The codes used for modelling the interaction of hydrogen isotopes with materials often do not adequately include the phenomenon of saturation. TMAP4 uses temperature dependent expressions for hydrogen diffusivity, saturation concentration and surface recombination parameters, which repro-

duce the observed saturation behaviour for hydrogen retention in metals [431, 909].

A further consideration, at least for beryllium in tokamak applications, is the production of helium and tritium by neutronic transmutations in the beryllium itself. This has been observed experimentally in thermal and fast fission reactor testing, and fairly reliable calculations have been made for representative fusion applications [910, 911]. A major outstanding issue for most materials, especially Be, is the influence of neutron damage on trapping. The ANFIBE code [908] has addressed this issue with some success. Tritium production is a concern for safety reasons, and helium is important because it can influence the retention of tritium and it causes swelling of the material. There are two important pathways for gas production. One is the  $(n, 2n)$  reaction in which the  $^9\text{Be}$  is reduced to  $^8\text{Be}$ , which then splits into two  $^4\text{He}$  atoms. The second is the  $(n, \alpha)$  reaction where the  $^9\text{Be}$  absorbs a neutron and then splits to a  $^4\text{He}$  and a  $^6\text{He}$ . The  $^6\text{He}$  rapidly undergoes a  $\beta^-$  decay to become  $^6\text{Li}$ . The  $^6\text{Li}$  then reacts with a thermal neutron to produce  $^4\text{He}$  and  $^3\text{H}$ . These processes are incorporated into the FISPACT code [912], which was used by Forty et al. [910, 913] to estimate gas and other reaction product generation rates in a typical tokamak.

### 5.6.2. Status of model validation

The computer codes cited above have been used to model several kinds of experiments designed to measure H-isotope retention, release and permeation under controlled conditions. There are numerous publications citing instances where the codes and fit parameters have been used to simulate experiments. References [880, 894, 906, 909, 914–922] are representative. Experiments have been performed and modelled on a wide range of potential plasma facing materials including Be [880, 907–909, 917, 918], C [914], Cu [456, 915], stainless steel [906], V alloy [915], and W [915, 920–922]. In many cases, a good fit between modelling and data from several experiments is obtained, lending confidence to predictions of the performance of plasma facing structures in next step devices.

The TMAP4 code with saturation and erosion effects has been used to successfully model a number of past and recent experiments in beryllium [909]. These include Hsu's glow discharge and vacuum outgassing experiments [923] from which the currently accepted recombination coefficient for hydro-

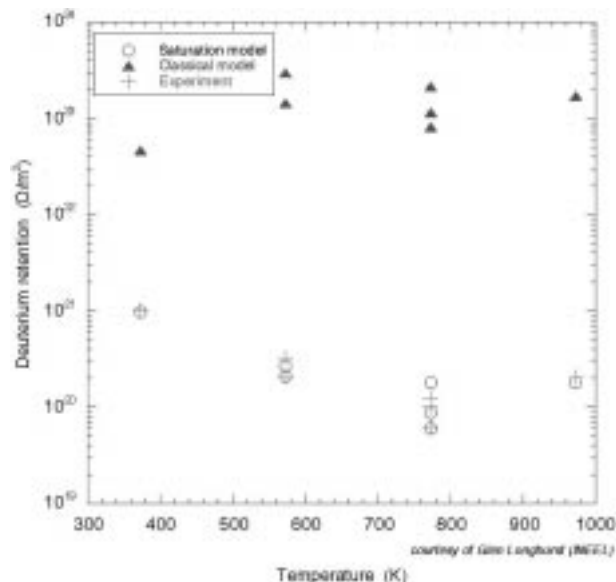


**Figure 88.** Comparison of measured deuterium retention in beryllium with that calculated by the saturation model and the classical model in the TMAP4 code for experiments in TPE [924]. (Figure provided by G. Longhurst, INEEL, Idaho Falls.)

gen on beryllium was derived, implantation experiments with beryllium at elevated temperatures at the INEEL [918], experiments to simulate hydrogen recycling in JET [887] and experiments with beryllium using the Tritium Plasma Experiment (TPE) at Los Alamos National Laboratory [924] (see glossary). Of these, only the INEEL and TPE experiments were at fluences high enough to encounter saturation effects. Figure 88 shows the results of calculations that were performed with the TMAP4 code to match the results of implantation experiments in beryllium performed in TPE [924]. An expression for Be was found, which was successful in replicating laboratory experiments that did not fit other models [431, 909]. These expressions approach the classical solution (diffusion with surface recombination) in the limit of low fluxes.

When modelling early experiments on tungsten at low implantation fluxes, the classical description was found to be adequate to give reasonable agreement with the experimental results if trapping was properly taken into account. However, in more recent studies at higher fluxes, the classical models do not fit the experimental data and the saturation effect needs to be taken into account in the more refractory materials. As an example, the TMAP4 code has also been used to simulate experiments performed on pure tungsten and on tungsten doped with about 1%

of  $\text{La}_2\text{O}_3$  (added to improve fabrication properties) that were exposed to deuterium and tritium plasmas in TPE and to ion beam implantation driven permeation experiments at INEEL [925]. In each case, there was a break point in temperature, above which classical recombination limited re-emission of implanted ions to the surface, based on literature values for trapping and transport parameters, appeared to be valid [925], and below which classical concepts proved inadequate to model the measured retention. The temperature at which that break point occurred was higher for higher ion flux densities. Analyses [922, 926] showed that these retention profiles, together with deuterium concentration profiles measured by NRA [927], could be reproduced by simply enhancing transport of implanted atoms from the implantation depth back to the surface, a process that appears to be characteristic of saturation and development of near surface interconnected cracks or porosity. Further work remains to establish the mechanism(s) for this enhanced transport.

5.6.3. Implanted tritium inventory analysis for next step devices

The retention and permeation of implanted tritium in ITER PFCs have been widely studied in the past (see, for example, Section 3.5.3.2 and Refs [3, 928, 929]). Table 22 summarizes the results of T-inventory and permeation calculations conducted with the TMAP4 code for the 1998 ITER design, which are discussed in Ref. [3]. Results for ITER-FEAT are similar and are described elsewhere [929].

On the basis of the results of these calculations, it can be concluded that the inventory of tritium in the beryllium first wall of a device such as ITER, because of implantation, diffusion, trapping and neutron induced transmutation, will be of the order of 100 g rather than the kilogram quantities estimated previously [930, 931], and most of that will result from neutron induced transmutations in the Be itself and from trapping in neutron induced traps. As was discussed in Section 5.3.2, co-deposition remains the major tritium repository for ITER. A comparison of the rate of tritium accumulation in the beryllium first wall (with and without neutron effects) and divertor co-deposition is shown in Fig. 89 for two indicative tritium co-deposition rates of 1 and 10 g/1000 s. In addition, permeation is very low; see Table 22.

**Table 22.** Summary of tritium inventory and permeation calculated by the TMAP4 code [906] through the PFCs of the 1998 ITER design for the Basic Performance Phase. This does not include tritium inventory due to co-deposition (Table reproduced from Ref. [3].)

Component	Tritium inventory (g)	Tritium permeation rate (g/day) <sup>a</sup>
First wall (impl.+breeding)	106 <sup>b</sup>	$7.0 \times 10^{-4}$
First wall (including n-effect)	194 <sup>c</sup>	$3.4 \times 10^{-11}$
Startup limiter	$9.2 \times 10^{-3}$	$4.7 \times 10^{-7}$
Upper baffle	0.78	$4.4 \times 10^{-5}$
Lower baffle	0.12	$6.5 \times 10^{-7}$
Upper vertical target	31	$8.1 \times 10^{-9}$
Dome	2.0	$1.5 \times 10^{-6}$
Totals	140 <sup>b</sup> /228 <sup>c</sup>	$7.5 \times 10^{-4}$

<sup>a</sup> It is assumed that  $\sim 10\,000$  pulses are distributed uniformly over 10 years.  
<sup>b</sup> Breeding is assumed on the basis of 14 MeV neutron current of  $1.15\text{ MW} \cdot \text{m}^{-2}$ , a peak value, as compared with  $0.94\text{ MW} \cdot \text{m}^{-2}$  poloidal average, and calculated production rates for the first wall; trapping characteristics were those of unirradiated beryllium (0.0005 atom fraction, 0.8 eV trap energy).  
<sup>c</sup> In addition to breeding, this calculation included neutron induced traps taken to be 2% atom fraction and 1.4 eV trap energy.

Note: Inventory in the bulk of carbon was estimated using the DIFFUSE code and was found to be small ( $\leq 1\text{ g} \cdot \text{m}^{-2}$ ).

6. Conclusions and future R&D priorities

Our knowledge of PMI processes in a fusion environment has greatly expanded during the past two decades as a result of extensive experimental and modelling efforts. These advances have provided a bridge to designing a next step device, and predicting and optimizing its performance. The ITER Design Activities have focused attention on an integrated solution to all design issues and have stimulated much PMI related research. Although the field is rapidly evolving, and the present review is one of work in progress, some key conclusions relevant to a next step device are presented below, together with some recommendations for future work. References to the section(s) of the review where the subject is

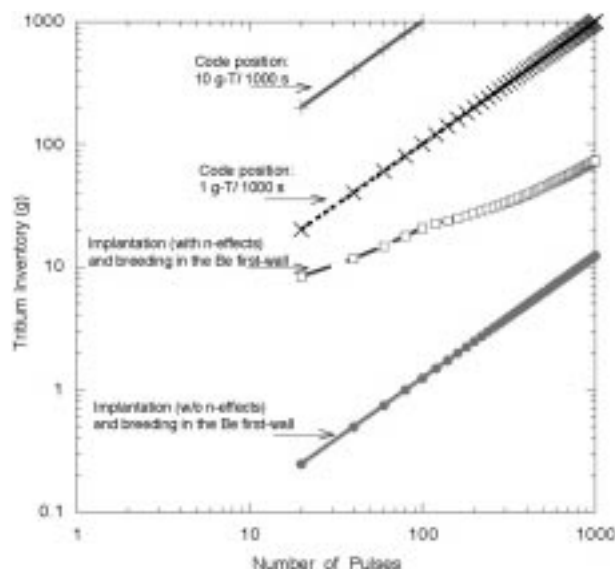


**Figure 89.** Comparison of the rate of tritium accumulation in the beryllium first wall of the 1998 ITER design (with and without  $n$  effects) and divertor co-deposition for two indicative tritium co-deposition rates of 1 and 10 g/1000 s.

discussed in detail are given.

### 6.1. Erosion and co-deposition effects

Summary of key findings:

- Net erosion rates of low  $Z$  materials in today's tokamaks are  $\approx 10 \text{ nm} \cdot \text{s}^{-1}$  for typical attached divertor plasmas ( $T_e \approx 20 \text{ eV}$ ), at target plate power densities of a few  $\text{MW} \cdot \text{m}^{-2}$ . Such power densities are similar to that expected in a next step long pulse machine, and these erosion rates will lead to unacceptably frequent replacements of PFCs (Section 5.3). The net erosion rates for hydrogen sputtering decreases with increasing atomic number of the plate material because of threshold effects for physical sputtering (Section 3.2.1).

- Detached plasmas allow a large heat flux reduction at the divertor plate, sufficient helium exhaust, and greatly reduce the incident particle energy at the divertor ( $T_e < 5 \text{ eV}$ ), reducing or eliminating physical sputtering of even low  $Z$  materials. However, carbon will still erode by chemical processes. The peak net erosion rate due to chemical sputtering at the ITER divertor target will be of the order of  $10 \text{ nm} \cdot \text{s}^{-1}$  and will require frequent replacements of the PFCs (Section 5.3).

- In divertor tokamaks, the main chamber wall is an area of net erosion, while both erosion and deposition occur in the divertor (Section 4.3). Co-

deposition of carbon with deuterium or tritium occurs mainly in the divertor region even when the divertor material is not carbon, as other carbon PFCs provide a source of carbon for co-deposition. This has been observed with the JET Mk-I beryllium and the ASDEX-Upgrade tungsten divertors (Section 4.7). Additionally, thick films accumulate in areas shaded from the plasma, and in gaps between tiles, e.g. as seen in TFTR (Section 4.7.1.1) and in JET (Section 4.7.1.2).

- In several tokamaks, the net erosion/deposition and associated H isotope retention is asymmetric with respect to the inner and outer strike points. This is, for example, the case in JET, DIII-D, ASDEX-Upgrade (for the case with Div-I only) and Alcator C-Mod (Section 4.3.1). The outer strike point is generally a region of net erosion, whereas net deposition of carbon is seen on the inner divertor. The asymmetry is particularly apparent in JET, where in the Mk IIA phase, heavy (flaking) deposition occurs on the water cooled louvres at the corner of the inner divertor, shaded from the plasma (Section 4.7.1.2).

- Intense co-deposition of carbon and deuterium is found in many tokamaks in regions which are shaded from ion flux but near carbon surfaces receiving high ion flux. Since ions cannot reach these shaded surfaces, this carbon deposition must be due to neutral carbon atoms or molecules/radicals resulting from dissociation of hydrocarbons released from carbon surfaces. In JET,  $D/C \approx 0.7$  was seen in co-deposits on the louvre surfaces (Sections 4.3.1 and 4.7.1.2).

- Erosion by arcing in current divertors warrants more detailed study of their effect. The principal limitation in the current understanding of arcing on divertor surfaces is the lack of diagnostic capabilities. Post exposure analysis of arc traces can be misleading. Detection of arcing in the divertor using electrical or optical methods, correlated with surface measurements, is needed to assess the impact of arcing in next step divertors.

Recommendations for further work:

- Some aspects of carbon sputtering and transport processes require clarification. Firstly, detailed dedicated experiments in plasma simulators and in tokamaks have shown, in some cases, a decreasing trend in the 'derived chemical erosion yield' of carbon/graphite for hydrogen fluxes above  $10^{22} \text{ m}^{-2} \cdot \text{s}^{-1}$  (Sections 3.2.3 and 4.3.1). Fluxes of this order of magnitude and higher are expected for next step devices, so any reduction would be beneficial. However, the derivation of yields from such plasma experiments is complicated by uncontrolled

changes in other plasma parameters and diagnostic limitations. Therefore, the flux dependence of the chemical erosion yield of carbon-based materials at high fluxes is still an open question.

In tokamaks some hydrocarbon molecules formed by erosion travel into shaded areas, with important consequences for tritium retention and recovery (Section 4.7). The complex role of molecular neutral and radical states and their transport/interactions with the plasma is posing a substantial challenge to PMI modelling. Experiments on this transport, and whether it can be used to advantage in a next step machine, are at an early stage. More research is needed to establish the absolute values of the sticking coefficients of such radicals.

- ‘Soft’ and ‘hard’ redeposited layers in tokamaks with carbon based targets have different properties (e.g. chemical sputtering yields (Section 3.2.6.4) and erosion by oxidation (Section 4.7.2.1)), and both are markedly different from the original material. Even in areas of net erosion, the plasma modifies the surface. Since erosion rates at these surfaces are crucial in modelling redeposition (and, hence, T retention) in next step devices, further measurements are essential.

- Estimates of erosion and tritium retention in next step devices depend on plasma edge modelling, but at present the models do not adequately explain the deposition seen in JET (Section 5.3). There are clearly additional processes occurring in the plasma boundary which require explanation and inclusion in the models. These include drifts in the SOL and interactions with the main chamber wall. A complete model of transport in the plasma boundary must be developed, and validated against deposition data from a range of tokamaks.

- Laboratory measurements on sputtering, hydrogen isotope retention and removal, etc. are generally performed on materials comprising a single element, for example, graphite or beryllium. However, the first wall of a next step device is likely to use multiple materials, for example, the ITER design includes areas of CFC, tungsten and beryllium. Erosion/deposition involves synergistic effects associated with these materials, requiring further exploration. Bench top experiments have a useful role to probe the synergistic effects at a fundamental level, but cannot alone provide the level of understanding required for prediction of all complex interactions in a fusion device environment. Tests are required on tokamaks with the appropriate impurities and wall materials to help answer questions, such as the magnitudes of ero-

sion and tritium co-deposition, dust formation in the vessel, and the ease of tritium removal from mixed materials.

- The plasma thermal energy divided by the surface area contacted by the plasma provides a measure of the severity of the PMIs in disruptions. This factor will be more than an order of magnitude greater in ITER than in existing large fusion machines. There exist strong material limits, for both W and CFC, which prohibit ELM sizes of  $>0.5 \text{ MJ}\cdot\text{m}^{-2}$ . Major disruptions and VDEs as well as Type I ELMs in ITER will cause ablation and melting of surface material in the divertor target area, and possibly at other parts of the divertor and at the first wall (Section 5.4). Calculations and experiments in plasma simulators predict that during disruptions in ITER a vapour shield forms in front of the divertor targets, dispersing the majority ( $>90\%$ ) of the incident energy flux to the divertor chamber walls via radiation that, in turn, causes shallow melting or sublimation on the nearby-surfaces (Sections 3.4, 4.5 and 5.4). However, there are still large uncertainties in determining the erosion associated with disruptions, in particular, the behaviour of the melt layer, and the effectiveness of the vapour shield to control the power on the surfaces. Vapour shielding has yet to be demonstrated in a tokamak. More work is needed to study erosion of metallic materials during an intense deposition of energy. Experiments and modelling are required to establish the role of brittle destruction of carbon based materials at these energies. Modelling must be further developed and tested against experimental results from disruption simulators to better understand the complex interactions at work.

- The past decade of divertor research has seen a return of interest to metals, which had been in the previous decade largely put aside in favour of carbon. This renewed interest is mainly due to the concerns about the chemical sputtering of carbon, even at the low energies present in the divertor (Section 3.2 and 4.3) and the consequent large hydrogenic retention in films forming primarily on cold surfaces (Sections 3.5 and 4.7). JET has experimented extensively with Be, as a low Z alternative to carbon. Operation with a relatively clean core plasma has been demonstrated for Alcator C-Mod with a high Z all Mo wall; in TEXTOR, with W clad limiters; and in ASDEX-Upgrade, with W coated divertor plates, and more recently, with a partially W clad central column. Impurity ion sputtering dominates the erosion rate. It is now realised that the proper selection and location of the PFCs, combined with the most recent plasma control

capabilities, allow us to take advantage of the low sputtering yields of these materials. Encouragingly, high heat flux components, clad with carbon-fibre materials or tungsten ‘brush’ materials have been developed and successfully tested up to  $25 \text{ MW} \cdot \text{m}^{-2}$  in steady state (Section 2.4), though more data and modelling of the response to off normal events are needed. It is clear that advances in materials technology alone are unlikely to resolve these issues, and improved plasma control, leading to reduction and mitigation of off normal events such as disruptions and ELMs, will be an essential part of the long term solution (Section 2.3.2.4). Type I and/or giant ELMs must be avoided.

## 6.2. Tritium retention and control of the in-vessel tritium inventory

Summary of key findings:

- Deuterium is retained in limiter machines with carbon PFCs at about 50% of the input (TFTR and JET pre-1989), and at around 5–15% (of a much greater input) in JET operating with a divertor and cryopump (Section 4.7.1.2). Tritium retention in the torus of carbon containing reactors will be dominated by co-deposition of carbon and tritium. Modelling predictions for ITER indicate up to few grams of retained tritium per pulse with pulse duration of several hundred seconds. The large in-vessel tritium inventory resulting from this high rate of retention has serious implications for the design, operation and safety of ITER, and may lead to the exclusion of carbon PFCs in future DT fusion reactors.

- Running discharges in D (or H) is an effective way to remove tritium from top surface of carbon PFCs without venting the machine (or exposing the surfaces to oxygen), so that no tritium enters the plasma in subsequent discharges (Section 4.7.1.2). However, the tritium retained in JET following DTE1 and subsequent D(H) discharges was only reduced by about a factor of two (to 17% of input T), because plasma operation could not reduce the retention in shaded areas (e.g. at the JET louvres) or tritium buried in co-deposits (e.g. at the TFTR limiters) (Section 4.7.1).

- Carbon can retain H isotopes to an atomic ratio of  $\text{H}:\text{C} > 1$  (Section 3.5.3), while retention in beryllium at low temperature is limited to an  $\text{H}:\text{Be}$  ratio of  $\approx 0.3$  (Section 3.5.2.4). However, outgassing from Be occurs at lower temperatures ( $\approx 600 \text{ K}$ ) compared to carbon based materials ( $> 800 \text{ K}$ ; see Section 3.5.3.3). Contamination of Be with C and/or O can greatly increase its retention capability. Recent

experiments showed that hydrogen implantation at low energies and high fluxes in beryllium results in little increase in inventory with dose at high fluence (Section 3.5.2.4), in part due to surface connected porosity that provides a rapid return path back to the plasma. This process is very favourable in a next step device lined with Be because it limits the tritium inventory and permeation rate in surfaces exposed to high particle fluxes (Section 5.6).

- Laboratory experiments involving thermo-oxidative erosion at temperatures above  $570 \text{ K}$ , or oxygen plasma discharges have been found to be effective in removing T containing films from carbon surfaces (Section 4.7.2). Erosion rates depend strongly on the microstructure of the co-deposited layers. Air ventilation (which entails oxidation) was found to be a simple and effective method of tritium removal, and, with other techniques, enabled the fraction of tritium retained to be reduced to 16% of input T in TFTR (Section 4.7.1.1), and to 6% in JET (Section 4.7.1.2). In TFTR, relatively more T was released with increasing temperature and/or air pressure, consistent with laboratory findings. Major drawbacks of techniques using oxygen, especially at elevated temperatures, include collateral effects on other reactor vessel components, and recovery time for normal plasma operation. Additionally, the handling of large quantities of HTO that would be produced in a next step DT device would require a large scale tritium processing plant (Section 2.3.3). Recently, promising results were obtained by laser heating that would avoid the introduction of oxygen (Section 4.7.2).

- Hydrogen retention on the main chamber wall of divertor tokamaks is limited to implantation by energetic charge exchange neutrals from the plasma. This inventory is not a significant part of the long term hydrogen inventory because the thickness of the implanted layer is small ( $< 0.1 \mu\text{m}$ ). However, even this quantity of hydrogen in the main chamber wall is much larger than the quantity of H in a plasma, and the dynamic variations of this wall inventory dramatically affect fuelling of individual discharges (Section 4.6).

Recommendations for further work:

- As long as carbon is used, even on limited areas of a next step device, operation requirements (due to safe operation limits and fuel economy considerations) will demand the frequent removal of the tritium from the co-deposited layers, or perhaps the removal of the layers altogether (Section 2.3.3). Alternatively, surfaces where co-

deposition is expected to occur could be kept 'hot' (i.e.  $\geq 770$  K) to prevent the accumulation of tritium, or very cold (i.e.  $< 273$  K) to enhance film deposition in localized areas, which could be periodically heated, or mechanically cleaned, to remove the tritium. However, both solutions are technically very difficult to implement in a reactor and, although several alternatives are being considered for the removal of the T rich co-deposited layers, their removal from a next step machine using carbon remains an outstanding challenge. Prototypes of most promising schemes should be demonstrated.

- Neutral atoms and molecules play a particularly important role in the high density, low temperature, detached-plasma regimes currently favoured for next step devices. Data on atomic and molecular processes, especially reaction pathways and reaction rates for heavy hydrocarbon molecules (i.e.  $C_xH_y$  with  $x \geq 2$ ) as a function of plasma conditions, are needed (Sections 3.2.3 and 4.3.1).

- Further work is also needed to better understand the effects of neutrons on creating traps in PFC materials and their effects on tritium retention. Further, the present techniques for accommodating the effects of surface saturation in the models are not very satisfactory. More detailed experiments/diagnostics are needed to test more detailed physics hypotheses leading to a deeper understanding from which improved models can then be drawn.

### 6.3. Requirements for modelling and interpretation of tokamak data

Predictive numerical codes are now available to simulate various aspects of PMIs and are recognized to be a vital tool in designing next step tokamaks (Section 5). Some of these codes have been successfully benchmarked against results from dedicated PMI experiments in current tokamaks. However, the comparison between data and models is sometimes difficult because some of the physical effects are still poorly understood and not included in the models. In addition, erosion/redeposition processes depend strongly on local plasma conditions that, in most cases, are not known very well. In general, the breadth and depth of diagnostic data from the wall/edge have generally lagged behind the sophistication of the computational resources. More time and space resolved wall diagnostic measurements are critically needed to match the computational opportunities and make progress toward integrated under-

standing of the complex relationship between the plasma edge and the wall (Section 6.4).

Nevertheless, dedicated measurements of in situ and ex situ erosion, with good near surface plasma diagnostics, have verified erosion/deposition models, for several materials and plasma regimes. In general, there is reasonably good confidence in the predictive value of the erosion/redeposition models for metals in all plasma regimes, and for carbon in attached regimes, given the validity of the input code computed plasma background solution. There has been considerable progress made in modelling detached plasma carbon erosion, but the codes are not yet validated for these conditions. Unlike existing machines where some measurements of near surface plasma conditions are often available, code computed plasma solutions of varying degrees of speculation must be used for ITER type reactor design analysis. Detached and/or partially detached plasma regimes involve highly uncertain physics, and analysis of these regimes needs further work. Moreover, there is highly conflicting experimental data on carbon chemical erosion (Section 6.1) and accordingly high uncertainty in modelling results. More work is needed in this area to develop reliable design information. As mentioned previously, critically important sub-models for detached plasma conditions include carbon chemical sputtering coefficients at low energies ( $\approx 5\text{--}15$  eV), rate coefficients for hydrocarbon molecular impact processes with plasma ions and electrons, hydrocarbon sticking coefficients, and the effects of mixed materials, e.g. beryllium and carbon, on sputtering and tritium trapping.

There are several critical issues resulting from particle recycling phenomena in a next step tokamak and we are still far from having fully predictive models that could be extrapolated with confidence to future fusion devices. They include: (i) sustaining density control during a long pulse; (ii) sustaining beneficial wall conditions during a long pulse; (iii) role of co-deposition and surface trapping/diffusion; and (iv) efficient, sustained fuelling of the core of a large ignited plasma. Present tokamaks have pulse lengths typically of the order of 10 s, and changes in recycling behaviour can often be observed even on this time scale. Pulse lengths in next step devices will be measured in several hundreds of seconds, so it is important to increase the pulse lengths in existing tokamaks, and operate simulation devices, to determine whether active control of recycling (e.g. by divertor cryopumps) will be required for next step devices (Sections 2.3 and 4.6).

Modelling work with the next generation of faster computers will likely involve kinetic model computation of mixed material surface evolution, and more use of molecular dynamic simulations for computing surface material properties. More integrated coupling of these simulations and codes for sheath dynamics, plasma core, SOL parameters, wall conditions etc. will lead to a better overall understanding of plasma surface behaviour. Additional model development, particularly for the near surface plasma, is required. The models should include erosion/deposition, retention and recycling of hydrogen in wall materials (Section 3.5), the energy and flux of H to the wall, and variations of these processes/parameters with space and time. The effects of the wall (e.g. recycled H) on plasma edge conditions also need to be considered.

Finally, understanding the physics of material response during off normal heating has improved, and now complex modelling tools are available. However, extrapolation to reactor conditions remains somewhat uncertain, and the modelling of the effect of vapour shielding, the stability of the melt layer and the role of brittle destruction in carbon must be further explored and tested against experimental results, particularly in tokamaks, to better understand the complex interactions at work.

#### 6.4. Need for improved wall diagnostics

There are a large number of issues regarding the processes occurring at the plasma boundary and wall regions that require active investigation. The complex and varied discharge history in tokamaks makes archaeological comparisons of post campaign in-vessel components with erosion/deposition and retention models of limited utility. This shortfall in our knowledge represents one of the largest uncertainties in the validation of existing codes. Measurements of erosion/deposition and H retention under different operational conditions such as startup/shutdown, disruptions, attached/detached plasma divertor, high power operations, etc. are required, e.g. by using film thickness monitors. There is a strong incentive to develop novel diagnostics in this area and to devote more dedicated run time to those that already exist (Section 4.2).

#### 6.5. Dust effects

Dust has not been a significant problem so far in magnetic fusion devices. Thus, the subject has received little attention within the fusion community. However, the amount of dust that will be gen-

erated in a next step device is likely to scale up by two to three orders of magnitude along with the erosion and discharge duration. In accident scenarios, chemical reactions of fine dust with steam and air create potential explosion and dispersal of radioactivity hazards. There is a need to couple models for erosion/sputtering and disruption to film and dust formation (e.g. physical adsorption, nucleation and condensation) and compare the results with tokamak experience and disruption simulations. This knowledge is vital for making reliable predictions of dust inventory for a next step device (Sections 2.3.4 and 4.8). Techniques for reliable measurement of dust inventory, particularly in hidden areas, are in their infancy, but are essential to assure compliance with regulatory limits. Even more critical is the development of reliable methods to remove dust.

Thick films of redeposited material found in present day tokamaks have been shown to break-up into flakes (Section 4.8.3). This material is potentially hazardous since the T content may be very high, as in the flaking films observed at the JET louvres (Sections 2.3.3, 4.7.1.2, and 4.8.3).

#### 6.6. A next step fusion reactor without carbon plasma facing components

If carbon were eliminated from the divertor of a next step device, the situation as far as tritium inventory is concerned would be radically different and the control of tritium inventory much more manageable. The FIRE design study has forgone the use carbon PFCs for this reason. The primary candidate in lieu of carbon for high heat flux regions is tungsten. In anticipation of positive developments in disruption and ELM mitigation, a high heat flux tungsten vertical target is being considered as a possible alternative in ITER. However, the primary shortcomings of W that need to be addressed are the lack of operational experience and the dearth of experimental data regarding formation of melt layers (and their properties) during disruptions. Operation at higher edge temperatures and lower densities in ‘advanced plasma scenarios’ (see glossary) results in more severe erosion by sputtering. Dust generation from beryllium and tungsten is still an outstanding issue (Section 6.5).

It is important to recognize that the plan to use carbon PFCs (and the consequent allocation of a significant fraction of the operational schedule for detritiation) follows directly from the projected levels of thermal loads expected during attached-plasma transients, ELMs and disruptions. Efforts to reduce tran-



sients and to mitigate disruptions must continue at the highest priority. Operation near the beta limit will require identification of disruption precursors and development of feedback control to avoid beta limits.

### 6.7. Concluding remarks

Designing a robust interface between a thermonuclear plasma and the material world remains a major challenge. The extensive data from existing tokamaks and simulators have enabled great strides to be made in our understanding of the processes involved in PMIs. However, there are many unresolved issues relating to a next step machine. Much more information can be learned from the existing facilities, particularly in areas such as mixed material effects, alternatives to the use of carbon targets (including disruption/ELM avoidance), transport effects in the plasma edge, and longer term retention and release of hydrogen isotopes. The consequences of a continuously burning plasma cannot be duplicated in existing devices. Predictive modelling is therefore essential. Unfortunately, the plasma edge region in a next step tokamak has a more complex geometry and a greater variety of interacting processes than the core plasma on which most effort has so far been concentrated in the fusion community. Much work remains to be done in this area, and more machine operational time and diagnostics dedicated to PMI issues are required. Initiatives on these fronts, together with modelling of the results, are essential to advance the understanding of PMIs.

Dependence on external energy supplies and the threat of climate change lend urgency to the quest for new energy sources such as nuclear fusion. A next step fusion reactor is a vital step that will accelerate the necessary technical solutions. A sustained and vigorous R&D programme in PMI issues focused on the key uncertainties identified in this review is vital for fusion to meet its promise as an attractive long term energy source for humanity.

## 7. Glossary of terms and acronyms

This glossary provides an explanation of some specific terms, which are used in this paper (e.g. some of the scientific vocabulary, the names of various research machines and devices used, the names of the various research laboratories, the mathematical symbols used and the acronyms frequently used as shorthand for some of the above). A good reference source for most of the common terms used in

fusion science can be found on the World Wide Web (<http://FusEdWeb.pppl.gov/Glossary/glossary.html>).

*(in alphabetical order)*

### a-C:H:

‘Amorphous hydrogenated carbon’ (normally as a deposited film).

### Activation:

Activation occurs when a particle interacts with an atomic nucleus, shifting the nucleus into an unstable state and causing it to become radioactive.

### ‘Advanced regimes’ or ‘advanced scenarios’:

Modes of operating a tokamak with improved plasma confinement and/or enhanced potential for continuous operation have been discovered in recent years and are studied in present tokamaks. Their study is an important part of the experimental programme foreseen for the next step fusion device. If proven to be of full reactor relevance, they would make it possible to construct a fusion power plant that is less costly than the existing designs. See also entry for internal transport barriers.

### AGHS:

Acronym for Advanced Gas Handling System.

### Alcator C-Mod

**(usually referred to as C-Mod):**

The name Alcator was given to a class of tokamaks designed and built at MIT; these machines are distinguished by high magnetic fields with relatively small diameters. The high magnetic field helps create plasmas with relatively high current and particle densities. The present incarnation is Alcator C-Mod (<http://cmmod2.psfc.mit.edu/cmmod/home.html>).

### ‘All carbon’ machine:

A tokamak wherein all particles travelling along field lines can only intersect with carbon components protecting the wall of the machine. However, much of the vessel wall may still be uncovered, so neutrals travelling radially from the plasma may still impinge upon non-carbon materials.

### ARIES:

Acronym for Advanced Reactor Innovation and Evaluation Studies. Set of fusion reactor design studies, which investigated the safety, economic and environmental implications of various advances in fusion reactor science and technology.

### ASDEX:

Acronym for Axially Symmetric Divertor Experiment. The original ASDEX, located in Garching, Germany and decommissioned in about 1990, would qualify today as a medium sized tokamak. It was designed for the study of impurities and their control by a magnetic divertor. The H mode or

high mode of operation with neutral beam injection was first observed on ASDEX. Its successor, *ASDEX-Upgrade* (a completely new machine, not really an ‘upgrade’), is larger and more flexible (<http://www.aug.ipp.mpg.de/>).

**Aspect ratio:**

In toroidal geometry, the ratio of the major diameter (total diameter of the torus) to the minor diameter.

**ATF:**

Acronym for Advanced Toroidal Facility.

**Baffle:**

Plates at the entrance of the divertor providing a transition between the divertor and the first wall, which also contribute to the retention of neutrals in the divertor.

**BET method:**

A gas adsorption technique devised by Brunauer, Emmett and Teller (BET) to measure the specific surface area of materials.

**Beta, or beta value:**

Ratio of plasma pressure to magnetic field pressure; proportional to the ratio of plasma thermal energy density to magnetic field energy density.

**Beta limit:**

It is also called Troyon limit and is the limit at which the plasma pressure in a tokamak becomes too high so that so-called ballooning modes become unstable and lead to a loss of confinement.

**Blanket:**

It is the region surrounding the fusion reactor core. The blanket of a fusion reactor has the threefold purpose of breeding the tritium by interactions of the neutrons with lithium, of converting the energy of the neutrons to high grade heat for electricity generation, and of shielding the super-conducting magnets from energy deposition and radiation damage.

**Bohr radius:**

It is the atomic unit of length,  $a_0 = 0.052918$  nm.

**Bootstrap current:**

Currents driven in toroidal devices by neoclassical diffusion. They may amount to a substantial fraction of the net current in a tokamak reactor, thus lengthening the pulse time or decreasing the power needed for current drive.

**Breakeven (scientific):**

When the fusion power equals the input power, i.e.  $Q = 1$ . See also entry for fusion power gain.

**Bremsstrahlung:**

German term for ‘Braking radiation’. Electromagnetic radiation from a charged particle as it slows

down (decelerates) or as it changes direction due to near collisions with other particles.

**Burning plasma:**

A plasma in which the heating is solely or primarily by alpha particles created by the fusion reaction itself. As an example, at  $Q = 10$  (see entry for fusion power gain), the power from the alpha particles would be two thirds of the total heating power. If *all* the heating is by alpha particles, this is termed an ‘ignited’ plasma.

**C II emission:**

Line emission due to electronic transitions in singly ionized carbon.

**CD band emission:**

Radiation emitted by a C–D molecule (CH band emission similarly comes from a C–H molecule).

**charge exchange**

Phenomenon in which an ion colliding with a molecule (or an atom) neutralizes itself by capturing an electron from the molecule/atom (becoming a charge exchange neutral), and transforming the molecule/atom into a positive radical/ion.

**CFC(s):**

Acronym for Carbon Fibre Composite(s).

**Composants internes et limiteur (CIEL):**

Major upgrade of Tore Supra in-vessel components, which will use a flat toroidal limiter to sustain a conducted heat flux of up to  $10 \text{ MW} \cdot \text{m}^{-2}$  and remove a total convective power of 15 MW for a pulse duration of 1000 s. The calculated pumping efficiency of this limiter is of the order of 12%, which corresponds to an extracted flux of  $4 \text{ Pa} \cdot \text{m}^3 \cdot \text{s}^{-1}$ . This capability is designed to be sufficient to ensure a good density control. Around the vessel, stainless steel actively cooled wafer panels will remove radiated power (up to 15 MW), to control water detraping and, therefore, to avoid any density excursion due to impurity release.

**Confinement times ( $\tau_E$ ,  $\tau_p$ ):**

$\tau_E$ ,  $\tau_p$  are the average times the plasma is contained (e.g. by magnetic fields) before energy ( $E$ ) or particles ( $p$ ) leak/dissipate away. The two times are, in general, similar but not equal. In a plasma device, the energy loss time (or the energy confinement time) can be expressed as the ratio of the total energy in the plasma and the externally supplied heating. This is one of three critical parameters determining whether fusion reactions could be sustained.

**Connection length:**

Half the distance along the magnetic field in the SOL between two points of contact with the solid surface.

**Coolant burnout:**

See entry for critical heat flux.

**Core plasma:**

Hot plasma at the centre of a fusion reactor.

**Count median diameter (CMD):**

50% of the particles in a distribution have diameters that are smaller than this.

**Critical heat flux (CHF):**

The heat flux that leads to the loss of liquid layer at the wall of the coolant channel and can result in a so-called coolant burnout.

**Current drive:**

A technique used to cause current flow in a plasma. See also entry for bootstrap current.

**Current quench time of disruptions:**

It is the characteristic time of the rapid current decay that follows the thermal quench. During this phase, the plasma magnetic energy is also dissipated, mostly by impurity radiation to the torus vessel or first wall surface; 100–1000 ms expected in ITER class tokamaks. See also thermal quench time entry.

**Cyclotron resonance:**

Charged particles in a magnetic field resonate with (and absorb energy from) an electric field (at an angle to the magnetic field), which oscillates at the particles' cyclotron frequency, or at a harmonic (multiple) of this frequency. See also electron cyclotron heating.

**DIII-D:**

A medium sized tokamak, but the largest tokamak still operational in the USA. Operated by General Atomics in San Diego (<http://fusion.gat.com/diii-d/>).

**D alpha:**

Spectroscopic emission line at 6561 Å from the  $n = 3 \rightarrow n = 2$  transition in deuterium. The most intense line in the visible wavelength range from deuterium plasmas, and the primary indicator of the influx of recycled deuterium into the 'plasma'.

**DEMO:**

Acronym for Demonstration Reactor.

**Detached regime:**

See plasma detachment.

**DiMES (Divertor Material Evaluation Studies):**

A retractable probe that allows the insertion and retraction of test material samples to the DIII-D divertor floor, e.g. for erosion/deposition studies.

**Displacements per atom (dpa):**

This is a measure of the amount of radiation damage in neutron irradiated materials, e.g. 10 dpa means that each atom in the material has been dis-

placed from its site within the structural lattice of the material an average of ten times (due to interactions between the atoms and the energetic neutrons irradiating the material).

**Disruption:**

Sudden loss of plasma confinement. The stored energy in the plasma is rapidly dumped into the rest of the plasma system (vacuum vessel walls, magnet coils, etc.) and can cause significant damage if precautions are not taken.

**DITE:**

Acronym for Divertor Injection Tokamak Experiment.

**DIVA:**

Acronym for Axisymmetric Divertor.

**Divertor:**

Component of a magnetically confined toroidal fusion device that diverts charged particles on the outer edge of the plasma into a separate chamber where they strike a barrier and become neutralized. In a reactor, the divertor would incorporate a system for pumping out the neutralised particles as exhaust from the machine. A divertor, like a limiter, prevents the particles (including helium ash) from striking and degrading the chamber walls and dislodging secondary particles that would cool and contaminate the plasma. See also limiter entry.

**DTE1:**

Acronym for Deuterium Tritium Experiment Number 1 — in JET in 1997.

**Duty factor (also called duty cycle):**

Ratio of the duration of time when a system is actually operating to the total time for a complete cycle of the system. For example, if a tokamak experiment runs for 5 s and then sits for 500 s, while the power supplies are recharged, then the duty factor is about 1%.

**D/XB:**

The ratio of the molecular influx to the intensity of accompanying molecular band emission. For methane a useful emission band is at 430 nm.

**Eddy current:**

Electric current induced inside a conductor when the conductor (a) moves through a non-uniform magnetic field, or (b) experiences a change in the magnetic flux through its surface.

**Edge localized modes (ELMs):**

ELMs are MHD related events that play a key role in mediating the energy and particle transport characteristics of the plasma edge in the regime of enhanced global energy confinement called the high confinement mode (see entry for High mode or

H mode). They involve the very rapid expulsion of energy and particles from the outer part of a confined plasma into the SOL and can transiently reduce the temperature and density in this region and thereby affect the core confinement. In addition, they can lead to increased peak heat loads on the divertor plates.

**Edge plasma:**

Cooler, less dense plasma away from the centre of a reactor (which includes the SOL), affected by contact with a limiter or divertor.

**Electron cyclotron discharge cleaning (ECDC):**

Using relatively low power microwaves (at the electron cyclotron frequency) to create a weakly ionized, essentially unconfined hydrogen plasma in the vacuum chamber. The ions react with impurities on the walls of the tokamak and help remove them from the chamber.

**Electron cyclotron heating (ECH or ECRH):**

Radiofrequency (RF) heating scheme that works by injecting electromagnetic wave energy at the electron cyclotron gyration frequency (or higher harmonics). RF energy is absorbed by electrons and then translated into ions through collisions.

**Energy amplification factor:**

See entry for fusion power gain.

**Ergodic divertor:**

It is a high density, low temperature, highly recycling and highly radiating region of the plasma formed by randomizing the field lines at the plasma edge.

**FIRE:**

FIRE is a design study for a major next step option in magnetic fusion. It aims at producing, understanding and optimizing alpha particle heated fusion plasmas and providing a stepping stone towards attractive magnetic fusion reactors. It is a compact (2 m major radius), high field (Cu coil, 10–12 T) design with a pulse duration (burn time) of 18 s. The duty cycle will be in the same range as in present machines, and FIRE is not designed to address the long pulse PMI issues that are the subject of this review. However, in response to concerns about tritium accumulation, the FIRE design has no carbon PFCs, the first wall is covered with Be tiles, and divertor uses W rods on a Cu backing plate.

**FT and FT-Upgrade (FTU):**

Acronyms for Frascati Tokamak and Tokamak-Upgrade, respectively.

**Fuel burnup or tritium burnup:**

See tritium fractional burnup.

**Fusion power gain,  $Q$ :**

The ratio of fusion power to the external power input. When  $Q = 1$  (a value transiently approached on JET in 1997), the fusion power is equal to the external power input. In this case, the self-heating power of a deuterium–tritium plasma is about 16% of the heating power necessary to maintain the plasma temperature. When  $Q = 5$ , the self-heating fraction equals 50%, becoming a significant factor of the plasma behaviour. The self-heating reaches 66% of the total heating power at  $Q = 10$  and 100% at an infinite  $Q$  (defining mathematically plasma ‘ignition’, a conceptual limit in magnetic confinement fusion).

**Glow discharge:**

Low density, low temperature plasma discharge sustained by current flowing between electrodes immersed in the plasma.

**Glow discharge cleaning (GDC):**

Cleaning in which impurities are removed by sputtering in a glow discharge.

**Greenwald density limit:**

An empirical limit to the density of a tokamak plasma when the line average electron density ( $10^{20} \text{ m}^{-3}$ ) equals the average plasma current density ( $\text{MA} \cdot \text{m}^{-2}$ ) times the plasma elongation (see entry).

**GSD:**

Acronym for Geometric Standard Deviation.

**Halo currents:**

Halo currents are currents generated during a disruption that flow along open field lines surrounding the plasma, in what is known as the ‘halo’ region, and return poloidally through the vessel. Large forces on the vessel components can result when these poloidal halo currents interact with the toroidal field. Toroidal halo currents do not contribute to forces on the vessel since they do not flow in the vessel wall.

**High mode or H mode:**

A regime of operation most easily attained during auxiliary heating of diverted tokamak plasmas when the injected power is sufficiently high. A sudden improvement in particle confinement time leads to increased density and temperature, distinguishing this mode from the normal ‘low mode’ or ‘L mode’. H modes are also possible in tokamaks without divertors, or without auxiliary heating, and have been observed in stellarators.

**High recycling:**

Plasma/surface boundary condition where almost all ( $\approx 99\%$ ) particles impinging on the surface (D, T, He, etc., ions and neutrals) come back out (by various processes including reflection and desorption), and

only  $\approx 1\%$  is removed (usually by active pumping), thereby tending to create high density and low temperature near surface and SOL plasma conditions.

**IAEA:**

Acronym for the International Atomic Energy Agency. It is an autonomous intergovernmental organization established in 1956 with the purpose of advancing peaceful uses of atomic energy, with headquarters in Vienna.

**Ignition:**

The point where the confinement of energy released from fusion reactions in the plasma is sufficient to maintain the plasma temperature so that no external heating is needed. See also entry for fusion power gain.

**Impurities:**

Atoms (or ions) of unwanted elements in the plasma, which tend to degrade plasma performance, and in the case of fusion, dilute the plasma so that fusion processes are less probable.

**Impurity screening:**

Impurities leaving the first wall (or the divertor target) as neutrals travel towards the core plasma, but are likely to be ionized and trapped in the edge of the plasma. From the edge, further inward movement is by cross-field diffusion. Thus, only a small fraction of impurities ever reach the plasma core; this blocking probability is impurity screening.

**Inconel:**

A range of nickel-based alloys containing chromium (Cr) and iron (Fe) with good high temperature strength and resistance to chemical corrosion. The JET vessel is manufactured from Inconel 600 (composition  $\text{Ni} + \text{Co} > 72\%$ , Cr 14–17%, Fe 6–10%).

**Internal transport barriers:**

Insulating layer established within the plasma resulting in significantly reduced transport, reduced particle influx, steeper density profiles and improved global energy confinement time. See also entry for advanced regimes.

**Ion cyclotron resonance heating (ICRH):**

Like electron cyclotron heating, but heats ions using waves near the ion cyclotron frequency. See entry for electron cyclotron heating.

**Isochronal annealing:**

A property is measured versus anneal temperature while the sample is heated to successively higher temperatures with constant time intervals at each temperature.

**ISX:**

Acronym for Impurity Study Experiment.

**ITER:**

Acronym for International Thermonuclear Experimental Reactor. Large fusion reactor design project being planned by the governments of the European Union, Japan, the Russian Federation (formerly, the USSR), and originally by the United States to develop a detailed engineering design for a reactor scale tokamak facility that would achieve controlled ignition and extended burn. As envisioned by the ITER Agreement, the ITER device would be the central element of an international, ‘one-step-to-a-reactor’ strategy. Research goals include engineering studies of reactor materials, component designs for steady state devices, and testing/proving commercial feasibility. Because of the concerns of costs, and thanks to the advances in physics and technology made during the ITER EDA, there has been both increased incentive and opportunity to seek an attractive lower cost design by modifying the detailed technical objectives. A reduced cost and reduced technical objectives ITER device is currently proposed (ITER-FEAT); it is expected to achieve an energy gain,  $Q$ , of at least 10 and explore steady state operation, at a direct capital cost of approximately 50% of the 1998 ITER design (<http://www.iter.org/>).

**JAERI:**

Acronym for Japan Atomic Energy Research Institute.

**JEBIS:**

Acronym for JAERI Electron Beam Irradiation Experiment.

**JET:**

Acronym for the Joint European Torus, a large tokamak located at the Culham Laboratory in Oxfordshire, England, jointly owned by the European Community. First device to achieve  $>1$  W of fusion power, in 1991, and the machine that has most closely approached  $Q = 1$  for DT operation ( $Q = 0.95$  in 1997). Largest tokamak currently in operation (<http://www.jet.efda.org/>).

**JFT:**

Acronym for JAERI Fusion Torus.

**JT-60 and JT-60U:**

A large Japanese tokamak, located north of Tokyo. JT-60U now in operation is an ‘upgrade’ to JT-60 (<http://www-jt60.naka.jaeri.go.jp>).

**JUDITH:**

Acronym for Jülich Divertor Test Facility in Hot Cells.

**Larmor radius:**

Radius at which an ion gyrates around a magnetic field line along which it circuits the torus.

**Last closed flux surface (LCFS):**

The boundary between the core plasma (see entry) in a tokamak (or other device), where the field lines close back on themselves, and the SOL (see entry), where they run into a material wall. See also entry for separatrix.

**LHD:**

Acronym for Large Helical Device.

**Limiters:**

Structures placed in contact with the edge of a confined plasma, which are used to define the shape of the outermost magnetic surface (see entry for LCFS). See also entry for divertor.

**Magnetohydrodynamics (MHD):**

Physical model describing the properties of electrically conducting fluids interacting with magnetic and electric fields. MHD theory is relevant at relatively low frequencies and for distance scales larger than the Larmor radius (see entry).

**Magnetohydrodynamic instability:**

Class of unstable (growing, not damped) waves and other modes of oscillation, which are described by MHD theory.

**MAST:**

Acronym for Mega Amp Spherical Tokamak (<http://www.fusion.org.uk/mast/main.html>).

**Mean Free Path (for a given event, e.g. collisions):**

Average distance a particle travels between occurrences of the given event, e.g. between collisions. For collisions, the mean free path is roughly equal to unity divided by the product of the ‘collision cross-section’ and the ‘particle density’.

**Melt layer thickness:**

Even in the presence of vapour shielding, the energy flux to the material surface is large enough to cause melting of metallic armours and the resulting melt layer thickness can be one to two orders of magnitude higher than surface vaporization losses. Therefore, the dynamic response of liquid metal layers exposed to various forces during the course of a disruption is a serious concern.

**Multi-faceted radiation from the edge (MARFE):**

An occasional toroidally symmetric, but poloidally localized, region at the plasma edge producing high radiation levels from impurities, self-sustaining at relatively low temperatures.

**Neutron wall loading:**

Energy flux carried by fusion neutrons into the first physical boundary that surrounds the plasma (i.e. the first wall).

**NBI:**

Acronym for Neutral Beam Injection.

**NRA:**

Acronym for Nuclear Reaction Analysis.

**NSTX:**

Acronym for National Spherical Tokamak eXperiment (<http://nstx.pppl.gov/index.shtml>).

**Ohmic heating:**

Heating that results from the flow of current through a medium with electrical resistance. In ohmically heated plasmas, ions are heated almost entirely by transfer of energy from the hotter, more mobile electrons.

**ORMAK:**

Early tokamak built at Oak Ridge National Laboratory.

**Partially detached plasmas:**

See plasma detachment.

**Particle recycling:**

In most tokamaks, the pulse length is at least an order of magnitude larger than the particle confinement time. Thus, on average, each plasma ion goes to the wall or limiter and returns to the plasma many times during the length of the discharge. This process is called ‘recycling’. See also entry for high recycling.

**Particle recycling coefficient:**

For a well defined surface, the recycling coefficient ( $R$ ) is the ratio of the returning particle flux from the surface to the plasma to the incident flux to the surface from the plasma. Therefore, for  $R < 1$ , the wall absorbs plasma particles, for  $R > 1$ , the wall fuels the plasma. The global recycling coefficient is an average over many local recycling coefficients at various surfaces inside a tokamak.

**PBX:**

Acronym for Princeton Beta eXperiment.

**PDX:**

Acronym for Poloidal Divertor eXperiment.

**Pedestal:**

In an H mode plasma (see entry), there is a region of high confinement and steep density gradient near the edge of the plasma. This region acts as a platform (or ‘pedestal’) to support the core of the plasma (which has lower confinement).

**Pellet injection/pellet injector:**

This is a device which accelerates (shoots) small (typically, few mm diameter) frozen pellets of hydrogen isotopes (or other elements); these are then launched at high speed (ca. 1000 m/s) into the core

plasma. Used mainly for plasma fuelling but also for wall conditioning, plasma diagnostics and disruption control.

**PFC(s):**

Acronym for Plasma Facing Component(s).

**PISCES:**

Acronym for the Plasma Interaction with Surface Components Experimental Station. Plasma simulator, at the University of San Diego in the United States (originally at University of California, Los Angeles), used to test materials and measure sputtering, retention, etc. expected in tokamaks (<http://cerfe.ucsd.edu/piscs/piscs.html>).

**Plasma detachment:**

Low temperature plasma regime where there is significant plasma pressure loss along field lines close to the target plate. This is usually accompanied by a significant decrease in the incident power and plasma flux density. One refers to full detachment if the plasma is detached from the entire length of the divertor target; and to partial detachment, (or to semi attached plasma) if the plasma is detached over some of the divertor target surface (typically near the separatrix), but still attached elsewhere (see Fig. 82).

**Plasma elongation ( $\kappa$ ):**

Parameter indicating the degree to which the cross-section of a toroidal plasma is non-circular;  $\kappa = b/a$ , where  $b$  and  $a$  are the vertical and horizontal minor radii. As  $\kappa$  is increased, the confinement in relation to the total current improves, but the plasma also becomes more unstable to vertical displacements.

**Plasma inductance:**

Parameter relating the magnetic flux generated through the plasma to the current in the plasma.

**PLT:**

Acronym for Princeton Large Torus.

**PMI(s):**

Acronym for Plasma–Material Interaction(s).

**Poloidal direction:**

In the vertical plane, around the minor cross-section of a torus.

**Private flux region:**

The region below the X point (see entry) and inside the separatrix (see inset in Fig. 1). It contains a thin layer of plasma lying along the two separatrix arms, terminating at the targets..

**PSI-1:**

Plasma generator located in the Max-Planck-Institut für Plasmaphysik in Berlin used for investigation of plasma boundary.

**PTE:**

Acronym for Preliminary Tritium Experiment — in JET in 1991.

**QSPA:**

Acronym for Quasi-Stationary Plasma Accelerators used for investigation of disruption erosion and damage of plasma facing materials.

**Radiation damage:**

General term describing changes in physical and/or metallurgical properties of materials caused by atomic displacement and nuclear transmutation events occurring as a result of exposure to a radiation environment (such as the neutrons emitted from a fission or DT fusion reactor).

**RBS:**

Acronym for Rutherford Backscattering Spectrometry.

**RF:**

Acronym for Radio Frequency.

**Runaway electrons:**

Those electrons in a plasma that gain energy from the toroidal electrical field at a faster rate than they lose it through collisions with other particles. These electrons tend to ‘run away’ in energy (not position) from the cooler remainder of the background plasma, because the collision cross-section decreases as the particle’s velocity increases, so that the faster the particle goes, the less likely it is to be stopped.

**Safety factor ( $q$ ):**

The number of times a field line goes around a torus toroidally for each time around poloidally. In a tokamak, this number is typically near unity in the centre of the plasma and between two and six or eight at the edge. So-called because it helps to determine the resilience the plasma has against certain instabilities. The safety factor is the inverse of the rotational transform, and for a large aspect ratio circular cross-section tokamak, can be approximated as  $q = (r \times B_t)/(R \times B_p)$ , where  $r$  and  $R$  are the minor and major radii of the torus, respectively, and  $B_t$  and  $B_p$  are the toroidal and poloidal magnetic fields, respectively.

**Sawtooth:**

When a tokamak operates with enough current to achieve  $q < 1$  on the magnetic axis, the plasma parameters ( $n$ ,  $T$ ,  $B$ ) oscillate with a ‘sawtooth’ waveform. The oscillation is localized to a region roughly within the  $q=1$  surface, and arises from internal MHD effects. Confinement is degraded within the sawtooth region.

**Scrape-off-layer (SOL):**

Outer layer of a plasma, which is affected (‘scraped off’) by a divertor or limiter. That is, the

outer layer of a magnetically confined plasma where the field lines intersect a material surface (limiter or divertor plate) rather than close upon themselves. Plasma crossing into the SOL is rapidly lost since transport along the field is much faster than that across the field.

**SEM:**

Acronym for Scanning Electron Microscopy.

**Separatrix:**

In a divertor tokamak (and some other configurations), the last closed flux surface (see entry) is formed not by inserting an object (limiter) but by manipulating the magnetic field, so that some field lines take a topologically different route (through the divertor, rather than simply around the central plasma). The boundary between the field lines that close back on themselves and those that penetrate a material surface is called the separatrix.

**SIMS:**

Acronym for Secondary Ion Mass Spectroscopy.

**Sputtering:**

Process by which atoms are ejected from a solid surface by bombardment with energetic particles.

**Sputtering yield:**

Number of target atoms sputtered per incident atom/ion; varies with target and plasma species and energy.

**START:**

Acronym for the Small Tight Aspect Ratio Tokamak Located at Culham, England. This spherical tokamak claims the record  $\beta$  value for a tokamak.

**Superconductor:**

A type of electrical conductor that permits a current to flow with zero resistance. Without superconducting coils, a toroidal magnetic confinement fusion reactor would not be possible, because too much energy would be required to maintain the magnetic fields against resistive energy losses in the coil conductors.

**Supershot:**

A high confinement regime in TFTR beam heated plasmas that was obtained after wall conditioning had depleted deuterium from the limiter.

**T-3, T-10...**

Series of tokamaks built at the Kurchatov Institute in Moscow. T-3 was the first machine to demonstrate fusion relevant plasma temperatures and to demonstrate the potential of the tokamak concept.

**TCV:**

Acronym for Tokamak à Configuration Variable.

**TdeV:**

Acronym for Tokamak de Varennes, i.e. a small

tokamak in Quebec, Canada, that has now been closed.

**TDS:**

Acronym for Thermal Desorption Spectroscopy.

**TEXT:**

Acronym for TEXas Tokamak.

**TEXTOR:**

Acronym for the Tokamak EXperiment for Technology Oriented Research. Medium-sized European tokamak located in Jülich, Germany. Research objectives include developing PFCs and studying effects of plasma-wall interactions (<http://www.kfa-juelich.de/ipp/>).

**TFR:**

Acronym for Torus Fontenay-aux-Roses.

**TFTR:**

Acronym for the Tokamak Fusion Test Reactor: Large tokamak at Princeton; first machine to use 50%–50% mix of DT fuel; current record holder for total fusion energy production. TFTR was the largest tokamak in the United States, but ceased operation in 1997 (<http://www.pppl.gov/tftr/>).

**Thermal quench time of disruptions:**

It is the characteristic time in which most of the plasma thermal energy is lost, primarily by conduction to the plasma defining surfaces (limiter or divertor targets). During a thermal quench, the core plasma temperature typically falls, first to less than several hundred eV, and subsequently to less than 100 eV; 1–10 ms expected in ITER-class tokamaks. See also entry for current quench time.

**Tokamak:**

Acronym created from the Russian words, “TOroidalnaya KAmera i eë MAgnitnaya Katushka” or Toroidal Chamber and Magnetic Coil.

**Tore Supra:**

It is the second largest tokamak in Europe, and is located in Cadarache (southern France). It uses superconducting toroidal field magnets. Tore Supra has a circular cross-section, which limits the achievable confinement time and experimental flexibility. In addition to developing superconducting technology, it concentrates on the physics of long pulses (<http://www-cad.cea.fr/r50.htm>).

**Toroidal direction:**

In the horizontal plane, around the vertical axis of the torus.

**TPE:**

Acronym for the Tritium Plasma Experiment, a plasma simulator used primarily for studies of tritium retention and effects in plasma facing surfaces. TPE is operated by Sandia National Labo-



ratories. TPE is presently being transferred from the Tritium System Test Assembly (TSTA) facility at Los Alamos National Laboratory to the Idaho National Environmental Engineering Laboratory in Idaho Falls, Idaho.

#### **Tritium breeding ratio (TBR):**

The amount of tritium generated by the breeding blanket of a DT fusion reactor, divided by the amount of tritium burned in the reactor. A tritium breeding ratio greater than unity is necessary for self-sufficient fuelling.

#### **Tritium fractional burnup:**

During normal operation of a DT tokamak, only a small fraction of the fuel will be consumed (i.e. burned by DT fusion reactions), the rest will be retained in the plasma facing surfaces or pumped out and reprocessed. The tritium fractional burnup,  $f_b$ , is defined as the ratio of the burn rate to the total rate of fuel loss from the vessel by either burning, pumping or retention. In existing tokamaks (e.g. TFTR and JET) this fraction is of the order of  $10^{-4}$ . In a next step device like ITER, the tritium fractional burnup will be of the order of few per cent.

#### **TZM :**

An alloy of molybdenum with 0.5% Ti, 0.1% Zr, which improves high temperature properties by raising the recrystallization temperature.

#### **Unipolar arc:**

Arc between a metal surface and a plasma in contact with it. Such an arc requires only one electrode and is maintained by the thermal energy of the electrons.

#### **Vapour shielding layer:**

During the initial stage of a plasma disruption, the energy deposited onto the exposed surface will cause ablation of the material and sudden formation of a vapour cloud above the exposed area. This vapour cloud, if well confined, will significantly reduce the subsequent net energy flux to the material surface, thus reducing vaporization losses, by orders of magnitude.

#### **VDE:**

Acronym for Vertical Displacement Event. See entry for vertical instability.

#### **Vertical instability:**

A type of MHD ( $n = 0$ ) instability where the plasma drifts vertically upward or downward. Nearly all tokamaks (especially, if D shaped) are vertically unstable. Controlling this instability is possible in many cases and is an important facet of machine design; control is often lost in the current quench phase of disruptions in D shaped tokamaks, result-

ing in what is termed a vertical disruption or vertical displacement event (VDE). Vertical instabilities give rise to halo effects (see entry for halo currents).

#### **Wall pumping:**

The term 'wall pumping' is commonly used for the spontaneously occurring net particle removal by the wall during standard plasma operation, as well as for the induced pumpout effect that occurs when the plasma is suddenly moved to a part of the wall that is able to provide net particle absorption, usually the inboard wall.

#### **X point:**

Place where the poloidal magnetic field vanishes in such a way that two flux surfaces appear to cross, e.g. where the main plasma joins the divertor region, or between magnetic islands.

#### **$Z_{eff}$ :**

It is the mean ion charge in the plasma:

$$Z_{eff} = \Sigma n_i Z_i^2 / \Sigma n_i Z_i$$

## **Acknowledgements**

The authors gratefully acknowledge the many helpful conversations with many researchers (see names below) within the European Union, Japan, the Russian Federation, the United States of America, Canada and other countries that have contributed in expanding on information available in the literature.

In particular, we would like to thank Vladimir Alinov, Masato Akiba, Igor Arkhipov, Nobozuki Asakura, Vladimir Barabash, Rainer Behrisch, Harald Bolt, David Campbell, Rion Causey, Glenn Counsell, Jim Davis, Russell Doerner, Vladimir Filatov, Peter Franzen, Charles Gentile, Alexander Gorodetsky, Yoshi Hirooka, John Hogan, Chris Ibbott, Wolfgang Jacob, Guenter Janeschitz, Charles Kessel, Andre Kukushkin, Christinal Linsmeier, Vladimir Litunovsky, Alberto Loarte, Glen Longhurst, Hans Maier, Rajesh Maingi, Alexey Makhankov, Andrey Markin, Matej Mayer, Igor Mazul, Dennis Mueller, Nobuaki Noda, Richard Nygren, Horst Pacher, Alan Peacock, Ralf-Dieter Penzhorn, Michael Pick, Marek Rubel, Valeri Safronov, Gabriella Saibene, Roberta Sartori, Michiya Shimada, Peter Stangeby, William Spears, Masayoshi Sugihara, Tetsuo Tanabe, Richard Tivey, Mike Ulrickson, Achim von Keudell, John Wesley, Phil West, Clement Wong, Chung Wu, Hermann Wuerz, Andrey Zakharov, Mardjan Zarrabian, Anatoly Zhitlukhin.

We owe a special thank to Kathy A. McCarthy, Dave A. Petti, Robert Anderl, W.J. Carmack and

John P. Sharpe of the Idaho National Engineering Environmental Laboratory for their kind help in collecting and reviewing the available database on dust; Houyang Guo and Mike Stamp of JET, Rudolf Neu, Volker Rohde, Arne Kallenbach and Karl Krieger of ASDEX-Upgrade, S. Higashijima, H. Kubo and Kei Masaki, of JT-60U, H.G. Esser, Albrecht Pospieszczyk, Egon Vietzke, J. von Seggern and Peter Wienhold of TEXTOR, and Philip Philippe Ghendrih of Tore Supra, for providing useful information from their respective machines for use in the review.

Finally, we are grateful to the assistance provided by David Ignat, Andreas Schott and Ujwal S. Sathyam in the final typesetting of this manuscript.

This paper was prepared by authors from several institutions and was prepared in part as an account of work undertaken within the framework of the ITER EDA Agreement. The views and opinions expressed herein do not necessarily reflect those of the Parties to the ITER Agreement, the IAEA or any agency thereof. Dissemination of the information in this paper is governed by the applicable terms of the ITER EDA Agreement.

## References

- [1] Toschi, R., *Fusion Eng. Des.* **36** (1997) 1.
- [2] Loarte, A., et al., in *Fusion Energy 2000* (Proc. 18th Int. Conf. Sorrento, 2000), IAEA, Vienna (2001). CD-ROM file ITERP/11(R), and <http://www.iaea.org/programmes/ripc/physics/fec2000/html/node245.htm#55022>.
- [3] Federici, G., et al., *Nucl. Mater.* **266–269** (1999) 14.
- [4] Skinner, C.H., et al., *Nucl. Fusion* **39** (1999) 271.
- [5] *Plasma–Surface Interactions in Controlled Fusion Devices*, Elsevier, Amsterdam, published by J. Nucl. Mater.
- [6] *Volumes of Atomic and Plasma–Material Interaction Data for Fusion*, published by the International Atomic Energy Agency as Supplements to *Nucl. Fusion*.
- [7] Post, D.E., Behrisch, R., (Eds) *Physics of Plasma–Wall Interactions in Controlled Fusion*, NATO ASI Series B: Physics, Plenum Press, New York (1986).
- [8] Stangeby, P.C., McCracken G.M., *Nucl. Fusion* **30** (1990) 1225.
- [9] Pitcher, C.S., Stangeby, P.C., *Plasma Phys. Control. Fusion* **39** (1997) 779.
- [10] Stangeby, P.C., *The Plasma Boundary of Magnetic Fusion Devices*, Institute of Physics Publishing, Bristol (2000) 712 pp.
- [11] Causey, R., Tritium retention in plasma-facing materials, *J. Nucl. Mater.* (to appear).
- [12] Abdou, M.A., et al., *Fusion Eng. Des.* **54** (2001) 181.
- [13] ITER Physics Basis, *Nucl. Fusion* **39** (1999) 2137.
- [14] Keilhacker, M., *Plasma Phys. Control. Fusion* **29** (1987) 1401.
- [15] Lipschultz, B., et al., *Phys. Plasmas* **6** (1999) 1907.
- [16] Kukushkin, A.S., et al., *Contrib. Plasma Phys.* **38** (1998) 20.
- [17] Parker, R., et al., *J. Nucl. Mater.* **241–243** (1997) 1.
- [18] Barabash, V., Federici, G., Matera, R., Raffray, A.R., ITER Home Teams, *Phys. Scripta T* **81** (1999) 74.
- [19] Janeschitz, G., et al., *Nucl. Fusion* **40** (2000) 1197.
- [20] Meade, D., *Nucl. Fusion* **14** (1974) 289.
- [21] Reiter, D., Wolf, G.H., Kever, H., *Nucl. Fusion* **30** (1990) 2141.
- [22] Behrisch, R., Prozesky V., *Nucl. Fusion* **30** (1990) 2166.
- [23] Wade, M.R., et al., *Nucl. Fusion* **38** (1998) 1839.
- [24] Goetz, J.A., et al., *Phys. Plasmas* **6** (1999) 1899.
- [25] Goetz, J.A., et al., *J. Nucl. Mater.* **266–269** (1999) 354.
- [26] Kallenbach, A., et al., *Nucl. Fusion* **35** (1995) 1231.
- [27] Umansky, M.V., Krasheninnikov, S.I., LaBombard, B., Lipschultz, B., Terry, J.L., *Phys. Plasmas* **6** (1999) 2791.
- [28] Chankin, A.V., et al., *J. Nucl. Mater.* **290–293** (2001) 518.
- [29] Erents, S.K., *Plasma Phys. Control. Fusion* **42** (2000) 905.
- [30] Asakura, N., *Phys. Rev. Lett.* **84** (2000) 3093.
- [31] Gouge, M.J., *Fusion Technol.* **34** (1998) 435.
- [32] Milora, S.L., Houlberg, W.A., Lengyel, L.L., Mertens, V., *Nucl. Fusion* **35** (1995) 657.
- [33] Skinner, C.H., et al., *Phys. Plasmas* **5** (1998) 1062.
- [34] Winter, J., *J. Nucl. Mater.* **176&177** (1990) 14.
- [35] Ongena, J., et al., in *Controlled Fusion and Plasma Physics* (Proc. 24th Eur. Conf. Berchtesgaden, 1997), Vol. 21A, part 4, EPS, Geneva (1997) 1693.
- [36] Dylla, H.F., Cohen, S.A., Rossnagel, S.M., *J. Vac. Sci. Technol.* **17** (1980) 286.
- [37] Poschenrieder, W., Staudenmaier, G., Staib, Ph., *J. Nucl. Mater.* **93–94** (1980) 322.
- [38] Waelbroeck, F., Winter, J., Wienhold, P., *J. Vac. Sci. Technol. A* **2** (1984) 1521.
- [39] Sakamoto, Y., et al., in *Fusion Technology* (Proc. 12th Symp. Jülich, 1982), Vol. 1 (1983) 347.
- [40] Sagara, A., et al., *J. Plasma Fusion Res.* **75** (1999) 263.
- [41] Esser, H.G., et al., *J. Nucl. Mater.* **241–243** (1997) 861.
- [42] Dietz, K.J., Waelbroeck, F., Wienhold, P., *Origin of Impurities in Hydrogen Plasmas*, Rep. JUEL-1448 (1977), KfS Jülich, Inst. für Plasmaphysik.

- [43] Greenwald, M., et al., Nucl. Fusion **37** (1997) 793.
- [44] Lipschultz, B., et al., Nucl. Fusion **41** (2001) 583.
- [45] Jackson, G.L., et al., Phys. Rev. Lett. **67** (1991) 3098.
- [46] Owen, L.W., et al., J. Nucl. Mater. **266–269** (1999) 891.
- [47] Higashijima, S., J. Nucl. Mater. **220–222** (1995) 375.
- [48] Samm, U., et al., J. Nucl. Mater. **220–222** (1995) 25.
- [49] Esser, H.G., et al., J. Nucl. Mater. **186** (1992) 217.
- [50] Sykes, A., et al., in Fusion Energy 2000 (Proc. 18th Int. Conf. Sorrento, 2000), IAEA, Vienna (2001) IAEA-CN-77, CD-ROM file OV4/1, and <http://www.iaea.org/programmes/ripc/physics/fec2000/html/node38.htm#7766>.
- [51] Skinner, C.H., et al., Effect of boronisation on ohmic plasmas in NSTX, Nucl. Fusion to appear.
- [52] Mansfield, D.K., et al., Phys. Plasmas **3** (1996) 1892.
- [53] Mansfield, D.K., et al., Phys. Plasmas **2** (1995) 4252.
- [54] Strachan, J.D., et al., J. Nucl. Mater. **217** (1994) 145.
- [55] Moir, R.W., Nucl. Fusion **37** (1997) 557.
- [56] Zakharov, L., Bull. Am. Phys. Soc. **44** (1999) 313.
- [57] Saibene, G., et al., J. Nucl. Mater. **220–222** (1995) 617.
- [58] Rohde, V., et al., in Controlled Fusion and Plasma Physics (Proc. 26th Eur. Conf., Maastricht, 1999), EPS, Geneva. CD-ROM file P4.038 <http://epsppd.epfl.ch/Maas/web/sessions.htm#p4038>.
- [59] Gauthier, E., et al., J. Nucl. Mater. **196–198** (1992) 637.
- [60] Strachan, J. D., Nucl. Fusion **39** (1999) 1093.
- [61] Ernst, D.R., et al., Phys. Rev. Lett. **81** (1998) 2454.
- [62] Monk, R.D., JET Team, Nucl. Fusion **39** (1999) 1751.
- [63] Matthews, G.F., et al., J. Nucl. Mater. **196–198** (1992) 374.
- [64] Whyte, D.G., Coad, J.P., Franzen, P., Maier, H., Nucl. Fusion **39** (1999) 1025.
- [65] Spitzer, L., Rep. NYO-993 (PM-S-1), US Atomic Energy Commission.
- [66] Spitzer, L., Phys. Fluids **1** (1958) 253.
- [67] Burnett, C.R., et al., Phys. Fluids **1** (1958) 438.
- [68] Craston, J.L., et al., in Peaceful Uses of Atomic Energy (Proc. 2nd Int. Conf. Geneva, 1958), Vol. 32, UN, Geneva (1958) 414.
- [69] Simonov, V.A., et al., in Plasma Physics Controlled Nuclear Fusion Research (Proc. Conf. Salzburg, 1961), Nucl. Fusion Supplement, part I, IAEA, Vienna (1962) 313.
- [70] Behrisch, R., Nucl. Fusion **12** (1972) 695.
- [71] McCracken, G.M., Stott, P.E., Nucl. Fusion **19** (1979) 889.
- [72] Garbunov, E.P., et al., 4th European Conf. on Control. Fusion and Plasma Phys., Rome, Italy, Nat. Nucl. Energy Committee (1970) 19.
- [73] Peacock, N.J., et al., Nature **224** 5218 (1969) 488.
- [74] Behrisch, R., “Surface erosion by electrical arcs”, Physics of Plasma–Wall Interactions in Controlled Fusion, NATO ASI Series B: Physics, Plenum Press, New York (1986) 495.
- [75] TFR Group, Nucl. Fusion **16** (1976) 473.
- [76] Ellis, R.A., Nucl. Fusion **25** (1985) 1145.
- [77] Zuhr, R.A., et al., J. Nucl. Mater. **85&86** (1979) 979.
- [78] Ascoli-Bartoli, U., et al., in Plasma Physics and Controlled Nuclear Fusion Research 1974 (Proc. 5th Int. Conf. Tokyo, 1974), Vol. 1, IAEA, Vienna, Austria (1975) 191.
- [79] TFR Group, in Plasma–Wall Interactions (Proc. Int. Symp. Jülich, 1976), Pergamon Press, Oxford (1977) 3.
- [80] Dimock, D., et al., in Plasma Physics and Controlled Nuclear Fusion Research 1971 (Proc. 4th Int. Conf. Madison, 1971), Vol. 1, IAEA, Vienna (1971) 451.
- [81] Bol, K., et al., in Plasma Physics and Controlled Nuclear Fusion Research 1978 (Proc. 7th Int. Conf. Innsbruck, 1978), Vol. 1, IAEA, Vienna (1979) 11.
- [82] Meade, D., et al., in Plasma Physics and Controlled Nuclear Fusion Research 1980 (Proc. 8th Int. Conf. Brussels, 1980), Vol. 1, IAEA, Vienna (1981) 665.
- [83] DIVA Group, Nucl. Fusion **18** (1978) 1619.
- [84] Meservey, E.B., et al., Nucl. Fusion **16** (1976) 593.
- [85] Bardet, R., et al., Nucl. Fusion Suppl. **2** (1977) 259.
- [86] Stodiek, W., Grove, D.J., Kessler, J.O., in Plasma Physics and Controlled Nuclear Fusion Research 1965 (Proc. 2nd Int. Conf. Culham, 1965), Vol. 2, IAEA, Vienna (1965) 687.
- [87] Princeton Plasma Physics Laboratory, Annual Rep. MATT-Q-23 (1965) 73.
- [88] Nagami, M., et al., J. Nucl. Mater. **76–77** (1978) 521.
- [89] Bortnikov, A.V., et al., in Controlled Fusion and Plasma Phys. (Proc. 8th Eur. Conf. Prague, 1977), Vol. 1, EPS, Geneva (1977) 41.
- [90] Stott, P.E., et al., Nucl. Fusion **17** (1977) 481.
- [91] Mahdavi, A.M., et al., Phys. Rev. Lett. **22** (1981) 1602.
- [92] Keilhacker, M., et al., Phys. Scripta T **2/2** (1982) 443.
- [93] Kugel, H.W., Ulrickson, M., Nucl. Technol. Fusion **2** (1982) 712.
- [94] Bol, K., Okabayashi, M., Fonck, R., Nucl. Fusion **25** (1985) 1149.

- [95] Samm, U., TEXTOR-94 Team, Plasma Phys. Control. Fusion **41** (1999) B57.
- [96] Chappuis, Ph., TORE-SUPRA Team, J. Nucl. Mater. **241–243** (1997) 27.
- [97] Gunn, J.P., et al., Plasma Phys. Control. Fusion **41** (1999) B243.
- [98] Meservey, E.B., et al., J. Nucl. Mater. **93–94** (1980) 267.
- [99] Eubank, H., et al., in Plasma Physics and Controlled Nuclear Fusion Research 1978 (Proc. 7th Int. Conf. Innsbruck, 1978), Vol. 1, IAEA, Vienna (1971) 167.
- [100] Burchell, T.D., Carbon **34** (1996) 297.
- [101] Thomas, P.R., et al., J. Nucl. Mater. **176–177** (1990) 3.
- [102] Mioduszewski, P.K., Nucl. Fusion **26** (1986) 1171.
- [103] Hackmann, J., Uhlenbusch, J., J. Nucl. Mater. **128–129** (1984) 418.
- [104] Hutchinson, I.H., et al., Phys. Plasmas **1** (1994) 1511.
- [105] Apicella, M.L., Nucl. Fusion **37** (1997) 381.
- [106] Jackson, G.L., et al., J. Nucl. Mater. **220** (1995) 173.
- [107] McSmith, M.D., et al., Fusion Technol. **26** (1994) 498.
- [108] Ulrickson, M., JET Team, TFTR Team, J. Nucl. Mater. **176–177** (1990) 44.
- [109] Strachan, J.D., et al., J. Nucl. Mater. **196–198** (1992) 28.
- [110] Whyte, D.G., et al., J. Nucl. Mater. **241–243** (1997) 660.
- [111] Guo, H.Y., et al., J. Nucl. Mater. **241–243** (1997) 385.
- [112] Shimizu, K., Takizuka, T., Sakasai, A., J. Nucl. Mater. **241–243** (1997) 167.
- [113] Wampler, W.R., et al., J. Nucl. Mater. **266–269** (1999) 217.
- [114] Pappas, D., et al., J. Nucl. Mater. **266–269** (1999) 635.
- [115] Krieger, K., Maier, H., Neu, R., ASDEX Upgrade Team, J. Nucl. Mater. **266–269** (1999) 207.
- [116] Wada, M., et al., J. Nucl. Mater. **241–243** (1997) 799.
- [117] Neu, R., et al., J. Nucl. Mater. **290–293** (2001) 206.
- [118] Technical Basis for the ITER Final Design Report, Cost Review and Safety Analysis, (FDR) ITER EDA Documentation Series No. 16, IAEA, Vienna (1998).
- [119] Technical Basis for the ITER-FEAT Final Design Report, to be published by IAEA, Vienna (2001).
- [120] Wesson, J., Tokamaks, 2nd Ed., The Oxford Engineering Science Series, Oxford University Press, Oxford (1997).
- [121] Hawryluk, R.J., Phil. Trans. R. Soc. Lond. A **357** (1999) 443.
- [122] Keilhacker, M., et al., Nucl. Fusion **39** (1999) 209.
- [123] Jacquinot, J., et al., Nucl. Fusion **39** (1999) 235.
- [124] Keilhacker, M., Watkins, M.L., JET Team, J. Nucl. Mater. **266–269** (1999) 1.
- [125] Van Houtte, D., Equipe Tore Supra, Nucl. Fusion **33** (1993) 137.
- [126] Zushi, H., et al., Nucl. Fusion **40** (2000) 1183.
- [127] Levinton, F.M., Bell, R.E., Batha, S.H., Synakowski, E.J., Zarnstorff, M.C., Phys. Rev. Lett. **80** (1998) 4887.
- [128] Levinton, F.M., Batha, S.H., Synakowski, E.J., Zarnstorff, M.C., Rev. Sci. Instrum. **68** (1997) 926.
- [129] Bell, R.E., Rev. Sci. Instrum. **68** (1997) 1273.
- [130] Bell, R.E., Levinton, F.M., Batha, S.H., Zarnstorff, M.C., Phys. Rev. Lett. **81** (1998) 1429.
- [131] Engelmann, F., Nucl. Fusion **40** (2000) 1025.
- [132] Post, D.E., et al., in ITER EDA Physics, ITER Documentation Series No. 21, IAEA, Vienna (1991).
- [133] ITER EDA Agreement and Protocol 1, ITER EDA Documentation Series No. 1, IAEA, Vienna (1992).
- [134] Aymar, R., Fusion Eng. Des. **49&50** (2000) 13.
- [135] Shimomura, Y., et al., Nucl. Fusion **41** (2001) 309.
- [136] Zohm, H., Plasma Phys. Control. Fusion **38** (1996) 105.
- [137] Federici, G., et al., J. Nucl. Mater. **283–287** (2000) 110.
- [138] Guilhem, D., et al., J. Nucl. Mater. **241–243** (1997) 542.
- [139] Federici, G., Raffray, A.R., J. Nucl. Mater. **244** (1997) 101.
- [140] Janeschitz, G., et al., J. Nucl. Mater. **220–222** (1995) 73.
- [141] Kukushkin, A.S., et al., in Fusion Energy 1996 (Proc. 16th Int. Conf. Montreal, 1996), Vol. 2, IAEA, Vienna (1997) 987.
- [142] Mertens, V., et al., *ibid.*, Vol. 1, p. 413.
- [143] Loarte, A., et al., Nucl. Fusion **38** (1998) 331.
- [144] Kallenbach, A., et al., Nucl. Fusion **39** (1999) 901.
- [145] Mahdavi, M.A., et al., in Fusion Energy 1996 (Proc. 16th Int. Conf. Montreal, 1996), Vol. 1, IAEA, Vienna (1997) 397.
- [146] Milora, S.L., et al., Nucl. Fusion **35** (1998) 331.
- [147] Baylor, L.R., et al., J. Nucl. Mater. **266–269** (1999) 457.
- [148] Lang, P.T., Phys. Rev. Lett. **79** (1997) 1487.
- [149] Baylor, L.R., et al., Phys. Plasmas **7** (2000) 1878.
- [150] Hogan, J.T., Conference Report in Nucl. Fusion **39** (1999) 271.
- [151] Bosch, H-S., et al., Plasma Phys. Control. Fusion **41** (1999) A401.
- [152] Sakasai, A., et al., in Fusion Energy 1998 (Proc. 17th Int. Conf. Yokohama, 1998), IAEA, Vienna (2001) IAEA-CN-69. CD-ROM file EX6/5, and <http://www.iaea.org/programmes/ripc/physics/fec1998/html/node79.htm#12737>.

- [153] Kukushkin, A.S., et al., in *Controlled Fusion and Plasma Physics* (Proc. 26th Eur. Conf. Maas-tricht, 1999), EPS. CD-ROM, file P4.046, <http://epsppd.epfl.ch/Maas/web/sessions.htm#p406>.
- [154] Brooks, J.N., Alman, D., Federici, G., Ruzic, D.N., Whyte, D.G., J. Nucl. Mater. **266–269** (1999) 58.
- [155] Pacher, H.D., et al., J. Nucl. Mater. **241–243** (1997) 255.
- [156] Lipschultz, B., et al., J. Nucl. Mater. **290–293** (2001) 286.
- [157] Verbeek, H., Stober, J., Coster, D.P., Eckstein, W., Schneider, R., Nucl. Fusion **38** (1998) 1789.
- [158] Federici, G., et al., J. Nucl. Mater. **290–293** (2001) 260.
- [159] Oren, L., Taylor, R.J., Nucl. Fusion **17** (1977) 1143.
- [160] Esser, H.G., et al., J. Nucl. Mater. **266–269** (1999) 240.
- [161] Nachtrieb, R.T., et al., J. Nucl. Mater. **266–269** (1999) 896.
- [162] Saidoh, M., et al., Jpn. J. Appl. Phys. **32** (1993) 3276.
- [163] Yamage, M., et al., J. Nucl. Mater. **220–222** (1995) 743.
- [164] Mansfield, D., Observations Concerning the Injection of a Lithium Aerosol into the Edge of TFTR Discharges, Rep. PPPL-3526, Princeton Plasma Physics Laboratory, Princeton NJ.
- [165] Schueller, F.C., Plasma Phys. Control. Fusion **37** (1995) A135.
- [166] Wesley, J., Fujisawa, N., Ortolani, S., Putvinski, S., Rosenbluth, M.N., in *Fusion Energy 1996* (Proc. 16th Int. Conf. Montreal, 1996), Vol. 2, IAEA, Vienna (1997) 971.
- [167] Granetz, R.S., et al., Nucl. Fusion **36** (1996) 545.
- [168] Wesley, J., Fujisawa, N., Putvinski, S., Rosenbluth, M.N., in *Fusion Engineering* (Proc. 17th IEEE/NPSS Symp. (San Diego, 1997), IEEE, Piscataway New Jersey, IEEE 97CH36131, Vol. 1 (1998) 483.
- [169] Hassanein, A., Konkashbaev, I., in *Fusion Technology* (Proc. 19th Symp. Lisbon, 1998), Elsevier, Vol. 1 (1997) 379.
- [170] Martin, G., personal communication (1997).
- [171] Nygren, R.E., et al., J. Nucl. Mater. **241–243** (1997) 522.
- [172] Leonard, A.W., et al., J. Nucl. Mater. **266–269** (1999) 109.
- [173] Hill, D.N., J. Nucl. Mater. **241–243** (1997) 182.
- [174] Taylor, P.L., et al., Phys. Plasmas **6** (1999) 1872.
- [175] Yoshino, R., et al., Plasma Phys. Control. Fusion **39** (1997) 313.
- [176] Yoshino, R., et al., in *Plasma Physics and Controlled Nuclear Fusion Research 1994* (Proc. 15th Int. Conf. Seville, 1994), Vol. 1, IAEA, Vienna (1995) 685.
- [177] Yoshino, R., Tokuda, S., Kawano, Y., Nucl. Fusion **39** (1999) 151.
- [178] Pautasso, G., et al., Nucl. Fusion **36** (1996) 1291.
- [179] Pautasso, G., et al., J. Nucl. Mater. **290–293** (2001) 1045.
- [180] Kellman, A.G., et al., in *Fusion Energy 1996* (Proc. 16th Int. Conf. Montreal, 1996), Vol. 1, IAEA, Vienna (1997) 739.
- [181] Whyte, D.G., et al., in *Controlled Fusion and Plasma Physics* (Proc. 24th Eur. Conf. Berchtesgaden, Germany, 1997), Vol. 21A, part 3, EPS Geneva (1997) 1137.
- [182] Granetz, R.S., et al., in *Fusion Energy 1996* (Proc. 16th Int. Conf. Montreal, 1996), Vol. 1, IAEA, Vienna (1997) 757.
- [183] Schmidt, G.L., in *Controlled Fusion and Plasma Physics* (Proc. 22nd Eur. Conf. Bournemouth, 1995), Vol. 19C, part 4 (1995) 21.
- [184] Mueller, D., et al., Fusion Technol. **30** (1996) 251.
- [185] Schmidt, G.L., Frederickson, E., personal communication (1997).
- [186] Whyte, D.G., et al., Phys. Rev. Lett. **81** (1998) 4392.
- [187] Putvinski, S., et al., J. Nucl. Mater. **241–243** (1997) 316.
- [188] Jernigan, T.C., et al., Bull. Am. Phys. Soc. **43** (1998) 1890.
- [189] Rosenbluth, M., Putvinski, S.V., Parks, P.B., Nucl. Fusion **37** (1997) 955.
- [190] Parks, P.B., Rosenbluth, M.N., Putvinski, S.V., Evans, T.E., Fusion Technol. **35** (1998) 267.
- [191] Jardin, S.C., et al., Nucl. Fusion **40** (2000) 923.
- [192] Takase, Y., et al., Phys. Plasmas **4** (1997) 1647.
- [193] Suttrop, W., et al., Plasma Phys. Control. Fusion **42** (2000) A97.
- [194] Leonard, A.W., Osborne, T.H., Fenstermacher, M.E., Lasnier, C.J., Mahdavi, M.A., J. Nucl. Mater. **290–293** (2001) 1097.
- [195] La Marche, P.H., et al., Fusion Technol. **26** (1994) 427.
- [196] Saville, C., et al., Fusion Technol. **28** (1995) 1078.
- [197] Nagy, A., et al., in *Fusion Engineering* (Proc. 16th IEEE/NPSS Symp. Champaign, 1995), IEEE, Piscataway New Jersey, IEEE 95CH35852, Vol. 2 (1996) 573.
- [198] Bell, A.C., Wykes, M., Green, B.J., Fusion Eng. Des. **19** (1992) 169.
- [199] DeLooper, J., Fusion Technol. **26** (1994) 1051.
- [200] Proc. IEA Workshop on Tritium Experience in Large Tokamaks, Application to ITER, (Princeton, 1998), Conf. Rep. Nucl. Fusion **32** (1999) 271.
- [201] Skinner, C.H., et al., J. Nucl. Mater. **266–269** (1999) 940.
- [202] Mueller, D., et al., in *Fusion Engineering* (Proc. 17th IEEE/NPSS Symp. FSan Diego, 1997), IEEE, Piscataway New Jersey, IEEE 97CH36131,

- Vol. 1 (1998) 279.
- [203] Andrew, P.L., et al., *Fusion Eng. Des.* **47** (1999) 233.
  - [204] Andrew, P.L., et al., *J. Nucl. Mater.* **266–269** (1999) 153.
  - [205] Causey, R.A., Chrisman, W.L., Hsu, W.L., Anderl, R.A., Wishard, B., *J. Vac. Sci. Technol. A* **7** (1989) 1078.
  - [206] Causey, R.A., Wampler, W.R., Walsh, D., *J. Nucl. Mater.* **176–177** (1990) 987.
  - [207] Chiu, S., Haasz, A.A., *J. Vac. Sci. Technol. A* **9** (1991) 747.
  - [208] Haasz, A.A., Davis, J.W., *J. Nucl. Mater.* **256** (1998) 65.
  - [209] Davis, J.W., Haasz, A.A., *J. Nucl. Mater.* **266–269** (1999) 478.
  - [210] Haasz, A.A., Chiu, S., Pierre, J.E., Gudimenko, Y.I., *J. Vac. Sci. Technol. A* **14** (1996) 184.
  - [211] Federici, G., et al., *Fusion Eng. Des.* **39–40** (1998) 445.
  - [212] Counsell, G.F., Wu, C.H., *Phys. Scripta* **T91** (2001) 70.
  - [213] Wampler, W.R., et al., in *Fusion Engineering* (Proc. 18th IEEE/NPSS Symp. Albuquerque, 1999), IEEE, Piscataway New Jersey, IEEE 99CH3705 (1999) 267.
  - [214] Najmabadi, F., et al., *Fusion Eng. Des.* **38** (1997) 3.
  - [215] Gouge, M., et al., *Fusion Technol.* **28** (1995) 1644.
  - [216] Barabash, V., Federici, G., Roedig, M., Snead, L.L., Wu, C.H., *J. Nucl. Mater.* **283–287** (2000) 138.
  - [217] Ho, S.K., Abdou, M.A., *Fusion Eng. Des.* **31** (1996) 323.
  - [218] Cheng, E.T., et al., *Fusion Eng. Des.* **38** (1998) 219.
  - [219] Rutherford, P., personal communication (1998).
  - [220] El-Guebaly, L.A., ARIES Team, *Fusion Eng. Des.* **38** (1997) 139.
  - [221] Gruen, M., *The Chemistry of Fusion Technology*, Plenum Press, New York, London (1992).
  - [222] Federici, G., Wu, C.H., Raffray, A.R., Billone, M.C., *J. Nucl. Mater.* **187** (1992) 1.
  - [223] Raffray, A.R., Billone, M.C., Federici, G., Tanaka, S., *Fusion Eng. Des.* **28** (1995) 240.
  - [224] Akiyama, M., (Ed.), *Design Technology of Fusion Reactors*, World Scientific, Singapore (1991).
  - [225] Abdou, M.A., Vold, E.L., Gung, C.Y., Youssef, M.Z., Shin, K., *Fusion Technol.* **9** (1986) 250.
  - [226] Asaoka, Y., Okano, K., Yoshida, T., Tomabechi, K., *Fusion Technol.* **30** (1996) 853.
  - [227] Kuan, W., Abdou, M.A., *Fusion Technol.* **35** (1999) 309.
  - [228] Murdoch, D.K., Day, Ch., Gierszewski, P., Penzhorn, R.D., Wu, C.H., *Fusion Eng. Des.* **46** (1999) 255.
  - [229] Kessel, C. personal communication (1999).
  - [230] McCarthy, K.A., Petti, D.A., Carmack, W.J., Smolik, G.R., *Fusion Eng. Des.* **42** (1998) 45.
  - [231] McCarthy, K. A., Petti, D. *Fusion Technol.* **34** (1998) 390.
  - [232] Petti, D.A., et al., *J. Nucl. Mater.* **233–237** (1996) 37.
  - [233] Piet, S.J., Costley, A., Federici, G., Heckendorn, F., Little, R., in *Fusion Engineering* (Proc. 17th IEEE/NPSS Symp. San Diego, 1997), IEEE, Piscataway New Jersey, IEEE 97CH36131, Vol. 1 (1998) 167.
  - [234] Carmack, W.J., Smolik, G.R., Anderl, R.A., Pawelko, R.J., Hembree, P.B., *Fusion Technol.* **34** (1998) 604.
  - [235] Peacock, A.T., et al., *J. Nucl. Mater.* **266–269** (1999) 423.
  - [236] Anderl, R.A., Scaffidi-Argentina, F., Davydov, D., Pawelko, R.J., Smolik, G.R., *J. Nucl. Mater.* **283–287** (2000) 1463.
  - [237] Petti, D.A., Smolik, G.R., Anderl, R.A., *J. Nucl. Mater.* **283–287** (2000) 1390.
  - [238] Gaeta, M.J., *Tokamak Dust Explosion Hazard Examination and Oxidation Database Review for ITER*, ITER Rep. ITER/US/94/TE/SA-11 (1994).
  - [239] Piet, S.J., Federici, G., ITER White Paper on Integrated Picture of In-Vessel Tritium and Dust, ITER Rep. S 81 RI 13 96-06-28 W 1.4 (1996).
  - [240] Technical Basis for the ITER Interim Design Report, Cost Review and Safety Analysis, ITER EDA Documentation Series No. 7, IAEA, Vienna (1996).
  - [241] Winter, J., *Plasma Phys. Control. Fusion* **40** (1998) 1201.
  - [242] Winter, J., Gebauser, G., *J. Nucl. Mater.* **266–269** (1999) 228.
  - [243] Cheng, Y.S., et al., *Health Phys.* **76** (1999) 120.
  - [244] Campbell, D.J., JET Team, *J. Nucl. Mater.* **241–243** (1997) 379.
  - [245] Neu, R., et al., *J. Nucl. Mater.* **241–243** (1997) 678.
  - [246] Kurz, C., et al., *J. Nucl. Mater.* **220–222** (1995) 963.
  - [247] Lipschultz, B., et al., *J. Nucl. Mater.* **266–269** (1999) 635.
  - [248] Meade, D.M., et al. (Proc. 18th Int. Conf. Sorrento, 2000), IAEA, Vienna (2001) IAEA-CN-77. CD-ROM file FTP2/16, and <http://www.iaea.org/programmes/ripc/physics/fec2000/html/node345.htm#69868>.
  - [249] Raffray, A.R., et al., *Fusion Eng. Des.* **45** (1999) 377.
  - [250] Barabash, V., Kalinin, G., Matera, R., in *Fusion Technology* (Proc. 20th Symp. Marseille, 1998), Vol. 1 (1998) 215.

- [251] Schlosser, J., et al., *Fusion Eng. Des.* **39&40** (1998) 235.
- [252] Barabash, V., et al., *J. Nucl. Mater.* **283–287** (2000) 1248.
- [253] Vieider, G., et al., *Fusion Eng. Des.* **46** (1999) 221.
- [254] Merola, M., et al., *J. Nucl. Mater.* **283–287** (2000) 1068.
- [255] Nygren, R.E., Youchison, D.L., Watson, R.D., O'Dell, S., *Fusion Eng. Des.* **49&50** (2000) 303.
- [256] Opportunities in the Energy Science Program, prepared by the Fusion Energy Science Advisory Committee for the Office of Science of the US Department of Energy (June 1999).
- [257] Parker, R., *Nucl. Fusion* **40** (2000) 473.
- [258] Janeschitz, G., et al., *Fusion Eng. Des.* **49&50** (2000) 107.
- [259] Ioki, K., et al., *Fusion Eng. Des.* **49&50** (2000) 467.
- [260] Ioki, K., et al., *J. Nucl. Mater.* **283–287** (2000) 957.
- [261] Cardella, A., et al., *Fusion Eng. Des.* **43** (1998) 75.
- [262] Arkhipov, I., et al., *J. Nucl. Mater.* **290–293** (2001) 394.
- [263] Keudell, A. von, Schwarz-Selinger, T., Jacob, W., Stevens, A., *J. Nucl. Mater.* **290–293** (2001) 231.
- [264] Makhankov, A., et al., *Fusion Eng. Des.* **49–50** (2000) 275.
- [265] Ibbott, C., et al., Overview of the engineering design of ITER divertor, *Fus. Eng. Des.*, to appear.
- [266] Roth, J., Eckstein, W., Guseva, M., *Fusion Eng. Des.* **37** (1997) 465.
- [267] Eckstein, W., García-Rosales, C., Roth, J., Ottenberger, W., Sputtering Data, Rep. IPP 9/82, Max-Planck-Institut für Plasmaphysik (1993).
- [268] Eckstein, W., Computer Simulation of Ion-Solid Interaction, Springer Series in Material Science, Vol. 10, Springer, Berlin (1991).
- [269] Sigmund, P., *Phys. Rev.* **184** (1969) 383.
- [270] Eckstein, W., García-Rosales, C., Roth, J., László, J., *Nucl. Instrum. Methods B* **83** (1993) 95.
- [271] Roth, J., et al., *J. Nucl. Mater.* **176&177** (1990) 132.
- [272] Eckstein, W., Bohdansky, J., Roth, J., Physical sputtering, Atomic and Plasma–Material Interaction Data for Fusion, Vol. 1, Supplement to Nucl. Fusion, IAEA, Vienna, (1991) 51.
- [273] Yamamura, Y., Bohdansky, J., *Vacuum* **35** (1985) 561.
- [274] Küstner, M., Eckstein, W., Dose, V., Roth, J., *Nucl. Instrum. Methods B* **145** (1998) 320.
- [275] Küstner, M., Eckstein, W., Hecht, E., Roth, J., *J. Nucl. Mater.* **265** (1999) 22.
- [276] Bohdansky, J., Lindner, H., Martinelli, A.P., Roth, J., *Nucl. Instrum. Methods B* **18** (1987) 509.
- [277] Thomson, M.W., *Phil. Mag.* **18** (1968) 377.
- [278] Eckstein, W., Stephens, J.A., Clark, R.E.H., Davis, J.W., Haasz, A.A., Vietzke, E., Hirooka, Y., Particle Induced Erosion of Be, C and W in Fusion Plasmas. Part B: Physical Sputtering and Radiation Enhanced Sublimation, in Atomic and Plasma–Material Interaction Data for Fusion, Vol. 7B (IAEA, Vienna, 2001).
- [279] Matsunami, N., et al., Rep. IPPJ-AM-32, Univ. Nagoya, Inst. of Physics (1983).
- [280] Roth, J., Wampler, W.R., Jacob, W., *J. Nucl. Mater.* **250** (1997) 23.
- [281] Eckstein, W., (Max-Planck Institut für Plasma-physik), personal communication (1999).
- [282] Vietzke, E., Haasz, A.A., in Physical Processes of the Interaction of Fusion Plasmas with Solids, Section 4: Chemical erosion, Academic Press, San Diego (1996) 135.
- [283] Roth, J., Bohdansky, J., Ottenberger, W., *J. Nucl. Mater.* **165** (1989) 193.
- [284] Eckstein, W., Roth, J., Gauthier, E., László, J., *Fusion Technol.* **19** (1991) 2076.
- [285] Eckstein, W., Roth, J., *Nucl. Instrum. Methods B* **53** (1991) 279.
- [286] Davis, J.W., Haasz, A.A., *J. Nucl. Mater.* **241–243** (1997) 37.
- [287] Roth, J., *J. Nucl. Mater.* **266–269** (1999) 51.
- [288] Haasz, A.A., et al., Atomic and Plasma–Material Interaction Data for Fusion, Vol. 7A (IAEA, Vienna, 1998).
- [289] Horn, A., et al., *Chem. Phys. Lett.* **231** (1994) 193.
- [290] Vietzke, E., et al., *J. Nucl. Mater.* **145–147** (1987) 443.
- [291] Mech, B.V., Haasz, A.A., Davis, J.W., *J. Appl. Phys.* **84** (1998) 1655.
- [292] Balden, M., Roth, J., *J. Nucl. Mater.* **280** (2000) 39.
- [293] Mech, B.V., Haasz, A.A., Davis, J.W., *J. Nucl. Mater.* **255** (1998) 153.
- [294] Vietzke, E., Philipps, V., *Fusion Technol.* **15** (1989) 108.
- [295] Haasz, A.A., et al., *J. Nucl. Mater.* **145–147** (1987) 412.
- [296] Roth, J., García-Rosales, C., *Nucl. Fusion* **36** (1996) 1647; with Corrigendum, *Nucl. Fusion* **37** (1997) 897.
- [297] Vietzke, E., *J. Nucl. Mater.* **290–293** (2001) 158.
- [298] Grote, H., et al., *J. Nucl. Mater.* **266–269** (1999) 1059.
- [299] Whyte, D.G., Tynan, G., Doerner, R.P., Brooks, J.N., *Nucl. Fusion* **41** (2001) 47.
- [300] Philipps, V., et al., *Phys. Scripta T* **64** (1996) 71.
- [301] Kallenbach, A., et al., *Nucl. Fusion* **38** (1998) 1097.
- [302] Monk, R.D., et al., *Phys. Scripta T* **81** (1999) 54.
- [303] Naujoks, D., Coster, D., Kastelewicz, H., Schneider, R., *J. Nucl. Mater.* **266–269** (1999) 360.
- [304] Stamp, M., Erents, S.K., Fundamenski, W., Matthews, G.F., Monk, R.D., *J. Nucl. Mater.* **290–**

- 293** (2001) 321.
- [305] Roth, J., Bohdansky, J., Nucl. Instrum. Methods B **23** (1987) 549.
- [306] García-Rosales, C., Roth, J., J. Nucl. Mater. **196–198** (1992) 573.
- [307] Kornejew, P., Bohmeyer, W., Reiner, H.D., Wu, C.H., Phys. Scripta **T91** (2001) 29.
- [308] Goebel, D.M., et al., Nucl. Fusion **28** (1988) 1041.
- [309] Gielen, J.W.A.M., van de Sanden, M.C.M., Schramm, D.C., Appl. Phys. Lett. **69** (1996) 152.
- [310] Refke, A., Philipps, V., Vietzke, E., J. Nucl. Mater. **250** (1997) 13.
- [311] Chen, A.Y.K., Davis, J.W., Haasz, A.A., J. Nucl. Mater. **266–269** (1999) 399.
- [312] Haasz, A.A., Chen, A.Y.K., Davis, J.W., Vietzke, E., J. Nucl. Mater. **248** (1997) 19.
- [313] Roth, J., Bohdansky, J., Blewer, R.S., Ottenberger, W., Borders, J., J. Nucl. Mater. **85&86** (1979) 1077.
- [314] Roth, J., J. Nucl. Mater. **145–147** (1987) 87.
- [315] Hechtel, E., Eckstein, W., Roth, J., László, J., J. Nucl. Mater. **179–181** (1991) 290.
- [316] Roth, J., Bohdansky, J., Ottenberger, W., Data on Low Energy Light Ion Sputtering, Rep. IPP 9/26, Max-Planck-Institut für Plasmaphysik (1979).
- [317] Roth, J., Bohdansky, J., Wilson, K.L., J. Nucl. Mater. **111&112** (1982) 775.
- [318] Philipps, V., Flaskamp, K., Vietzke, E., J. Nucl. Mater. **111&112** (1982) 781.
- [319] Vietzke, E., Flaskamp, K., Hennes, M., Philipps, V., Nucl. Instrum. Methods B **2** (1984) 617.
- [320] Eckstein, W., Philipps, V., Physical sputtering and radiation-enhanced sublimation, Physical Processes of the Interaction of Fusion Plasma with Solids, Academic Press (1996) 93.
- [321] Philipps, V., Vietzke, E., Schorn, R.P., Trinkaus, H., J. Nucl. Mater. **155–157** (1988) 319.
- [322] Franzen, P., Davis, J.W., Haasz, A.A., J. Appl. Phys. **78** (1995) 817.
- [323] Franzen, P., Haasz, A.A., Davis, J.W., J. Nucl. Mater. **226** (1995) 15.
- [324] Gauthier, E., Eckstein, W., László, J., Roth, J., J. Nucl. Mater. **176&177** (1990) 438.
- [325] Begrambekov, L.B., et al., J. Nucl. Mater. **170** (1990) 101.
- [326] Roth, J., Möller, W., Nucl. Instrum. Methods B **7&8** (1985) 788.
- [327] Philipps, V., Vietzke, E., Trinkaus, H., J. Nucl. Mater. **179–181** (1991) 25.
- [328] Haasz, A.A., Davis, J.W., J. Nucl. Mater. **151** (1987) 77.
- [329] Haasz, A.A., Davis, J.W., J. Nucl. Mater. **224** (1995) 141.
- [330] Tobin, S.J., et al., Plasma Phys. Control. Fusion **38** (1996) 251.
- [331] Philipps, V., et al. J. Nucl. Mater. **196–198** (1992) 1106.
- [332] Ueda, Y., et al., J. Nucl. Mater. **227** (1996) 251.
- [333] Roth, J., “Chemical sputtering and radiation enhanced sublimation of carbon”, Physics of Plasma–Wall Interactions in Controlled Fusion, NATO ASI Series B: Physics, Plenum Press, New York (1986) 389.
- [334] Roth, J., “Physical sputtering of solids at ion bombardment”, *ibid.*, p. 351.
- [335] Behrisch, R., Roth, J., Staudenmaier, G., Verbeek, H., Nucl. Instrum. Methods B **18** (1987) 629.
- [336] García-Rosales, C., Roth, J., Behrisch, R., J. Nucl. Mater. **212–215** (1994) 1211.
- [337] Kallenbach, A., et al., Nucl. Fusion **34** (1994) 1557.
- [338] Naujoks, D., Eckstein, W., J. Nucl. Mater. **230** (1996) 93.
- [339] Thoma, A., et al., Plasma Phys. Control. Fusion **39** (1997) 1487.
- [340] Hirooka, Y., Phys. Scripta T **64** (1996) 84.
- [341] Goldstraß, P., Eckstein, W., Linsmeier, Ch., J. Nucl. Mater. **266–269** (1999) 581.
- [342] Eckstein, W., Krieger, K., Roth, J., J. Nucl. Mater. **258–263** (1998) 912.
- [343] Doerner, R.P., et al., J. Nucl. Mater. **266–269** (1999) 392.
- [344] Krieger, K., Roth, J., J. Nucl. Mater. **290–293** (2001) 107.
- [345] Sze, F.C., et al., J. Nucl. Mater. **246** (1997) 165.
- [346] Bach, F.P., diploma thesis (Univ. Bayreuth 1996, in German); F.P. Bach, Jacob, W., unpublished results.
- [347] Maruyama, K., Jacob, W., Roth, J., J. Nucl. Mater. **264** (1999) 56.
- [348] Doerner, R.P., et al., Phys. Scripta T **81** (1999) 35.
- [349] Chen, A.Y.K., Haasz, A.A., Davis, J.W., J. Nucl. Mater. **227** (1995) 66.
- [350] Balden, M., et al., J. Nucl. Mater. **290–293** (2001) 52.
- [351] Simonov, V.A., Shvilkin, B.N., Katukov, G.P., Nucl. Fusion Supplement AEC-No. 5589 (1962) 325.
- [352] McCracken, G.M., J. Nucl. Mater. **93&94** (1980) 3.
- [353] Mioduszewski, P., Comments Plasma Phys. Control. Fusion **6** (1980) 7.
- [354] Wolff, H., Arcing in magnetic fusion devices, Atomic and Plasma–Material Interaction Data for Fusion, Vol. 1, Supplement to Nucl. Fusion, IAEA, Vienna (1991) 93.
- [355] Schwirzke, F., Taylor, R.J., J. Nucl. Mater. **93&94** (1980) 780.
- [356] Sethuraman, S.K., Barrault, M.R., J. Nucl. Mater. **93&94** (1980) 791.
- [357] Drouet, M.G., Jap. J. Appl. Phys. **20** (1981) 1027.
- [358] García-Rosales, C., et al., in Controlled Fusion



- and Plasma Physics (Proc. 21st Conf. Montpellier, 1994), Vol. 18B, part 2, EPS, Geneva (1994) 718.
- [359] Hassanein, A., *J. Nucl. Mater.* **122&123** (1984) 1453.
- [360] Hassanein, A., Konkashbaev, I., *J. Nucl. Mater.* **233–237** (1996) 713.
- [361] Hassanein, A., *Fusion Technol.* **15** (1989) 513.
- [362] Hassanein, A., Konkashbaev, I., *Fusion Eng. Des.* **28** (1995) 27.
- [363] Hassanein, A., Response of Materials to High Heat Fluxes During Operation in Fusion Reactors, Rep. ASME, 88-WA/NE-2 (1988).
- [364] Hassanein, A., Federici, G., Konkashbaev, I., Zhitlukhin, A., Litunovsky, V., *Fusion Eng. Des.* **39&40** (1998) 201.
- [365] Hassanein, A., Konkashbaev, I., *Plasma Dev. Oper.* **5** (1998) 297.
- [366] Hassanein, A., Konkashbaev, I., *J. Nucl. Mater.* **273** (1999) 326.
- [367] Lengyel, L.L., et al., *Nucl. Fusion* **36** (1996) 1679.
- [368] Lengyel, L.L., Rozhansky, V.A., Veselova, J.Yu., in *Controlled Fusion and Plasma Physics* (Proc. 24th Conf. Berchtesgaden, 1997), Vol. 21A, part 4 (1997) 1549.
- [369] Landman, I.S., Wuerz, H., *ibid.*, p. 1821.
- [370] Wuerz, H., Pestchanyi, S., Bazylev, B., Kappler, F., in *Fusion Technology* (Proc. 20th Symp. Marseille, 1998), Vol. 1 (1998) 271.
- [371] Hassanein, A., et al., *J. Nucl. Mater.* **241–243** (1997) 288.
- [372] Hassanein, A., *Fusion Technol.* **30** (1996) 713.
- [373] Wuerz, H., et al., *J. Nucl. Mater.* **233–237** (1996) 798.
- [374] Hassanein, A., Konkashbaev, I., *J. Nucl. Mater.* **258–263** (1998) 645.
- [375] Vassen, R., Kaiser, A., Stover, D., *J. Nucl. Mater.* **233–237** (1996) 713.
- [376] Guseva, M., et al., *J. Tech. Phys.* **66** (1966) 106.
- [377] Pestchanyi, S.E., Usov, N.A., Wuerz, H., in *Fusion Technology* (Proc. 20th Symp. Marseille, 1998), Vol. 1 (1998) 275.
- [378] Moeller, W., Roth, J., “Implantation, retention and release of hydrogen isotopes in solids”, *Physics of Plasma–Wall Interactions in Controlled Fusion*, NATO ASI Series B: Physics, Plenum Press, New York (1986) 439.
- [379] Wilson, K.L., et al., “Trapping, de-trapping and release of implanted hydrogen isotopes”, *Atomic and Plasma–Material Interaction Data for Fusion*, Vol. 1, Nucl. Fusion Supplement, IAEA, Vienna (1991) 31.
- [380] Myers, S.M., Richards, P.M., Wampler, W.R., Besenbacher, F., *J. Nucl. Mater.* **165** (1989) 9.
- [381] Andrew, P.L., Haasz, A.A., *J. Appl. Phys.* **72** (1992) 2749.
- [382] *Handbook of Ion Implantation Technology*, North Holland, Amsterdam (1992).
- [383] Eckstein, W., “Reflection”, *Atomic and Plasma–Material Interaction Data for Fusion*, Vol. 1, Nucl. Fusion Supplement, IAEA, Vienna (1991) 17.
- [384] Birtcher, R.C., Averback, R.S., Blewitt, T.H., *J. Nucl. Mater.* **75** (1978) 167.
- [385] Ziegler, J.F., Biersack, J.P., Littmark, U., *The Stopping and Range of Ions in Solids*, Pergamon Press, New York, (1985).
- [386] LeBlanc, L., Ross, G.G., *Nucl. Instrum. Methods B* **83** (1993) 15.
- [387] Wipf, H., “Diffusion of hydrogen in metals”, *Hydrogen in Metals III*, Springer Topics in Applied Physics, Vol. 73, Springer, Berlin (1997) 51.
- [388] Kidson, G.V., “The diffusion of H, D and T in solid metals”, *Landolt–Börnstein Numerical Data and Functional Relationships in Science and Technology, Group III: Crystal and Solid-State Physics*, Vol. 26, Diffusion in Solid Metals and Alloys, Springer, Berlin (1990) 504.
- [389] Wampler, W.R., *J. Appl. Phys.* **69** (1991) 3063.
- [390] Pick, M.A., Sonnenberg, K., *J. Nucl. Mater.* **131** (1985) 208.
- [391] Baskes, M.I., *J. Nucl. Mater.* **92** (1980) 318.
- [392] Wampler, W.R., *J. Appl. Phys.* **65** (1989) 4040.
- [393] Antoniazzi, A.B., Haasz, A.A., Stangeby, P.C., *J. Vac. Sci. Technol.* **5** (1987) 2325.
- [394] Antoniazzi, A.B., Haasz, A.A., Stangeby, P.C., *J. Nucl. Mater.* **162–164** (1989) 1065.
- [395] Andrew, P.L., Haasz, A.A., *J. Vac. Sci. Technol. A* **8** (1990) 1807.
- [396] Haasz, A.A., Andrew, P.L., Antoniazzi, A.B., *J. Vac. Sci. Technol.* **A7** (1989) 1042.
- [397] Andrew, P.L., Haasz, A.A., *J. Less Common Metals* **172–174** (1991) 732.
- [398] Andrew, P.L., Haasz, A.A., *J. Appl. Phys.* **70** (1991) 3600.
- [399] Doyle, B.L., Brice, D.K., *Radiat. Eff.* **89** (1985) 21.
- [400] Doyle, B.L., *J. Nucl. Mater.* **111&112** (1982) 628.
- [401] Ham, F.S., *J. Phys. Chem. Solids* **6** (1958) 335.
- [402] Myers, S.M., Nordlander, P., Besenbacher, F., Nørskov, J.K., *Phys. Rev. B* **33** (1986) 854.
- [403] Nordlander, P., Nørskov, J.K., Besenbacher, F., *J. Phys. F: Met. Phys.* **16** (1986) 1161.
- [404] Eleveld, H., van Veen, A., *J. Nucl. Mater.* **191–194** (1992) 433.
- [405] Fransens, J.R., Abd El Keriem, M.S., Pleiter, F., *J. Phys. Condensed Matter* **3** (1991) 9871.
- [406] Krimmel, H., Fahnle M., *J. Nucl. Mater.* **255** (1998) 72.
- [407] Frauenfelder, R., *J. Vac. Sci. Technol.* **6** (1969) 388.
- [408] Tamm, P.W., Schmidt, L.D., *J. Chem. Phys.* **54** (1971) 4775.
- [409] Nahm, T.U., Gomer, R., *Surface Sci.* **375** (1997) 281.
- [410] Nørskov, J.K., *Phys. Rev. B* **26** (1982) 2875.

- [411] Nørskov, J.K., Besenbacher, F., J. Less Common Metals **130** (1987) 475.
- [412] Myers, S.M., et al., Rev. Mod. Phys. **64** (1992) 559.
- [413] Katsuta, H., McLellan, R.B., Furukawa, K., J. Phys. Chem. Solids **43** (1982) 533.
- [414] Myers, S.M., Besenbacher, F., J. Appl. Phys. **60** (1986) 3499.
- [415] Chou, M.Y., Lam, P.K., Cohen, M.L., Phys. Rev. B **28** (1983) 4179.
- [416] Krimmel, H., Fähnle M., J. Nucl. Mater. **213** (1996) 159.
- [417] Shapovalov, V.I., Dukel'ski, Yu.M., Russ. Metall. **5** (1988) 210.
- [418] Myers, S.M., Follstaedt, D.M., J. Nucl. Mater. **145–147** (1987) 322.
- [419] Hemmes, H., Driessen, A., Griessen, R., J. Phys. C: Solid State Phys. **19** (1986) 3571.
- [420] Greenwood, G.W., Foreman, A.J.E., Rimmer, D.E., J. Nucl. Mater. **4** (1959) 305.
- [421] Chernikov, V.N., Alimov, K.Kh., Markin A.V., Zakharov, A.P., J. Nucl. Mater. **228** (1996) 47.
- [422] Altstetter, C.J., Behrisch, R., Scherzer, B.M.U., J. Vac. Sci. Technol. **15** (1978) 706.
- [423] Blewer, R.S., Behrisch, R., Scherzer, B.M.U., Schultz, R., J. Nucl. Mater. **76&77** (1978) 305.
- [424] Hindmarsh, A.C., in Scient. Comp., North Holland, Amsterdam (1983) 55.
- [425] Wienhold, P., Profant, M., Waelbroeck, F., Winter, J., J. Nucl. Mater. **93&94** (1980) 866.
- [426] Baskes, M.I., DIFFUSE-83, Rep. SAND83-8231, Sandia National Laboratories (1983).
- [427] Moeller, W., PIDAT - A Computer Program for Implant Diffusion and Trapping, Rep. IPP-9/44, Max-Planck-Institut für Plasmaphysik, Garching (1983).
- [428] Holland, D.F., Merrill, B.J., Engineering Problems of Fusion Research (Proc. 9th Symp. Chicago, 1981), IEEE, New York (1981) 1209.
- [429] Scaffidi-Argentina, F., Dalle Donne, M., Ronchi, C., Ferrero, C., Fusion Technol. **32** (1997) 179.
- [430] Zakharov, A.P., et al., J. Nucl. Mater. **241–243** (1997) 52.
- [431] Anderl, R.A., et al., J. Nucl. Mater. **273** (1999) 1.
- [432] Causey, R.A., Venhaus, T.J., "The use of tungsten in fusion reactors: a review of the hydrogen retention and migration properties", papers presented at Conference on Hydrogen Isotopes in Solids, Stockholm, Sweden, May 2000.
- [433] Serra, E., Benanati, G., Ogorodnikova, O.V., J. Nucl. Mater. **255** (1998) 105.
- [434] Jones, P.M.S., Gibson, R., J. Nucl. Mater. **21** (1967) 353.
- [435] Swansiger, W.A., J. Vac. Sci. Technol. A **4** (1988) 1216.
- [436] Abramov, E., Riehm, M.P., Thompson, D.A., J. Nucl. Mater. **175** (1990) 90.
- [437] Tazhibaeva, I.L., et al., in Fusion Technology (Proc. 18th Symp. Karlsruhe, 1994), Vol. 1, Elsevier, Amsterdam (1994) 427.
- [438] Haasz, A.A., Davis, J.W., J. Nucl. Mater. **241–243** (1997) 1076.
- [439] Wampler, W.R., J. Nucl. Mater. **122&123** (1984) 1598.
- [440] Moeller, W., Scherzer, B.M.U., Bohdansky, J., Retention and Release of Deuterium Implanted into Beryllium, Final Report, Rep. IPP-JET-26, Max-Planck-Institut für Plasmaphysik, Garching (1985).
- [441] Haasz, A.A., Davis, J.W., Poon, M., Macaulay-Newcombe, R.G., J. Nucl. Mater. **258–263** (1998) 889.
- [442] Alimov, V.K., Scherzer, B.M.U., J. Nucl. Mater. **240** (1996) 75.
- [443] Eleveld, H., van Veen, A., J. Nucl. Mater. **212–215** (1994) 1421.
- [444] National Neutron Cross Section Center, Brookhaven National Laboratory, Neutron Cross Sections, (3rd Ed.), Vol. 2, BNL 325.
- [445] Seagrave, J.D., Cranberg, L., Simmons, J.E., Phys. Rev. **119** (1960) 1981.
- [446] Doyle, B.L., Wampler, W.R., Brice, D.K., J. Nucl. Mater. **103&104** (1981) 513.
- [447] Davis, J.W., Haasz, A.A., Walsh, D.S., J. Nucl. Mater. **176&177** (1990) 992.
- [448] Chiu, S., Haasz, A.A., J. Nucl. Mater. **196–198** (1992) 972.
- [449] Wampler, W.R., Brice, D.K., Magee, C.W., J. Nucl. Mater. **102** (1981) 304.
- [450] Staudenmaier, G., et al., J. Nucl. Mater. **84** (1979) 149.
- [451] Haasz, A.A., Davis, J.W., J. Nucl. Mater. **232** (1996) 219.
- [452] Doyle, B.L., Wampler, W.R., Brice, D.K., Picraux, S.T., J. Nucl. Mater. **93&94** (1980) 551.
- [453] Causey, R.A., J. Nucl. Mater. **162–164** (1989) 151.
- [454] Chernikov, V.N., Wampler, W.R., Zakharov, A.P., Gorodetsky, A.E., J. Nucl. Mater. **264** (1999) 180.
- [455] Haasz, A.A., Davis, J.W., J. Nucl. Mater. **209** (1994) 155.
- [456] Haasz, A.A., Franzen, P., Davis, J.W., Chiu, S., Pitcher, C.S., J. Appl. Phys. **77** (1995) 66.
- [457] Emmoth, B., Nucl. Fusion **30** (1990) 1140.
- [458] Kushita, K.N., Youle, I., Haasz, A.A., Sawicki, J.A., J. Nucl. Mater. **179–181** (1991) 235.
- [459] Penzhorn, R.D., et al., J. Nucl. Mater. **288** (2001) 170.
- [460] Wampler, W.R., Doyle, B.L., Causey, R.A., Wilson, K.L., J. Nucl. Mater. **176&177** (1990) 983.
- [461] Chernikov, V.N., et al., J. Nucl. Mater. **217** (1994)

- 250.
- [462] Chernikov, V.N., et al., J. Nucl. Mater. **220–222** (1995) 921.
- [463] Kanashenko, S.L., J. Nucl. Mater. **233–237** (1996) 1207.
- [464] Moeller, W., J. Nucl. Mater. **162–164** (1989) 138.
- [465] Sawicki, J.A., Roth, J., Howe, L.M., J. Nucl. Mater. **162–164** (1989) 1019.
- [466] Pospieszczyk, A., et al., J. Nucl. Mater. **266–269** (1999) 138.
- [467] Jacob, W., Thin Solid Films **326** (1998) 1.
- [468] Wampler, W.R., Magee, C.W., J. Nucl. Mater. **103&104** (1981) 509.
- [469] Moeller, W., Borgesen, P., Scherzer, B.M.U., Nucl. Instrum. Methods B **19/20** (1987) 826.
- [470] Roth, J., et al., J. Nucl. Mater. **93&94** (1980) 601.
- [471] Wampler, W.R., Myers, S.M., J. Nucl. Mater. **111&112** (1982) 616.
- [472] Wampler, W.R., Doyle, B.L., J. Nucl. Mater. **162–164** (1989) 1025.
- [473] Langley, R.A., J. Nucl. Mater. **162–164** (1989) 1030.
- [474] Brice, D.K., Nucl. Instrum. Methods B **44** (1990) 302.
- [475] Wang, W., Jacob, W., Roth, J., J. Nucl. Mater. **245** (1997) 66.
- [476] Causey, R.A., Walsh, D.S., J. Nucl. Mater. **254** (1998) 84.
- [477] Mayer, M., J. Nucl. Mater. **240** (1997) 164.
- [478] Stott, P.E., Gorini G., Sindoni, E., Diagnostics for Experimental Thermonuclear Fusion Reactors, Plenum Press New York 1996.
- [479] High Temperature Plasma Diagnostics (Proc. 12th Top. Conf. 1998), published as Rev. Sci. Instr. **70** (1999) 255.
- [480] Samm, U., Trans. Fusion Technol. **33** (2T) (1998) 338.
- [481] Counsell, G.F., et al., J. Nucl. Mater. **290–293** (2001) 255.
- [482] Behringer, K., Summers, H.P., Denne, B., Forrest, M., Stamp, M., Plasma Phys. Control. Fusion **31** (1989) 2059.
- [483] Cohen, S.A., J. Nucl. Mater. **63** (1976) 65.
- [484] Kallenbach, A., et al., J. Nucl. Mater. **266–269** (1999) 343.
- [485] Doerner, R.P., et al., J. Nucl. Mater. **290–293** (2001) 166.
- [486] Isler, R.C., Nucl. Fusion **24** (1984) 1599.
- [487] Philipps, V., Vietzke, E., Erdweg, M., J. Nucl. Mater. **162–164** (1989) 550.
- [488] Hillis, D.L., et al., Conference Report in Nucl. Fusion **39** (1999) 271.
- [489] Verbeek, H., et al., Nucl. Fusion **39** (1999) 95.
- [490] Wampler, W.R., et al., J. Vac. Sci. Technol A **7** (1989) 1083.
- [491] Bastasz, R., et al., J. Nucl. Mater. **176&177** (1990) 1038.
- [492] LaBombard, B., et al., J. Nucl. Mater. **241–243** (1997) 149.
- [493] Walsh, D.S., Doyle, B.L., Jackson, G.L., J. Vac. Sci. Technol. A **10** (4) (1992) 1174.
- [494] Coad, J.P., Rubel, M., Wu, C.H., J. Nucl. Mater. **241–243** (1997) 408.
- [495] Wampler, W.R., et al., J. Vac. Sci. Technol. A **6** (3) (1988) 2111.
- [496] Rubel, M., von Seggern, J., Karduck, P., Philipps, V., Vevecka-Priftaj, A., J. Nucl. Mater. **266–269** (1999) 1185.
- [497] Naujoks, D., Behrisch, R., Philipps, V., Schweer, B., Plasma Phys. Control. Fusion **36** (1994) 2021.
- [498] Hancock, C.J., et al., Fusion Technology (Proc. 15th Symp. Utrecht, 1988), Vol. 1, Elsevier, Amsterdam (1989) 309.
- [499] Wong, C.P.C., et al., J. Nucl. Mater. **196–198** (1992) 871.
- [500] Krieger, K., et al., J. Nucl. Mater. **241–243** (1997) 684.
- [501] Wampler, W.R., et al., J. Nucl. Mater. **233–237** (1996) 791.
- [502] Matthews, G.F., et al., J. Nucl. Mater. **290–293** (2001) 668.
- [503] Behringer, K., J. Nucl. Mater. **176&177** (1990) 606.
- [504] Liu-Hinz, C., Terreault, B., Martin, F., J. Nucl. Mater. **220–222** (1995) 1126.
- [505] Poschenrieder, W., Venus, G., ASDEX Team, J. Nucl. Mater. **111&112** (1982) 29.
- [506] Mertens, P., Silz, M., J. Nucl. Mater. **241–243** (1997) 842.
- [507] Kondo, K., et al., J. Nucl. Mater. **145–147** (1987) 501.
- [508] Goehlich, A., Roewekamp, M., Dobeles, H.F., J. Nucl. Mater. **176&177** (1990) 1055.
- [509] Lebedev, S.V., Moshkalev, S.A., Razdobarin, G.T., Semenov, V.V., Shakhovets, K.G., Nucl. Fusion **25** (1985) 931.
- [510] Herrmann, A., et al., Plasma Phys. Control. Fusion **37** (1995) 17.
- [511] Hill, D.N., Ellis, R., Ferguson, W., Perkins, D.E., Rev. Sci. Instrum. **59** (1988) 1878.
- [512] Kobayashi, T., et al., J. Nucl. Mater. **121** (1984) 17.
- [513] Owens, D.K., et al., J. Nucl. Mater. **93&94** (1980) 213.
- [514] Duan, W., Chen, J., Yang, S., J. Nucl. Mater. **111&112** (1982) 502.
- [515] Juettner, B., Buchl, K., Weinlich, M., Contrib. Plasma Phys. **34** (1994) 472.
- [516] Goodall, D.H.J., J. Nucl. Mater. **93&94** (1980) 154.
- [517] Juettner, B., et al., Nucl. Fusion **20** (1980) 497.
- [518] Hillis, D.L., et al., Phys. Plasmas **6** (1999) 1985.

- [519] Keudell, A. von, et al., Nucl. Fusion **39** (1999) 1451.
- [520] Naujoks, D., Behrisch, R., J. Nucl. Mater. **220–222** (1995) 227.
- [521] Coad, J.P., et al., J. Nucl. Mater. **200** (1993) 360.
- [522] Jones, R., Wykes, C., Holographic and Speckle Interferometry, University Press, Cambridge (1989).
- [523] Koch, A.W., Ruprecht, M., Wilhelm, R., Laser Speckle Techniques for in situ Monitoring of Erosion and Re-deposition at Inner Walls in Large Experimental Fusion Devices, Rep. IPP 4/271, Max-Planck-Institut für Plasmaphysik, Garching (1995).
- [524] Azzam, R.M.A., Bashara, N.M., Ellipsometry and Polarized Light, North-Holland, Amsterdam (1989).
- [525] Bastasz, R., Hirooka, Y., Khandagle, M., J. Nucl. Mater. **220–222** (1995) 352.
- [526] Wienhold, P., Waelbroeck, F., Bergsaker, H., Winter, J., Esser, H.G., J. Nucl. Mater. **162–164** (1989) 369.
- [527] Wienhold, P., Weschenfelder, F., Winter, J., J. Nucl. Mater. **220–222** (1995) 452.
- [528] Weschenfelder, F., et al., Plasma Phys. Control. Fusion **38** (7) (1996) 1043.
- [529] Bourgoin, D., Ross, G.G., Savoie, S., Drolet, Y., Haddad, E., J. Nucl. Mater. **241–243** (1997) 765.
- [530] Rohde, V., Maier, H., Krieger, K., Neu, R., Perchermaier, J., J. Nucl. Mater. **290–293** (2001) 317.
- [531] Manos, D.M., Bennett, T., Herzer, M., Schwarzmann, J., J. Nucl. Mater. **196–198** (1992) 933.
- [532] Franzen, P., et al., Nucl. Fusion **37** (1997) 1375.
- [533] Guo, H.Y., Terreault, B., Rev. Sci. Instr. **64** (1993) 700.
- [534] Summers, D., et al., J. Nucl. Mater. **290–293** (2001) 496.
- [535] Skinner, C.H., et al., J. Vac. Sci. Technol. A **14** (6) (1996) 3267.
- [536] Kumar, A., Kugel, H.W., Ascione, G., in Fusion Engineering (Proc. 17th IEEE/NPSS Symp. San Diego, 1997), IEEE, Piscataway New Jersey, IEEE 97CH36131, Vol. 2 (1998) 845.
- [537] Whyte, D.G., et al., J. Nucl. Mater. **266–269** (1999) 67.
- [538] Menon, M.M., et al., in Fusion Engineering (Proc. 18th IEEE/NPSS Symp. Albuquerque, 1999), IEEE, Piscataway New Jersey, IEEE 99CH3705 (1999) 261.
- [539] Razdobarin, G.T., Detecting dust on plasma-facing components in a next step tokamak using a laser-induced breakdown spectroscopy technique, Fusion Science and Technol., to appear.
- [540] Reichle, R., et al., J. Nucl. Mater. **290–293** (2001) 701.
- [541] Roth, J., et al., J. Nucl. Mater. **220–222** (1995) 231.
- [542] Naujoks, D., Roth, J., Krieger, K., Lieder, G., Laux, M., J. Nucl. Mater. **210** (1994) 43.
- [543] Bastasz, R., et al., J. Nucl. Mater. **220–222** (1995) 310.
- [544] Lingertat, J., et al., J. Nucl. Mater. **241–243** (1997) 402.
- [545] Kubo, H., et al., J. Nucl. Mater. **196–198** (1992) 71.
- [546] Higashijima, S., et al., J. Nucl. Mater. **241–243** (1997) 574.
- [547] Pitcher, C.S., et al., Nucl. Fusion **26** (1986) 1641.
- [548] Klepper, C., et al., in Controlled Fusion and Plasma Physics (Proc. 20th Eur. Conf. Lisbon, 1993), Vol. 17C, part 2, EPS, Geneva (1994) 59.
- [549] Ruggieri, R., Gauthier, E., Hogan, J., Layet, J.M., Loarer, T., J. Nucl. Mater. **266–269** (1999) 660.
- [550] Higashijima, S., personal communication.
- [551] Kubo, H., personal communication.
- [552] Ehrhardt, A.B., Langer, W.D., Collisional Processes of Hydrocarbon in Hydrogen Plasmas, Rep. PPPL-2477, Princeton Plasma Physics Laboratory (1987).
- [553] Kato, S., et al., J. Nucl. Mater. **266–269** (1999) 406.
- [554] Guo, H. Y., et al., in Controlled Fusion and Plasma Physics (Proc. 22nd Eur. Phys. Soc. Conf. Bournemouth, 1995), Vol. 19C, part 2, EPS, Geneva (1995) 313.
- [555] Wienhold, P., et al., Nucl. Instrum. Methods B **94** (1994) 503.
- [556] Brooks, J.N., Whyte, D.G., Nucl. Fusion **39** (1999) 525.
- [557] Mech, B.V., Haasz, A.A., Davis, J.W., J. Nucl. Mater. **241–243** (1997) 1147.
- [558] Masaki, K., et al., in Fusion Technology (Proc. 20th Symp. Marseille, 1998), Vol. 1 (1998) 67.
- [559] Maier, H., et al., in Controlled Fusion and Plasma Physics (Proc. 26th Eur. Conf. Maastricht, 1999), EPS. CD-ROM, file P4.037 <http://epsppd.epfl.ch/Maas/web/sessions.htm#p4037>.
- [560] Brooks, J.N., Causey, R., Federici, G., Ruzic, D.N., J. Nucl. Mater. **241–243** (1997) 294.
- [561] Keudell, A. von, Jacob, W., J. Appl. Phys. **79** (1996) 1092.
- [562] Nakano, T., Toyoda, H., Sugai, H., Jap. J. Appl. Phys. **30** (1992) 2908.
- [563] Motlagh, S., Moore, J., J. Chem. Phys. **109** (1998) 432.
- [564] Tabasso, A., Maier, H., Krieger, K., Roth, J., ASDEX-Upgrade Team, Nucl. Fusion **40** (2000) 1441.
- [565] LaBombard, B., et al., Nucl. Fusion **40** (2000) 2041.

- [566] Coad, J.P., et al., in *Controlled Fusion and Plasma Physics* (Proc. 14th Eur. Conf. Madrid, 1987), Vol. 11D, part 2, EPS, Geneva (1987) 744.
- [567] McCracken, G.M., et al., *J. Nucl. Mater.* **162–164** (1989) 356.
- [568] Behrisch, R., et al., *J. Nucl. Mater.* **162–164** (1989) 598.
- [569] Hsu, W. L., Mills, B.E., Ehrhardt, A.B., Sun, Y.C., *J. Vac. Sci. Technol. A* **7** (3) (1989) 1065.
- [570] Walsh, D.S., Knox, J.M., Doyle, B.L., *Nucl. Instrum. Methods B* **45** (1990) 62.
- [571] Hua, T.Q., Brooks, J.N., *J. Nucl. Mater.* **196–198** (1992) 514. Note corrected units for Figs 5 and 7 are 100 Å/s (T.Q. Hua, personal communication).
- [572] Gentile, C., Parker, J.J., Zweben, S.J., In situ imaging and quantification of surface tritium contamination via coherent fiber bundle, T2001 Int. Conf. on Tritium Science and Technol., November 11–16, 2001, Tsukuba, Japan, to appear in *Fusion Science and Technol.*
- [573] Skinner, C.H., Gentile, C.A., Young, K.M., in *Fusion Engineering* (Proc. 18th IEEE/NPSS Symp. Albuquerque, 1999), IEEE, Piscataway New Jersey, IEEE 99CH3705 (1999) 89.
- [574] Skinner, C.H., et al., *J. Nucl. Mater.* **290–293** (2001) 486.
- [575] Philipps, V., et al., *J. Nucl. Mater.* **258–263** (1998) 858.
- [576] Philipps, V., et al., *Nucl. Fusion* **34** (1994) 1417.
- [577] Staudenmaier, G., Wampler, W.R., *J. Nucl. Mater.* **145–147** (1987) 569.
- [578] Wampler, W.R., Cohen, S.A., *Nucl. Fusion* **25** (1985) 771.
- [579] Wampler, W.R., *J. Vac. Sci. Technol. A* **3** (1985) 1067.
- [580] Voss, D.E., Cohen, S.A., *J. Nucl. Mater.* **93–94** (1980) 405.
- [581] Ruzic, D.N., et al., *J. Nucl. Mater.* **145–147** (1987) 527.
- [582] Verbeek, H., and the ASDEX Team, *J. Nucl. Mater.* **145–147** (1987) 523.
- [583] Verbeek, H., Schiavi, A., The Low Energy Neutral Particle Analyser (LENA) at W7-AS, Rep. IPP9/103, Max-Planck-Institut für Plasmaphysik (1994).
- [584] Umansky, M.V., Krasheninnikov, S.I., La Bombard, B., Terry, J.L., *Phys. Plasmas* **5** (1998) 3373.
- [585] Kögler, U., et al., *J. Nucl. Mater.* **241–243** (1997) 816.
- [586] Staudenmaier, G., *J. Vac. Sci. Technol. A* **3** (1985) 1091.
- [587] Roth, J., Ehrenberg, J.K., Wittmaack, K., Coad, J.P., Roberto, J.B., *J. Nucl. Mater.* **145–147** (1987) 383.
- [588] Mayer, M., et al., *J. Nucl. Mater.* **266–269** (1999) 604.
- [589] Mayer, M., Behrisch, R., Andrew, P.L., Coad, J.P., Peacock, A.T., *Phys. Scripta T* **81** (1999) 13.
- [590] Wang, W., Roth, J., Behrisch, R., Staudenmaier, G., *J. Nucl. Mater.* **162–164** (1989) 422.
- [591] Roth, J., et al., in *Controlled Fusion and Plasma Physics* (Proc. 10th Eur. Conf. Budapest, 1985), Vol. 9F, part 2, EPS, Geneva (1985) 543.
- [592] Roth, J., Janeschitz, G., *Nucl. Fusion* **29** (1989) 915.
- [593] Krieger, K., et al., *J. Nucl. Mater.* **241–243** (1997) 734.
- [594] Maier, H., Krieger, K., Balden, M., Roth, J., *J. Nucl. Mater.* **266–269** (1999) 1003.
- [595] Shiratani, M., Jolly, J., Videlot, H., Perrin, J., *Jap. J. Appl. Phys.* **36** (1997) 4752.
- [596] Behrisch, R., et al., *J. Nucl. Mater.* **145–147** (1987) 731.
- [597] McCracken, G.M., Goodall, D.H.J., *Nucl. Fusion* **18** (1978) 537.
- [598] Ohtsuka, H., Ogiwara, N., Maeno, M., *J. Nucl. Mater.* **93&94** (1980) 161.
- [599] Wampler, W.R., Whyte, D.G., Wong, C.P.C., West, W.P., *J. Nucl. Mater.* **290–293** (2001) 346.
- [600] Safronov, V., et al., *J. Nucl. Mater.* **290–293** (2001) 1052.
- [601] Van der Laan, J.G., *J. Nucl. Mater.* **162–164** (1989) 964.
- [602] Van der Laan, J.G., Akiba, M., Hassanein, H., Seki, M., Tanchuk, V., *Fusion Eng. Des.* **18** (1991) 135.
- [603] Linke, J., in *Fusion Technology* (Proc. 16th Symp. London, 1990), Vol. 1, Elsevier, Amsterdam (1991) 428.
- [604] Van Osch, E.V., et al., *J. Nucl. Mater.* **220–222** (1995) 781.
- [605] Anisimov, S.I., Gal'burt, V.A., Ivanov, M.F., Poyurovskaya, I.E., Fisher, V.I., *Sov. Phys. Tech. Phys.* **24** (3) (1979) 295.
- [606] Anisimov, S.I., Khokhlov, V.A., *Instabilities in Laser-Matter Interaction*, CRC Press Inc. 1995.
- [607] Tanaka, S., et al., *Rev. Sci. Instrum.* **62** (1991) 761.
- [608] Akiba, M., et al., *Plasma Dev. Oper.* **1** (1991) 205.
- [609] Nakamura, K., et al., *J. Nucl. Mater.* **233–237** (1996) 730.
- [610] Duwe, R., Kühnlein, W. Münstermann, H., in *Fusion Technology* (Proc. 18th Symp. Karlsruhe, 1994), Vol. 1, Elsevier, Amsterdam (1995) 355.
- [611] Engelko, V., et al., *J. Nucl. Mater.* **220–222** (1995) 1071.
- [612] Engelko, V., et al., *J. Nucl. Mater.* **233–237** (1996) 818.
- [613] Astrelin, V.T., *Nucl. Fusion* **37** (1997) 1541.
- [614] Astrelin, V.A., et al., in *Fusion Technology* (Proc. 18th Symp. Karlsruhe, 1994), Vol. 1, Elsevier, Amsterdam (1995) 371.
- [615] Hassanein, A., *Fusion Technol.* **26** (1995) 532.

- [616] Burdakov, A.V., et al., *J. Nucl. Mater.* **233–237** (1996) 697.
- [617] Bolt, H., Linke, J., Penkalla, H.J., Tarret, E., *Phys. Scripta T* **81** (1999) 94.
- [618] Van der Stad, R.C.L., Klippel, H.Th., Kraaij, in *Fusion Technology* (Proc. 17th Symp. Rome, 1992), Vol. 1, Elsevier, Amsterdam (1993) 401.
- [619] Burdakov, A.V., et al., *J. Nucl. Mater.* **212–215** (1994) 1345.
- [620] Arkhipov, N.I., et al., in *Plasma Physics and Controlled Nuclear Fusion Research 1988* (Proc. 12th Int. Conf. Nice, 1988), Vol. 2, IAEA, Vienna (1989) 683.
- [621] Arkhipov, N.I., et al., *J. Nucl. Mater.* **233–237** (1996) 767.
- [622] Arkhipov, N.I., et al., *J. Nucl. Mater.* **266–269** (1999) 751.
- [623] Gahl, J., et al., *J. Nucl. Mater.* **191–194** (1992) 454.
- [624] Litunovsky, V., et al., in *Fusion Engineering* (Proc. 16th IEEE/NPSS Symp. Champaign, 1995) IEEE, Piscataway New Jersey, IEEE 95CH35852, Vol. 1 (1996) 435.
- [625] Drozdov, A.A., Kuznetsov, V.E., Ljublin, B.V., Ovchinnikov, I.B., Titov, V.A., *Plasma Dev. Oper.* **5** (1997) 77.
- [626] Belan, V., et al., *J. Nucl. Mater.* **233–237** (1996) 763.
- [627] Chebotarev, V.V., et al., *J. Nucl. Mater.* **233–237** (1996) 736.
- [628] Hassanein, A., Konkashbaev, I., in *Fusion Technology* (Proc. 20th Symp. Marseille, 1998), Vol. 1 (1998) 245.
- [629] Arkhipov, N.I., et al., in *Fusion Technology* (Proc. 18th Symp. Karlsruhe, 1994), Vol. 1, Elsevier, Amsterdam (1995) 395.
- [630] Arkhipov, N.I., et al., in *Fusion Technology* (Proc. 18th Symp. Karlsruhe, 1994), Vol. 1, Elsevier, Amsterdam (1995) 463.
- [631] Wuerz, H., et al., *Fusion Technol.* **32** (1997) 45.
- [632] Martynenko, Yu.V., et al., *J. Nucl. Mater.* **258–263** (1998) 1120.
- [633] Scaffidi-Argentina, F., et al., *J. Nucl. Mater.* **283–287** (2000) 1111.
- [634] Hassanein, A., et al., *J. Nucl. Mater.* **241–243** (1997) 288.
- [635] Litunovsky, V., Kuznetsov, V.E., Ovchinnikov, I.B., Titov, V.A., in *Fusion Technology* (Proc. 20th Symp. Marseille, 1998), Vol. 1 (1998) 245.
- [636] Makhankov, A., Barabash, V., Mazul, I., Youchison, D., *J. Nucl. Mater.* **290–293** (2001) 1117.
- [637] Tubbing, B.J.D., et al., in *Controlled Fusion and Plasma Physics* (Proc. 22nd Eur. Conf. Bournemouth, 1995), Vol. 19C, part 3, EPS, Geneva (1995) 453.
- [638] JET Team, presented by G. Janeschitz, in *Plasma Physics and Controlled Nuclear Fusion Research 1992* (Proc. 14th Int. Conf. Würzburg, 1992), Vol. 1, IAEA, Vienna (1993) 239.
- [639] Deksnis, E.B., Peacock, A.T., Altmann, H., Ibbot, C., Falter, H.D., Beryllium Plasma-facing Components: JET Experience, Rep. JET-P(97) 01, JET Joint Undertaking, Abingdon, Oxfordshire, OX14 3EA, UK (1997).
- [640] Bastasz, R., et al., *J. Nucl. Mater.* **241–243** (1997) 650.
- [641] West, P., personal communication (2000).
- [642] Buzhinskij, O.I., et al., *J. Nucl. Mater.* **266–269** (1999) 793.
- [643] Janos, A.C., et al., *Plasma Physics and Controlled Nuclear Fusion Research 1992* (Proc. 14th Int. Conf. Würzburg, 1992), Vol. 1, IAEA, Vienna (1993) 527.
- [644] Martin, G., Chatelier, M., Doloc, C., in *Controlled Fusion and Plasma Physics* (Proc. 22nd Eur. Conf. Bournemouth, 1995), Vol. 19C, part 2, EPS, Geneva (1995) 44.
- [645] Gill, R.D., *Nucl. Fusion* **33** (1993) 1613.
- [646] Gill, R.D., et al., *Nucl. Fusion* **40** (2000) 163.
- [647] Ciotti, M., Franzoni, G., Maddaluno, G., *J. Nucl. Mater.* **220–222** (1995) 567.
- [648] Maddaluno, G., Pierdominici, F., Vittori, M., *J. Nucl. Mater.* **241–243** (1997) 908.
- [649] Maddaluno, G., Esposito, B., *J. Nucl. Mater.* **266–269** (1999) 593.
- [650] Maddaluno, G., personal communication (1999).
- [651] Ehrenberg, J.K., et al., *J. Nucl. Mater.* **196–198** (1992) 992.
- [652] Ehrenberg, J.K., Philipps, V., De. Kock, L., Causey, R.A., Hsu, W.L., *J. Nucl. Mater.* **176&177** (1990) 226.
- [653] Ehrenberg, J.K., et al., *J. Nucl. Mater.* **162–164** (1989) 63.
- [654] Ehrenberg, J.K., “Wall effects on particle recycling in tokamaks”, *Physical Processes of the Interaction of Fusion Plasma with Solids*, Academic Press (1996) 35.
- [655] Mueller, D., et al., *J. Vac. Sci. Technol. A* **9** (1991) 2713.
- [656] Waelbroeck, F., Esser, H.G., Winter, J., *J. Nucl. Mater.* **162–164** (1989) 713.
- [657] Jackson, G.L., Taylor, T.S., Taylor, P.L., *Nucl. Fusion* **30** (1990) 2305.
- [658] Dylla, H.F., et al., *J. Nucl. Mater.* **162–164** (1989) 128.
- [659] Philipps, V., Vietzke, E., Erdweg, M., Winter, J., *J. Nucl. Mater.* **200** (1993) 355.
- [660] Grisolia, C., et al., *J. Nucl. Mater.* **266–269** (1999) 146.
- [661] Gauthier, E., et al., *J. Nucl. Mater.* **241–243** (1997) 553.
- [662] Lysoivan, A., et al., in *Controlled Fusion*

- and Plasma Physics (Proc. 22nd Eur. Conf. Bournemouth, 1995), Vol. 19C, part 3, EPS, Geneva (1995) 341.
- [663] Winter, J., Plasma Phys. Control. Fusion **38** (1996) 1503.
- [664] Jackson, G.L., et al., J. Nucl. Mater. **176&177** (1990) 311.
- [665] Stott, P.E., et al., Nucl. Fusion **15** (1975) 431.
- [666] Goodall, D.H., J. Nucl. Mater. **111&112** (1982) 11.
- [667] Mioduszewski, P.K., et al., Nucl. Fusion **27** (1987) 195.
- [668] Bures, M., et al., J. Nucl. Mater. **176&177** (1990) 387.
- [669] Bures, M., et al., Fusion Eng. Des. **12** (1990) 251.
- [670] Kugel, H.W., et al., in Fusion Engineering (Proc. 17th IEEE/NPSS Symp. San Diego, 1997), IEEE, Piscataway New Jersey, Vol. 2 (1998) 869.
- [671] Campbell, D.J., et al., The influence of beryllium on plasma operation in JET, to appear in Fusion Eng. Des.
- [672] Winter, J., J. Nucl. Mater. **145–147** (1987) 131.
- [673] Schissel, D.P., et al., in Controlled Fusion and Plasma Physics (Proc. 17th Eur. Conf. Amsterdam, 1990) Vol. 14B, part 1, EPS, Geneva (1990) 275.
- [674] Schneider, U., et al., J. Nucl. Mater. **176&177** (1991) 350.
- [675] Dylla, H.F., J. Nucl. Mater. **176&177** (1991) 337.
- [676] Buzhinskij, O.I., Semenets, Yu.M., Fusion Technol. **32** (1997) 1.
- [677] Buzhinskij, O.I., Semenets, Yu.M., Fusion Eng. Des. **45** (1999) 343.
- [678] Rapp, J., et al., in Controlled Fusion and Plasma Physics (Proc. 26th Eur. Conf. Maastricht, 1999), EPS. CD-ROM, file P2.019 <http://epsppd.epfl.ch/Maas/web/sessions.htm#p2019>.
- [679] Waidman, G., Guangla K., Nucl. Fusion **32** (1992) 645.
- [680] Snipes, J.A., J. Nucl. Mater. **196–198** (1992) 686.
- [681] Jackson, G.L., et al., J. Nucl. Mater. **241–243** (1997) 655.
- [682] Kondo, K., et al., J. Nucl. Mater. **241–243** (1997) 956.
- [683] Sugai, H., et al., J. Nucl. Mater. **220–222** (1995) 254.
- [684] Terreault, B., J. Nucl. Mater. **220–222** (1995) 790.
- [685] Toyoda, H., et al., J. Nucl. Mater. **241–243** (1997) 1031.
- [686] Hogan, J.T., Nucl. Fusion **37** (1997) 705.
- [687] Hirooka, Y., J. Nucl. Mater. **274** (1999) 320.
- [688] Saibene, G., et al., J. Nucl. Mater. **241–243** (1997) 476.
- [689] Haas, G., et al., in Controlled Fusion and Plasma Physics (Proc. 22nd Eur. Conf. Bournemouth, 1995), Vol. 19C, part 1, EPS, Geneva (1995) 321.
- [690] Loarer, T., et al., Plasma Phys. Control. Fusion **37** (11) (1995) A203.
- [691] Mahdavi, M.A., et al., in Controlled Fusion and Plasma Physics (Proc. 20th Eur. Conf. Lisbon, 1993), Vol. 17C, part 2, EPS, Geneva (1994) 647.
- [692] Loarer, T., et al., *ibid.*, p. 607.
- [693] Maingi, R., et al., Nucl. Fusion **36** (1996) 245.
- [694] Mioduszewski, P.K., et al., J. Nucl. Mater. **220–222** (1995) 91.
- [695] Petrie, T.W., et al., Nucl. Fusion **37** (1997) 643.
- [696] Grisolia, C., Ghendrih, Ph., Peegourié, B., Grosman, A., J. Nucl. Mater. **196–198** (1992) 281.
- [697] Andrew, P.L., Pick, M.A., J. Nucl. Mater. **220–222** (1995) 601.
- [698] Grisolia, C., et al., in Controlled Fusion and Plasma Physics (Proc. 20th Eur. Conf. Lisbon, 1993), Vol. 17C, part 2, EPS, Geneva (1994) 595.
- [699] Coad, J.P., et al., J. Nucl. Mater. **226** (1995) 156.
- [700] Sartori, R., J. Nucl. Mater. **176&177** (1990) 624.
- [701] Maingi, R., et al., J. Nucl. Mater. **241–243** (1998) 672.
- [702] Lazarus, E.A., et al., Phys. Rev. Lett. **77** (1996) 2714.
- [703] Strachan, J.D., et al., Phys. Rev. Lett. **58** (1987) 1004.
- [704] Koide, Y., JT 60U Team, Phys. Plasmas **4** (1997) 1623.
- [705] Mahdavi, M.A., et al., J. Nucl. Mater. **176&177** (1991) 32.
- [706] Chankin, A., Saibene, G., Plasma Phys. Control. Fusion **41** (1999) 913.
- [707] Janeschitz, G., et al., in Controlled Fusion and Plasma Physics (Proc. 26th Eur. Conf. Maastricht, 1999), EPS. CD-ROM, file P4.021 and <http://epsppd.epfl.ch/Maas/web/sessions.htm#p4021>.
- [708] Grisolia, C., Ghendrih, P., Martin, G., Van Houtte, D., J. Nucl. Mater. **241–243** (1997) 538.
- [709] Cohen, S.A., “Particle confinement and control in existing tokamaks”, Physics of Plasma–Wall Interactions in Controlled Fusion, NATO ASI Series B: Physics, Vol. 131 (1984) 773.
- [710] TFR Group, J. Nucl. Mater. **111&112** (1982) 199.
- [711] Grisolia, C., Horton, L.D., Ehrenberg, J.K., J. Nucl. Mater. **220–222** (1995) 516.
- [712] Mayer, M., Philipps, V., Esser, H.G., Wienhold, P., Rubel, M., NATO Advanced Research Workshop (Proc. St. Petersburg, 1999), in NATO Science Series 2: Mathematics, Physics and Chemistry, Vol. 1 (2000) 9.
- [713] Mayer, M., et al., J. Nucl. Mater. **290–293** (2001) 381.
- [714] Sugihara, M., et al., J. Nucl. Mater. **266–269** (1999) 691.
- [715] Garin, P., Tore Supra Team, in Fusion Technology

- (Proc. 20th Symp. Marseille, 1998), Vol. 2 (1998) 1709.
- [716] The JET Team, Nucl. Fusion **32** (1992) 187.
- [717] Dylla, H.F., Wilson, K.L., (Eds), Tritium Retention in TFTR, Rep. PPPL-2523, Princeton Plasma Physics Laboratory and Rep. SAND88-8212, Sandia National Laboratory (1988).
- [718] Mills, B.E., Buchenauer, D.A., Pontau, A.E., Ulrickson, M.A., J. Nucl. Mater. **162–164** (1989) 343.
- [719] McGrath, R.T., Brooks, J.N., J. Nucl. Mater. **162–164** (1989) 350.
- [720] Pitcher, C.S., et al., J. Nucl. Mater. **196–198** (1992) 241.
- [721] Ramsey, A.T., et al. Nucl. Fusion **31** (1991) 1811.
- [722] Hildebrandt, D., Akbi, M., Juettner, B., Schneider, W., J. Nucl. Mater. **266–269** (1999) 532.
- [723] Ulrickson, M.A., Dylla, H.F., LaMarche, P.H., J. Vac. Sci. Technol. A **6** (1988) 2001.
- [724] Langley, R.A., Blewer, R.S., Roth, J., J. Nucl. Mater. **76&77** (1978) 313.
- [725] Ramsey, A.T., Manos, D.M., J. Nucl. Mater. **196–198** (1992) 509.
- [726] Skinner, C.H., et al., J. Nucl. Mater. **241–243** (1997) 214.
- [727] Ulrickson, M., et al., in Plasma Physics and Controlled Nuclear Fusion Research 1988 (Proc. 12th Int. Conf. Nice, 1988), Vol. 3, IAEA, Vienna (1989) 419.
- [728] Skinner, C.H., Stotler, D.P., Budny, R.V., Alder, H. Ramsey, A.T., Rev. Sci. Instrum. **66** (1995) 646.
- [729] Budny, R.V., et al., in Controlled Fusion and Plasma Physics (Proc. 21st Eur. Conf. Montpellier, 1994), Vol. 18B, part 1, EPS, Geneva (1995) 82.
- [730] Skinner, C.H., et al., Nucl. Fusion **35** (1995) 143.
- [731] Efthimion, P.C., et al., in Plasma Physics and Controlled Nuclear Fusion Research 1997 (Proc. 15th Int. Conf. Seville, 1994), Vol. 1, IAEA, Vienna (1995) 289.
- [732] Skinner, C.H., et al., J. Nucl. Mater., **241–243** (1997) 887.
- [733] Stotler, D.P., et al., Phys. Plasmas **3** (1996) 4084.
- [734] Skinner, C.H., et al., in Fusion Technology (Proc. 20th Symp. Marseille, 1998), Vol. 1 (1998) 153.
- [735] Mueller, D., et al., J. Nucl. Mater. **241–243** (1997) 897.
- [736] Mueller, D., et al., Fusion Technol. **30** (1996) 840.
- [737] Zweben, S.J., et al., in Rev. Sci. Instrum. **70** (1999) 1119.
- [738] Skinner, C.H., Gentile, C.A., Menon, M.M., Barry, R.E., Nucl. Fusion **39** (1999) 1081.
- [739] Coad, J.P., et al., J. Nucl. Mater. **162–164** (1989) 533.
- [740] Coad, J.P., Farmery, B., Vacuum **45** (1994) 435.
- [741] Coad, J.P., Andrew, P.L., Peacock, A.T., Phys. Scripta T **81** (1999) 7.
- [742] Amemiya, S., Masuda, T., Ando, T., Kodama, K., Masaki, K., J. Nucl. Mater. **220–222** (1995) 443.
- [743] Wong, C.P.C., et al., J. Nucl. Mater. **258–263** (1998) 433.
- [744] Masaki, K., personal communication (1999).
- [745] Mayer, M., Behrisch, R., Andrew, P.L., Peacock, A.T., J. Nucl. Mater. **241–243** (1997) 469.
- [746] Dylla, H.F., et al., J. Nucl. Mater. **155–157** (1988) 15.
- [747] Coad, J.P., Orchard, J., Monahan, J., J. Nucl. Mater. **160** (1988) 95.
- [748] Coad, J.P., Gibson, A., Haigh, A., Kaveney, G. Orchard, J., in Controlled Fusion and Plasma Physics (Proc. 18th Eur. Conf. Berlin, 1991), Vol. 15C, part 3, EPS, Geneva (1992) 81.
- [749] Nemeto, M., et al., J. Nucl. Mater. **220–222** (1995) 385.
- [750] Miya, N., Nemeto, M., Toyoshima, N., Fusion Technol. **26** (1994) 507.
- [751] Masaki, K., et al., Fusion Eng. Des. **31** (1996) 181.
- [752] Taylor, P.L., Kellman, A.G., Lee, R.L., J. Fusion Energy **12** (1993) 35.
- [753] Wampler, W.R. et al., Nucl. Fusion **39** (1999) 271.
- [754] Goodall, D.H.J., et al., J. Nucl. Mater. **162–164** (1989) 1059.
- [755] Sun, G.Y., et al., J. Nucl. Mater. **246** (1997) 9.
- [756] Andrew, P.L., et al., Nucl. Fusion **33** (1993) 1389.
- [757] Andrew, P.L., et al., J. Nucl. Mater. **196–198** (1992) 143.
- [758] Peacock, A.T., Coad, J.P., Dietz K. J., Knight, A. P., in Fusion Technology (Proc. 17th Symp. Rome, 1992), Vol. 1, Elsevier, Amsterdam (1993) 329.
- [759] Gibson, A., JET Team, Phys. Plasmas **5** (1998) 1839.
- [760] Laesser, R., et al., Fusion Eng. Des. **46** (1999) 307.
- [761] Hemmerich, J.L., et al., Fusion Eng. Des. **19** (1992) 161.
- [762] Peacock, A.T., et al., in Fusion Technology (Proc. 20th Symp. Marseille, 1998), Vol. 1 (1998) 233.
- [763] Peacock, A.T., et al., Fusion Eng. Des. **49&50** (2000) 745.
- [764] Coad, J.P., et al., J. Nucl. Mater. **290–293** (2001) 224.
- [765] Schleussner, D., et al., J. Nucl. Mater. **266–269** (1999) 1296.
- [766] Nygren, R.E., Sandia National Laboratories, Albuquerque, personal communication (1999).
- [767] Skinner, C.H., et al., Tritium removal from co-deposits on carbon tiles by a scanning laser, J. Nucl. Mater., in press.
- [768] Hollis, K.J., Castro, R.G., Maggiore, C.J., Ayala, A., J. Nucl. Mater. **283–287** (2000) 1085.
- [769] Hollis, K.J., Castro, R.G., Doerner, R.P., Maggiore, C.J., Fus. Eng. Des. **55** (2001) 437.
- [770] Guile, A.E., Juttner, B., IEEE Trans. Plasma Sci.,



- Vol. PS-8, No. 3259.
- [771] Alberici, S., Hinssen, H.K., Moormann, R., Wu, C.H., *J. Nucl. Mater.* **266–269** (1999) 754.
  - [772] Balden, M., Mayer, M., *J. Nucl. Mater.* **283–287** (2000) 1057.
  - [773] Orchard, J.C., et al., *J. Nucl. Mater.* **200** (1993) 395.
  - [774] Davis, J.W., Hamilton, C.G., Haasz, A.A., *J. Nucl. Mater.* **288** (2001) 148.
  - [775] Philipps, V., et al., *J. Nucl. Mater.* **266–269** (1999) 386.
  - [776] Cowgill, D.F., Sandia National Laboratories, personal communication (1997).
  - [777] Cowgill, D.F., 18th Symp. Fusion Technol., Karlsruhe (1994) and IUVESTA Conditioning Workshop, Geneva (1995).
  - [778] Outten, C.A., Barbour, J.C., Wampler, W.R., *J. Vac. Sci. Technol. A* **9** (1991) 717.
  - [779] Sakamoto, Y., et al., *J. Nucl. Mater.* **93&94** (1980) 333.
  - [780] Sakamoto, Y., et al., *J. Nucl. Mater.* **111&112** (1982) 485.
  - [781] Jacob, W., Landkammer, B., Wu, C.H., *J. Nucl. Mater.* **266–269** (1999) 552.
  - [782] Landkammer, B., Keudell, A. von, Jacob, W., *J. Nucl. Mater.* **264** (1999) 48.
  - [783] Winter, J., Formation of Dust and its Role in Fusion Devices, Rep. 68-B8-99, Institut für Experimentalphysik II, Ruhr University, Bochum, Germany (April 1999).
  - [784] Patel, B., Knipe, S., Macheta, P., Peacock, A., in Fusion Engineering (Proc. 18th IEEE/NPSS Symp. Albuquerque, 1999), IEEE, Piscataway New Jersey, IEEE 99CH3705 (1999) 338.
  - [785] Charuau, J., et al., in Fusion Technology (Proc. 17th Symp. Rome, 1992), Vol. 2, Elsevier, Amsterdam (1993) 1700.
  - [786] Pasini, D., et al., *J. Nucl. Mater.* **176&177** (1990) 186.
  - [787] Whyte, D., *Nucl. Fusion* **39** (1999) 271.
  - [788] Carmack, W.J., McCarthy, K.A., Petti, D.A., Kellman, A.G., Wong, C.P.C., *Fusion Eng. Des.* **39&40**, part A (1998) 477.
  - [789] Gorman, S.V., Carmack, W.J., Hembree, P.B., *Fusion Technol.* **34** (1998) 745.
  - [790] McCarthy, K.A., et al., *Fusion Technol.* **34** (1998) 728.
  - [791] Carmack, W.J., DIIL-D Dust Particulate Characterisation (June 1998 Vent) Rep. INEEL/EXT-1999-00095, US Department of Energy INEEL (January 1999).
  - [792] Carmack, W.J., et al., Analysis and Characterisation of TFTR Tokamak Dust, ITER Engineering Design File ITER/US/98/TE/SA-8 (April 1998).
  - [793] Chappuis, Ph., et al., *J. Nucl. Mater.* **290–293** (2001) 245.
  - [794] Hinds, W.J., *Aerosol Technology: Properties, Behaviour, and Measurement of Airborne Particles*, John Wiley, New York (1982).
  - [795] Anderl, R.A., Pawelko, R.J., in Tritium Effects in Plasma-facing Components (Proc. 4th Int. Workshop, Sante Fe, 1998), Rep. SAND99-8222, Sandia National Laboratories, Albuquerque (1999) 20.
  - [796] Brunauer, S., Emmett, P.H., Teller, E., *J. Am. Chem. Soc.* **60** (1938) 309.
  - [797] Smolik, G.R., et al., in Fusion Engineering (Proc. 17th IEEE/NPSS Symp. San Diego, 1997) IEEE, Piscataway New Jersey, IEEE 97CH36131, Vol. 1 (1998) 183.
  - [798] German, R.M., *Int. J. Powder Metall.* **32** (1996) 4.
  - [799] Weschenfelder, F., et al., *Plasma Phys. Control. Fusion* **38** (1996) A311.
  - [800] Garscadden, A., Ganguly, B.N., Haaland, P.D., Williams, J., *Plasma Sources Sci. Technol.* **3** (1994) 239.
  - [801] Hollenstein, Ch., Dorier, J.L., Dutta, J., Sansonnens, L., Howling, A.A., *Plasma Sources Sci. Technol. A* **3** (1994) 278.
  - [802] Sharpe, J.P., Bourham, M., Gilligan, J.G., in Fusion Engineering (Proc. 17th IEEE/NPSS Symp. San Diego, 1997), IEEE, Piscataway New Jersey, IEEE 97CH36131, Vol. 1 (1998) 153.
  - [803] Sharpe, J.P., Bourham, M., Gilligan, J.G., *Fusion Technol.* **34** (1998) 634.
  - [804] Sharpe, J.P., Bourham, M., Gilligan, J.G., *Fusion Technol.* **30** (1996) 1424.
  - [805] Philipps, V., personal communication (1999).
  - [806] Coad, J.P., Skorodumov, B.G., Ulanov, V.G., Wu, C.H., *Vacuum* **47** (1996) 986.
  - [807] Von Seggern, J. et al., *Phys. Scripta T* **81** (1999) 31.
  - [808] Bosch, H-S., et al., *J. Nucl. Mater.* **220–222** (1995) 558.
  - [809] Pitcher, C.S., Goetz, J.A., LaBombard, B., Lipschultz, B., in Controlled Fusion and Plasma Physics (Proc. 24th Eur. Conf. Berchtesgaden, 1997), Vol. 21A, part 2, EPS, Geneva (1997) 581.
  - [810] McCracken, G.M., Stangeby, P.C., *Plasma Phys. Control. Fusion* **27** (1985) 1411.
  - [811] Stangeby, P.C., *Nucl. Fusion* **33** (1993) 1695.
  - [812] Krasheninnikov, S.I., Pigarov, A.Yu., Sigmar, D.J., *Contrib. Plasma Phys.* **36** (1996) 314.
  - [813] Borrass, K., Janeschitz, G., *Nucl. Fusion* **34** (1994) 1203.
  - [814] Lipschultz, B., *J. Nucl. Mater.* **266–269** (1999) 370.
  - [815] Pitcher, C.S., et al., *J. Nucl. Mater.* **241–243** (1997) 696.
  - [816] Braginskii, S.I., *Rev. Plasma Phys.* **1** (1965) 205.
  - [817] Braams, B., NET Rep. EUR-FU/XII-80-87-68 (1987).
  - [818] Braams, B.J., Thesis, Utrecht University, Nether-

- lands (1986).
- [819] Schneider, R., et al., *J. Nucl. Mater.* **196–198** (1992) 810.
  - [820] Rognlien, T.D., Milovich, J.L., Rensink, M.E., Porter, G.D., *J. Nucl. Mater.* **196–198** (1992) 347.
  - [821] Knoll, D.A., Prinja, A.K., Campbell, R.B., *J. Comput. Phys.* **104** (1993) 418.
  - [822] Rognlien, T.D., Braams, B.J., Knoll, D.A., *Control. Plasma Phys.* **36** (1996) 105.
  - [823] Simonini, R., et al., *J. Nucl. Mater.* **196–198** (1992) 369.
  - [824] Simonini, R., Corrigan, G., Radford, G., Spence, J., Taroni, A., *Contrib. Plasma Phys.* **34** (1994) 368.
  - [825] Petravic, M., *Phys. Plasmas* **1** (1994) 2207.
  - [826] Shimizu, K., et al., *J. Nucl. Mater.* **220–222** (1995) 410.
  - [827] Pitcher, C.S., *Vac. Technol. Appl. Ion Phys.* **38** (1988) 1059.
  - [828] Heifetz, D.B., et al., *J. Comput. Phys.* **46** (1982) 309.
  - [829] Stotler D., Karney C., *Contrib. Plasma Phys.* **34** (1994) 392.
  - [830] Reiter, D., Randschicht-Konfiguration von Tokamaks: Entwicklung und Anwendung stochastischer Modelle zur Beschreibung des Neutralgas-transportes Rep. JUEL-1947, Kernforschungsanlage Jülich, Germany (1984) (in German).
  - [831] Reiter, D., May, C., Coster, D., Schneider, R., *J. Nucl. Mater.* **220–222** (1995) 987.
  - [832] Cupini, E., De Matteis, A., Simonini, R., Hotston, E.S., Harrison, M.F.A., Monte-Carlo Studies of Helium Pumping and Sputtering in the INTOR Divertor, Rep. (DE) EUR-XII-324-26/NET-NR. 26 (1984), Commission of the European Communities, Brussels(BE)/NET Next European Torus, Garching.
  - [833] Knoll, D.A., Krashenninnikov, S.I., McHugh, P.R., Sigmar, D., *Phys. Plasmas* **3** (1996) 3358.
  - [834] Becker, G., *Nucl. Fusion* **39** (1999) 95.
  - [835] Kukushkin, A.S., personal communication (1999).
  - [836] Brooks, J.N., *Phys. Fluids* **8** (1990) 1858.
  - [837] Stangeby, P.C., Elder, J.D., *J. Nucl. Mater.* **196–198** (1992) 258.
  - [838] Evans, T.E., Finkenthal, D.F., in *Atomic Processes in Plasmas* (Proc. Amer. Inst. Phys. Conf., New York, 1998), AIP Press **443** (1998) 58.
  - [839] Hogan, J.T., BBQ: Impurity Scrape-Off Layer Transport Code, Rep. ORNL-TM-13 312, Oak Ridge National Lab, Oak Ridge, Tennessee, USA (1996).
  - [840] Brooks, J.N., in *Atomic and Plasma–Material Interaction Processes in Controlled Thermonuclear Fusion*, Elsevier, Amsterdam (1993) 403.
  - [841] Brooks, J.N., *Nucl. Technology/Fusion* **4** (1983) 33.
  - [842] Naujoks, D., Behrisch, R., Coad, J.P., De Kock, L., *Nucl. Fusion* **33** (1993) 581.
  - [843] Kirschner, A., Philipps, V., Winter, J., Kögler, U., *Nucl. Fusion* **40** (2000) 989.
  - [844] Alman, D.A., Ruzic, D.N., Brooks, J.N., *Phys. Plasmas* **7** (2000) 1421.
  - [845] Brooks, J.N., Brice, D.K., Dewald, A.B., McGrath, R.T., *J. Nucl. Mater.* **162–164** (1989) 363.
  - [846] Hua, T.Q., Brooks, J.N., *J. Nucl. Mater.* **220–222** (1995) 342.
  - [847] Coad, J.P., et al., in *Controlled Fusion and Plasma Physics* (Proc 26th Eur. Conf. Maastricht, 1999), EPS. CD-ROM, file OR.14 and <http://epsppd.epfl.ch/Maas/web/sessions.htm#or14>.
  - [848] Khandagle, M.J., et al., *J. Nucl. Mater.* **207** (1993) 116.
  - [849] Hogan, J.T., et al., *Plasma Physics and Controlled Nuclear Fusion Research* (Proc. 16th Int. Conf. Montreal, 1996), Vol. 2, IAEA, Vienna (1997) 625.
  - [850] Guo, H.Y., et al., *J. Nucl. Mater.* **266–269** (1999) 825.
  - [851] Erents, S.K., et al., in *Controlled Fusion and Plasma Physics* (Proc 26th Eur. Conf. Maastricht, 1999), EPS. CD-ROM, file P1.040 and <http://epsppd.epfl.ch/Maas/web/sessions.htm#p1040>.
  - [852] Brooks, J.N., *Fusion Technol.* **18** (1990) 239.
  - [853] Brooks, J.N., “Recent progress in tritium co-deposition modelling”, *Hydrogen Isotope Recycling at Plasma-Facing Materials in Fusion Reactors* (Proc. 9th Advanced Research Workshop), proceedings to be published.
  - [854] Brooks, J.N., Ruzic, D.N., Hayden, D.B., *Fusion Eng. Des.* **37** (1997) 455.
  - [855] Sestero, A., Ventura, A., *J. Nucl. Mater.* **128&129** (1984) 828.
  - [856] Gilligan, J., Hanh, D., *J. Nucl. Mater.* **145–147** (1987) 391.
  - [857] Bolt, H., Harano H., Madarame, H., Okamoto, K., Tanabe, K., *J. Nucl. Mater.* **196–198** (1992) 948.
  - [858] Hobel, H., et al., *J. Nucl. Mater.* **196–198** (1992) 537.
  - [859] Wuerz, H., et al., *J. Nucl. Mater.* **212–215** (1994) 1349.
  - [860] Wuerz, H., et al., *J. Nucl. Mater.* **220–222** (1995) 1066.
  - [861] Bazylev, B., et al., in *Controlled Fusion and Plasma Physics* (Proc. 22nd Eur. Conf. Bournemouth, 1995), Vol. 19C, part 2, EPS, Geneva (1995) 277.
  - [862] Lengyel, L.L., et al., *Nucl. Fusion* **38** (1998) 1435.
  - [863] Pestchanyi, S., Wuerz, H., Bazylev, B., Kappler, F., Landman, I., in *Controlled Fusion and Plasma Physics* (Proc. 24th Eur. Conf. Berchtesgaden, 1997), Vol. 21A, part 3, EPS, Geneva (1997) 981.

- [864] Lalousis, P., Lengyel, L., Rozhansky, V., Spathis, P., Veselova, I., in *Controlled Fusion and Plasma Physics (Proc. 22nd Eur. Conf. Bournemouth, 1995)*, Vol. 19C, part 2, EPS, Geneva (1995) 285.
- [865] Hassanein, A., et al., *Fusion Technol.* **1** (1994) 223.
- [866] Hassanein, A., Evaluation of Disruption Erosion, Task report, Rep. ITER/US/98-IV-DV-0.4 (1998).
- [867] Kawamura, T., Obayashi, H., Miyahara, A., *Fusion Eng. Des.* **9** (1989) 45.
- [868] Kunugi, T., *Fusion Eng. Des.* **23** (1993) 329.
- [869] Merola, M., *J. Nucl. Mater.* **202** (1993) 29.
- [870] Bartels H.W., in *Fusion Technology (Proc. 17th Symp. Rome, 1992)*, Vol. 1, Elsevier, Amsterdam (1993) 181.
- [871] Raffray, A.R., Federici, G., *J. Nucl. Mater.* **244** (1997) 85.
- [872] Federici, G., et al., in *Fusion Engineering (Proc. 16th IEEE/NPSS Symp. Champaign, 1995)*, IEEE, Piscataway New Jersey, IEEE 95CH35852, Vol. 1 (1996) 430.
- [873] Raffray, A.R., et al., in *Fusion Technology (Proc. 20th Symp. Marseille, 1998)*, Vol. 1 (1998) 211.
- [874] Cohen, S.A., et al., *Plasma Phys. Control. Fusion* **29** (1987) 1205.
- [875] Hirooka, Y., Masuzaki, S., Suzuki, H., Kenmotsu, T., Kawamura, T., *J. Nucl. Mater.* **290–293** (2001) 423.
- [876] Horton, L.D., et al., *J. Nucl. Mater.* **196–198** (1992) 139.
- [877] Reiter, D., The edge plasma, *Physical Processes of the Interaction of Fusion Plasma with Solids*, Academic Press (1996) 1.
- [878] Hogan, J.T., et al., *J. Nucl. Mater.* **241–243** (1998) 612.
- [879] Mioduszewski, P.K., et al., *J. Nucl. Mater.* **121** (1984) 285.
- [880] Andrew, P.L., Peacock, A.T., Pick, M.A., *J. Nucl. Mater.* **196–198** (1992) 997.
- [881] Hogan, J.T., et al., *J. Nucl. Mater.* **196–198** (1992) 1083.
- [882] Eckstein, W., *J. Nucl. Mater.* **248** (1997) 1.
- [883] Audenarde, K., Emmert, G.A., Gordinier, M., *J. Comput. Phys.* **34** (1980) 268.
- [884] Sugihara, M., et al., in *Controlled Fusion and Plasma Physics (Proc. 24th Eur. Conf. Berchtesgaden, 1997)* Vol. 21A, part 3, EPS, Geneva (1997) 997.
- [885] Rehker, S., Wobig, H., *Plasma Phys.* **15** (1973) 1083.
- [886] Brice, D.K., Doyle, B.L., Wampler, W.R., Picraux, S.T., Haggmark, L.G., *J. Nucl. Mater.* **114** (1983) 277.
- [887] Saibene, G., et al., *J. Nucl. Mater.* **176–177** (1990) 618.
- [888] Rossi, A., et al., *J. Nucl. Mater.* **266–269** (1999) 922.
- [889] Philipps, V., Ehrenberg, J.K., *J. Vac. Sci. Technol. A* **11** (2) (1993) 437.
- [890] Haas, G., Maingi, R., Neuhauser, J., *J. Nucl. Mater.* **266–269** (1999) 1065.
- [891] Hillis, D.L., et al., *J. Nucl. Mater.* **290–293** (2001) 418.
- [892] Nakamura, H., et al., Rep. JAERI-M-86-175, JAERI (1986).
- [893] Grisolia, C., Gauthier, E., Grosman, A., Monier-Garbet, P., Tsitrone, E., in *Controlled Fusion and Plasma Physics (Proc. 20th Eur. Conf. Lisbon, 1993)*, Vol. 17C, part 2, EPS, Geneva (1994) 595.
- [894] Goodall, D.H.J., Andrew, P.L., Ehrenberg, J., *J. Nucl. Mater.* **196–198** (1992) 1002.
- [895] Martin, G., Lewin, G., *J. Vac. Sci. Technol.* **3** (1) (1965) 6.
- [896] Dylla, H.F., *J. Vac. Sci. Technol. A* **6** (3) (1988) 1276.
- [897] Wilson, K., Hsu, W.S., *J. Nucl. Mater.* **145** (1987) 121.
- [898] McCracken, G.M., et al., *Nucl. Fusion* **18** (1978) 35.
- [899] Terrault, B., TFR Group, Terrault, B., *J. Nucl. Mater.* **127** (1985) 18.
- [900] LaMarche, P.H., Dylla, H.F., McCarthy, P.J., Ulrickson, M., *J. Vac. Sci. Technol. A* **4** (3) (1986) 1198.
- [901] Ehrenberg, J.K., *J. Nucl. Mater.* **145–147** (1987) 551.
- [902] Stangeby, P.C., Auciello, O., Haasz, A.A., Doyle, B., *J. Nucl. Mater.* **122&123** (1984) 1592.
- [903] Federici, G., Wu, C.H., *J. Nucl. Mater.* **186** (1992) 131.
- [904] Waelbroeck, F., Influence of Bulk and Surface Phenomena on the Hydrogen Permeation through Metals, Rep. JUEL-1966, Jülich, Institut für Plasmaphysik, Association Euratom-KfA (1984).
- [905] Wienhold, P., et al., Computer Code PERI, Rep. JUL-1825, IPP-KfA Jülich (1983).
- [906] Longhurst, G.R., Holland, D.F., Jones, J.L., Merrill, B.J., TMAP4 User's Manual, Rep. EGG-FSP-10315, Idaho National Engineering and Environmental Laboratory (1992).
- [907] Cho, S., Raffray, R.A., Abdou, M.A., *J. Nucl. Mater.* **212–215** (1994) 961.
- [908] Dalle Donne, M., Scaffidi-Argentina, F., Ferrero, C., Ronchi, C., *J. Nucl. Mater.* **212–215** (1994) 954.
- [909] Longhurst, G.R., et al., *J. Nucl. Mater.* **258–263** (1998) 640.
- [910] Forty, C.B.A., Forrest, R.A., Compton, J.J., Rayner, C., *Handbook of Fusion Activation Data, Part 1: Elements Hydrogen to Zirconium*, Rep. AEA UFS 180, AEA Technol. Fusion, Euratom/UKAEA Fusion Association (1992).
- [911] Behrisch, R., Khripunov, V., Santoro, R.T., Yesil,

- J.M., J. Nucl. Mater. **258–263** (1998) 686.
- [912] Forrest, R.A., Endacott, D.A.J., Fispack User Manual, Rep. AERE-M-3654 (Rev), Harwell Laboratory, Oxfordshire, UK (1990).
- [913] Forty, C.B.A., Forrest, R.A., Compton, J.J., Rayner, C., Handbook of Fusion Activation Data, Part 2: Elements Niobium to Bismuth, Rep. AEA UFS 232, AEA Technol. Fusion, Euratom/UKAEA Fusion Association (1993).
- [914] Moeller, W., Scherzer, B.M.U., Ehrenberg, J., J. Nucl. Mater. **111&112** (1982) 669.
- [915] Anderl, R.A., Longhurst, G.R., Struttman, D.A., J. Nucl. Mater. **145–147** (1987) 344.
- [916] Anderl, R.A., Holland D.F., Longhurst, G.R., J. Nucl. Mater. **176&177** (1990) 683.
- [917] Longhurst, G.R., et al., Verification and Validation of TMAP4, Rep. EGG-FSP-10347, INEEL Report, Idaho Nat. Eng. and Env. Lab. (July 1992).
- [918] Anderl, R.A., Hankins, M.R., Longhurst, G.R., Pawelko, R.J., Macaulay-Newcombe, R.G., J. Nucl. Mater. **196–198** (1992) 986.
- [919] Lomidze, M.A., Gorodetsky, A.E., Zakharov, A.P., Fusion Technol. **28** (1995) 1211.
- [920] García-Rosales, C., Franzen P., Plank, H., Roth, J., Gauthier, E., J. Nucl. Mater. **233–237** (1996) 803.
- [921] Franzen, P., et al., J. Nucl. Mater. **241–243** (1997) 1082.
- [922] Venhaus, T., Causey, R.A., Doerner, R., Abeln, T., J. Nucl. Mater. **290–293** (2001) 505.
- [923] Hsu, W.L., et al., J. Nucl. Mater. **176&177** (1990) 218.
- [924] Causey, R.A., Longhurst, G.L., Harbin, W., J. Nucl. Mater. **241–243** (1997) 1041.
- [925] Anderl, R.A., et al., Fusion Technol. **21** (1992) 745.
- [926] Longhurst, G.R., personal communication (1999).
- [927] Wampler, W.R., Sandia National Laboratories, Albuquerque, NM, unpublished data.
- [928] Federici, G., et al. in Fusion Engineering (Proc. 16th IEEE/NPSS Symp. Champaign, 1995), IEEE, Piscataway New Jersey, Vol. 1 (1996) 418.
- [929] Federici, G., et al., Phys. Scripta, **T91** (2001) 76.
- [930] Longhurst, G.R., Anderl, R.A., Dolan, T.J., Mulock, M.J., Fusion Technol. **28** (1995) 1217.
- [931] Federici, G., Holland, D., Janeschitz, G., Wu, C.H., J. Nucl. Mater. **241–243** (1997) 260.

E-mail address of G. Federici:

federici@post.rzg.mpg.de

Subject classification: Po, Ti; I2, Tm; I1, Tm